Evolution of Magnetic Fields in the Solar Atmosphere

A THESIS

submitted for the Award of Ph.D. degree of

Mohan Lal Sukhadia University

in the

Faculty of Science

BY

B. Ravindra

Under the Supervision of

Professor P. Venkatakrishnan

Professor and Head

UDAIPUR SOLAR OBSERVATORY

PHYSICAL RESEARCH LABORATORY, UDAIPUR

MOHANLAL SUKHADIA UNIVERSITY, UDAIPUR

Year of Submission: 2004

CERTIFICATE

This is to certify that the thesis entitled "Evolution of Magnetic Fields in the Solar Atmosphere" submitted for the award of the degree of Doctor of Philosophy of Mohanlal Sukhadia University in the faculty of Science is a record of bona fide investigations carried out by Shri. B. Ravindra under my supervision and guidance.

This is an original piece of work on which no one has been awarded a degree in this University or in any other University.

The literary presentation of the thesis is satisfactory and it is in a form suitable for publication. The work presented in the thesis has been done after registration in this University.

Further, the candidate has put in attendance of more than 200 days in this institution as required under rule 7(b) and thus completed the residential requirement.

Professor P. Venkatakrishnan
(SUPERVISOR)

To my parents, brother and sister.

Contents

List of Figures

List of Tables

Acknowledgements

It is of great pleasure to thank my supervisor Prof. P. Venkatakrishnan for his valuable guidance throughout this work. He gave me lots of encouragement and confidence in pursuing this thesis whenever I was stuck with some problem. His aspiration to carry out outstanding research work has always been a source of inspiration for me. It was a great experience to work with him. I thank him for having given me this opportunity.

I thank the Director, Prof. Girish Agarwal, Physical Research Laboratory for providing me all the necessary facilities to carry out my thesis work. I thank the Chairman, Academic committee for his support throughout my stay at USO.

I would like to express my gratitude to Dr. R. Sridharan and Dr. K. Sankarasubramanian for their help and encouragement at various stages of my thesis.

I am thankful to Brajesh, Sanjay and Raja for their help and company at USO.

Thanks to Dr. Ashok Ambastha, Dr. Nandita Srivastava, Dr. Sushant Chandra Tripathy, Dr. Debi Prasad Choudhary, Dr. Kiran Jain and Dr. Shibu Mathew for their help at various stages of my thesis.

No words can express my gratitude to "Dr. SOHO". I am deeply indebted to the SOHO/EIT and SOHO/MDI teams for the use of their data. SOHO is a joint ESA and NASA program for international cooperation. Also, many thanks to the NSO/Kitt Peak team. The NSO/KP data used in this thesis were produced cooperatively by NSF/NOAO, NASA/GSFC and NOAA/SEC. The velocity data of CMEs used in this thesis is generated and maintained in a CME catalog by NASA and The Catholic University of America in cooperation with the Naval Research Laboratory. I would like to thank Dr. N. Gopalswamy for generously providing the data on the CME speed which were not available in the CME catalog. I also thank BBSO team for maintaining the H_α *full disk data in BBSO FTP archive.*

I thank the staff Mr. Raju Koshy, Mr. Rakesh Jaroli, Mr. C. P. Suthar, Mr. Sudhir Kumar Guptha, Mr. Naresh Jain, Mr. B. L. Paneri, Mr. Ramachandra Carpenter, Mr. Laxmilal Suthar, Mr. Dalchand Purohit, Mr. Shankarlal Paliwal and Mr. Jagadish Singh Chouhan for their help at various stages and providing me the friendly

environment at USO.

The help of library staff Mr. Jitesh Jain is acknowledged. The library with wealth of knowledge in the form of books and journals is one of the helping hands and it helped me whenever I needed some references in physics, solar physics and other things unrelated to my thesis. I also thank Nirvikar, Lokesh, Tilak and Virendra for creating friendly atmosphere at USO.

Many thanks to the BGS and administrative section of IIA for providing me all the facilities during my stay at IIA. I can not forget the company of my friends at IIA, Manoj, Mahesh, Ravinder, Rajesh, Arun, Sivarani and Dr. Partho are thanked for bearing with me. Special thanks to Mr. Ravinder Kumar for downloading and sending me the solar data whenever I needed, without him it would have been impossible for me to progress in my work. I thank my batch-mates Manoj, Preeti and Geethanjali and all my juniors and seniors at IIA for having given me the memorable environment.

I would like to thank the Ph.D section of Mohanlal Sukhadia University for their kind co-operation throughout my thesis.

Thanks to Mrs. Madhulika for providing me delicious food during the final stages of my thesis and Mrs. Leela Bai for her kind services.

I remember the homely environment provided by Prof. P. Venkatakrishnan and his family, Dr. Ashok Ambastha and his family, Mr. Brajesh Kumar and his family, Mr. Sudhir Guptha and his family and Mr. Sanjay and his family with frequent invitations for lunch and dinner. I thank all of them.

Finally, not-in-least, I thank my family, to whom this thesis is dedicated. Without their encouragement and support it would have been very difficult to finish this thesis. They gave enough support without bothering me which made me concentrate on the work much more than what I could have. I thank all of them for this. I hope they will continue their support in the same way in future.

B. Ravindra

Abstract

Understanding the solar magnetic field has always been a vital issue in solar physics. Recent space missions such as YOHKOH, SOHO, and TRACE showed a new view of the transition region and corona which are structured by the magnetic field. These missions highlighted the pervasive role of magnetic fields in determining the nature of the important physical processes driving solar activity and variability. Most importantly, these new observations have laid new emphasis on the intrinsic relationship between small-scale processes and large-scale phenomena. Solar activity takes many forms, from the large-scale, long-term patterns of the solar cycle to the relatively short-term transients like solar flares and CMEs. Even the quiet Sun displays a startling level of activity and dynamics. All these diverse activities are magnetic in origin. An important consequence of solar activity is the effect of it on the Earth. The long-term variations of the solar radiative output can have an effect on terrestrial climate as evidenced by the Little Ice Age associated with the Maunder sunspot minimum. On a much shorter time scale, transient activity at the Sun creates dramatic responses at the Earth. The modern demands for satellite communications for our daily activities have made us far more susceptible to the capriciousness of the Sun. The motivation of the present study is to investigate the relationship between the high energy radiation, particle emission and the evolution of magnetic fields on all spatial and temporal scales. This work presents a combination of small-scale dynamics and small-scale phenomena, and large-scale dynamics and large-scale phenomena. This thesis is organized as follows:

The first Chapter highlights the importance of magnetic field evolution in the production of high energy radiation and particle emission, which affect the terrestrial climate and space weather. The various types of magnetic field evolution in the solar atmosphere are described. Finally, a brief description about the contents of each Chapter is presented.

The second Chapter is concerned with the assertion that the magnetic field is a source of excitation of helium ion in the solar atmosphere. The difficulty with the first proposed source of excitation such as coronal radiation in brightening the network cells observed in He II $\lambda 304$ Å images is explained. A detailed comparison of the photospheric magnetic field morphology with the network morphology observed in He II $\lambda 304$ Å and their one-to-one

association is discussed. Also, quantitative relationship between the intensity of the network element observed in He II λ304 Å and the absolute value of the magnetic field is presented. Finally, the height of formation of the He II λ304 Å network elements is discussed.

The third Chapter is concerned with the estimation of lifetime and size of the network cells observed in photospheric magnetograms and He II λ304 Å filtergrams. The estimated lifetime and sizes of the network cells formed at two different heights are compared. The similarity in the characteristics of the extrapolated magnetic network at a height of 3000 km above the photosphere with the He II λ304 Å network cells is discussed.

The prime objective of the fourth Chapter is to study the sources of the active region chromosphere/coronal brightening. The magnetic field variations found at 3 mHz and 5.5 mHz with the help of power spectrum analysis are presented. The phenomena of inward and outward motion of features that appear to be originating from the penumbra are described. The possible contribution of these features to the long-term magnetic field variations are also discussed. The energy flux available from the magnetic field fluctuations to heat the active region corona is discussed.

The prime objective of the fifth Chapter is to look for the driver for the large-scale eruptive phenomena. A detailed study showed that the active region magnetic energy is the driver for the eruptive phenomena like CME. The relationship between the velocity of a CME and the estimated magnetic potential energy is discussed in comparison with the Sedov relation between the speed of a blast wave and the blast energy. There is no change in magnetic flux and magnetic energy when one considers the active region as a whole. The non-potential nature of the active region magnetic field and its contribution to the active region magnetic energy is discussed. At the end, the relationship between the estimated CME velocity and the observed GOES X-ray peak flux is presented.

The last Chapter provides the summary and conclusion of this thesis work. The thesis ends with a brief description of the future work.

Chapter 1

Introduction

1.1 The Sun and the Earth

The Sun is our nearest and dearest star. It is the source of energy, which sustains life on the planet Earth. It gives steady warmth and light. The Sun is the earth's universal time-keeper, governing the seasons, the harvests, and even the sleep patterns of the creatures populating our planet. Apart from providing steady warmth and light, the Sun affects the near Earth space and terrestrial atmosphere in a variety of ways. Broadly, there are two kinds of processes by which it can affect the Earth's atmosphere, namely

- the high energy radiation and
- the particle emission.

The formation of the ionosphere and the density and temperature variations in the thermosphere, primarily depend on the solar high energy radiation especially from the extreme ultraviolet (EUV) and X-rays. The high energy radiation from the Sun in the form of EUV rays can destroy the ozone layers during extreme conditions of solar activity.

The coronal mass ejections (CMEs) are phenomena in which material is ejected from the corona in the form of charged particles. The more energetic component of these particles can damage the satellites, communication systems and power grids as well as can be hazardous to the astronauts. Apart from these, energetic particles manifest as aurora in the polar regions.

It is now well believed that the solar magnetic field plays a major role in the production of high energy radiation and particle emissions. This strong belief follows from the observed enhancement in the high energy radiation and particle emission during solar maximum activity. In a way, the solar magnetic field can also be said to influence the Earth's weather and climate (e.g. Parker, 1999).

1.2 The solar magnetic fields

Solar magnetic fields virtually control all the dynamics observed in the solar atmosphere. By means of this control, the solar magnetic fields affect the terrestrial climate and weather. The solar EUV radiation varies in parallel with solar activity cycle, being higher during maximum solar activity conditions. The major features which can contribute to the solar EUV radiation are, network, faculae, pores and sunspots. These features are structured and energized by the magnetic field. The magnetic polarity of the global magnetic field is reversed in every 11-years. The 11-year periodicity in the Sun's activity is called the solar cycle. The total radiation output is also known to vary with the solar cycle. The total magnetic flux reaches a maximum during the peak of a cycle and drops almost to zero during the minimum. Figure 1.1 shows a series of magnetograms spanning a period of almost a solar activity cycle. The East-West orientation of the magnetic field in active regions was found to be opposite in the northern and southern hemispheres, and switches every 11-year cycle. Almost all the radiation mechanisms in the chromosphere, transition region and corona are coupled to the dissipation of magnetic energy, which leads to plasma heating. The radiation output is correspondingly modulated from solar maximum to minimum, e.g. in soft and hard X-rays, γ-rays and radio wavelengths. This modulation can be seen in the coronal images. Coronal images show that the regions in the corona which are spatially related to sunspots, display pronounced X-ray and EUV emissions. This enhanced emission can be seen clearly in Figure 1.2. The coronal image obtained in soft X-ray shows that there is an enhanced emission during solar maximum and reduced emission during minimum.

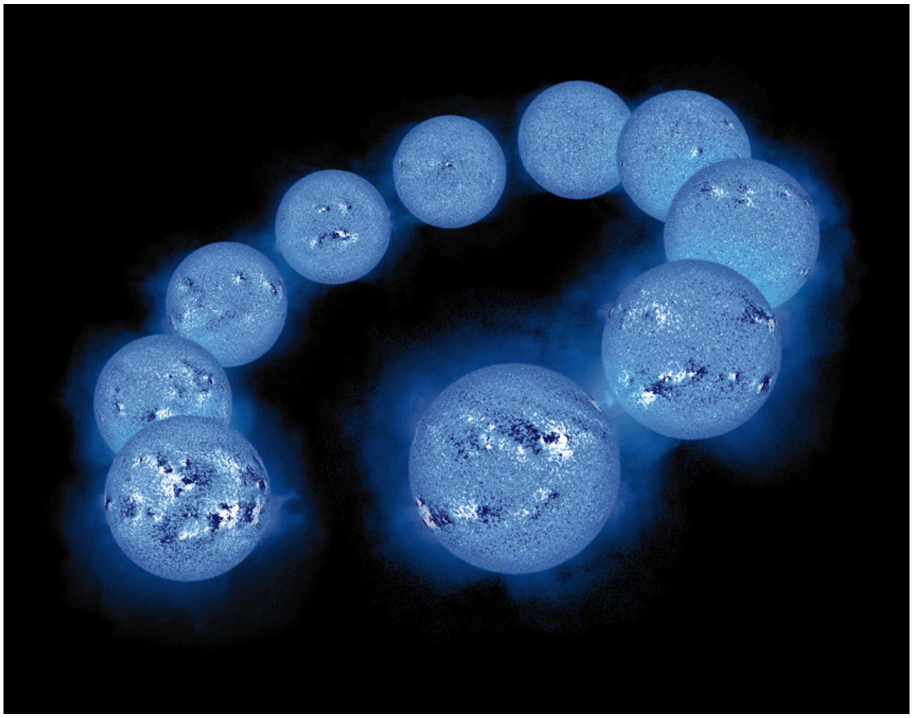

Figure 1.1: A series of photospheric magnetograms spanning a period of almost a solar activity cycle from 8 January 1992 to 25 July 1999, recorded with the vacuum telescope of the National Solar Observatory at Kitt Peak. Black and white patches represent opposite polarities of the line-of-sight magnetic field on the Sun. The gray shade represents the zero magnetic field.

Solar flares and CMEs are powered by the release of magnetic energy stored in coronal magnetic fields (Gold and Hoyle, 1960; Moore *et al.*, 1980; Sturrock, 1980).

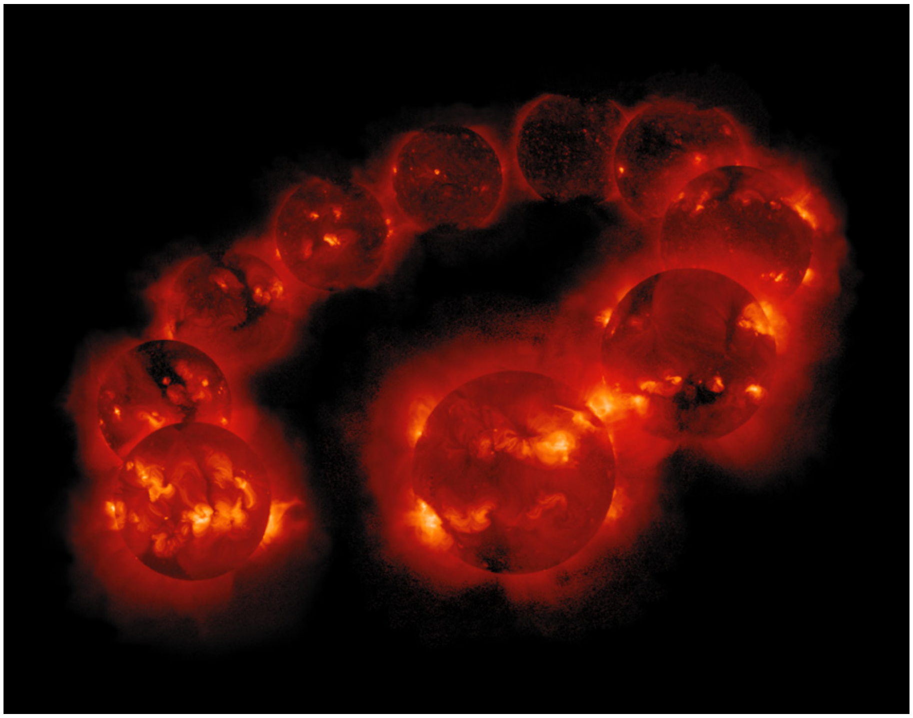

Figure 1.2: A series of soft X-ray images of the Sun, covering the same period as in Figure 1.1. These images have been recorded with the Solar X-ray Telescope (SXT) on the YOHKOH spacecraft.

This conclusion is reinforced by observations of CMEs such as one shown in Figure 1.3. The image shows that a CME has loop like structure, expands in the forward direction and carries material to the interplanetary space. CMEs tend to occur when the balance of forces, that maintain a coronal loop in equilibrium, is upset. The upward forces dominate over the downward forces in the process of ejection. Even though the gas pressure is dominant in the photosphere, the CMEs occur at coronal heights where the plasma $\beta << 1$, i.e., where the magnetic pressure dominates the plasma pressure, especially within the active regions. Therefore the only energy which can push the material to the distant heliosphere is magnetic energy. The magnetic energy builds up from the gradual stressing of the field by foot-point motions. This is a phase of quasi-static evolution.

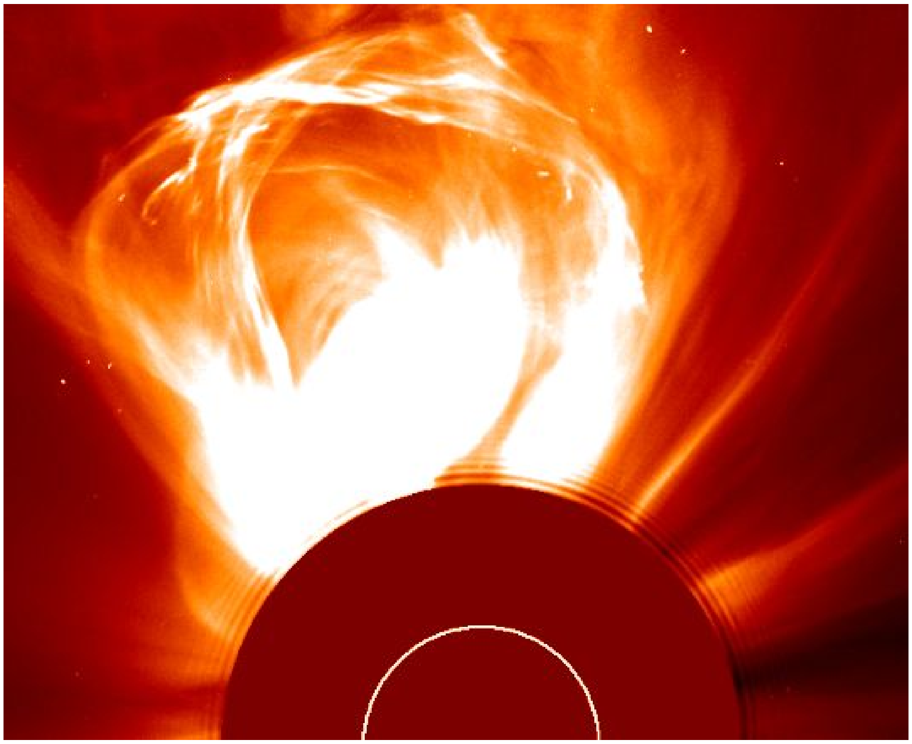

Figure 1.3: An image of the outer solar corona showing a large coronal mass ejection. The expanding loop in the corona is seen to carry material to the interplanetary space.

1.3 The Sun-Earth connection

The EUV radiation and particle emission affects the terrestial atmosphere. These EUV and X-ray radiations form the source of heating of the Earth's upper atmosphere and also create the ionosphere. The solar magnetic field is the main cause for these excess EUV radiation and particle emissions. A static magnetic field cannot be responsible for the aforesaid phenomena, it is the sun's ever changing magnetic field that holds the key to the aforementioned processes. In other words, evolution of the magnetic fields in the solar atmosphere influences some aspects of the space weather and the Earth's climate. It is very important to study the evolution of magnetic field to predict the space weather and understand the subtle long-term variations in the Earth's climate.

1.4 Evolution of the solar magnetic fields

Magnetic field evolution occurs on various time scales, from minutes to that of the solar activity cycle. The key to understand the solar activity is to study the Sun's ever-changing magnetic field. All manifestations of solar activity and perhaps the solar chromosphere / transition region / corona and solar wind, exist because of solar magnetism. Basically, there are three types of evolution of magnetic fields in the solar atmosphere, they are:

- global
- active region
- small-scale

1.4.1 Global evolution of magnetic field

The newly born, compact bipolar magnetic field regions associated with sunspots, always obey Hale's polarity law. According to this law, the East-West polarity orientation is opposite in the northern and southern hemispheres and the orientation gets reversed when a new 11-year activity cycle starts. The law does not always hold good in the case of older, partially decayed magnetic regions, since the spread-out fluxes merge with the remnants of other bipolar regions and with the background field. During the course of the 11-year cycle, the zones of emergence of bipolar magnetic flux migrate towards the equator. New cycle starts when sunspot groups of reversed polarity orientation first appear at higher latitudes. During sunspot minimum, the background magnetic field is of mixed polarity. At the south pole, the flux of one polarity and at the north pole, the flux of opposite polarity will be dominating. The polarity of the preceding spot will be the opposite polarity of the follower spot. The same polarity will repeat after every 22-year, called as magnetic activity cycle. The 22-year magnetic activity cycle is a long-term activity of the Sun's large-scale magnetic field. A full magnetic cycle of about 22-years, after which the original magnetic configuration is restored, is called a Hale cycle.

The 11-year solar activity consists of a solar maximum and a minimum. During solar maxima a large number of sunspots are present. The presence or absence of sunspots influences the Earth's climate. In the 17th century, the absence of sunspots during the Maunder Minimum made the temperature of the Earth cooler than the present (Eddy, 1983).

1.4.2 Evolution of magnetic fields in active regions

A variety of evolving patterns can be found in the active regions. Some of these are:

- evolution related to eruptive phenomena, which includes the solar flares and coronal mass ejections.
- short time magnetic field fluctuations, which includes solar magnetic oscillations.

1.4.2.1 Evolution related to eruptive phenomena

Active regions are the sites of sudden release of energy like solar flares and ejection of material like CME. The frequency of occurrence of CMEs is related to the solar cycle, but unlike the global magnetic fields, these events have a duration of a few minutes to hours. At the cycle maximum, several large as well as small flares can be observed on most of the days. These solar flares are always located near sunspots and occur more often when sunspots are numerous. This does not mean that sunspots cause solar flares, but it does suggest that solar flares are energized by the magnetism associated with sunspots.

Solar flares and CMEs are magnetic phenomena, thought to derive their energy from the coronal magnetic fields. However, the flares and CMEs originate in the corona, while it is very difficult to measure the coronal field strengths. With advances in the measurement of the photospheric magnetic field, now it is possible to reconstruct the coronal magnetic field using extrapolations with photospheric flux distribution as the boundary condition and some reliable assumptions such as the field at the corona is force-free. The coronal magnetic fields are tied to the photosphere and hence it is useful to examine the photospheric magnetic field changes before, during and after the flare or CME events.

Detection of variations of magnetic fields associated with solar flares and CMEs has been one of the most important problems in solar physics for many years. Such detection would provide direct evidence of magnetic energy release in the flares and CMEs. Many researchers looked for the change in magnetic field parameters since 1980s, with ambiguous results. Using vector magnetic field data, one could measure the magnetic shear in an active region by comparing the observed magnetic field direction with the potential field computed from the line-of-sight field. The results were ambiguous: the shear angle associated with the active region which produced M and X class flares would decrease (Sakurai *et al.*, 1992; Ambastha, Hagyard and West, 1993), increase (Wang *et al.*, 1994) or remain unchanged (Hagyard, Stark, and Venkatakrishnan, 1999; Li *et al.*, 2000). Chen *et al.* (1994) studied more than 20 M class flares and concluded that there was essentially no change in active region magnetic fields associated with the flares.

Studies of flares have shown that they frequently occur in magnetically complex regions, such as δ spots (Gaizauskas *et al.*, 1998) which are known to have highly sheared fields. Flares seem to be linked with emerging flux regions (Martres *et al.*, 1968). Zhang and Wang (2002) examined the magnetic evolution in the source active region for a few flare-CME events. They found that the main magnetic changes are magnetic flux emergence in the form of moving magnetic features (MMFs) in the vicinity of the main (positive) magnetic field and concluded that the repeated flare-CME activities are triggered by the continuous emergence of MMFs.

Further, many researchers attempted to predict the onset of CMEs from the photospheric vector magnetic field data (Falconer, Moore, and Gary, 2002) and recently from the line-of-sight magnetograms (Falconer, Moore, and Gary, 2003). Falconer (2001) showed that the measurements of strong-field strong-shear main neutral line and global net current are the more reliable predictors of the CME productivity of active regions than the presence or absence of sigmoidal structure in coronal X-ray images of the regions. They further suggested that there might be threshold values of these predictors above which CME production is likely and below which CME production is unlikely.

Since the coronal instability initiating the CME is not able to alter the photospheric vertical magnetic field strength significantly, one cannot expect to observe the magnetic field changes at the photospheric level as a result of a flare or CME. However, in the current era of space based observations, researchers have started examining the changes in the active region and its magnetic field parameters during a flare or a CME. Lara, Gopalswamy, and DeForest (2000) used MDI data to search for the change in photospheric active region magnetic flux of 8 active regions before, during and after the CMEs. They found that the observed magnetic flux in the entire active region showed no obvious change during CME, but the flare associated CMEs occurred during the maximum phase of magnetic flux emergence. Localized modes of variability with an average period of 13 minutes are found in one-minute temporal resolution solar magnetic fields at the time of CME activity (Boberg and Lundstedt, 2000) and these field variations are not found during quiet conditions. Kosovichev and Zharkova (2001) studied high resolution MDI magnetogram data for the 2000 July 14 “Bastille Day Flare” and found a permanent decrease in magnetic flux and a short-term magnetic transient. The first phenomenon was interpreted as the release of magnetic energy and the second by high-energy electrons bombarding the solar surface.

Spirock, Yurchyshyn, and Wang (2002) studied the X20 flare on 2001 April 2, (the largest solar flare near the limb) and found that, after the flare, the magnetic flux of the leading polarity increased by ≈ 6×10^{20} Mx, however there was no obvious change in the magnetic flux in the following polarity. The explanations for the observed characteristics are: (1) the observed changes were the result of new flux emergence and/or (2) a change of the direction of the field from vertical to tangential. Wang *et al.* (2002a) reported the changes in the longitudinal magnetic field at the photospheric level around the time of flare associated with six X-class flares. They found an impulsive change in each of the six cases studied which they proposed to be permanent. For two events they found that impulsive increase of the transverse field strength and magnetic shear after the flares, as well as new sunspot area in the form of penumbral structure. They give three possible explanations to explain the observed changes: (1) the emergence of very inclined flux loops, (2) a change in the magnetic field direction and (3) the expansion of the spot, which moved some flux out of Zeeman saturation. They also found that the flux of leading polarity tends to increase while the flux of following polarity tends to decrease slightly. On the other hand, Wang *et al.* (2002b) found an evidence for the rapid disappearance of a small sunspot associated with a M2.4 flare. The sunspot with size 45 arc $\sec^2$ disappeared in about 60 minutes, coinciding with the on-set of the flare. The disappearing sunspot was located near the edge of the main hard X-ray source observed by Reuven Ramaty High-Energy Solar Spectroscopic Imager (RHESSI). This hard X-ray source was located in the magnetic neutral line dividing the disappearing spot and the opposite polarity flux. They have given the following two possible explanations for the events: (1) the disappearing spot is due to the rapid magnetic reconnection and subsequent submergence and (2) the disappearing sunspot represents impulsive emergence and detachment of a magnetic “bubble”.

Recently Moon *et al.* (2002a) have shown that the occurrence of homologous flares in an active region is physically related to the injection of magnetic helicity by horizontal photospheric motions. By computing the change in magnetic helicity using SOHO/MDI magnetograms, they showed that the flare X-ray flux integrated over the X-ray emission time strongly correlates with the magnetic helicity injected during the flaring interval. The integrated X-ray flux increased logarithmically with the injected magnetic helicity.

The works of many people have shown that there is no unambiguous evidence of photospheric magnetic field change during flares. One of the reason for this result can be that the magnetic field is measured at the photospheric level, but most of the energy release occurs in the upper solar atmosphere, transition region and corona. Also while using the longitudinal data to study CME or flare on-sets, it is better to look for the long-term evolution of the magnetic field in the period leading up to the CME or flare to find clues on the instability which results in an eruption. In addition, one has to study in detail the magnetic field parameter in relation with the energetics of CME and flare. An initial approach is to establish simple empirical relationships, which connect the magnetic field parameters and the energetics of CMEs and flares. Understanding the empirical relationships and their connections to the theoretical models will help to identify the sources and origin of the energetic events.

1.4.2.2 Short time magnetic field fluctuations

In early 70's the discovery of sunspot umbral oscillations (Bhatnagar, Livingston, and Harvey, 1972; Giovanelli, 1972; Beckers and Schultz, 1972) attracted the attention of many theorists, as it seemed that the umbral oscillations could provide unique information about the sub-photospheric structure of sunspots. Observations in spectral lines formed at different heights of a sunspot atmosphere show oscillations of velocity (Doppler shifts) and of intensity (that is, of thermodynamic quantities). There are apparently three different kinds of oscillations in sunspot umbrae, with periods around 3 minutes, 5 minutes and $\geq$ 20 minutes. These oscillations are likely to be produced by different physical mechanisms. The 5 minute oscillations may be represented as the passive response of the sunspot to forcing by the p-mode oscillations in the surrounding convection zone (Thomas, Cram, and Nye, 1981), whereas the 3 minute oscillations could represent a resonant oscillation of the sunspot itself (Staude, 1999;

Bogdan, 2000).

With recent progress in measuring the magnetic field with high sensitivity and low noise, many investigators found evidence for magnetic oscillations within the sunspots. Many researchers (Horn, Staude, and Landgraf, 1997; Rüedi *et al.*, 1998; Norton *et al.*, 1999; Kupke, LaBonte, and Mickey, 2000; Bellot Rubio *et al.*, 2000) have found magnetic field strength oscillations in the 3 and 5 minute band. The signal obtained by these authors is not strong. The recent observations show high power in usually small, inhomogeneously distributed patches, that is these oscillations are limited to much smaller regions in contrast to the ubiquitous velocity oscillations and often occur near umbral penumbral boundary (Rüedi *et al.*, 1998). Balthasar (1999) does not find a periodic signature and looks for stochastic excitation mechanism. The reality of the measured field strength fluctuations has been doubted on different grounds. Zhugzhda, Balthasar, and Staude (2000) finds that the strongest power of magnetic field oscillations was concentrated in the centers of small spots or pores, which were found outside the large spots. In the larger spots the enhanced power is found mainly at the boundary between umbra and penumbra, which is a ring like structure, while velocity power covers a great part of the umbra. They conclude in their paper that “the discovery of the magnetic field oscillations shows that a modeling of sunspot oscillations as a single-mode oscillations is not sufficient. These magnetic oscillations are not a single mode oscillations, they are multi-mode oscillations and multi-frequency oscillations as well”.

Magnetic oscillations in sunspot atmosphere are still under investigation. Various processes could result in spurious magnetic signals and should be carefully studied and corrected for. However the existing observations, high resolution polarimeter two-dimensional data covering complete sunspots in particular, often show significant magnetic field strength oscillation power at the boundary of umbra-penumbra and in small flux concentrations (pores). These magnetic field strength oscillations cannot be explained by the cross talk from velocity, density and temperature oscillations only.

This field of research is still awaiting for more reliable data preferably in the infra-red regimes with high resolution, so that the localized oscillations are not diluted by averaging with the neighboring flux tubes in the resolution element. Along with the high frequency fluctuations there are low frequency fluctuations of magnetic field strength (Lites *et al.*, 1998) in sunspots. Only a few attempts have been made to detect those fluctuations, but the origin for those fluctuations still remains a question. With the present space based high resolution magnetogram data there are no attempts to search for those low frequency fluctuations, which are less likely to be contaminated by the cross talk.

1.4.3 Small-scale magnetic field evolution

Convection is one of the important energy transport mechanisms in the solar interior. There are four solar convective patterns observed or proposed: (1) granulation, (2) mesogranulation, (3) supergranulation and (4) giant cells. Only granules and supergranules have been unambiguously identified and well studied.

Even though the supergranulation is a convective manifestation, it forms a pattern called network cells in association with the magnetic field, first discovered by Hart (1956) and then followed by Simon and Leighton (1964). The network coincides with the boundaries of the photospheric velocity cells. The large horizontal motions of the plasma inside the supergranular cells sweep the frozen-in field lines towards the cell boundaries. The edges of the supergranulation match the chromospheric network. The magnetic network coincides with the emission network seen in different spectral lines, with highest contrast for lines formed in the chromosphere and transition region.

Feldman, Dammasch, and Wilhelm (2000) describe the transition region as the solar upper atmosphere below 8×10^5 K temperature with unresolved fine structures. In the transition region, many elements such as He I, He II, Ne VII, C III, S VI, O VI, Ne VIII, etc. emit in ultraviolet wavelength. The transition region is not simply a thin, spherically symmetric shell around the Sun. It is highly structured due to the presence of magnetic field. The magnetic field fills all the available space in transition region, albeit inhomogeneously. The location of the transition region varies in time along a given magnetic field line in response to the coronal heat input (Solanki and Hammer, 2001).

The most prominent structure of the transition region is the network, an extension of the supergranular network cells from the chromosphere. These structures are brightest in the network boundaries, less bright in the interior of the cells. At upper transition region temperature (beyond $\approx 2.5\times10^5$ K) the network widens more rapidly and diffuses, hence they cannot be recognized beyond $\approx 10^6$ K. Even the appearance of the structures in the coronal hole and quiet Sun are similar except for their brightness. The network elements are always in motion, they collide with each other and move away from each other. While colliding, if they are of similar polarity, they will merge with each other and if they are of opposite polarity they seem to annihilate possibly through a reconnection process. The reconnection events could explain most of the dynamics of the transition region and these reconnections can reconfigure the field lines. Dowdy (1993) studied the magnetic field configuration over supergranulation cells and found some evidence for loop structures at transition region temperatures. The detailed comparison between the magnetograms and O VI spectroheliograms showed some evidence for the mixed polarity magnetic region in the supergranulation network to be related to the emitting structures observed in O VI. He suggested that the observed structures were loops producing a major portion of the total O VI transition region emission. As a result, the network has ever changing patterns of the magnetic flux tubes. With increasing temperature, the network structure starts disappearing, other structures like loops start dominating.

Even though, a number of elements and ions in transition region emit in UV and EUV and the energy available in the transition region is sufficient to keep them in the excitation state, the available energy is not sufficient to explain the excitation of helium and its ion in the solar atmosphere. The excitation of the helium ion in the solar atmosphere is not clearly understood. This field of research is currently very active and ongoing. Recent results from instruments like SUMER and CDS on SOHO satellite, combined with simultaneous ground-based observations and rocket experiment such as SERTS gave a lot of new information about the excitation mechanism of the helium in transition region. There were many attempts to compare the lines of helium with the other lines both spatially and temporally (Athay, 1988; Andretta *et al.*, 2000). The present situation is that the data are complex and the interpretation needs input from the magnetohydrodynamic calculations.

1.5 Organization of the thesis

As has been already mentioned, there are two kinds of solar processes that is high energy radiation and particle emission that affect the space weather and Earth's atmosphere. The Sun's magnetic field controls these two processes. In order to predict the variability in the Earth's climate and space weather, one needs to understand the Sun's ever-changing magnetic field. All types of aforementioned evolution of magnetic fields in the solar atmosphere is worthy of study. Many attempts have been made to study all the patterns of magnetic evolution in the past. But there are some unsolved and challenging problems to be addressed. In this thesis, we have studied the solar magnetic field evolution in relation to specific cases of high energy radiation and particle emission from the Sun. We have devoted the next three Chapters of the thesis to the study of magnetic field evolution and its influence on the producion of high energy radiation. Lastly, we discuss the relationship between the kinematics of particle emission (CME) and the active region magnetic field parameters.

The thesis is organized as follows:

- In the second Chapter we discuss the excitation of helium ion in the solar atmosphere. We chose this topic because the He II 304 Å line is one of the brightest extreme ultraviolet emission line next to H I Lyman α in the solar atmosphere and a dominant source of ionizing radiation in the thermosphere of the Earth's upper atmosphere. The excitation mechanism of helium ion in the solar atmosphere is still an unsolved question. Starting from Zirin (1975) to Andretta *et al.* (2000) several authors have proposed different mechanisms, ranging from radiative excitation to collisonal excitation. We studied the magnetic field to address this problem. The question we posed is: Is there any quantitative relationship between the magnitude of the magnetic field and the brightness of the network cells observed in He II 304 Å? We found that one cannot ignore the role of magnetic field in the network brightening observed in He II 304 Å (Ravindra and Venkatakrishnan, 2003a). We further showed that there is a relationship between the magnitude of the magnetic field and network brightness observed in He II 304 Å. In addition we discussed the height of formation of network elements observed in He II 304 Å.

- Patsourakos *et al.* (1999) have shown that as the temperature increases the size of the network element increases. Then the question that follows is: What is the lifetime of the network cells observed in transition region line, for example in He II 304 Å line and what are their sizes? Another unsolved problem is that: why the lifetime of the photospheric magnetic network cells differs from that of the transition region network cells? With the availability of continuous space-based data, which are free from seeing and night time interruptions, we have attempted to answer the aforementioned questions (Ravindra and Venkatakrishnan, 2003b). In the third Chapter, we show that the discrepancy in the lifetime and cell size observed at two different heights can be solved by using the magnetic field extrapolation of the photospheric magnetic field to a height of about 3000 km above the photosphere.

- In the fourth Chapter, we have made an attempt to answer the important question: What is the reason for the brightening of the active region corona in the solar upper atmosphere? Motivated by the earlier results (Ulrich, 1996) on the solar magnetic field oscillations, we attempted to answer this important question. We discuss the peak in the power spectrum of magnetic field fluctuations found at 5.5 and 3 mHz. We also discuss the origin of low frequency oscillations in sunspots.

- Motivated by the results that the intensity of geomagnetic storms is well related to the initial velocity of CME (Srivastava and Venkatakrishnan, 2002), we sought an answer to the question: Which property of the associated AR determines the initial velocity of the CME? In order to answer this question, we chose a magnetic field parameter, namely magnetic energy. In the fifth Chapter, we discuss the empirical relationship between the velocity of a CME and magnetic potential energy of the associated active region (Venkatakrishnan and Ravindra, 2003). No sudden change in flux and potential magnetic energy was observed during the CMEs for all the selected cases. We also discuss the importance of non-potential nature of the active region magnetic field to the CME speed.

In summary, with the help of space-based observations which are free from seeing effect and night time interruptions, we have worked on some problems highlighting the influence of magnetic field in the production of high energy radiation and particle emission. We studied the structure and evolution of different sized solar features on different time scales. We also studied the energetics involved in the small as well as in large spatial and temporal scales. An attempt to determine empirical relationships between the parameters of magnetic field and energetics of CMEs was made. Finally, we end the thesis by summarizing the results obtained in each Chapter.

Chapter 2

A study of correlation between the He II λ304 Å network brightening and photospheric magnetic field

2.1 Introduction

Helium, the second most abundant element in the universe, was first detected in the Sun during a total solar eclipse. Since helium is an inert gas, it cannot form molecules with other elements. Because of its very high first excitation potential ($\approx$ 20 eV), it is very difficult to detect its existence in the photosphere of the Sun. Helium lines are associated with the chromosphere and transition region of the Sun and the solar type stars. In fact, the presence of helium lines is considered as a typical chromospheric and transition region indicator for stars of spectral type later than A.

He II λ304 Å images obtained from *Skylab* and from Extreme ultraviolet Imaging Telescope (EIT, Delaboudiniere *et al.*, 1995) on board Solar and Heliospheric Observatory (SOHO, Domingo, Fleck, and Poland, 1995), show clumpy plasma structures with temperature of $\approx 8\times10^4$ K in the quiet Sun. These clumpy plasma structures are brightest at network boundaries and are less bright in the interiors of cells. This difference in the appearance of their brightness has to do with the excitation mechanism of the helium ions. The excitation mechanism for helium and its ion in the solar atmosphere has not yet been identified conclusively. Helium spectroheliogram exhibit dual nature. It shows the morphology of the chromosphere, such as plages and network. At the same time it follows the morphology of the corona as well, such as coronal holes. This dual connection of the helium spectroheliogram with the chromospheric and coronal structures added an interesting question viz., what mechanism can excite the helium ion in the solar atmosphere?

2.1.1 Photo-ionization versus collisonal excitation

The photoionization-recombination (PR) mechanism (Goldberg, 1939; Hirayama, 1971; Zirin, 1975) was the first mechanism proposed for the excitation of helium ion. Essentially, coronal photons at wavelengths shortward of 228 Å ionize He II, which on recombination to an excited level can produce 304 Å radiation. In Zirin's (1975) view, this PR mechanism would be responsible for the formation of the entire helium spectrum in the Sun, including the resonance lines and continua of He I and He II.

On the other hand, Jordan (1975) suggested that the observed absolute and relative line intensities can be explained by rapid mixing of low temperature helium atoms and ions with higher temperature electrons (temperature greater than the ionization equilibrium value). At the same time, Shine, Gerola, and Linsky (1975) computed diffusion models and found that diffusion can lead to an enhancement of helium emission, since diffusion lifts helium ions to regions of higher electron temperature. The diffusion of ions increases with steeper temperature gradients and with increasing excitation potential. Avrett, Vernazza, and Linsky (1976) showed that collisional excitation at temperatures beyond 2.2 $\times 10^4$ K can produce a He II λ304 Å photon and the He I and He II continua are formed by recombination following photoionization by coronal lines. Later, by using Doppler images of C IV (1548 Å) and He II (1640 Å), Athay (1988) concluded that collisions in high temperature (8×10^4 K) plasma play a major role in the excitation of He II in both active and quiet regions. Kohl (1977) found that $\approx 28\%$ photoionization recombination and $\approx 72\%$ collisional excitation can together explain the observed He II λ1640.4 Å profile. Jordan *et al.* (1993) supported the conclusion of Kohl (1977) that the 304 Å line is formed by collisional excitation in the quiet Sun, but PR mechanism may play a significant role in active regions and in many flares. Andretta *et al.* (2000) showed that small-scale (micro-turbulent) velocities could explain the enhancement of the He II λ304 Å line with respect to other transition region emission lines produced in the same temperature range (velocity redistribution).

In the case of He I excitation, the PR mechanism is feasible (Hirayama, 1971; Zirin, 1975). Detailed calculations by Hearn (1969a, 1969b) show that radiative and collisional excitation processes are important for He I lines while collisional excitation process alone dominates for the He II resonance line. Andretta and Jones (1997) investigated the formation of He I line by complete radiative transfer calculations using a grid of model atmospheres. They favor a mixed (PR with collisional) formation mechanism as it explains the hybrid (chromospheric and coronal) character of the He I triplet line and the strength and shape of the observed He I resonance lines.

2.1.2 Helium and magnetic field

A comparison of *Skylab* mission's He II λ304 Å spectroheliograms with the Ca II K λ3934 Å spectroheliograms (Tousey *et al.*, 1973) shows that their morphology is similar. Harvey and Sheeley (1977) found one -to- one association between the He II λ304 Å and He I λ10830 Å images. They went one step further and confirmed that strong network elements observed in He II λ304 Å and He I λ10830 Å were associated with small magnetic bipolar network regions. The *Skylab* mission observations showed that the helium network tends to be brighter adjacent to large-scale reversal of magnetic polarity. The same results were confirmed later (Thompson *et al.*, 1993) using the SERTS-3 images of He II λ304 Å and these images are compared with the He I λ10830 Å images and with the magnetograms taken in Fe I λ8688 Å. From the morphological differences between the coronal and He II λ304 Å images, Venkatakrishnan (1999) argued that He II excitation is independent of coronal radiation and the magnetic field distribution is more important for the He II network brightening. He proposed collisional excitation by non-thermal electrons produced in nano-flare events as a mechanism to excite the He II ions.

The Extreme ultraviolet Imaging Telescope on board SOHO spacecraft gives a unique opportunity to compare the coronal image with that of the transition region He II image at 304 Å. Notwithstanding recent progress towards understanding the excitation mechanisms of the helium ion emission lines (Andretta *et al.*, 2000) in terms of a dynamical plasma, it is imperative to look for the physical conditions that can sustain the dynamics. The enhancement of chromospheric and transition region emission at the network boundaries suggests that the magnetic field might be important. In this Chapter, we make a quantitative study of the correlation between He II λ304 Å network brightness and the line-of-sight magnetic field (hereafter magnetic field) strength. We go further and establish that a better correlation is obtained at some height above the photosphere, which is consistent with Gabriel's (1976) model. We also find that exceptions to the general relation between the magnetic field and He II λ304 Å brightness occur in regions where the topology of the magnetic field appears different from the general network topology. In the following Section, we describe the details of the data selected for our study and its analysis. The results and discussions are summarized in subsequent Sections.

2.2 Data

The EIT is one of the 12 instruments on board the SOHO satellite. It is a telescope of Ritchey-Chretien design and obtains full disk images of the Sun in four narrow pass-bands. The detailed information about the instrument can be found in Delaboudiniere *et al.* (1995). The four narrow pass-bands are selected to provide temperature sensitivity to plasmas in the range from 0.06 to 3 MK. In this way, the EIT is able to obtain images of the magnetically confined hot plasma in coronal loops as well as much cooler material in features such as the chromospheric network. The EIT obtains full disk solar images in passbands centered at λ171 Å (Fe IX), λ195 Å (Fe XII), λ284 Å (Fe XV) and λ304 Å (He II) over a 45 arc-min square field of view with a spatial resolution limited only by the $2''.629$ pixel size of the CCD image sensor.

The Michelson Doppler Imager (MDI, Scherrer *et al.*, 1995) on board SOHO provides magnetograms in addition to providing the Doppler velocity and continuum intensity images for helioseismology purposes. MDI instrument constructs the line-of-sight magnetograms by measuring the Doppler shifts (from the weighted minimum of the line profile) separately in right and left circularly polarized components of the incoming beam in Ni I λ6768 Å line. The difference between these two is a measure of the Zeeman splitting and is proportional to the magnetic flux density, for vertical magnetic flux elements observed near the center of the solar disk (the measured line-of-sight component of the magnetic field averaged over the resolution element). SOHO/MDI provides a full disk magnetogram with a two pixel resolution of 4 arc-sec.

At National Solar Observatory, Kitt Peak (NSO/KP), the photospheric Fe I λ8688 Å (g-factor is 1.661) line is isolated by a Littrow spectrograph. The left and right circularly polarized light of the longitudinal Zeeman splitting of the spectral lines are analyzed by the liquid crystal retarders and detected by a CCD camera (with spatial resolution $1''.14$ pixel^{-1}) (Jones *et al.*, 1992). The line-of-sight fields are obtained by taking the difference of the wavelengths of the weighted minima of the line profiles of the left and right circular polarization measurements.

We collected 49 images of He II λ304 Å from the archive of SOHO/EIT along with the corresponding Fe I λ8688 Å full-disk line-of-sight magnetograms of NSO/KP vacuum telescope for different days spanning the period from 1996 to 1999 (hereafter data-set I). The selection criteria were the following:

(1) There should not be any active region within 500″ from the disk center.

(2) The EIT He II λ304 Å image snapshot time should lie within the NSO/KP magnetogram build-up time slot.

(3) The He II λ304 Å images should have minimum missing blocks and there should be a full-disk, high resolution magnetogram for the selected He II λ304 Å image time.

We also collected another set of line-of-sight magnetograms from the archive of MDI recorded with a cadence of 1 minute along with He II λ304 Å images recorded with a cadence of 7 minute for one full day (05 March 1999) (hereafter data-set II).

We chose ten images of the corona taken in extreme ultraviolet wavelength at λ171 Å, λ195 Å and λ284 Å along with He II λ304 Å images of different days spanning the period from 1996 to 2000. We used this data to compare the features of the coronal and transition region images when the Sun is at different epochs of its activity.

2.2.1 Data analysis

2.2.1.1 Pre-processing

The level zero data of He II λ304 Å images, collected from the SOHO/EIT data archive were dark subtracted, flat fielded, degridded, normalized to one second exposure rate and then saved in the flexible image transport format (FITS) with date and time of observation as the file name using the solar soft routines (Freeland and Handy, 1998). The NSO/KP Fe I λ8688 Å full disk magnetic images were multiplied by a constant 1.46 to convert them to units of Gauss. This correction factor takes into account, the Landé g-factor of the Fe I λ8688 Å line, the dispersion of the spectrograph, the efficiency of the polarimeter and a phase lag associated with the CCD camera (Wang *et al.*, 1997).

2.2.1.2 Limb matching

The plate scale of NSO/KP magnetogram ($1''.14$ pixel^{-1}) is different from that of He II λ304 Å image ($2''.629$ pixel^{-1}). First, the full size 1788×1788 pixel images of NSO/KP were interpolated (using bilinear interpolation) to 1024×1024 pixels which is the window size of the He II λ304 Å image. In order to match the limb (hence FOV and plate scale), the ratio of the of the Sun's image in He II λ304 Å and Fe I λ8688 Å magnetograms was multiplied with the window size of the Fe I λ8688 Å magnetogram and the magnetogram was then interpolated to match the limb of the He II λ304 Å image. Then the matching of the limbs of the full disk He II λ304 Å images and magnetograms were confirmed by visual inspection. The apparent limb heights in He II λ304 Å and in continuum differ by only 0.72% of the radius of the continuum limb. Hence, the small difference in the apparent limb heights in the limb matching calculation can be neglected.

2.2.1.3 Registration and gradient estimation

To compensate for the solar rotation during the time between the two observations, we derotated the magnetogram by choosing a strong feature on the solar disk. As the magnetogram has been degraded to the resolution of SOHO/EIT, the mis-match of the network features within two swaths (of the magnetogram build up procedure) is well within a pixel. Then we selected a 220×220 pixel region of the magnetograms and He II λ304 Å images from the center of the disk and registered them with sub-pixel accuracy. The registration was achieved by cross-correlating (Sridharan, 2003) the absolute value of the magnetic field with the He II λ304 Å images. We then selected a 200×200 pixel image portion from the registered images to avoid the wrapped areas. By this procedure the transition region images were registered with the magnetograms to well below the size of the magnetic network element. The magnetograms were smoothed by 3×3 pixels to reduce the weak field noise. The horizontal gradient maps of the magnetic fields were made using the relation,

$$|\nabla B_z| = \sqrt{\frac{(B_z(x_2) - B_z(x_1))^2}{(x_2 - x_1)^2} + \frac{(B_z(y_2) - B_z(y_1))^2}{(y_2 - y_1)^2}}$$

where $B_z(x_1)$, $B_z(x_2)$, $B_z(y_1)$ and $B_z(y_2)$ are the vertical magnetic field strengths at the adjacent pixels in the x and y directions respectively.

2.2.1.4 Potential extrapolation

The extrapolation of the photospheric magnetic field using a constant α force-free magnetic field (with α=0) in plane geometry, in terms of Fourier transforms was developed (Alissandrakis, 1981; Nakagawa and Raadu, 1972) and the algorithm was tested on the double vertical dipole model (Gary, 1989) and with the solution of the Helmholtz equation (Arfken and Weber, 1995). For the potential extrapolation of the line-of-sight magnetic field, we selected a 128×128 pixel region from the registered magnetogram (registered with the corresponding He II λ304 Å filtergrams). The height of the extrapolated magnetic field was measured in terms of the horizontal length (length of the selected window) as a reference scale. The potential extrapolation is another form of low pass filter and all the small-scale features and noise will be attenuated as the height increases. In our potential extrapolation calculation, only the mean field will remain at large heights (upper boundary condition). Since the value of the extrapolated field at network boundary is much larger than the mean field, the domain of our calculations is far removed from the effects of the upper boundary condition. The absolute value of the computed magnetic field at different heights was cross-correlated with the He II λ304 Å images. While cross-correlating the potential extrapolated magnetic field with the He II λ304 Å images, we have made 2 assumptions:

(1) The intensity of the He II λ304 Å image is related to the local magnetic field strength.

(2) The size of the potential extrapolated magnetic field network elements should become equal to the size of the He II λ304 Å network elements at some height.
If the enhancement of the network element is due to the magnetic field, then the potential extrapolated field should take the same size and shape of the He II λ304 Å network elements at the height of formation of He II λ304 Å network element. If the above mentioned assumptions are correct, then we should get a maximum cross-correlation of the absolute value of extrapolated magnetic field with He II λ304 Å images at that height and that height could well be the formation height of the He II λ304 Å network elements.

We selected 82 line-of-sight magnetograms from the data-set II closest in time to the 82 He II λ304 Å images. We followed the same analysis procedure as mentioned above and used this data set for the potential extrapolation calculation.

2.2.1.5 Registration of magnetograms and He II λ304 Å image series

For studying the influence of magnetic field on the He II λ304 Å network structure with time, we used data-set II. The magnetograms were interpolated to the size of He II λ304 Å image and then derotated (to the first image time). We improved the signal to noise ratio by averaging 10 magnetograms recorded at an interval of 1-minute. The 350×350 pixel image portions were extracted from the averaged magnetograms and then saved in FITS format. The series of magnetogram portions were co-aligned with each other using a two-dimensional cross-correlation program. For each image, the previous image (which was registered to the first image) was the reference image. After each image registration we extracted a 200×200 pixel window image. A similar procedure was applied to the series of He II λ304 Å images. These registered sets of images were used to calculate the changes in the cross-correlation coefficient as a function of time.

2.3 Results

2.3.1 Comparison of coronal image with He II λ304 Å image

Figures 2.1 and 2.2 show a portion of the Sun obtained from the full disk images observed in He II λ304 Å and Fe XII λ195 Å wavelength. The Fe XII λ195 Å image shows the morphology of corona such as loops and coronal holes. Instead, the He II λ304 Å image shows network like morphology in the quiet as well as in the coronal hole part of the Sun. The comparison of He II λ304 Å image with the coronal image in Fe XII λ195 Å shows that there is a He II λ304 Å network brightening for every brightening of the coronal emission, but the converse is not true. If the network brightening is mainly due to PR mechanism, then the shower of photons from the corona should make the features in the He II λ304 Å much broader and more diffused than the coronal features. Since the morphology of He II λ304 Å images is dominated by chromospheric morphology while the coronal images show a different morphology,

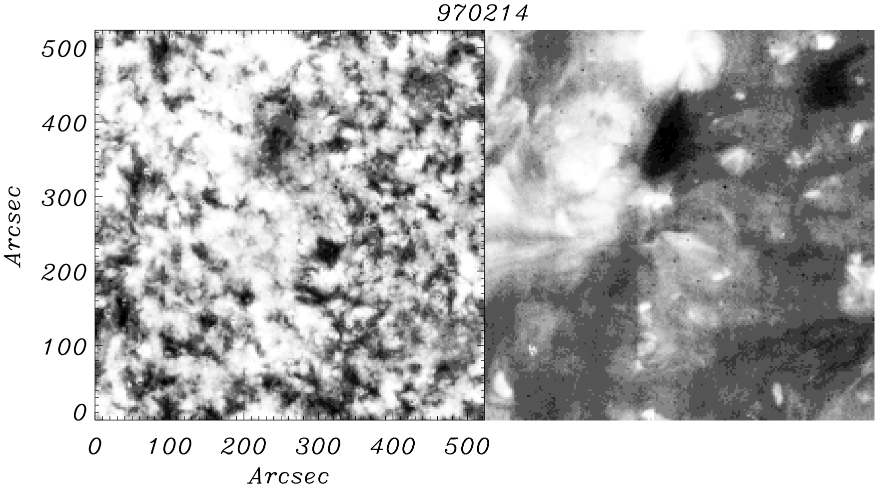

Figure 2.1: A portion of the Sun's image obtained from the central part of the full disk image of He II λ304 Å (left) and Fe XII λ195 Å (right) filtergrams.

one has to look for agents other than coronal EUV radiation to enhance the network brightening observed in He II λ304 Å (Venkatakrishnan, 1999; Feldman, Dammasch, and Wilhelm, 2000). One such agent may be the magnetic field.

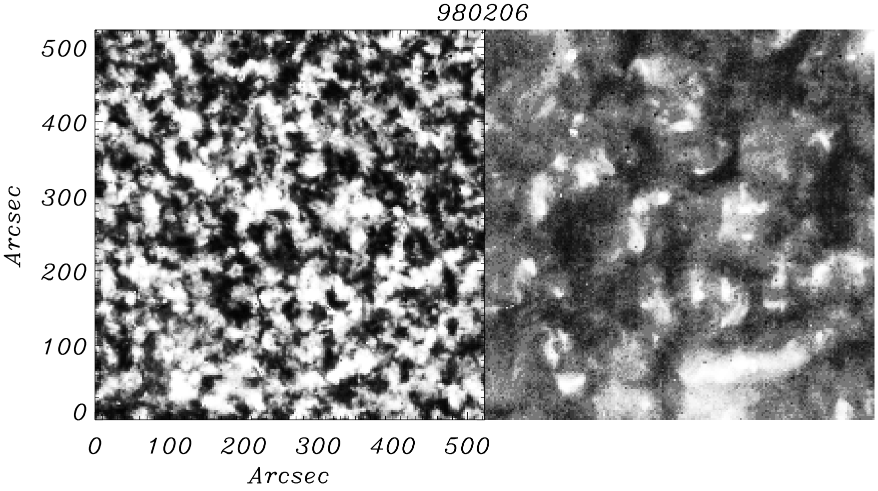

Figure 2.2: A portion of the Sun's image obtained from the central part of the full disk image of He II λ304 Å (left) and Fe XII λ195 Å (right) filtergrams recorded on 06 February 1998.

2.3.2 Comparison of magnetograms with He II λ304 Å images

2.3.2.1 Morphology

It is well known that the supergranular network cells are associated with the magnetic field and velocity field (Simon and Leighton, 1964). We now wish to examine the relationship of the He II network brightening to the strength of the underlying photospheric magnetic field.

The relationship between the observed magnetic field and the He II λ304 Å network brightening is best seen by comparing the magnetograms with the He II λ304 Å images.

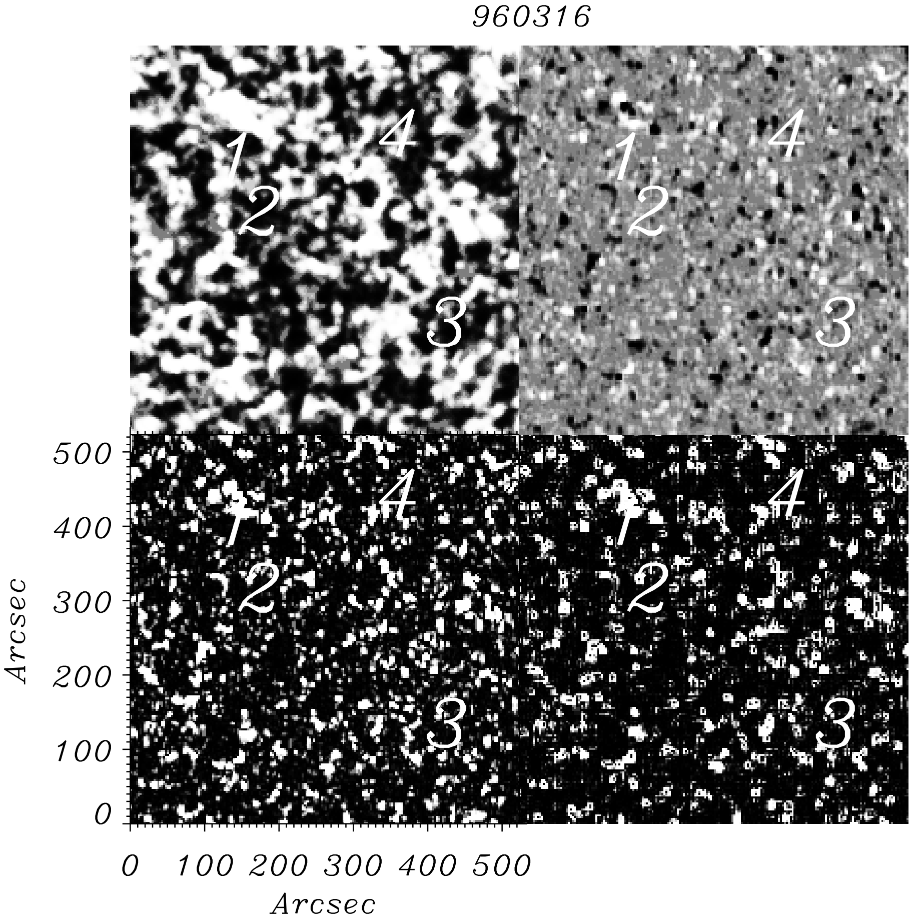

Figure 2.3: The He II λ304 Å image (top left) and the corresponding magnetogram (top right) recorded on 16 March 1996 are shown along with the absolute value of the magnetic field (bottom left) and gradient of the magnetic field (bottom right). The regions marked with numbers show some examples of similarity in morphology of He II λ304 Å with the map of magnetic field and its parameters.

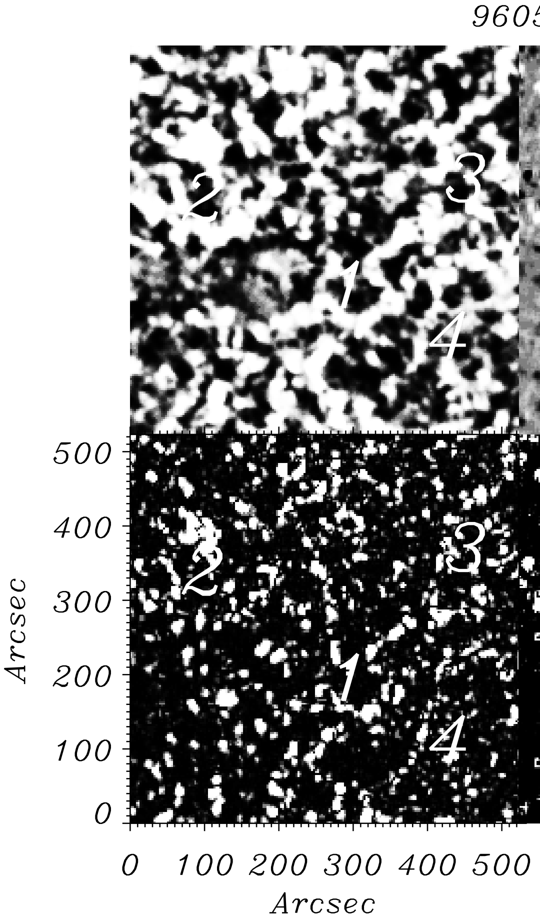

Figure 2.4: Another example of the He II λ304 Å image (top left) and the corresponding magnetogram (top right) recorded on 26 May 1996 are shown along with the absolute value of the magnetic field (bottom left) and gradient of the magnetic field (bottom right). The regions marked with numbers show some examples of similarity in morphology of He II λ304 Å with the map of magnetic field and its parameters.

Figures 2.3 and 2.4 show the maps of He II λ304 Å filtergram, magnetogram, absolute value of the magnetic field ($|B_z|$) and gradient of the magnetic field ($|\nabla B_z|$). The maps show that He II λ304 Å network cells are irregular in shape as seen in Ca II K network (Simon and Leighton, 1964). The comparison of He II λ304 Å network elements with the corresponding magnetogram shows that their morphology is similar. The regions marked 1, 2, 3 and 4 in Figures 2.3 and 2.4 show some examples of association of He II λ304 Å network brightening with the magnetic field and such associations can be seen in most of the regions of quiet Sun network. More specifically, the morphology surrounding the region marked number 1 in He II λ304 Å image (Figure 2.4) looks like an inverted Ω. The same region is associated with bipoles in the magnetogram and is present in the gradient map also. Some of the network elements look bright in the He II λ304 Å images. The encircled region in He II λ304 Å image (Figure 2.5a and b) looks brighter compared to its surrounding and this bright network element is associated with a compact bipole as seen in the magnetogram.

Association between the He II λ304 Å network structure and photospheric magnetic field can be seen in more detail in a contour map (Figures 2.6 and 2.7) of the line-of-sight magnetic field overlaid upon the magnified He II λ304 Å image corresponding to the same region on the Sun. These contours were drawn for magnetic field strength ranging from ±3 G to ±60 G. These contour maps show that the He II λ304 Å network morphology and the photospheric network morphology are related. They also show that magnetic flux concentrations and He II λ304 Å network brightening are related. The brightening occurs at the foot-points of the magnetic flux concentrations near the bipoles. Because of the time difference between the EIT image snapshot and the magnetogram ($\approx$ 30 minute), we can expect some changes in the photospheric magnetic field. In the contour maps it is seen that some of the network elements are not associated with the distribution of the magnetic flux. This lack of association could be due to the evolution of the magnetic field in the network with time or could be due the presence of unresolved bipoles.

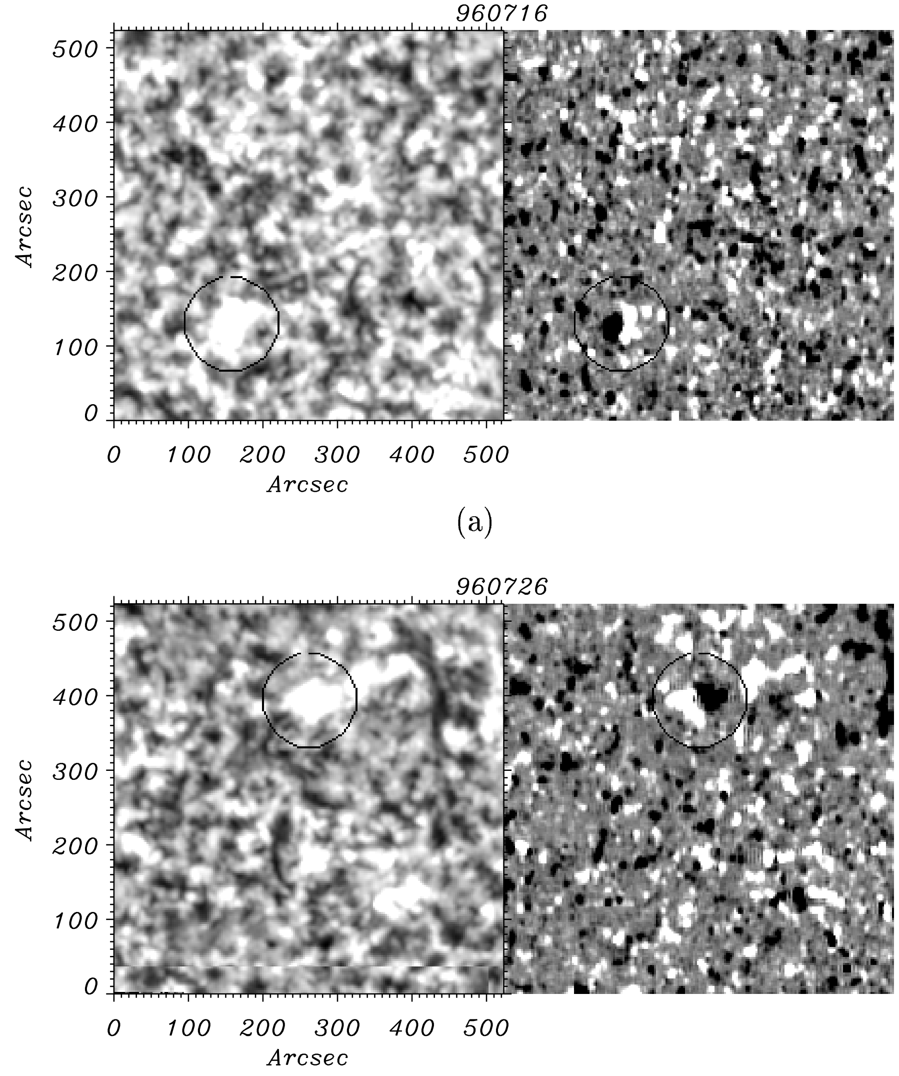

(a)

(b)

Figure 2.5: The encircled regions (in a and b) in the He II λ304 Å images (left) show the filled in nature of the network element and corresponding magnetograms (right) show compact bipole which is responsible for the network element brightening.

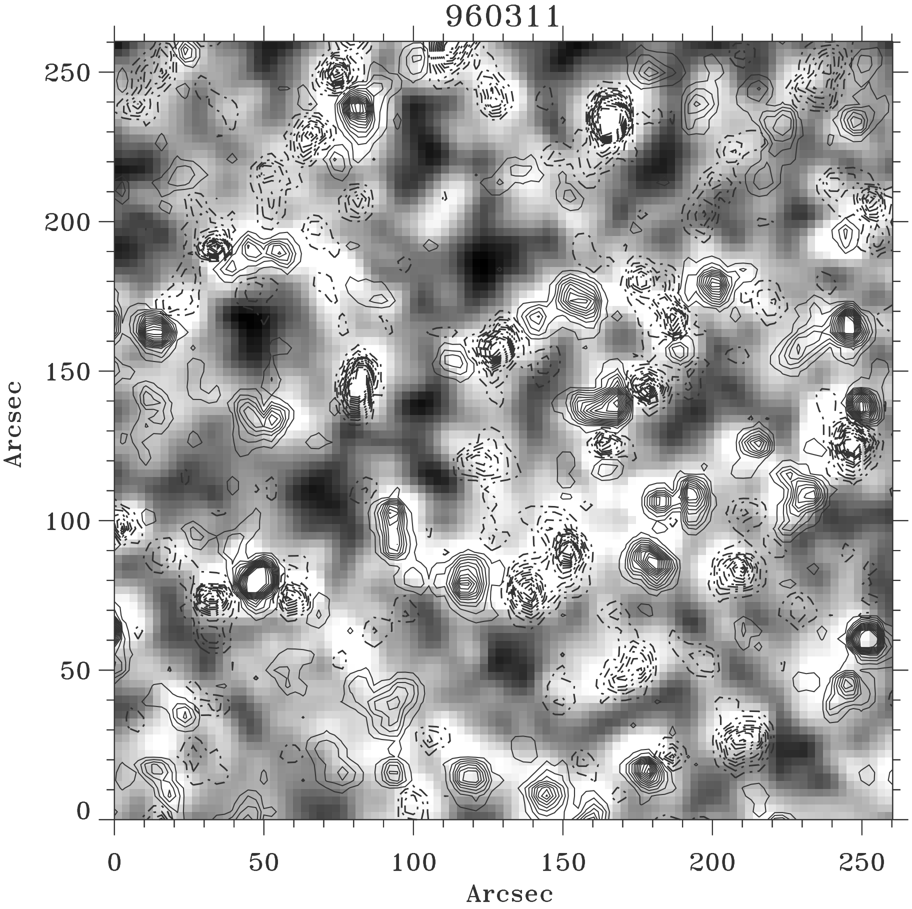

Figure 2.6: Overlay of contours of magnetic field upon the He II λ304 Å image. The contours were drawn for ±3 G to ± 60 G. Here the dashed and solid lines indicate the negative and positive polarity of the magnetic field respectively.

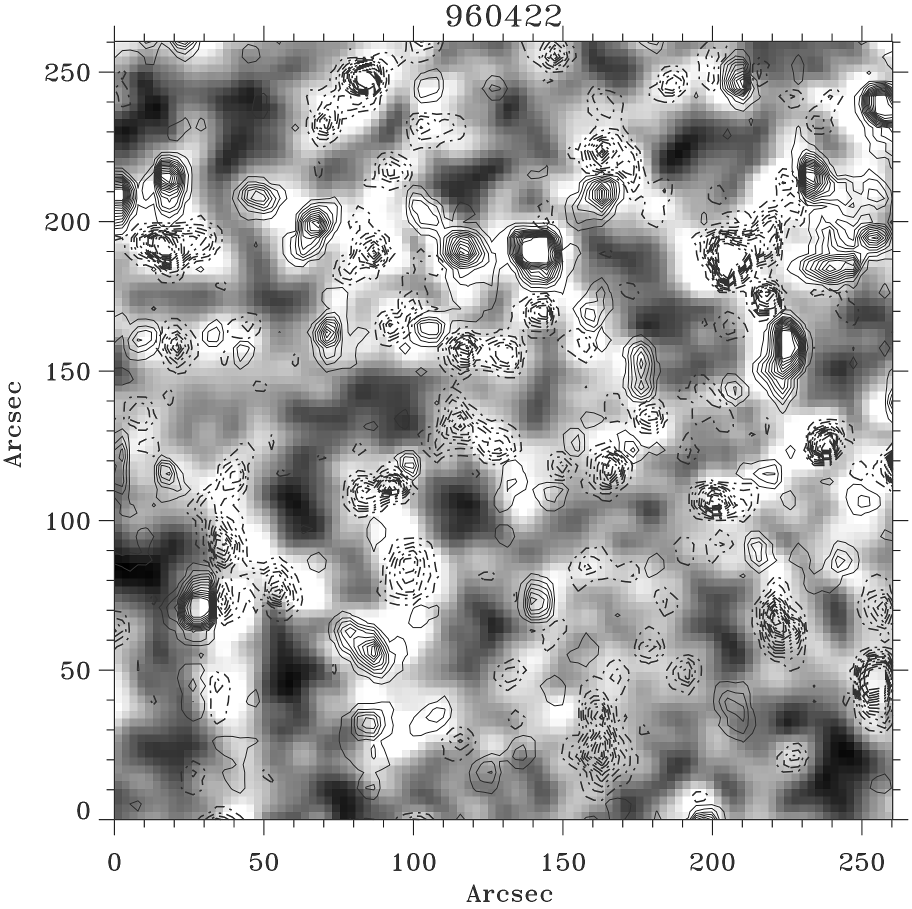

Figure 2.7: Overlay of contours of magnetic field upon a He II λ304 Å image. The contours were drawn for ±3 G to ± 60 G. Here the dashed and solid lines indicate the negative and positive polarity of the magnetic field respectively.

2.3.2.2 Statistical comparison

The visual inspection indicated a good correlation between the He II $\lambda 304$ Å images and the corresponding photospheric line-of-sight magnetograms, $|B_z|$ and $|\nabla B_z|$. The contour map showed that most of the photospheric magnetic field and the He II $\lambda 304$ Å network brightening are related. Table 2.1 shows the mean value of the correlation coefficient between 25 He II $\lambda 304$ Å images and corresponding magnetic field parameters, namely, B_z, $|B_z|$ and $|\nabla B_z|$. Even though the visual inspection implied that the network brightening is stronger near bipoles, Table 2.1 shows a cross-correlation coefficient of only -0.091 between the He II $\lambda 304$ Å images and magnetograms. This is because the positive correlation with positive flux almost exactly cancels the negative correlation with negative flux. This is confirmed by cross-correlating $|B_z|$ with the He II $\lambda 304$ Å image. In the case of $|B_z|$ and $|\nabla B_z|$, the cross-correlation coefficients look similar. Figure 2.4 may shed some light on this. The comparison of $|B_z|$ and $|\nabla B_z|$ maps with the He II $\lambda 304$ Å image shows that the magnetic network element size is well within the He II $\lambda 304$ Å network element. Thus the gradient of the magnetic field will have maxima close to the field strength maxima. Since the sizes of both the maxima are smaller than the He II $\lambda 304$ Å network element and located within the element, the $|B_z|$ and $|\nabla B_z|$ maps show similar cross-correlation with the He II $\lambda 304$ Å images. It should be noted that this cross-correlation coefficient includes network and intra-network regions.

2.3.2.3 Temporal evolution of He II $\lambda 304$ Å network cell and magnetic field

We now look at the time evolution of a series of He II $\lambda 304$ Å images and a series of magnetograms. The cross-correlation between the first He II $\lambda 304$ Å image (taken at zeroth hour) and the successive images shows that the correlation coefficient decreases with time lag (Figure 2.8). A similar trend is found in magnetogram series of the same day. This suggests that the magnetic field may be playing an important role in the

Table 2.1: Comparison of cross-correlation coefficient between He II λ304 Å image and the corresponding magnetic field parameters. This comparison was made using 25 image sets and the mean values of cross-correlation coefficients (CC) are shown.

He II λ304 Å versus	CC
B_z	-0.091
$\|B_z\|$	0.502
$\|\nabla B_z\|$	0.528

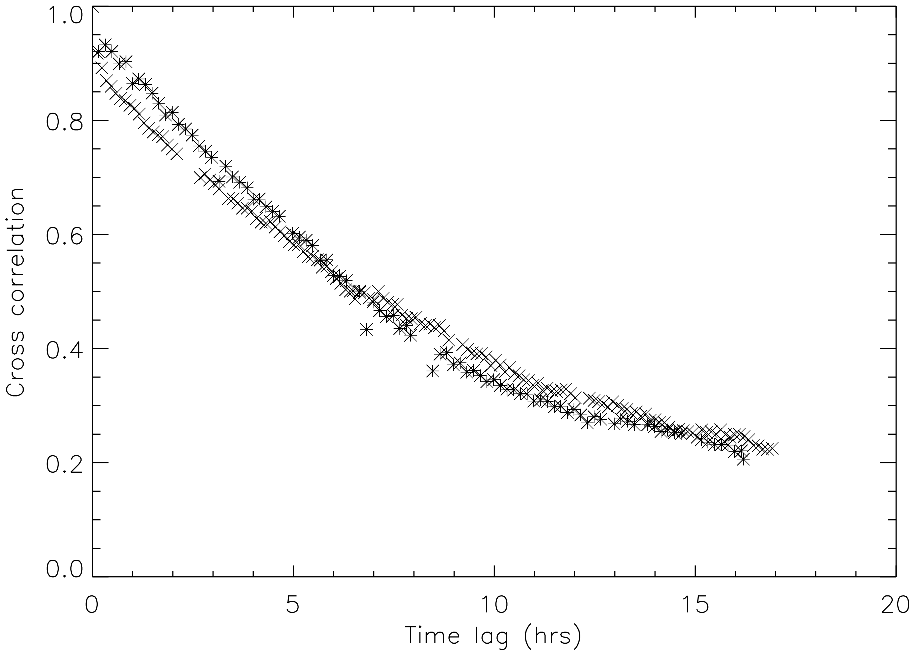

Figure 2.8: A plot of cross-correlation coefficient versus time lag. The curve with asterisks is obtained from the cross-correlation between the magnetograms taken at zeroth hour and those taken at subsequent hours and the cross sign is for the He II λ304 Å image time series.

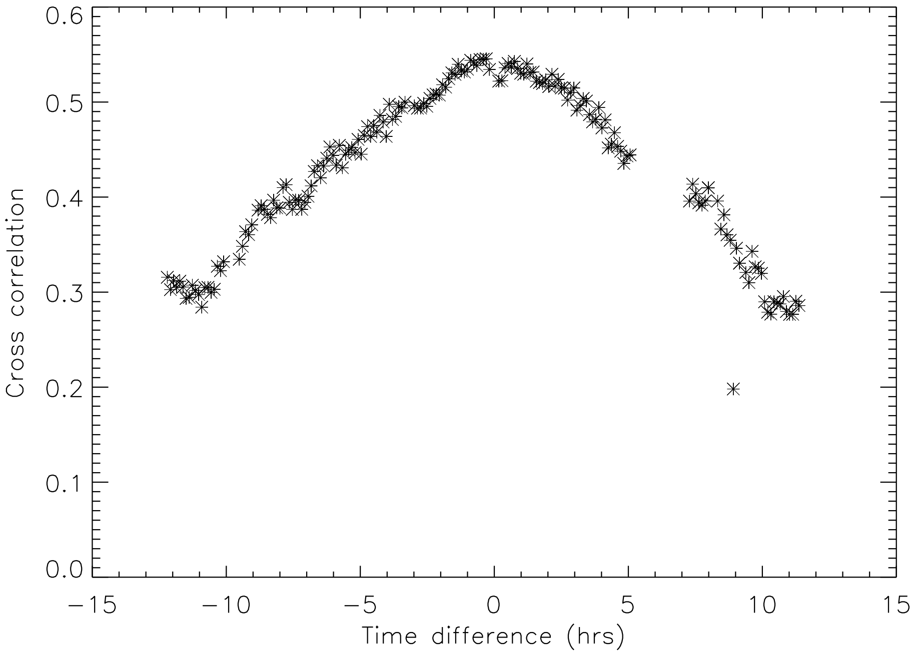

Figure 2.9: A plot of cross-correlation coefficient between the absolute value of photospheric magnetic field (obtained from SOHO/MDI) and a series of He II λ304 Å images obtained before, during and after the magnetogram snapshot time versus the time difference between the two. The cross-correlation coefficient is maximum when the time difference between the two is small.

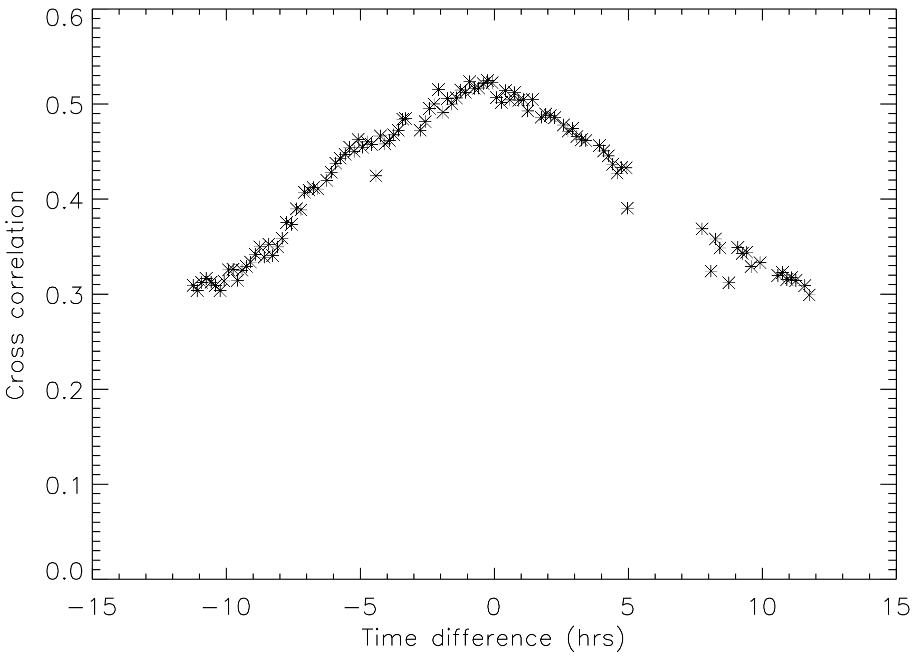

Figure 2.10: A plot of cross-correlation coefficient between the He II λ304 Å image and a series of absolute value of magnetic field obtained before, during and after the He II λ304 Å image snapshot time versus the time difference between the two. The cross-correlation coefficient is maximum when the time difference is small and decreases when the time difference between the two increases.

temporal evolution of the He II λ304 Å network elements.

Figure 2.9 shows a plot of cross-correlation coefficient versus time difference between a MDI magnetogram and a series of SOHO/EIT He II λ304 Å images taken before, during and after the time of acquisition of the selected MDI magnetogram. The plot shows that the cross-correlation coefficient decreases with the time difference. The same trend can be seen when one He II λ304 Å image and a series of MDI magnetograms taken before, during and after the selected He II λ304 Å image snapshot time (Figure 2.10) are correlated.

Figure 2.11 shows some examples of the time sequence of He II λ304 Å images and corresponding magnetograms. Figure 2.11 shows the images of He II λ304 Å network and their association with the magnetic field at different epochs. Here we have suppressed the noise in the magnetograms by replacing the values less than ±5 Gauss with zeros (this is only for display purposes). Figure 2.11 shows that there is one-to-one correspondence between the network element brightening in He II λ304 Å and the magnetic field in most of the places. Most of the brightest elements observed in He II λ304 Å are associated with the bipoles. This sequence of He II λ304 Å filtergrams and corresponding magnetogram pairs give an impression that there is a one-to-one association between the He II λ304 Å network elements and the photospheric magnetic field at any given time.

2.3.2.4 Scatter plots

We plotted the He II λ304 Å intensity versus absolute value of the magnetic field strength (Figures 2.12a and b & 2.13a and b). Only elements with maximum intensities above 1σ level (of He II λ304 Å) were considered for the scatter plot. These scatter plots have two parts, (a) a linear part and (b) a cluster of points. These cluster of points are related to the intra-network as well as to the network points with small magnetic field strength. But the linear part of the scatter plot is related mainly to the network elements. The linear part of the scatter plot shows the linear relationship

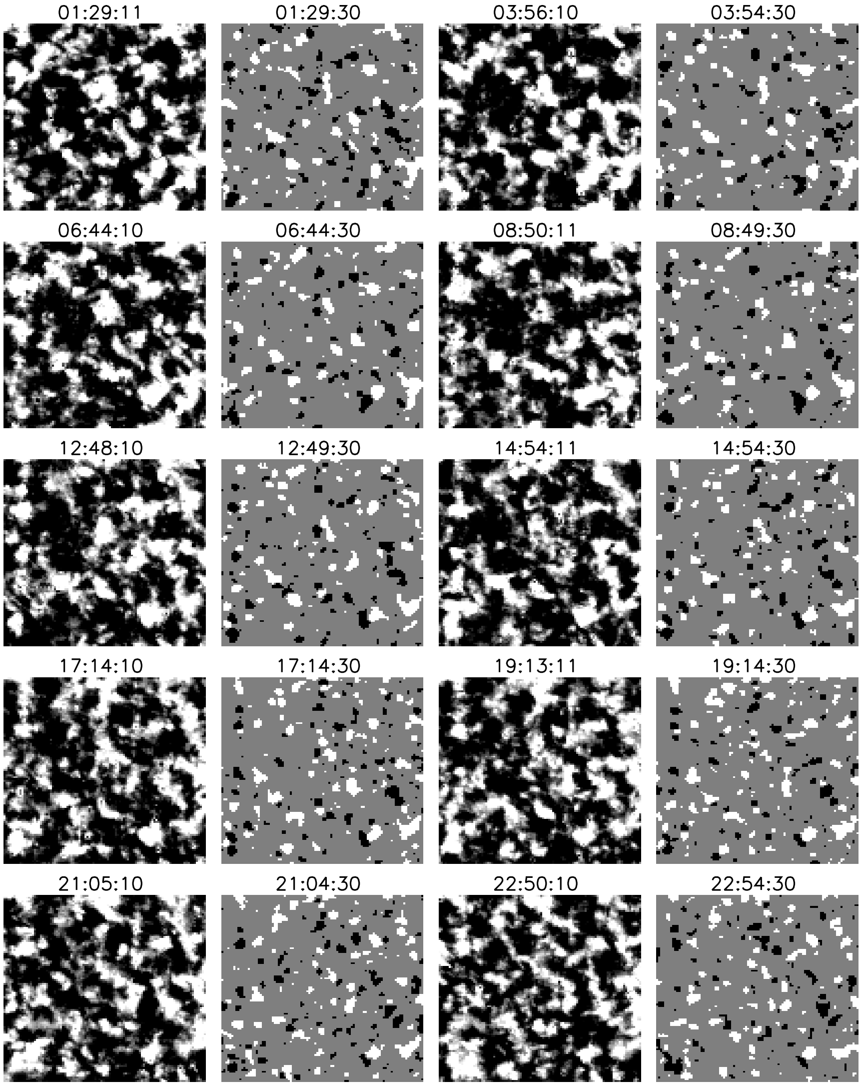

Figure 2.11: A sequence of He II λ304 Å images and corresponding photospheric magnetograms. In most of the places one can see one-to-one association between the network elements observed in He II λ304 Å and magnetogram. The noise in the magnetograms has been suppressed by replacing low values by zero. The window size of each image is 263 arc sec × 263 arc sec.

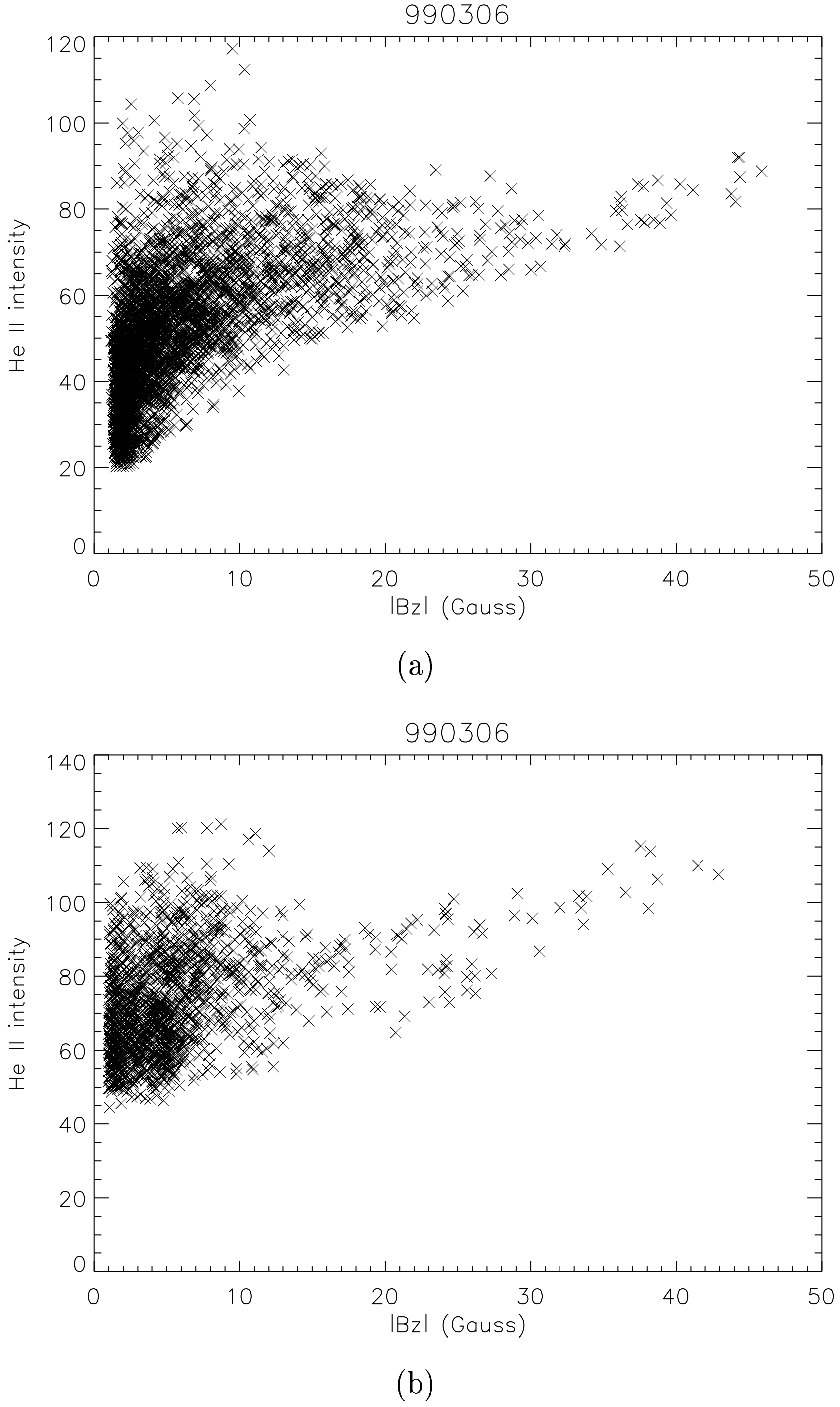

Figure 2.12: A scatter plot of intensity of He II $\lambda 304$ Å filtergrams versus $|B_z|$ for different data-sets of days (a) 26 May 1996 and (b) 06 March 1999. The best fit to the linear part of the scatter is found for values of $|B_z|$ above 12 G.

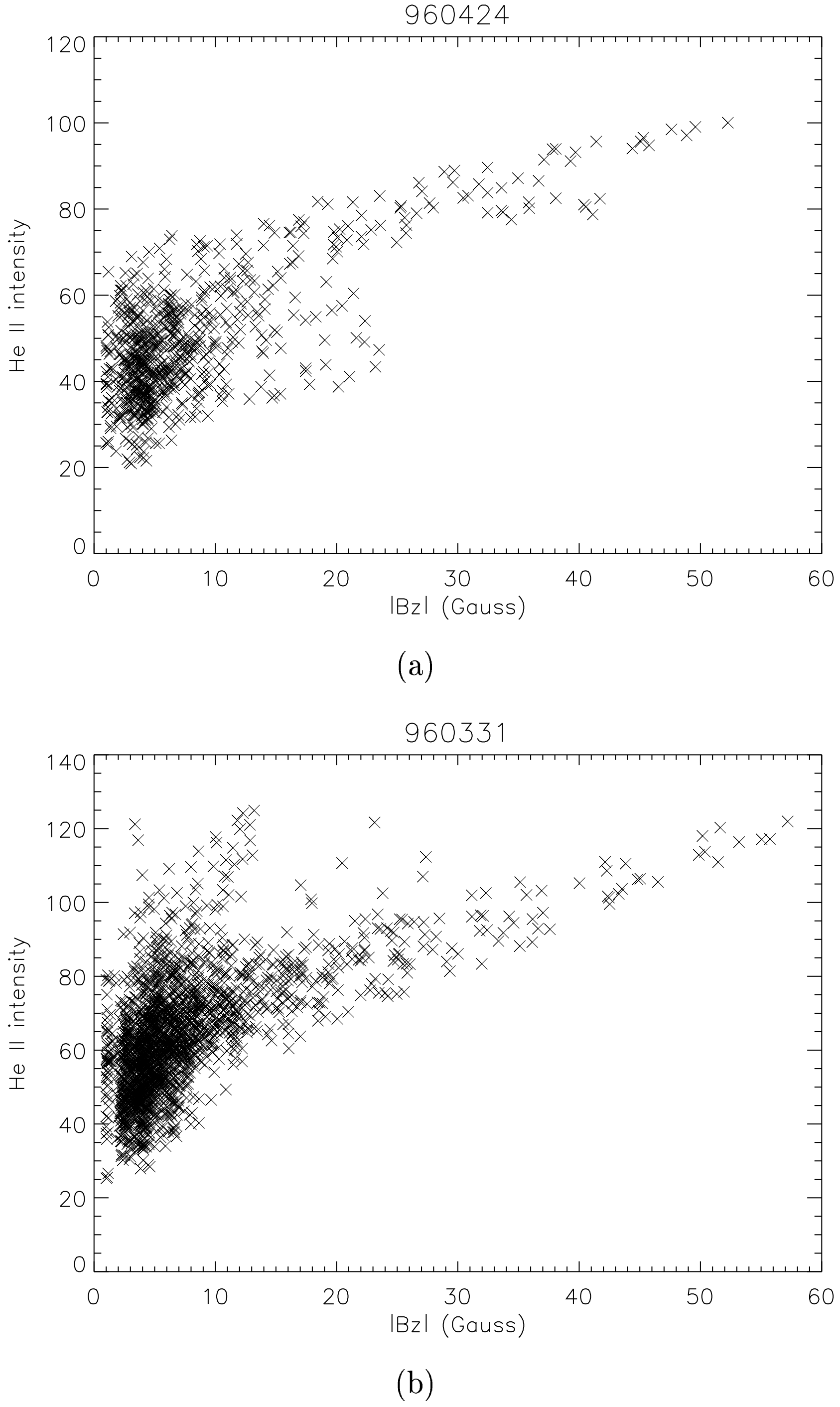

Figure 2.13: A scatter plot showing the intensity of He II $\lambda 304$ Å versus $|B_z|$ for different data-sets of days (a) 24 April 1996 and (b) 31 March 1996. The best fit to the linear part of the scatter is found for values of $|B_z|$ above 10 G.

of the He II λ304 Å network intensity with the absolute value of the network magnetic field. The cross-correlation coefficient increases for the linear part and lies in the range of 0.6 to 0.77. We computed linear-least-square fit to the linear part of the scatter plot (Figures 2.12a and b & 2.13a and b). The best fit could be found beyond 12 G for the 26 May 1996 and 06 March 1999 and beyond 10 G for the 24 April 1996 and 31 March 1996 data sets. The linearity almost disappears below 10 G. By fitting a straight line to the linear portion of the plots, we could derive the following relation between the He II λ304 Å network intensity and $|B_z|$ for the 26 May 1996, 06 March 1999, 24 April 1996 and 31 March 1996 respectively,

$I_{He\ II} = 53.13(\pm0.44)+0.80(\pm0.03)|B_z|$,

$I_{He\ II} = 59.35(\pm1.49)+1.10(\pm0.11)|B_z|$,

$I_{He\ II} = 50.70(\pm0.19)+0.95(\pm0.01)|B_z|$ and

$I_{He\ II} = 62.30(\pm0.34)+1.01(\pm0.02)|B_z|$

where $I_{He\ II}$ is the He II intensity. The terms within the brackets are error bars.

2.3.2.5 'm' maps

In order to clearly identify the spatial locations of the points that show a linear relationship between the He II λ304 Å network brightness and $|B_z|$, we overlaid the contours of the slopes 'm' on the He II λ304 Å image (hereafter 'm' maps). The slopes 'm' were computed using the linear relationship between the magnetic field and He II λ304 Å network brightening as shown below:

$$m = \frac{I_{He\ II} - I_{int}}{|B_z|}$$

where, $I_{He\ II}$ is the He II λ304 Å intensity and I_{int} is the intercept obtained from the scatter plot for corresponding He II λ304 Å intensity and magnetic field strength. We have separately plotted the maps for values of 'm' in the range from 0.5 to 1.5 counts Gauss^{-1} and from 2 to 20 counts Gauss^{-1}. Figures 2.14 and 2.15 show the 'm' maps with slopes ranging from 0.5 to 1.5 counts Gauss^{-1} and 2 to 20 counts Gauss^{-1}

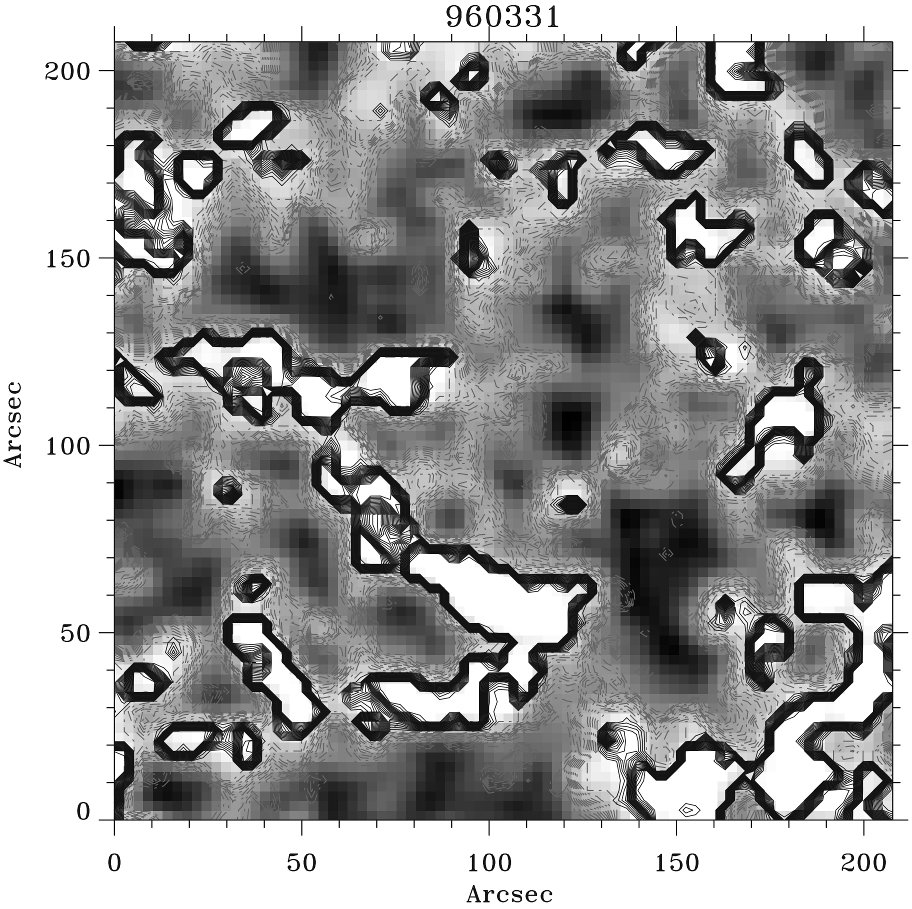

Figure 2.14: 'm' map showing the contours of slope ranging from 0.5 to 1.5 counts Gauss^{-1} overlaid upon the He II λ304 Å image. The dashed contours represent the negative part (-1 to -7 counts Gauss^{-1}) of the slope and solid contours represent the positive part. The value of slopes between 0.5 to 1.5 counts Gauss^{-1} correspond to network features (shown as solid contours).

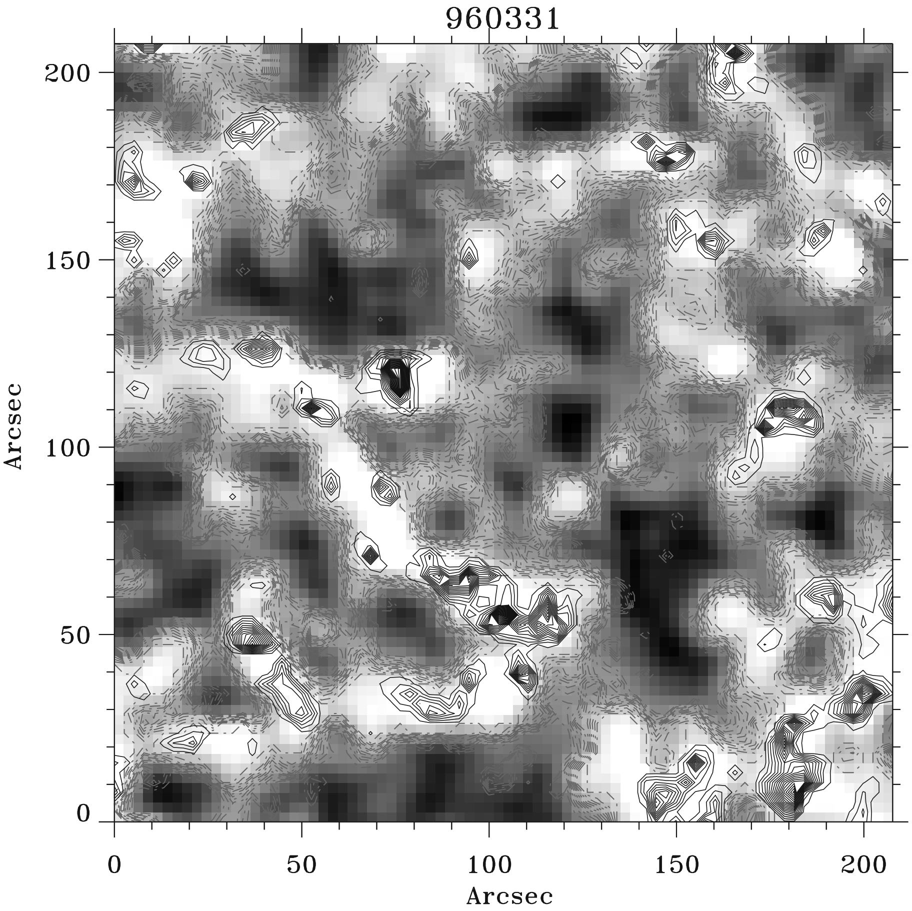

Figure 2.15: 'm' map showing the contours of slope ranging from 2 to 20 counts Gauss^{-1} overlaid upon the He II λ304 Å image. The dashed contours represent the negative part (-1 to -7 counts Gauss^{-1}) of the slope and solid contours represent the positive part. Here, the value of slopes between 2 to 20 counts Gauss^{-1} correspond to neutral line.

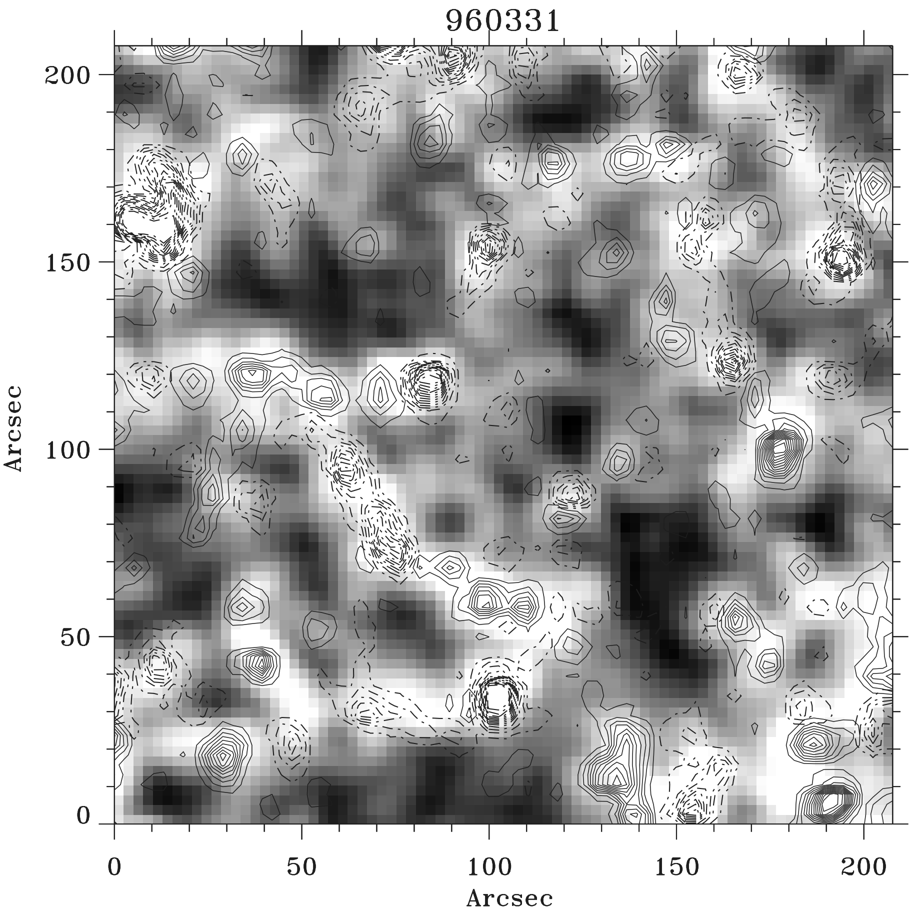

Figure 2.16: Contour map of magnetic field overlaid upon the He II intensity image. Here, the contours were drawn from ±3 to ±60 G. This contour map is to identify the network cells, neutral line and the polarity of the magnetic network elements. The solid contours represent the positive polarity and the dashed contours represent the negative polarity.

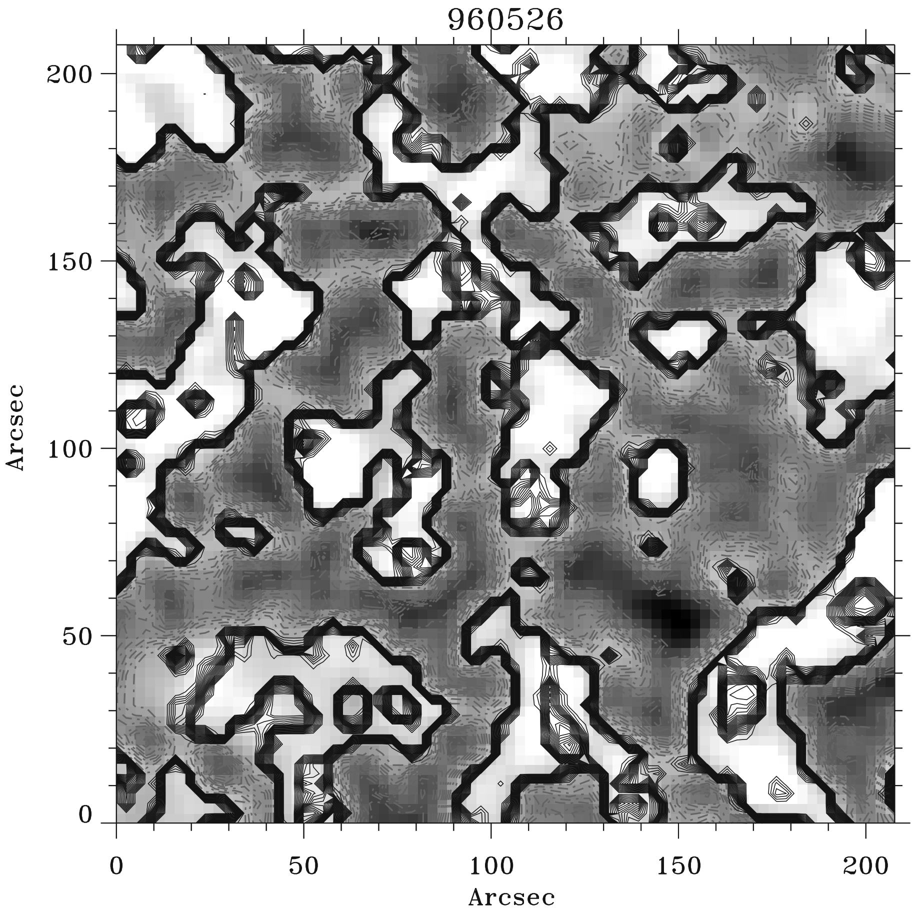

Figure 2.17: 'm' map showing the contours of slope ranging from 0.5 to 1.5 counts Gauss^{-1} overlaid upon the He II λ304 Å image. The dashed contours represent the negative part (-1 to -7 counts Gauss^{-1}) of the slope and solid contours represent the positive part. Here, the value of slopes between 0.5 to 1.5 counts Gauss^{-1} corresponds to network features (shown as solid lines).

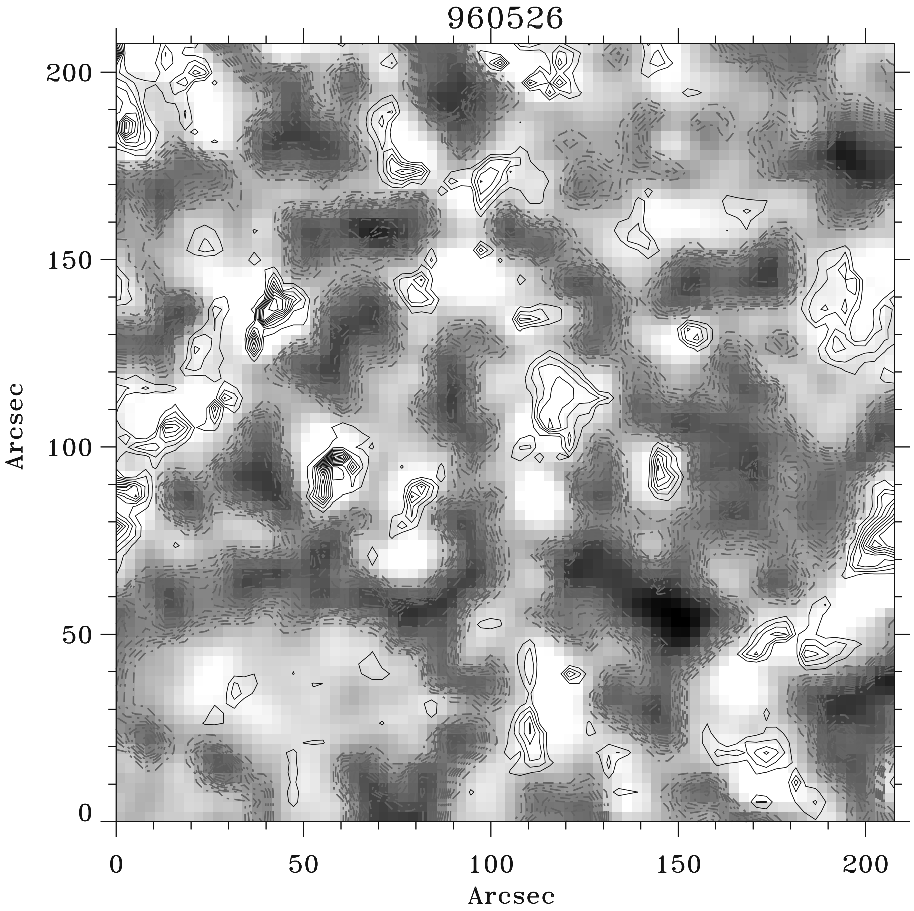

Figure 2.18: 'm' map showing the contours of slope ranging from 2 to 20 counts Gauss^{-1} overlaid upon the He II λ304 Å image. The dashed contours represent the negative part (-1 to -7 counts Gauss^{-1}) of the slope and solid contours represent the positive part. Here, the value of slopes between 2 to 20 counts Gauss^{-1} correspond to neutral line.

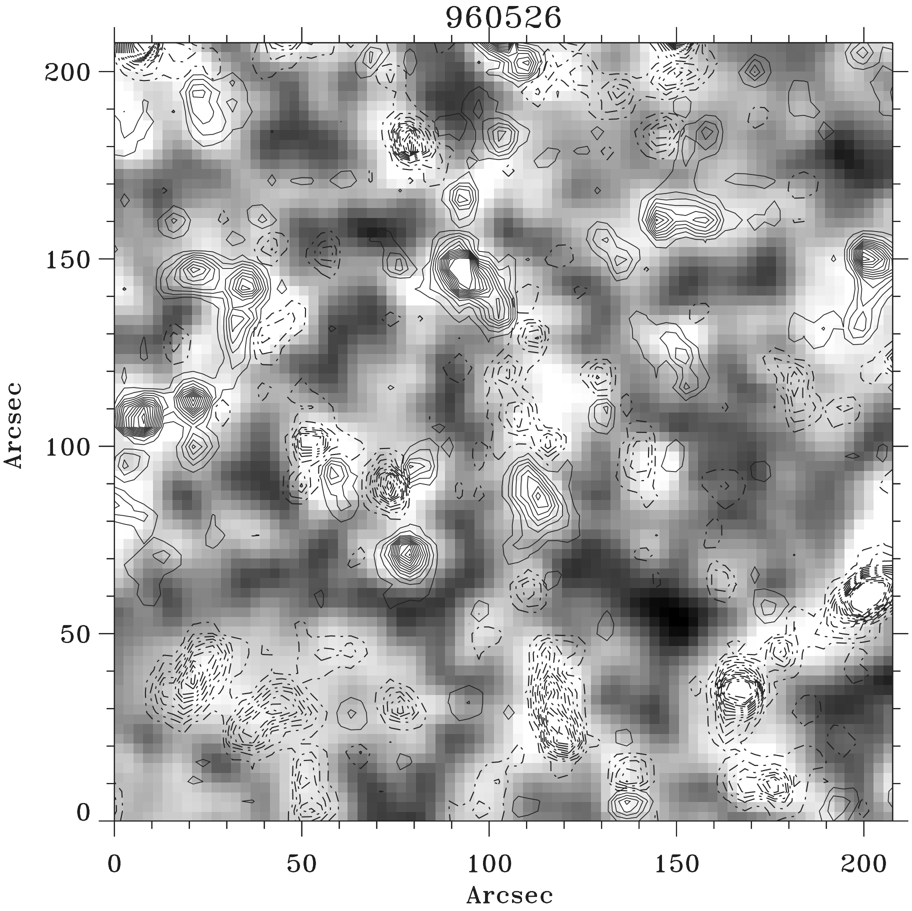

Figure 2.19: Contour map of magnetic field overlaid upon the He II intensity map. The contours were drawn from ±3 to ±60 G. This contour map is to identify the network cells, neutral line and the polarity of the magnetic network elements. The solid contours represent the positive polarity and the dashed contours represent the negative polarity.

respectively for the data of 31 March 1996. Figures 2.17 and 2.18 show the ‘m’ maps with slopes ranging from 0.5 to 1.5 counts Gauss^{-1} and 2 to 20 counts Gauss^{-1} respectively for the data of 26 May 1996. The dashed contours show the negative slopes and they are at borders of network cells and in the intra-network region. The positive slopes ranging from 0.5 to 1.5 counts Gauss^{-1} are mostly related to the mono-polar regions and are related to the linear part of the scatter plots. In Figures 2.15 and 2.18 positive contours (m>2 counts/Gauss), coincide with locations of the neutral lines of the magnetic field, which also coincide with slightly higher value of He II λ304 Å network brightness. Most of the neutral line regions do not contribute to the linear part of the scatter plot, rather they simply reduce the correlation. When we compare the ‘m’ maps with the contour map of magnetic field overlaid upon the intensity map of He II λ304 Å (Figures 2.16 and 2.19), we see that ‘m’ maps can (1) easily differentiate the network and intra-network regions and (2) separates the neutral lines. These ‘m’ maps clearly show that most of the network regions contribute to the linear part of the scatter plot, except the neutral line regions. The ‘m’ maps show that the neutral line (and its surrounding) has a large range of slopes ranging from 2 to 20 counts Gauss^{-1}. Therefore in those regions there is a different relationship between the strength of the magnetic field and the intensity of the He II λ304 Å. Finally, we could not see any strong correlation between the intra-network field and the He II λ304 Å intra-network brightening. This could be due to the time difference between the magnetogram and He II λ304 Å image snapshot during which, the intra-network field might have moved towards the boundary of the supergranular network region.

2.3.3 Height of formation of He II λ304 Å network elements

The aforementioned results indicate that the network brightening observed in He II λ304 Å is related to the photospheric magnetic field parameters. In such a one-to-one association between the magnetic field and network brightening, the question that arises is that how is the size of the magnetic network element related to the size of He II λ304 Å network elements?

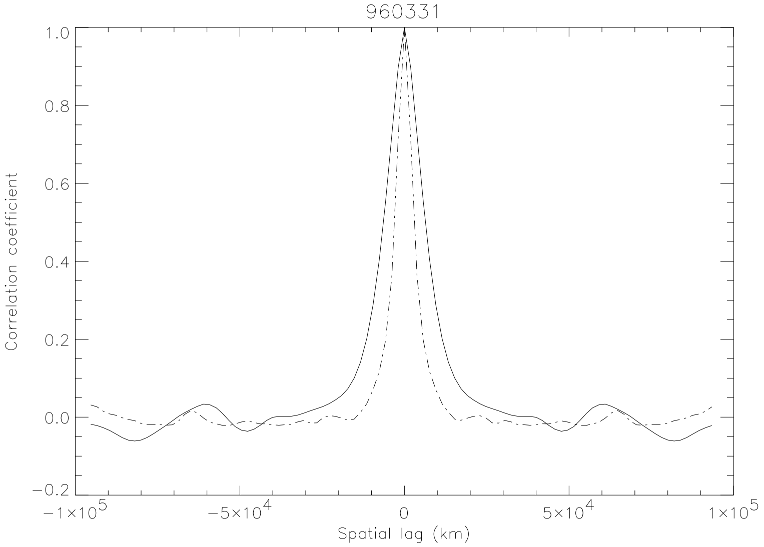

Figure 2.20: A plot showing the AC as a function of spatial lag (km). The dash-dot line represents the AC curve for the absolute value of photospheric magnetic field and the solid line for He II λ304 Å filtergram. The plot clearly shows the mismatch in the sizes of the network cells and its elements.

The visual comparison of He II λ304 Å images with the magnetograms reveals that the He II λ304 Å network elements are bigger in size than the photospheric magnetic features. The discrepancy in the sizes is shown in Figure 2.20 by the auto-correlation (AC) curve. In Figure 2.20, the dash-dot curve represents the AC of the quiet Sun magnetogram and the solid curve represents the AC of the corresponding He II λ304 Å filtergram. The full width at half maximum (FWHM) of the AC is interpreted as the size of the network element (Simon and Leighton, 1964). Therefore, the size of network element observed in He II λ304 Å is 13200±1890 km and that of magnetogram is 5250±1450 km. Comparison of the FWHM of the AC of the two suggests that there is a discrepancy in the sizes of the network elements observed in He II λ304 Å filtergrams

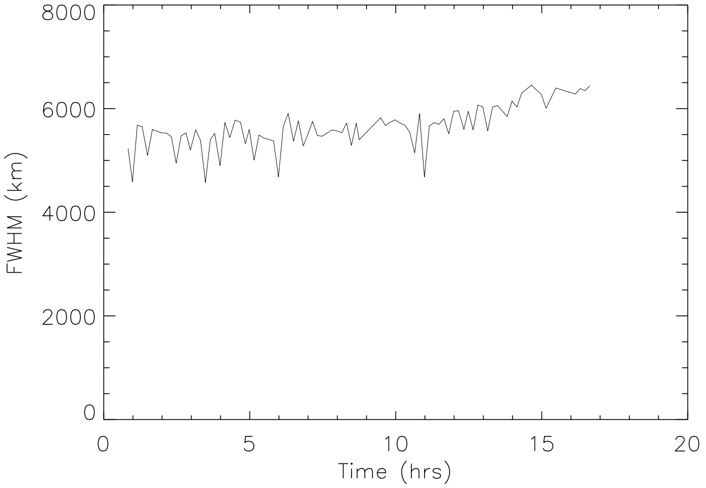

Figure 2.21: A plot of full width at half maximum (km) of the auto-correlation of the magnetogram versus time (hours) obtained from the registered set of MDI magnetogram.

and magnetograms. This discrepancy in the sizes may be due to the evolution of magnetic field with time or height. In order to prove or disprove first option as the reason for the discrepancy in the sizes of the He II λ304 Å and magnetic network elements we adopted the following method. Figure 2.21 shows that the FWHM of the AC of the MDI magnetograms versus time (difference between the first and subsequent images). The FWHM of the AC function varies with an amplitude of $\approx$ 500 km on a time scale of an hour with a gradual increase in mean value from 5000 to 6000 km over a period of 15 hours. The observed size of the He II λ304 Å network element is much larger than the amplitude of evolution of magnetic network element in time. The time difference between the NSO/KP magnetogram and He II λ304 Å images snapshot ranges from 10 to 40 minute. This indicates that we can study the steady state features of the network rather than the rapidly varying features. In the case of SOHO/MDI magnetograms, the time difference between the magnetogram and He II λ304 Å observations was ≈ 10 minute. In both the cases we could see significant size differences between the He II λ304 Å features and their photospheric counterparts. It is clear that the photospheric magnetic network element and He II λ304 Å network element are different in size and the evolution of magnetic field in time cannot compensate for the observed size differences. We then examine whether a better match can be obtained between the He II λ304 Å images and the magnetograms extrapolated to various heights.

Table 2.2: Calculated height for the network elements observed in He II λ304 Å using the potential extrapolation of the photospheric magnetic field.

Filtergrams used	Corresponding magnetograms used	Number	Height range in km	No. of images in this range of height
He II λ304 Å (quiet)	NSO/KP	49	2400-3000	31
			3000-3500	10
			No definite height	8
He II λ304 Å (quiet)	SOHO/MDI	76	2400-3000	30
			3000-3500	46
He II λ304 Å (quiet + compact bipole)	SOHO/MDI	06	4000-5000	06

We computed magnetograms at various heights using the potential extrapolation of the photospheric magnetograms. At every computed height the computed absolute magnetogram has been cross-correlated with the corresponding He II λ304 Å filtergrams. Figures 2.22(a) and (b) show the cross-correlation coefficient as a function of height at which the extrapolated magnetogram has been computed for two sets of observations. Table 2.2 gives the height at which the correlation is maximum (between

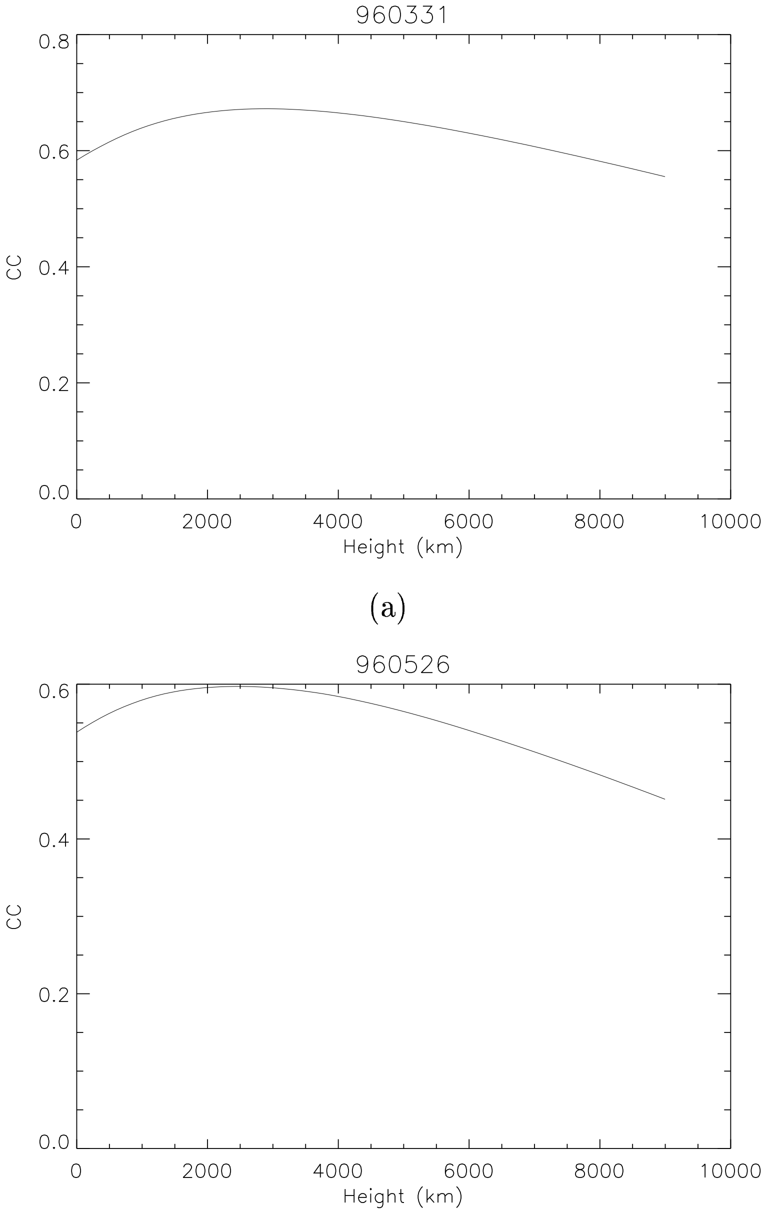

(b)

Figure 2.22: A plot of cross-correlation coefficient between the extrapolated $|B_z|$ and the He II λ304 Å filtergrams versus height shown for two different dates (a) 31 March 1996 and (b) 26 May 1996.

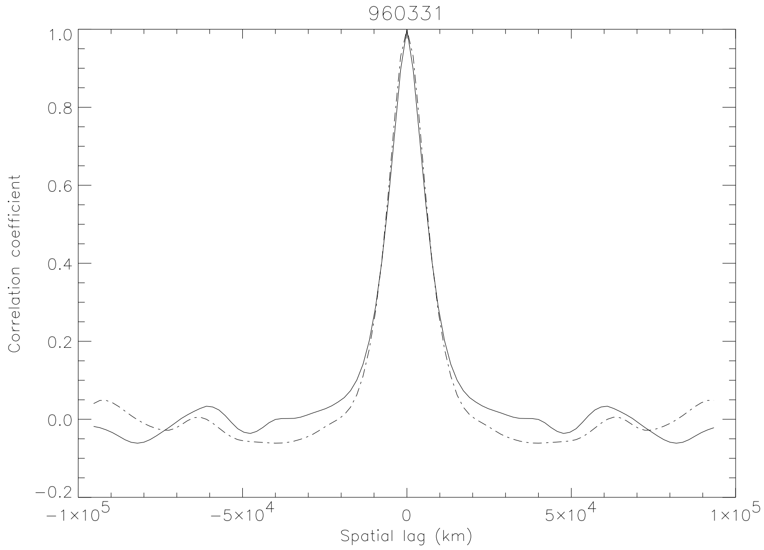

Figure 2.23: A plot of AC as a function of spatial lag (km). The dash-dot line represents the AC curve for the extrapolated absolute magnetogram and the solid line for He II λ304 Å filtergram. The plot clearly shows that the FWHM of the AC of the extrapolated magnetogram matches with the FWHM of the AC of the He II λ304 Å filtergrams at ∼3000 km above the photosphere.

extrapolated $|B_z|$ and He II λ304 Å intensity). The error involved in the height determination was found by using the following steps: (a) estimate the value of rms fluctuation for the cross-correlation function, which was detrended using the cross-correlation value and smoothed cross-correlation value. (b) Subtract this rms fluctuation from the maximum correlation value obtained in the cross-correlation vs height plot. (c) Find the points on the y-axis of the cross-correlation vs height plot that corresponds to the subtracted value. (d) The separation between the abscissae corresponding to the ordinates obtained in the previous step is taken as twice the error in height estimation. The resulting "error" in height determination is ±90 km, which is small, compared to the value of 3000 km for the height of maximum cross-correlation. Out of the set of 49 He II λ304 Å images and NSO/KP magnetogram pairs, 8 pairs show low cross-correlation coefficient and no definite height. In the set of 82 He II λ304 Å images and MDI magnetogram pairs, we find that 6 pairs have strong compact bipoles in the magnetograms and corresponding bright emission in the He II λ304 Å network. The corresponding heights for these 6 pairs were consistently larger than the normal heights obtained for quiet regions. Figure 2.23 shows the AC curve for the He II λ304 Å network and extrapolated $|B_z|$ of the same region. The dash-dot curve corresponds to the AC of extrapolated $|B_z|$ and the solid curve corresponds to the AC of He II λ304 Å filtergram. The AC plot clearly shows that after some height ($\approx$ 3000 km) the magnetic network element size has become equal to the size of the He II λ304 Å network element size while keeping the size of the network constant ($\sim$36000 km) and similar results were obtained from original (non-rescaled) magnetograms. This indicates that the large-scale network magnetic field may be more important for network brightening.

2.4 Summary and Discussion

Using the SOHO/EIT EUV images, along with the NSO/KP photospheric magnetograms and SOHO/MDI magnetograms, we find that:

(1) The presence of network like morphology in He II λ304 Å images and its absence in the coronal images (Fe XII λ195 Å) indicates that the He II λ304 Å network brightening is not caused solely by coronal radiation.

(2) The contour map of magnetic field overlaid upon the He II λ304 Å image shows that there is one-to-one association between the magnetic field and He II λ304 Å network brightening.

(3) The scatter plot of He II λ304 Å network element intensity versus $|B_z|$ shows that there is a definite relationship between the network brightening and the magnetic field.

(4) The 'm' maps show that there is no definite relationship between the intra-

network magnetic field and He II λ304 Å intra-network brightening, while neutral line deviates from the general relationship.

(5) The potential extrapolation of the photospheric magnetograms show that the probable height of He II λ304 Å network element formation is at or around 3000 km above the height of the layer at which the sources of magnetic flux are deployed.

The result (1) above has already been demonstrated in a detailed comparison of Mg X emission (formed at logT=6.0) with He II lines (Macpherson and Jordan, 1999). The results (2) to (4) indicate that we cannot ignore the role of the magnetic field in the network brightening observed in He II λ304 Å.

The network model of Gabriel (1976) might be of some use in assessing the probable height of formation of He II λ304 Å network element. When one plots the thickness of the He II network element obtained by our AC on to the Figure 6 of Patsourakos *et al.* (1999), one obtains a temperature of logT=6.0 for the location of the He II λ304 Å network element in the Gabriel model. This corresponds to a height of $\approx$ 5000 km in the Gabriel model. The Gabriel model uses a curl free extrapolation of the magnetic field above the edge of the supergranulation cell, which is about 1500 km above the photosphere. Our own extrapolation gives a height of 3000 km above the layers of the sources of magnetic flux. If we assume that the flux elements are constrained to retain their sizes (by the supergranulation flow) till the top of the cell at a height of 1500 km, then we obtain a total height of $\approx$ 4500 km for the helium structure. This height is quite consistent with the observations of Feldman, Winding, and Warren (1999).

In summary, we have shown that the network brightness observed in He II λ304 Å is related to the magnetic field. It remains to be seen how the velocity redistribution (which can explain the enhancement of He II λ304 Å brightness relative to other transition region lines formed at the same temperature range) is related to the strength and topology of the magnetic field.

Chapter 3

A study of structure and evolution of transition region network observed in He II λ304 Å.

3.1 Introduction

In this Chapter, we study the characteristics of the transition region network cells observed in He II λ304 Å line and the photospheric network cells using magnetograms. The network cells are a surface manifestation of a 'supergranulation' pattern of convective currents which originate at relatively great depths inside the Sun. Information about the cell size, shape and lifetime can throw some light on the physical characteristics of the network cells as well as on the deeper convective layers.

Simon and Leighton (1964) studied the supergranular velocity pattern extensively, following the discovery of this pattern by Hart (1954, 1956). Leighton, Noyes, and Simon (1962) found a similarity in the appearance of this velocity pattern with the appearance of images obtained in Ca+, H_α and in magnetic fields.

The lifetime and size of a network cell is an essential parameter for modeling the associated physical phenomena. These parameters can be estimated from Dopplergrams, magnetograms, and filtergrams of Ca II K, H_α, He II λ304 Å and other chromospheric and transition region emission lines. The estimated lifetime of the network cell depends on the method chosen and the selected region of interest. Various measurements show that the lifetime of the network cells are in the range of 20 to 50 hours (Simon and Leighton, 1964; Rogers, 1970; Raju, Srikanth, and Singh, 1998). The estimated lifetime of the network cell from various methods are different for different features such as active network and quiet network (Raju, Srikanth, and Singh, 1998). Wang (1988) estimated the mean lifetime of the photospheric network cells (using the photospheric magnetograms) to be about 11 hours for a mixed polarity quiet region. By applying the cross-correlation (CC) technique on the KPNO magnetograms, Komle (1979) obtained a mean lifetime of the network cell of about 8 hours.

There are several ways to estimate the lifetime of the network. The lifetime of the network can be found (a) by plotting CC as a function of time, where 1/e times the y-intercept gives the average lifetime of the network cell (Simon and Leighton, 1964) or by plotting the CC as a function of time in a log-linear plot, wherein the -1/slope of the straight line fit gives the lifetime of the network; (b) by estimating the ratio of the number of surviving cells (as a function of time) to the total number of cells (Wang *et al.*, 1989); and (c) by identifying and tracing each cell from birth to death, so that the average lifetime of these cells can be estimated directly by averaging the lifetime of individual cells (Wang, Zirin, and Ai, 1991). Since the network elements move relative to each other, the network changes its shape due to the rearrangement of network elements while retaining its identity. The correlation method does not distinguish between the true changes in the image such as appearance, disappearance and motion of the individual network elements. The network is essentially a thin system and represents the walls of the supergranulation. Hence any change in the shape of network boundary will reduce the correlation. This will lead to underestimation of lifetime of the network cells (Wang, 1988). The lifetime of the individual network cell depends on the size of the cell (Srikanth, Raju, and Singh, 1999). Even though visual inspection gives the lifetime of any individual network and its evolution, it is very hard to track each and every network of different sizes from birth to death.

Apart from lifetime, the other important parameter of the network cell is its size. Various measurements using different techniques on Dopplergrams and filtergrams of Ca II K resulted in a range of sizes of the network cells, that is from 10000 to 32000 km (Simon and Leighton, 1964; Singh and Bappu, 1981; Raghavan, 1983; Hagenaar, Schrijver, and Title, 1997; Berrilli, Florio, and Ermolli, 1998; Raju, Srikanth, and Singh, 1998; Srikanth, Singh, and Raju, 2000). On the other hand, the photospheric counterpart (magnetogram) of the network cells showed a sizes of about 15000 - 20000 km (Wang, 1988). Among the various methods used by several authors to estimate the size of the network cell, auto-correlation (AC) function is favored by many. However, visual inspection (Singh and Bappu, 1981) gives better results for a limited number of samples. Other methods, such as steepest descent algorithm (Hagenaar, Schrijver, and Title, 1997) and tessellation based on a two-dimensional basin finding algorithm (Srikanth, Singh, and Raju, 2000) consider network as a thin boundary of the supergranulation and tend to give smaller length scales.

Most of the earlier results were based on ground based data. In deriving the lifetime and size of the network cells, chromospheric magnetic field proxies (Ca II K filtergrams and H_α filtergrams), photospheric Dopplergrams and magnetograms were used. Extreme ultraviolet Imaging Telescope (EIT, Delaboudiniere *et al.*, 1995) on board Solar and Heliospheric Observatory (SOHO) gives a unique opportunity in studying the transition region network cells observed in He II $\lambda304$ Å which is free from atmospheric seeing and interruption due to diurnal cycle. Though, the lifetime is best obtained by visual inspection, the CC function has its own advantage and disadvantage. Correlation function is useful for a system whose mean value remains constant in time and space. Hence, the correlation function can be applied to a stationary/homogeneous system. But, for a system whose mean value changes with time, the correlation function cannot be applied. In such cases the structure function can be used. In general, a system, which is random in nature, can be described using statistically averaged quantities. One such quantity is the structure function. In this Chapter, we studied the network cell properties observed in He II λ304 Å, using the AC, Spatial Structure Function (SSF) and Temporal Structure Function (TSF). We also estimated the mean velocity of the network element. In the following Section we describe the selected data, and the details of the analysis performed on the data. Results and discussions are included in the later Sections.

3.2 Data

Our results are based on eight sets of He II λ304 Å filtergrams collected from the data archive of the EIT and four sets of magnetograms collected from the Michelson Doppler Imager (MDI, Scherrer *et al.*, 1995) data archive. The data selection criteria were the following:

For He II λ304 Å images:

(1) There should not be any active region within the region of interest.

(2) There should be a continuous data-set of He II λ304 Å images taken approximately at an equal interval of time for at least up to 30 hours.

(3) The He II λ304 Å images should have minimum missing blocks.

For magnetograms:

There should be full disk magnetograms corresponding to the selected He II λ304 Å images of the same day taken at an interval of 1-minute; if not, any other day with the absence of active region in the center of the Sun.

The date and duration of observations are shown in Table 3.1.

Table 3.1: The date, type of data, duration and the mode of observation are listed in the table. HC indicates high cadence (7 minute for EIT He II λ304 Å and 1 minute for MDI magnetograms) and SM indicates sub-mode (15 minute).

No	Date	Data	≈ Duration (hrs)	Mode
1	97-Mar-19	He II λ304 Å	31	HC
2	98-Mar-31	He II λ304 Å	33	SM
3	98-Apr-01	He II λ304 Å	32	SM
4	98-Apr-02	He II λ304 Å	33	SM
5	98-Apr-03	He II λ304 Å	26	SM
6	98-Nov-14	He II λ304 Å	45	HC
7	99-Mar-05	He II λ304 Å	30	HC
8	99-Mar-06	He II λ304 Å	30	HC
9	97-Oct-03	MDI magnetograms	23	HC
10	99-Mar-05	MDI magnetograms	23	HC
11	99-Mar-06	MDI magnetograms	40	HC
12	99-Apr-01	MDI magnetograms	23	HC

3.2.1 Data analysis

3.2.1.1 Pre-processing

The level zero data of collected sets (of He II λ304 Å) were dark subtracted, flat fielded, degridded, normalized to 1-second exposure rate and then saved in the flexible image transport format (FITS) with the date and time of the observation as a file name using the solar soft routines (Freeland and Handy, 1998).

3.2.1.2 Registration

After pre-processing of the He II λ304 Å images, we derotated these full disk images to compensate for the solar rotation (solar surface rotation speed is about ≈ 2.844 μ rad s^{-1} at the equator) and then extracted an area of 350×350 pixels size around the disk center and saved it in FITS format. For finer alignment of the images, a two-dimensional cross-correlation (Sridharan, 2003) program was used. For each image, the previous image (which was registered to its preceding image and hence to the first image) was the reference image. We extracted a 200×200 pixel window from the spatially registered set of images.

Out of four sets of magnetograms, two sets of magnetograms were resized to the FOV of SOHO/EIT He II λ304 Å, so that these magnetograms can be compared with the He II λ304 Å images (hereafter data-set I). The other 2 sets of magnetograms were used as it is, as they did not have corresponding He II λ304 Å images (hereafter data-set II).

In data-set I, the magnetograms (05 Mar 1999) were derotated to the first image time and then averaged over 10 minute to improve the signal-to-noise ratio, there by reducing the noise from ±20 to ±6.2 G. The other (06 Mar 1999) data sets were averaged over 5 minute (after derotating the images) to check for any change in the result for the 10 minute and 5 minute averages of the magnetograms. A similar procedure (as above) was followed to register the magnetograms spatially and then a 200×200 pixel window was extracted from these registered sets.

The magnetograms of the data-set II were averaged over 10 minute after derotation. Similar procedures (as above) were incorporated in the registration of the sliced (350×350) magnetograms which yielded a 260×260 pixel window (FOV is same as registered set of He II λ304 Å images).

3.2.1.3 Structure function

The lifetime of the network cells was estimated using structure function (SF). A statistical quantity, structure function can be used for a system under random process with stationary increments (Goodman, 1985). TSF of the spatially aligned images as a function of time gives statistical information about the evolution of the network cells. The TSF for any random function with stationary increments, 'ϕ' is defined as,

$$D_{\phi}(\Delta t) = \left\langle |\phi(t + \Delta t) - \phi(t)|^2 \right\rangle \tag{3.1}$$

where, $\langle\rangle$ represents the ensemble average and Δt is time lag. In applying this technique to our images we assume that the intensity of the image is a random variable. The lifetime of the network cells is approximated as the time at which the TSF saturates.

The following steps were incorporated in estimating the TSF:

(a) Spatially aligned images as a function of time are stacked in 2-D arrays with time increasing along the column of the array.

(b) The TSF were calculated according to Equation (3.1) by taking the ensemble average over all the pixels having same time differences.

The SSF of a random function with stationary increments, 'ϕ' is defined as

$$D_{\phi}(\Delta r) = \left\langle |\phi(r + \Delta r) - \phi(r)|^2 \right\rangle \tag{3.2}$$

where, Δr is spatial lag. The size of the network cell is estimated as the scale of length at which the SF saturates.

3.3 Results

3.3.1 Lifetime of the network cells

The lifetime of the network cells observed in He II λ304 Å images, magnetograms and potential extrapolated magnetograms have been discussed in the following Sections.

3.3.1.1 Lifetime of He II λ304 Å network cells

In order to know the range of lifetime of the network cells, we have visually followed six network cells from their birth to death. We have made a movie of each data set and followed some of the network cells. The movie gave an impression that the individual network cell vanishes by (a) merging with the other network cells, (b) contracting, and (c) disappearance of its elements. Figures 3.1 and 3.2 show some examples of this.

In Figure 3.1, a network did not exist before 07:03:11 UT (on 05 Mar 1999, the arrow mark indicates for a particular network cell location). It is born at 08:27:10 UT and it became a complete network at 10:54:10 UT. At 15:50:10 UT of next day this network is completely merged with the other neighboring network cell. If we consider the morphological changes in the form of merger of two cells, then this particular cell can be assigned a lifetime of $\approx$ 32.5 hrs.

Figure 3.2 shows another example for the date 02 Apr 1998 (the arrow mark indicates for a particular network cell location). The network cell has just started growing at 05:54:45 UT and it matured at 08:30:45 UT. At 12:27:47 UT of next day it opened to another network cell. In between the birth and death of the network, it has interacted with the other network cells and changed its shape. The lifetime of the network cell is estimated as $\approx$ 29 hrs. Similarly the other four network cells had a lifetimes of $\approx$ 24 hr, 26 hr, 26 hr and 16.5 hr respectively.

From these observations it is clear that the network cells have a range of lifetimes. We then used a statistical approach, that is TSF. Figure 3.3 shows the logarithm of TSF as a function of time lag for 7 different days of observation. We approximate the lifetime as the time at which the TSF saturates. We approximate the saturation as the time lag at which the TSF almost becomes parallel to the x-axis. The saturation of the SF means that the same feature no longer exists. The TSF has been estimated from large number of averages ($\approx 10^7$). The error in computing the TSF has been obtained as follows: (a) we first computed the TSF at all the available time lag. (b) We then

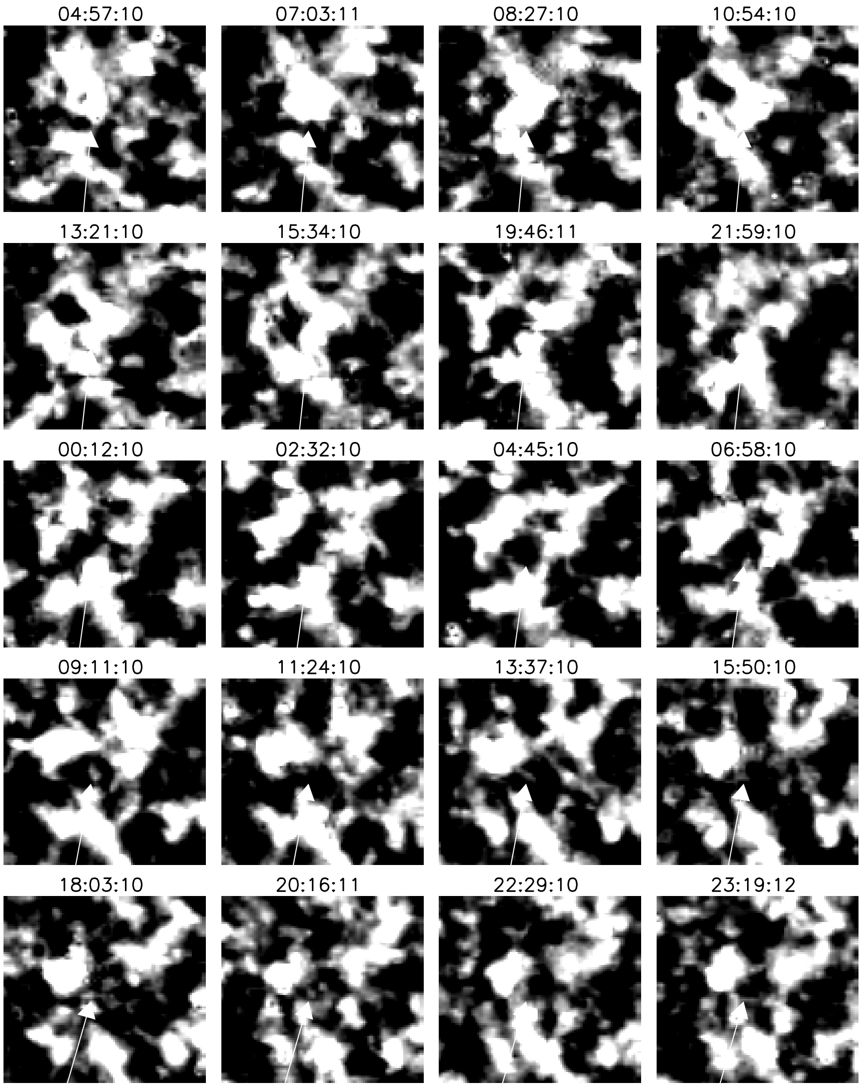

Figure 3.1: Evolution of a network cell from its birth to death. At 08:27:10 UT the network has just started forming. At 10:54:11 UT it is matured and at 15:50:10 UT on the next day the network was observed to disrupt. The lifetime of the network cell is $\approx$ 32.5 hrs. The size of each image is 132 arc sec $\times$ 132 arc sec.

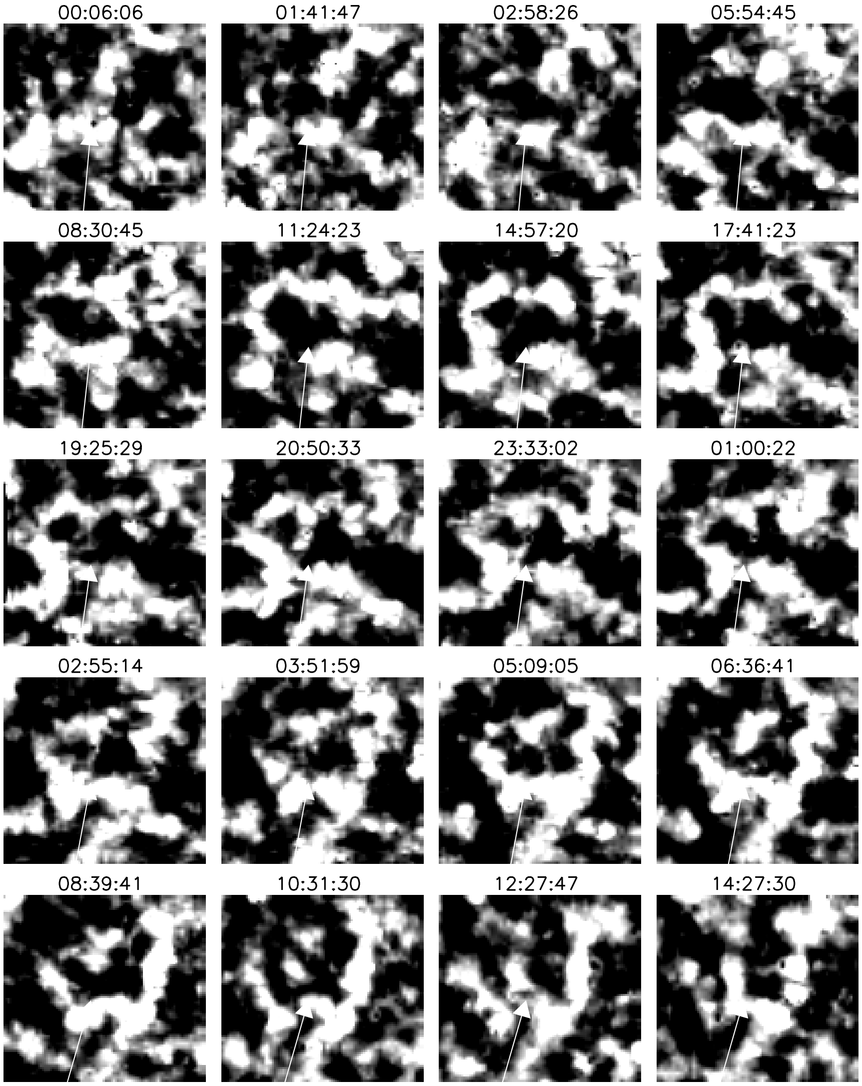

Figure 3.2: Evolution of a network cell from its birth to death. At 05:54:45 UT the network cell (marked by an arrow) started growing and matured at 08:30:45 UT. Next day at 12:27:47 UT this network cell merged with the neighboring network cells. The lifetime of this network cell is ≈ 29 hrs. The size of each image in this figure is 132 arc sec × 132 arc sec.

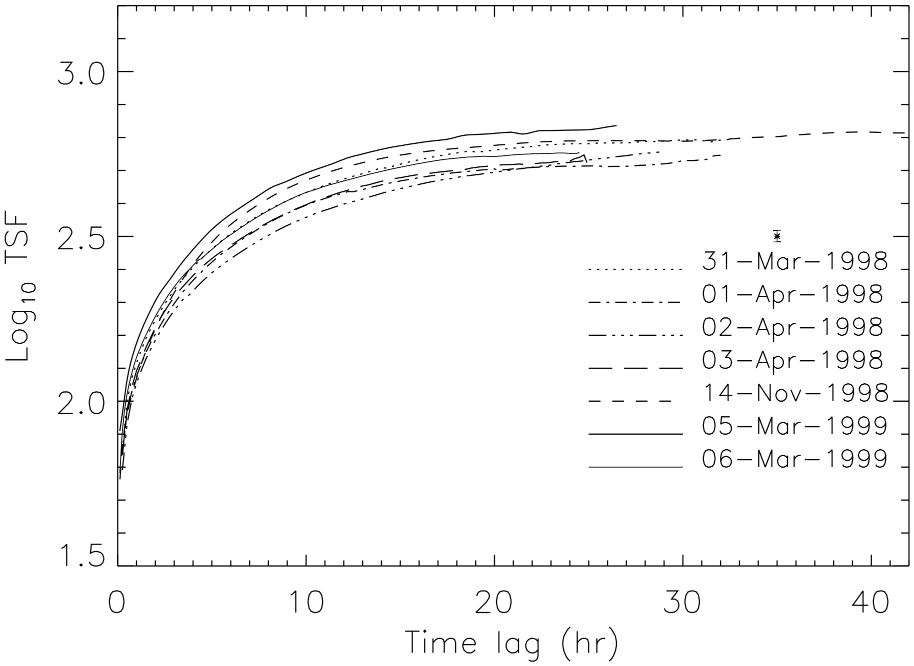

Figure 3.3: A plot of logarithm of TSF versus time lag (hrs) for different data sets of He II λ304 Å taken on different dates. Each curve looks similar in shape except for its TSF values. A vertical line with asterisk symbol shows an error bar in computing the TSF.

shifted the temporal window over a two hour time scale with an interval of 7 minute. (c) In each shift, we computed the TSF as mentioned in (a). (d) We then computed the mean and rms value of the TSF (at each time lag) from the TSF obtained in each temporal shift (of 7 minute interval). The mean value is used in the plot for estimating the lifetime and the rms value is interpreted as error bar. The maximum error in estimating the TSF is 3 % and is shown in the plot (as a vertical line over the cross). The 3 % error occurs at larger time lag and at smaller time lag it is much smaller than 3 %. The plot shows that TSF saturates between 23 and 27 hrs for most of the days of observation. This means that the lifetime of the network cells is in the range from 23 to 27 hrs. The shapes of the TSF are similar irrespective of the observational days.

3.3.1.2 Lifetime of photospheric magnetic network cells

Network is always associated with velocity and magnetic fields (Simon and Leighton, 1964). In Chapter 2, we have shown that there is one-to-one correspondence between the network element brightening observed in He II λ304 Å and the magnetic field in most of the locations. In that case, a logical question that follows is that, what is the lifetime of the magnetic network in view of the one-to-one correspondence between the He II λ304 Å network element and magnetic field.

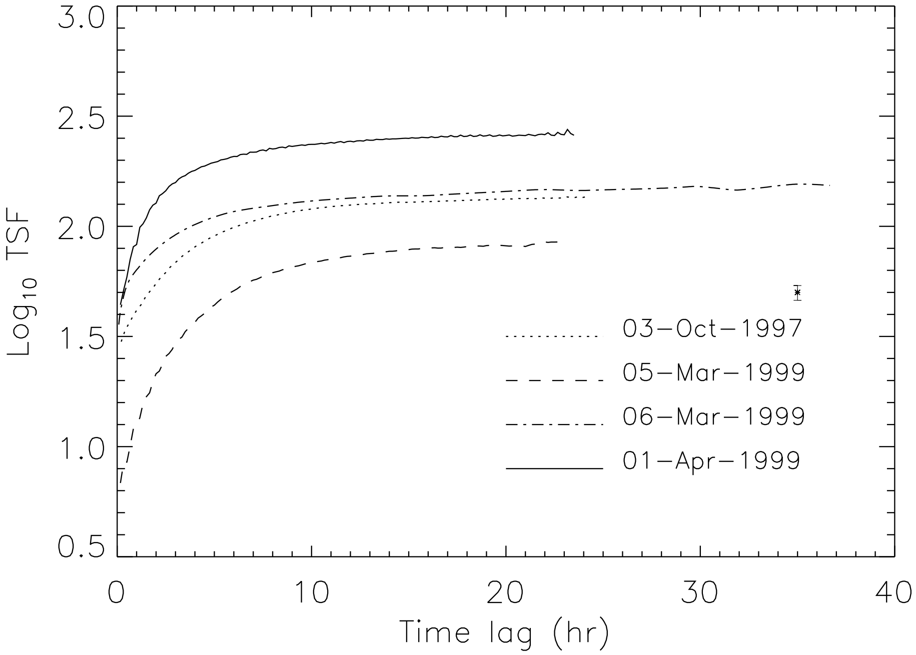

Figure 3.4: A plot of logarithm of TSF versus time lag (hrs) for magnetogram data of different days. Here one can see that the TSF saturates between 13-16 hrs. A vertical line with asterisk symbol shows an maximum value of error bar in computing the TSF.

Figure 3.4 shows the logarithm of TSF as a function of time lag for 4 different days of observations. The TSF saturates between 13 to 16 hrs. This means that the lifetime of the magnetic network cells ranges between 13 to 16 hrs. The error bar has been estimated by shifting our temporal window over a 3 hr time scale with an interval of 10 minute. This procedure gave a mean as well as rms value of TSF. The mean value has been used in the plot for estimating the lifetime and the rms value for the error bar. The error in computing the TSF is shown in the plot. The error is very small at smaller time lag and increases as the time lag increases. The maximum error in computing the TSF is 2% of the mean value of the TSF. The TSF of 06 March 1999 shows a small dip at ≈ 32 hrs. This dip is due to the missing data of the magnetogram and has been interpolated using cubic interpolation and hence the decrease in the TSF values.

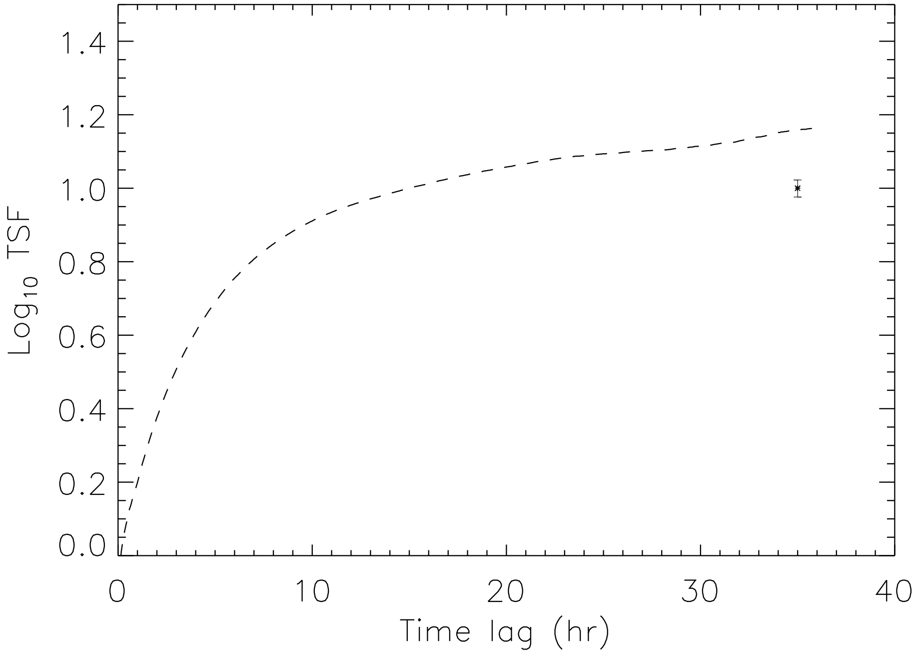

Figure 3.5: A plot of logarithm of TSF of the extrapolated magnetic field versus time lag (hrs). Here the photospheric magnetic field has been extrapolated to the height of 2800 km above the photosphere. The asterisk symbol with vertical bar denotes the size of the error bar.

3.3.1.3 Lifetime of extrapolated magnetic network cells

The lifetimes of the network cells observed in He II λ304 Å and the photospheric magnetic network cells are different. The potential extrapolated magnetic field sheds some light on the difference in the lifetimes of the He II λ304 Å network cells and photospheric magnetic network cells. Figure 3.5 shows a plot of TSF of the extrapolated magnetic network cells. The potential extrapolated data used here were generated using 06 Mar 1999 data. The magnetograms were extrapolated to a height of ≈ 2800 km above the level at which the magnetic elements are deployed. The TSF of the extrapolated magnetic field has a different shape compared to the TSF of the photospheric magnetic field. Here, in 36 hr interval, it has not yet reached saturation. This means that the lifetime of the extrapolated magnetic network is more than 30 hr. The error bar in computing the TSF is very small and is shown in the plot.

3.3.2 Size of the network cells

The size and shape of the network cells are important because they may throw some light on the origin of the convective cells. Even though the AC tends to show larger sizes, it is robust and simple. This tool can be used to compare network cells observed at different heights such as a comparison of size of the magnetic network with that of He II λ304 Å network. The AC curve shows several secondary maxima. The appearance of the secondary maxima implies a periodicity of the network cells. The distance between the primary and secondary maxima are interpreted as the size of the network cells (Simon and Leighton, 1964). In the following Sections we estimate the size of the network cells (observed in He II λ304 Å, magnetogram and potential extrapolated magnetograms) using AC and SSF.

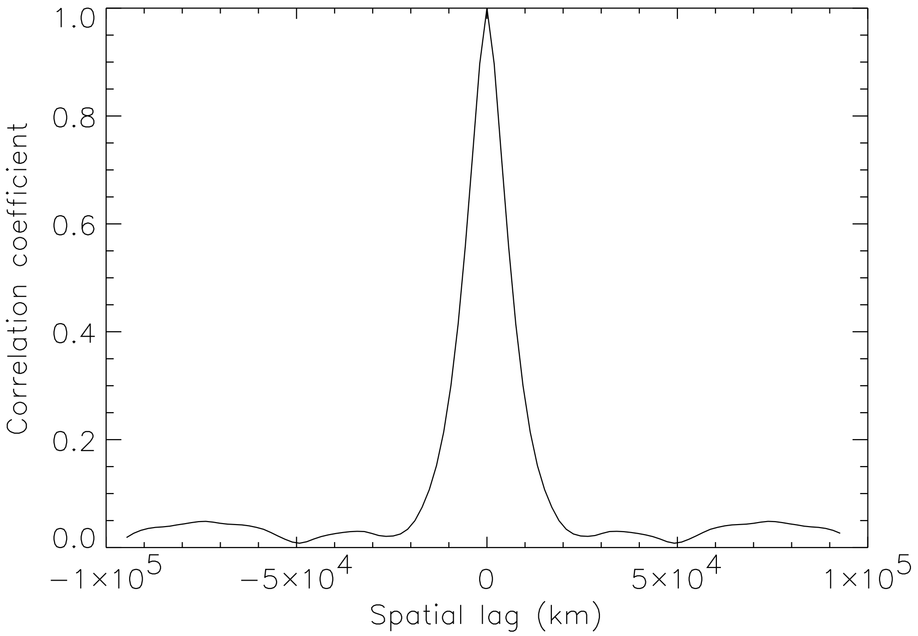

Figure 3.6: A plot of AC as a function of spatial lag (km) of He II λ304 Å filtergram. The distance between the primary and secondary peak is a measure of size of the network cell and FWHM of the AC is a measure of size of the network elements.

3.3.2.1 Size of He II λ304 Å network cells and its elements

Like Ca II K network cells, the network cells observed in He II λ304 Å are polygonal in shape. Figure 3.6 shows the typical AC of He II λ304 Å network cells. The AC of the He II λ304 Å filtergrams show that the typical size of the network cell is 32000 km. Apart from the size of the network, the AC curve gives another important parameter, full width at half maximum (FWHM). The FWHM of the AC curve is interpreted as the size of the network elements (Simon and Leighton, 1964). From the analysis of 25 frames (of He II λ304 Å images), we estimated the FWHM as 12800±1890 km.

The size of the network cells can be found by another statistical approach, that is, the SSF (described in Section 3.2.1.3). We plot a graph of logarithm of SSF as a function of spatial lag (Figure 3.7). The graph shows that the SSF saturates for a

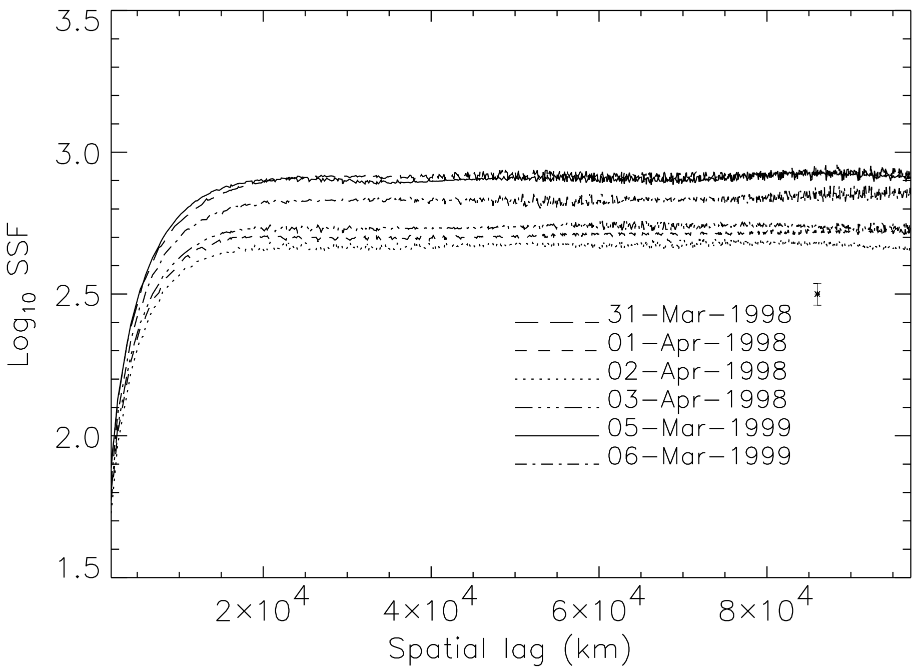

Figure 3.7: A plot of logarithm of SSF versus spatial lag (km) for various data sets of He II λ304 Å. Plot shows that the SSF saturates between 25000-30000 km. A vertical line with asterisk symbol shows an error in computing the SSF.

spatial lag in the range of 25000 to 30000 km. This means that the size of network cells observed in He II λ304 Å wavelength has a range from 25000 to 30000 km. The error in computing the SSF has been obtained as follows: (a) we chose a 460×460 arc sec^2 image window and slided it over a 525×525 arc sec^2 window in steps of 2.62 arc sec. (b) In each position we computed the SSF for different spatial lags. (c) From 625 such positions we could estimate the mean (which has been used for estimating the size of the network cell) and rms value (interpreted as error bar) of SSF at each spatial lag. The maximum error bar is shown in Figure 3.7 and it is found to be 6%. The error is negligible at smaller spatial lags.

We also measured the distance between the primary and secondary peak of AC curve for 121 images. We then plotted a histogram of distribution of cell size versus

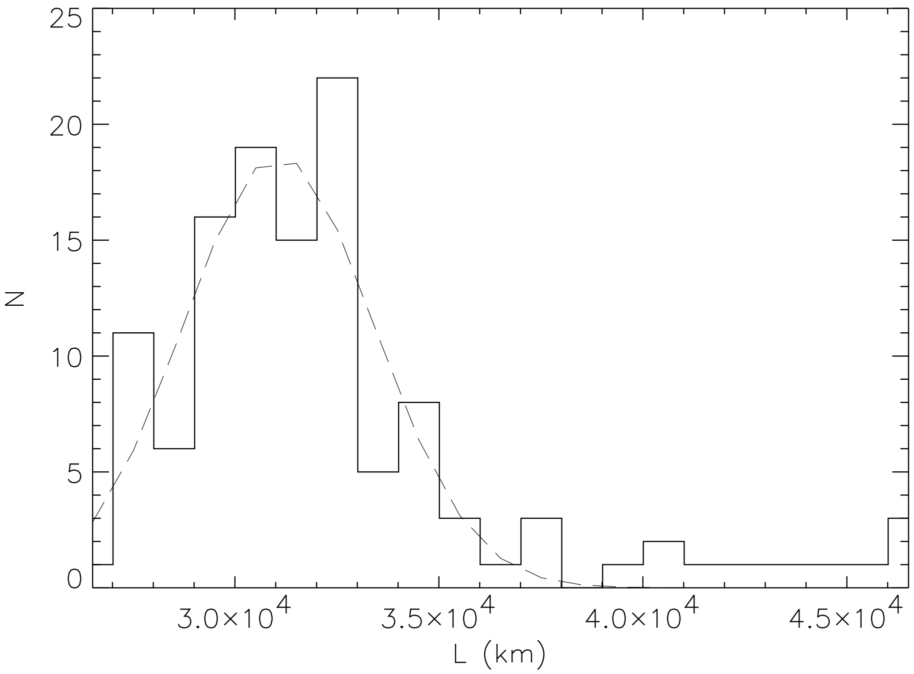

Figure 3.8: A histogram showing the distribution of network cell sizes observed in He II λ304 Å. The dashed curve represents the Gaussian fit to the histogram.

number of observations (Figure 3.8). We fit a normal distribution function to the histogram. The fit peaks at 31070±2348 km. The observed size of the network has a wide range of distribution from 27000 to 50000 km, indicating that there is a range in cell size. The difference in size of the network cells obtained from two different methods described here must be viewed against the difficulties of interpreting the AC curve for random functions that do not possess a constant mean.

3.3.2.2 Size of magnetic network cells and its elements

The AC curve of the photospheric magnetogram shows a secondary peak at $\approx$ 15000 km (Wang, 1988). The SSF applied to different magnetograms shows similar results. Figure 3.9 shows the logarithm of SSF as a function of spatial lag for different data sets. In computing the mean and rms value of SSF, we followed the same procedure as

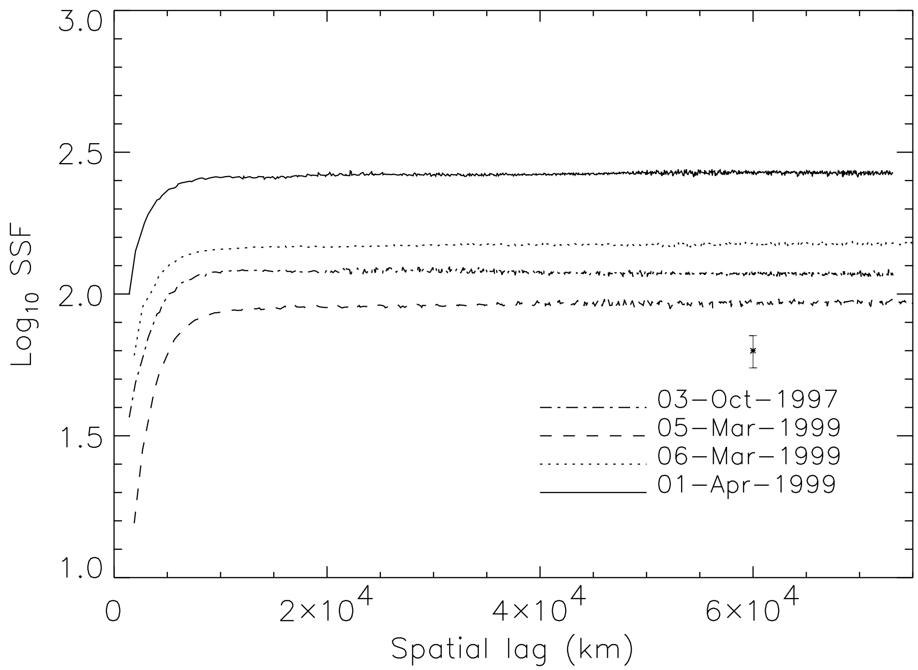

Figure 3.9: A plot of logarithm of SSF versus spatial lag (km) for different day magnetograms. Plot shows that the SSF saturates between 12000-15000 km. The asterisk symbol with vertical bar denotes the size of the error bar.

mentioned in the previous Subsection 3.3.2.1. The plot shows that the SSF saturates between 12000 to 15000 km for different days of observation. The saturation suggests that the size of the magnetic network cells is in the range from 12000 to 15000 km. At the same time, the FWHM of the AC of the magnetogram shows that the size of the magnetic network element is ≈ 5000 km. This discrepancy in the size of the magnetic network cell and its elements compared to the size of the He II λ304 Å network cell and its elements may be due to the different heights of formation of the network cells.

3.3.2.3 Size of the extrapolated magnetic network cells and elements

Figure 3.10 shows a series of magnetic images extrapolated to various heights above the photosphere. The magnetic images show how the magnetic elements evolve with

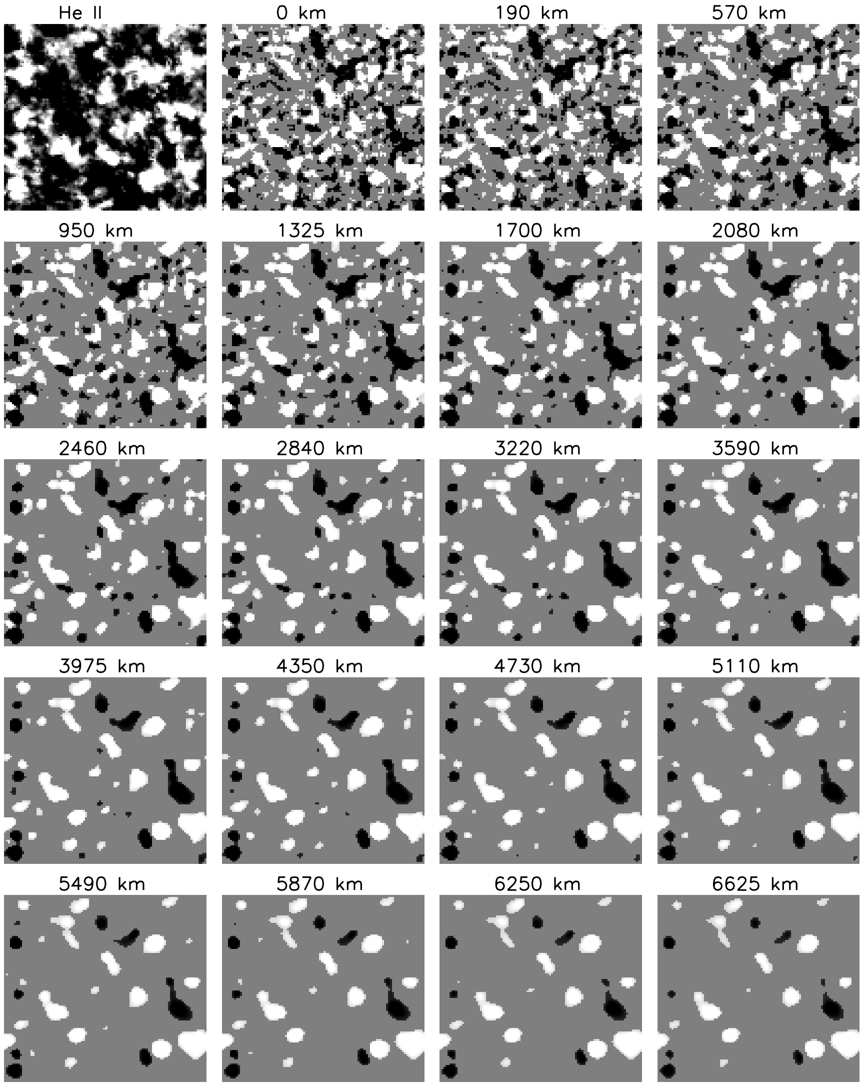

Figure 3.10: The top left image shows the portion of the Sun's image observed in He II $\lambda304$ Å. The other images are magnetograms generated from potential extrapolation of the photospheric magnetic field extrapolated to various heights. Here we have suppressed the noise in the magnetogram by replacing the values less than ±2 Gauss with zeros. The size of each image is 263 arc sec × 263 arc sec.

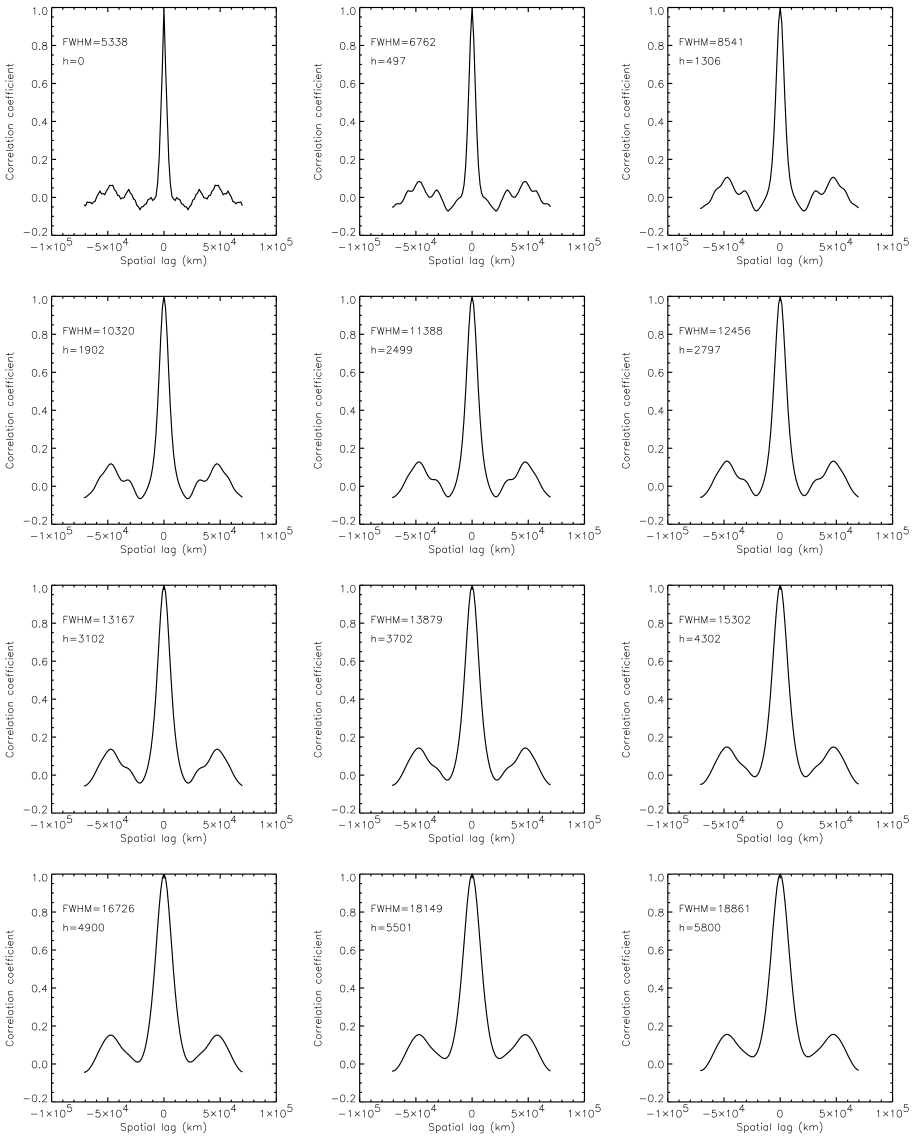

Figure 3.11: A plot of AC of extrapolated magnetograms, extrapolated to various heights. At 2800 km above the photosphere the FWHM of the AC of the extrapolated magnetic field matches with the FWHM of AC of the He II λ304 Å filtergram. In the plot ‘h’ represents the height (km) above the photosphere.

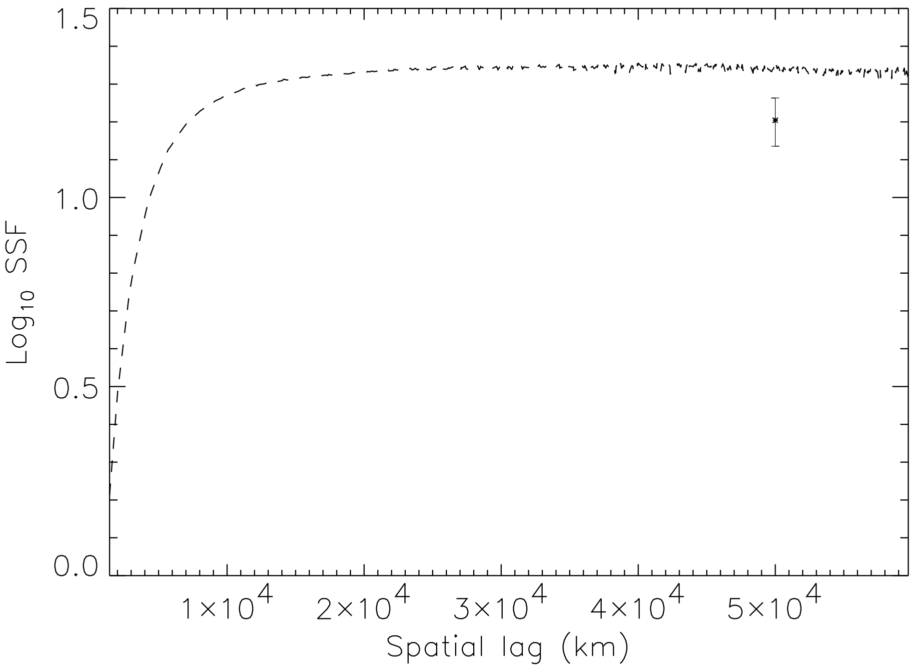

Figure 3.12: A plot of logarithm of SSF of the extrapolated magnetic field versus spatial lag (km). The magnetogram was extrapolated to the height of 2800 km above the photosphere. The asterisk symbol with vertical bar denotes the size of the error bar.

height. Examination of the extrapolated magnetograms reveals that the small-scale features disappear as we go higher in the atmosphere. The magnetogram shows that intra-network (IN) magnetic elements emerge as mixed polarities within the network cell. These IN elements are smaller in size compared to the network elements. The extrapolated magnetogram shows that IN elements disappear at a height of $\approx$ 2800 km above the photosphere. At larger heights only the large-scale features of the network element remain and it looks like only monopolar regions dominate. The comparison of these extrapolated magnetograms with the He II λ304 Å image (top left in the figure) gives some idea about matching of the sizes of network elements at higher heights. This can be shown more clearly using the FWHM of the AC of the extrapolated magnetograms. The AC curve of the photospheric magnetogram and its extrapolated values at different heights gives an idea of how the FWHM of the AC of the extrapolated magnetogram increases with height. Figure 3.11 shows an AC curve for the extrapolated magnetic field at different heights. The AC of the photospheric magnetogram shows several secondary peaks. The first secondary peak is at $\approx$ 15000 km. The FWHM obtained from the AC curve of the photospheric magnetogram is $\approx$ 5000 km. The AC curves of the potential extrapolated magnetogram show that the 15000 km secondary peak will disappear at 800 km above the photosphere. Above this height, the only available secondary peak of AC is at 30000-35000 km. The potential extrapolation of the magnetic field to further heights broadens the primary peak and hence the FWHM of the AC increases. Around 3000 km above the photosphere the FWHM of the AC curve of the extrapolated magnetogram matches the FWHM of the AC of He II λ304 Å filtergram. Extrapolation to further heights, increases the FWHM of the AC while keeping the distance to the secondary maxima constant at $\approx$ 30000 km. Above a certain height from the photosphere the secondary peak at 30000 km also disappears. The secondary maxima is then found at a higher length scale.

The SSF of the extrapolated magnetic field (extrapolated to the height of 2800 km above the photosphere) gave a size of the extrapolated magnetic network cell as $\approx$ 25000 km (Figure 3.12). This gives an impression that in the upper atmosphere the size of the magnetic network cell is not the same as in the photosphere.

3.3.3 Speed of the network elements

The network elements are always in motion. They wander about their mean position in a random manner. In order to estimate the approximate speed of the network elements we have made the space-time diagrams for the He II λ304 Å filtergrams as well as for the corresponding magnetograms. After averaging over 5 pixels in the spatial y-direction, we stacked the resulting one dimensional images in time and obtained the

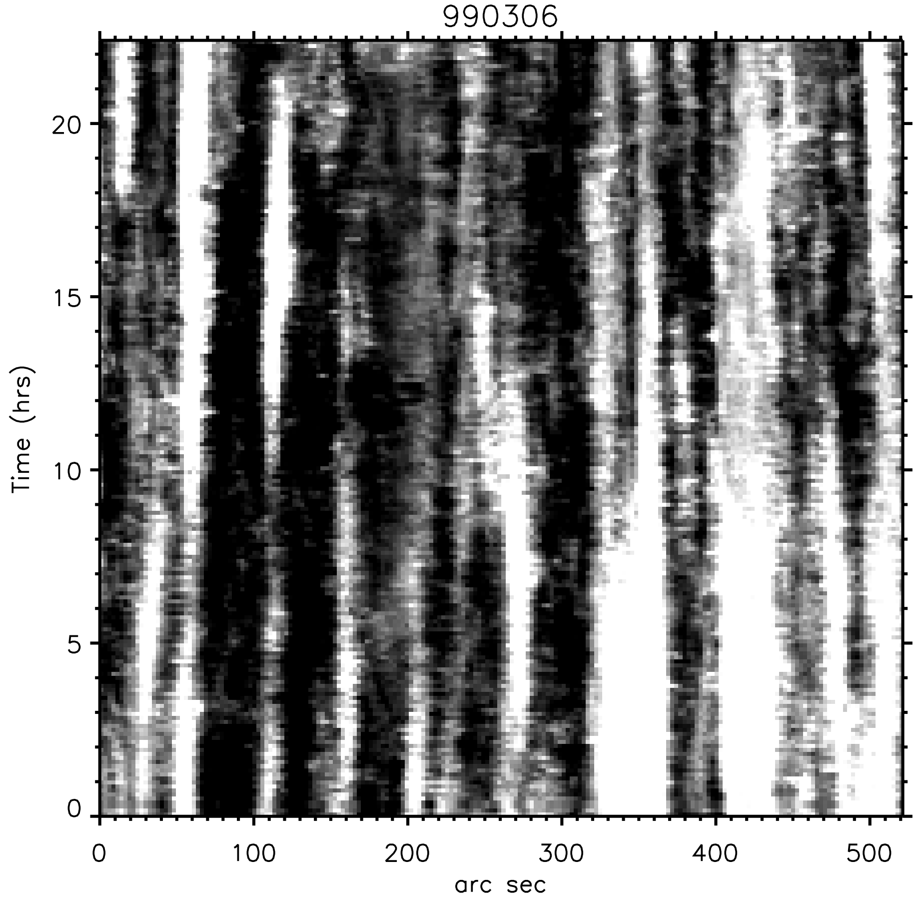

Figure 3.13: Space-time diagram of He II λ304 Å spanning an interval of about 23 hrs.

so called space-time diagrams. These are used to follow the individual He II λ304 network elements and magnetic elements in time and space. Figure 3.13 shows the space-time diagram of the He II λ304 Å for 06 Mar 1999 and Figure 3.14 shows the space-time diagram for the same elements followed in the magnetogram. In Figure 3.15 absolute value of the magnetic field has been shown for easy comparison with the intensity map. A qualitative comparison of both the space-time diagrams suggests that both the magnetic field and the He II λ304 Å network elements are related to each other. By tracking 10 such network elements in space-time diagram of He II λ304 Å, we could derive the speed of the network element as 0.08 km s^{-1}. The magnetic network

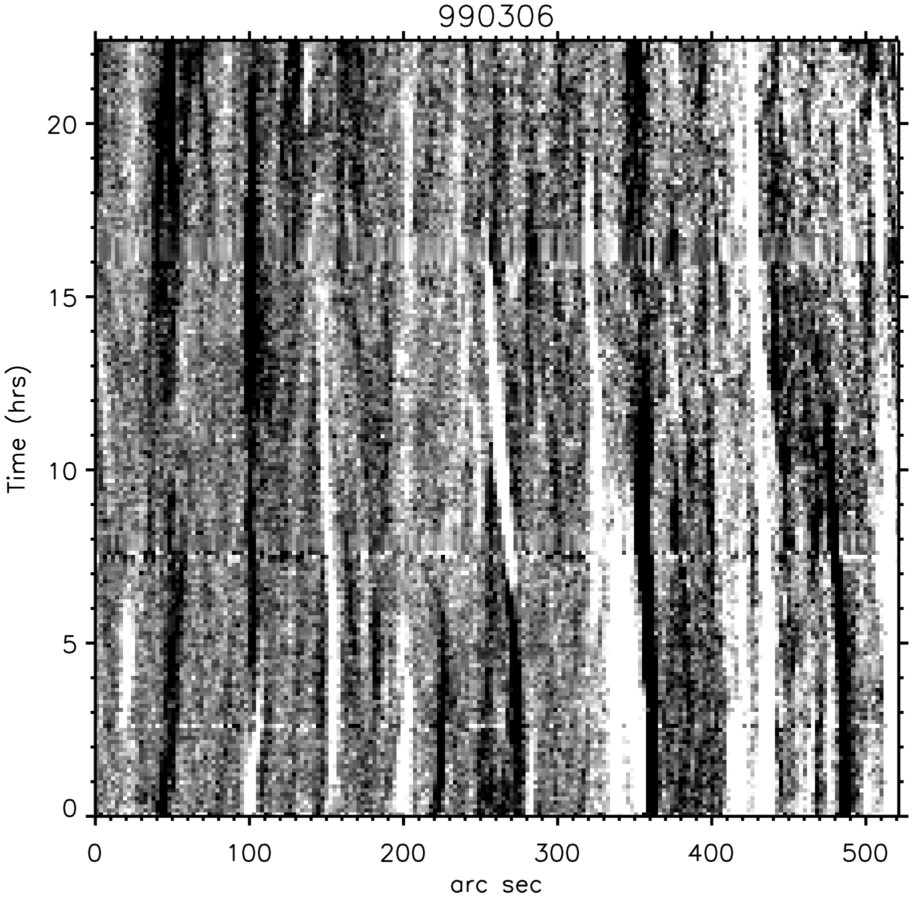

Figure 3.14: Space-time diagram obtained from magnetograms of the same region as that of He II λ304 Å images. Here the three horizontal lines at 2.5 hrs, 7.5 hrs and 16 hrs are artifacts due to the interpolation of the data sets.

elements had a speed of about 0.106 km s^{-1}. The observations show that the network element disappears before crossing the spatial scale of 5 pixels. Therefore, if one takes 5 pixel average in one spatial direction then one can consider the motion only along one direction (x-direction). This may lead to an underestimated values of the speed. We therefore followed the individual network element motion using local correlation tracking (LCT) technique (November, 1986).

The LCT method works by comparison of intensity in two selected windows. The

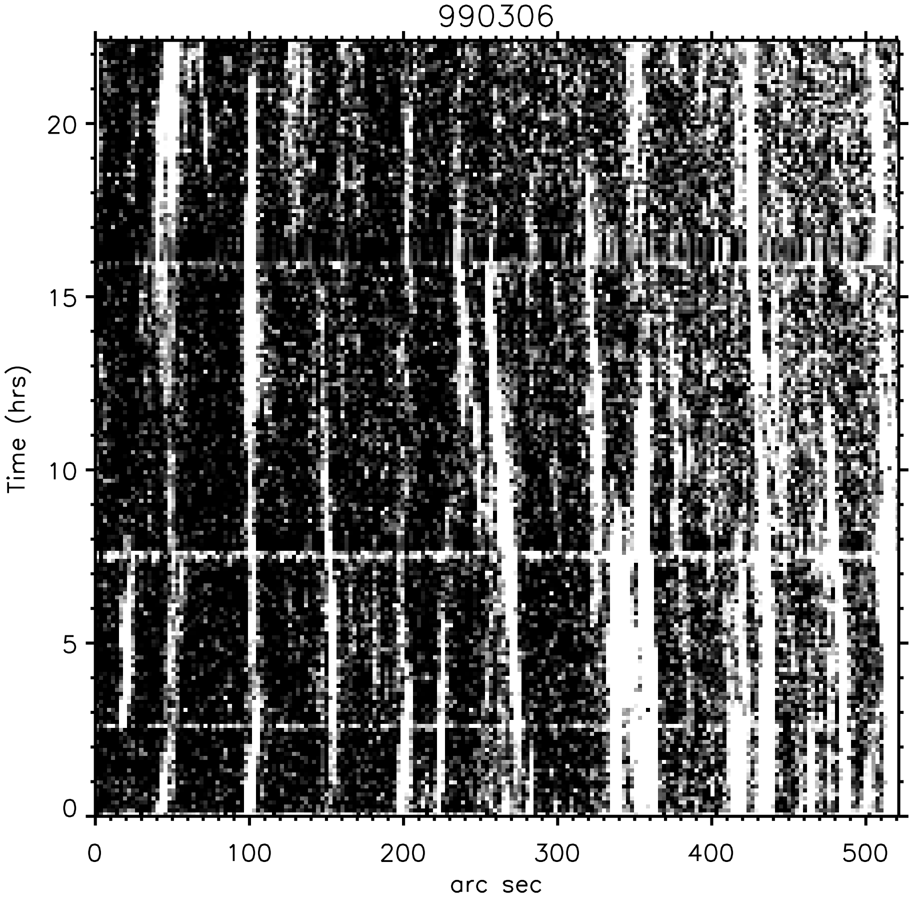

Figure 3.15: Space-time diagram obtained from absolute value of the magnetograms of the same region as that of He II λ304 Å images. Here the three horizontal lines at 2.5 hrs, 7.5 hrs and 16 hrs are artifacts due to the interpolation of the data sets.

rigid shift that gives the best match for each window pair is an (x, y) offset for the center of the window. The data values in a cell are apodized with a centered Gaussian. This Gaussian apodization on the selected windows makes the features near the center to be weighted more than those near the edges of the window. EIT images have a coarse resolution ($2''.62$ pixel^{-1}). The network element size is about $17''$ when observed in He II λ304 Å line using EIT. For detecting the motions of the network elements we chose a Gaussian apodization window of FWHM=$23''$ (which is larger than the

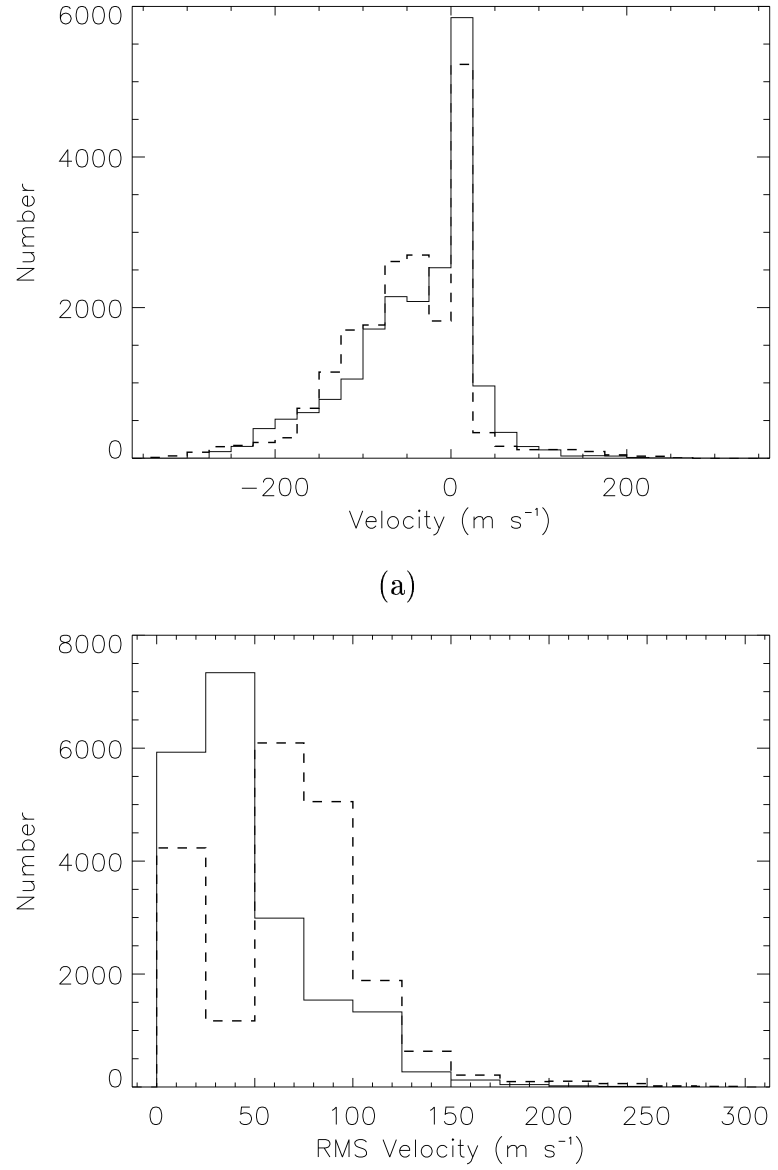

(a)

(b)

Figure 3.16: Histograms of the velocity in x (V_x-solid line) and y (V_y-dashed line) directions of the network elements observed in He II λ304 Å images. (a) Histogram of the mean velocity of the network elements and (b) histogram of the rms velocity of the network elements are shown.

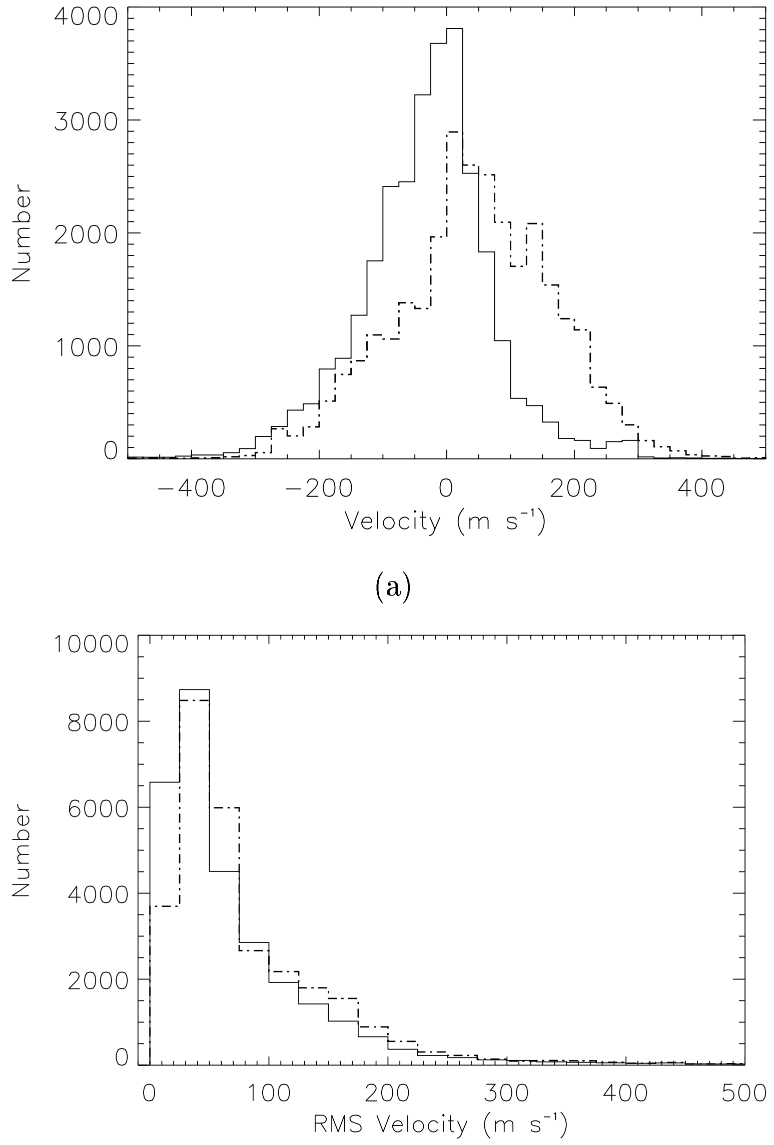

(a)

(b)

Figure 3.17: Histograms of velocity in x (V$_x$-solid line) and y (V$_y$-dash-dot line) directions of the magnetic network elements. (a) Histogram of the mean velocity of the network elements and (b) histogram of the rms velocity of the network elements are shown.

individual network element size) and the time interval between the two images is about 3 hours. While applying the LCT technique on the intensity images we have made an assumption that the network element does not disappear in 3 hour interval (as can be seen in the space-time diagrams) and it travels a certain distance which is detectable. We estimated the mean and rms value of velocity in the x-direction (V_x) and in the y-direction (V_y) separately by tracking the features for about 2 hrs. We plotted an histogram of the mean as well as rms values of V_x and V_y. Figure 3.16(a) and (b) shows histograms of the mean and rms value of V_x and V_y. The histograms show that most of the network elements move with small velocity and its distribution range is up to 200 m s^{-1}. The error in measuring the velocity is less than 20 m s^{-1}. We have already shown that the loop height of intra-network field is about 3000 km and at a height of formation of He II 304 Å network elements, most of the small-scale features including small-scale intra-network elements will disappear. Hence, we believe that most of the velocity measurements correspond to the network element velocity. As we have used a time interval of 3 hr between the reference image and subsequent image for LCT, intra-network elements may disappear or they may reach the network boundary within that time.

We also measured the network element velocity of the photospheric magnetic features. First of all, we have used the magnetogram data sets which are interpolated to the resolution of He II λ304 Å, that is $2''.62$ pixel^{-1}. In this coarse resolution, most of the intra-network bipoles will disappear since they have a size of $\approx 2''$. To eliminate the residual intra-network elements, we replaced the magnetic field values, which are below 10 G with zeros. In this way, most of the intra-network elements are eliminated and hence the contribution from the remaining intra-network elements to the velocity measurement is small. We chose the FWHM of the Gaussian apodizing window as $10''$ which is little larger than the magnetic network element size ($8''$) and a time interval of 3 hour between two magnetograms. We computed the mean and rms values of V_x and V_y. We then plotted a histogram of mean (Figure 3.17a) and rms (Figure 3.17b) values of V_x and V_y. Even though most of the elements show very small velocity, the spread in V_x and V_y is large. The large spread may be due to the velocity of the residual intra-network elements. The histogram shows that the rms value of V_x and V_y peaks at 40 m s^{-1}. The error in estimating the velocity is less than 20 m s^{-1}.

3.4 Summary and Discussion

We have studied the properties of network cells and elements observed in He II λ304 Å filtergrams and photospheric magnetograms. The obtained results are summarized as follows:

(a) The visual inspection of the individual network cell showed a range of lifetimes. The statistically estimated lifetime of the network cells observed in He II λ304 Å is in the range 23-27 hours.

(b) The photospheric magnetograms showed a lifetime in the range of 13-16 hours for the magnetic network cells. On the other hand extrapolated magnetic network cells (extrapolated to a height of 2800 km above the photosphere) showed a lifetime larger than 30 hour.

(c) The estimated size of the network cells observed in He II λ304 Å ranges between 25000 to 30000 km. The photospheric magnetic network cells showed a size of about 12000-15000 km. The magnetogram extrapolated to a height of 2800 km above the photosphere gave a size of about 25000 km.

(d) The size of the network elements as estimated from the FWHM of the AC of the He II λ304 Å filtergram is 12800 km. The size of the photospheric magnetic network elements is about 5000 km, while the size of the extrapolated magnetic network elements at a height of 2800 km above the photosphere is 12450 km. The discrepancy in the size of the network elements at two different heights can been attributed to the expanding nature of the network magnetic element with height.

(e) The average speed of the quiet-Sun network elements observed in He II λ304 Å is

$\approx$ 0.08 km s^{-1} and that for the photospheric magnetic network elements is $\approx$ 0.106 km s^{-1}. The estimated mean and rms velocity using LCT is small (<0.1 km s^{-1}) for large number of network elements.

The estimated lifetime of the network cells (using TSF) are compatible with the earlier results obtained for the chromospheric network cells (Raju, Srikanth and Singh, 1998) and the photospheric magnetic network cells (Wang, 1988). The visual inspection of the network cells from its birth to death showed that network cells have a range of lifetimes. This range of lifetimes is related to the nature of the network elements. Visual inspection and space-time diagrams showed that the transition region network elements (and hence the network cell) are related to the magnetic field. Our results suggest that the lifetime of the extrapolated magnetic network is better matched to the network cells formed at that height.

The computed SSF of the He II λ304 Å filtergram and magnetogram showed a discrepancy in the size of the network cell. The results derived from the AC function also showed a similar discrepancy between the two. Interestingly enough, FWHM of the AC showed that the features formed at different heights have different FWHM. The FWHM of the AC of the photospheric magnetogram is $\approx$ 5000 km and that of the He II λ304 Å is $\approx$ 12800 km. The discrepancy in size of the network elements at different heights can be interpreted as the expansion nature of the magnetic flux tubes with height. The potential extrapolation of the photospheric magnetic field sheds some light on this. As the height of the extrapolation increases, the size of the network elements increases while keeping the size of the network constant. At some height, the prominent size ($\approx$ 32000 km) is filled by the network elements and hence at that height the network property vanishes. The potential extrapolation of the magnetic field to various heights has shown that small-scale features including IN fields disappear at a height of about 3000 km above the photosphere. The mixed polarity nature, small size and disappearance of IN elements above some height may indicate that IN flux tubes are closed small-scale loops and IN fields may not extend to the higher atmosphere. Because of complete flux balance in the IN loops, the IN elements cannot change the flux of the network element significantly as they reach the network boundary. The time evolution of extrapolated field is different from the time evolution of the photospheric field. Further, the lifetime of the extrapolated magnetic network is larger than the photospheric magnetic network cells. This necessarily means that in the upper atmosphere the lifetime is different. Figure 3.11 shows that the upper atmosphere contains the network cells of size larger than 32000 km. The longer lifetime of the extrapolated magnetic network cell can be interpreted as a longer lifetime for larger size network. Thus, the in-situ magnetic field measurements would shed more light on the He II network evolution than the photospheric magnetic field alone.

Images obtained from space based telescopes, being free from Earth's atmosphere seeing, have great potential for determining the static and dynamic properties of the other transition region network cells in the emission of O VI, Mg X, C IV etc., in the future.

Chapter 4

A study of magnetic variations in sunspots

4.1 Introduction

The heating of the solar corona is a long standing issue since the time of its first observation. Many physical processes in the solar magnetic field have been considered to account for the heating of the solar corona (Ulmschneider, Priest, and Rosner, 1991; Zirker, 1993; Aschwanden, Poland, and Rabin, 2001). Various mechanisms and processes have been proposed and speculated, among them are magnetic reconnection, resonant absorption (Wright and Rickard, 1995), micro-flares, nano-flares (Parker, 1988, 1994), ohmic dissipation, resistivity (Aschwanden, Poland, and Rabin, 2001) and ion-cyclotron wave dissipation (Cranmer, 2000; Li, 2002). The conversion of MHD waves into shocks has been proposed as a heating mechanism for the solar corona (Boynton and Torkelsson, 1996). These periodic MHD waves are generated by moving the foot-points of magnetic field lines. Theories have shown that primarily 3 modes of wave can exist in the magnetic flux tubes they are: torsional Alfvén wave, kink wave and sausage wave (Spruit, 1982; Edwin and Roberts, 1983). Theoretical results suggest that all the three modes may contribute to chromospheric/coronal heating (Herbold *et al.*, 1985; Musielak, Rosner, and Ulmschneider, 1990; Poedts and Boynton, 1996; Nakariakov, Zhugzhda, and Ulmschneider, 1996).

Plasma in the solar upper atmosphere above the active region is always bright. Space based high resolution observations of the regions of the corona which are spatially related to the active regions like sunspots showed pronounced emission in the ultraviolet, extreme-ultraviolet and X-rays compared to the nearby regions. Active region (AR) corona has temperature of $\approx 15\times10^6$ K compared to 2×10^6 K for the quiet corona. The equivalent mechanical energy associated with this temperature is $\approx 10^7$ erg cm^{-2} sec^{-1} in the AR corona (Narain and Ulmschneider, 1990). With different model of sunspots, Chitre (1992) and Roberts (1992) found that sunspots are capable of sustaining a variety of oscillatory modes. In a way, the wave theory of coronal heating can be extended to the AR corona.

Discovery of sunspot umbral oscillations (Beckers and Schultz, 1972; Bhatnagar and Tanaka, 1972) attracted the attention of many, as it could provide information about the sub-photospheric structure of sunspots. Velocity and intensity oscillations in the sunspot umbrae have been well studied in different spectral lines. Recent advancement in the technique of helioseismology and its application to the magnetized regions of the Sun has shown that along with a suppression of the regular 5 minute velocity oscillations, there is an enhancement in power at higher frequencies (Horn, Staude, and Landgraf, 1997; Hindman and Brown, 1998; Venkatakrishnan, Kumar, and Tripathy, 2002). In-spite of these, very little is known about the magnetic oscillations in sunspots and their relation to the velocity and intensity oscillations. The detection of the magnetic field strength oscillations in sunspots is not yet widely accepted. The strong magnetic field introduces spatial inhomogeneities in the sunspot atmosphere and these inhomogeneous plasma structures alter the regular 5 minute p-mode oscillations and produce new modes of oscillations which are not present in the quiet Sun. These clumpy magnetic regions also absorb and scatter the acoustic power in the p-mode oscillations (Braun, Duvall, and LaBonte, 1987, 1988; Braun, LaBonte, and Duvall, 1990; Bogdan, *et al.*, 1993; Braun, 1995; Bogdan *et al.*, 1998). Apart from the intensity and velocity oscillations in sunspots, many have reported the observation of magnetic oscillations (Ulrich, 1996; Rüedi *et al.*, 1998; Norton *et al.*, 1999). Earlier attempts to measure magnetic oscillations at the photospheric levels of sunspots led to puzzling results. In the 80's there were only a few papers reporting oscillatory power of magnetic field components in the 3 and 5 minute bands (Milovanov, 1980; Gurman and House, 1981). Some observations indicated that apparent variations of the magnetic field could be introduced by seeing fluctuations (Landgraf, 1997). Lites *et al.* (1998) reported 4 G rms (upper limit) of the magnetic fluctuations for the amplitude of 5 minute oscillations using the one-dimensional data obtained from the Advanced Stokes Polarimeter. They also report that their measured magnetic oscillations are partly due to instrumental and inversion cross-talk between the velocity and magnetic signals and that the actual magnetic field strength fluctuations are weaker than 4 G.

There are some reasonable hints that these magnetic oscillations are not distributed randomly over the active regions. There has been reasonable observational support for solar MHD modes (Ulrich, 1996; Horn, Staude, and Landgraf, 1997; Lites *et al.*, 1998; Rüedi *et al.*, 1998; Norton *et al.*, 1999; Balthasar, 1999; Kupke, LaBonte, and Mickey, 2000; Settele, Sigwarth, and Muglach, 2002), but with varying results. Ulrich (1996) reported the observations of Alfvénic oscillations in Mount Wilson Observatory data. He showed that the power spectrum of the magnetic variations includes a peak at frequencies greater than the center of the 5 minute velocity oscillations superimposed on a background spectrum that includes substantial power at low frequencies. Horn, Staude, and Landgraf (1997) found 5 and 3 minute oscillations of the longitudinal magnetic field strength from two-dimensional spectro-polarimetric measurements. This result was confirmed by Rüedi *et al.* (1998) from data taken with the MDI instrument, with a rms value of 6.4 G. In the measurements of Rüedi *et al.* (1998), the magnetic oscillations are restricted to rather small locations in the sunspots and in most cases close to the umbra-penumbra boundary. They occur at different places for 5 and 3 minute oscillations. Norton *et al.* (1999) (using the MDI magnetograms) have reported that the variations of magnetic fields are persistent all through the active region and that the frequency of oscillations decrease with decrease of field strength. The characteristics of these oscillations vary with the field strength, peaking in three frequency regimes: 0.5 - 1.0, 3.0 - 3.5 and 5.5 - 6.0 mHz. Balthasar (1999) has found magnetic oscillations with rms values between 40-70 G in umbra-penumbra border of the sunspots using time series of spectro-polarimeter data at the VTT on Tenerife. However, Norton (2000) has found a rms value of 18.1 G in sunspot umbrae using MDI data. Kupke, LaBonte, and Mickey *et al.* (2000) reports oscillations in both 5 and 3 minute, mainly at the umbral-penumbral border, with a rms value of 22 G using data taken with the Mees spectropolarimeter. Settele, Sigwarth, and Muglach (2002) have shown localized magnetic oscillations having a rms value of 13.9 G using vector magnetic field data measured with the Advanced Stokes Polarimeter at the Dunn Solar Telescope. An analysis of velocity and magnetic field strength oscillations in a sunspot's umbra based on the inversion of the full Stokes vector of the pair of infrared lines (Fe I 1.56 μm) was performed by Bellot Rubio *et al.* (2000). They reported that the amplitude of the magnetic field oscillations decreases as one moves from the center of the umbra to the umbra-penumbra boundary.

Intensity and velocity variations have been observed in regions where the magnetic field is strong such as in sunspot umbrae, plages and supergranulation boundaries. In sunspots Zirin and Stein (1972), Giovanelli (1972), Moore and Tang (1975) and Christopoulou, Georgakilas, and Koutchmy (2000) have found running penumbral waves. These are observed in H_α films of penumbra as regular outgoing ripples with a period between 150 and 290 seconds. These wave motions are predominantly up and down and it may well be excited by the shorter period umbral oscillations. These oscillations are absent in the complex active regions. Also, inside umbrae one some times finds chromospheric umbral flashes which are small upward moving elements lasting

50 sec (Beckers and Tallant, 1969). They are often repetitive but are uncorrelated with the photospheric oscillations. Antia and Chitre (1979) have suggested that they are overstable magneto-acoustic modes and have investigated magneto-acoustic gravity modes in a polytropic stratified atmosphere in the presence of a uniform vertical magnetic field.

Even with all these efforts, it is yet not clear whether these observed oscillations are intrinsic in origin or represent the response of the sunspot to the global p-modes or whether the quiet Sun acoustic waves are transformed into magnetoacoustic waves in the magnetized clumpy plasma of the sunspot. In addition to this, it is very hard to differentiate these oscillations from the instrumental artifacts (if existing) or time dependent opacity effects (Lites *et al.*, 1998; Rüedi *et al.*, 1999; Bellot Rubio *et al.*, 2000). Various observations show that the magnetic field strength in sunspots decreases with height of the order of 1-3 G km^{-1} (Wittmann, 1974; Balthasar and Schmidt, 1993; Bruls *et al.*, 1995; Ruëdi *et al.*, 1998; Solanki, 2003). Any compressible wave passing through the magnetized atmosphere which is having magnetic field gradient in the vertical direction will produce oscillations of the line forming region and hence be manifested as oscillations in the magnetic field strength.

In this Chapter, we try to find the magnetic field variations and their locations using 4 active region time-series magnetograms. SOHO/MDI magnetograms, being free from 'seeing' effects, are best suited for this analysis. The SOHO/MDI high resolution magnetograms are best suited for the analysis of long term fluctuations since the sound travel time and the pixel resolution and the cadence of the magnetograms are well suited. We also search for the possible sources of low frequency magnetic field fluctuations.

Table 4.1: Active region number, date, location and time of observations are shown in the table.

Serial No.	Active Region (NOAA No.)	Date of Observation	Location	Time of Observation (UT)
1	AR 8113	Dec. 02, 1997	N20W00	15:00-20:59
2	AR 8668	Aug. 20, 1999	N23W04	09:00-14:30
3	AR 8760	Nov. 10, 1999	N14W01	15:00-20:59
4	AR 9354	Feb. 18, 2001	S09E10	17:00-22:59

4.2 Data

Apart from a regular cadence of 96 minute, SOHO/MDI acquires occasionally magnetograms at every minute in full disk mode and sometimes in high resolution mode. We chose the magnetograms of NOAA AR 8113, 8668, 8760 and 9354 in the MDI high resolution mode with a resolution of $0''.6$ pixel^{-1}. These active regions were primarily chosen on the basis of availability of good quality magnetograms from SOHO/MDI with minimum instrumental problems during the observation. While choosing these data sets we have kept in mind that active regions should be close to the central meridian and each should be in the different stages of evolution. Each data set consists of a time series of high resolution magnetograms taken at a cadence of one-minute, spanning 6 hr interval. The date and time of observations are summarized in Table 4.1. These data sets have been complimented with white light images from SOHO/MDI to examine the saturated pixels (if present) and to locate the regions of magnetic field variations in sunspots.

4.3 Pre-processing

One-minute cadence magnetograms were corrected for the mean solar rotation for the data set summarized in Table 4.1 by taking the time of acquisition of the first magnetogram as the reference time. Then magnetograms were registered using two-dimensional cross-correlation program. A test for identifying saturated pixels was done in the magnetograms by plotting the intensity versus magnetic field values to avoid the measurement errors (c.f., Liu and Norton, SOI Technical Note 01-144). No saturated pixels were found in the sunspot umbra.

4.4 Results

4.4.1 Temporal variations of magnetic signal

We examined the temporal variations of magnetic signal from individual pixels without any spatial averaging. Figure 4.1(a) shows the sample of temporal variations from a particular pixel. Apart from the rapid variations, the magnetic signal also shows a long term trend consisting of slow variations. Previous workers used a polynomial fit or Gaussian filter of certain width (temporal) to detrend the signal. Figure 4.1(b) shows the residual magnetic field variations after detrending the signal (detrended using a Gaussian filter having a 30 minute width). After the subtraction of the detrending curve only the high frequency oscillatory part remains. We estimated the rms values of the oscillatory part of the magnetic signal in the sunspot umbral region on subtracting a 30 minute Gaussian detrending curve. The rms value of the magnetic field fluctuations is found to be 6.8, 13.7, 11.8 and 11.2 G in sunspot umbra of active regions AR 9354, AR 8760, AR 8113, and AR 8668 respectively. Similar values were obtained when we detrended the magnetic signal with a fourth order polynomial fit (Ulrich, 1996). The obtained rms value is the integrated rms fluctuations available at 5 and 3 minute band.

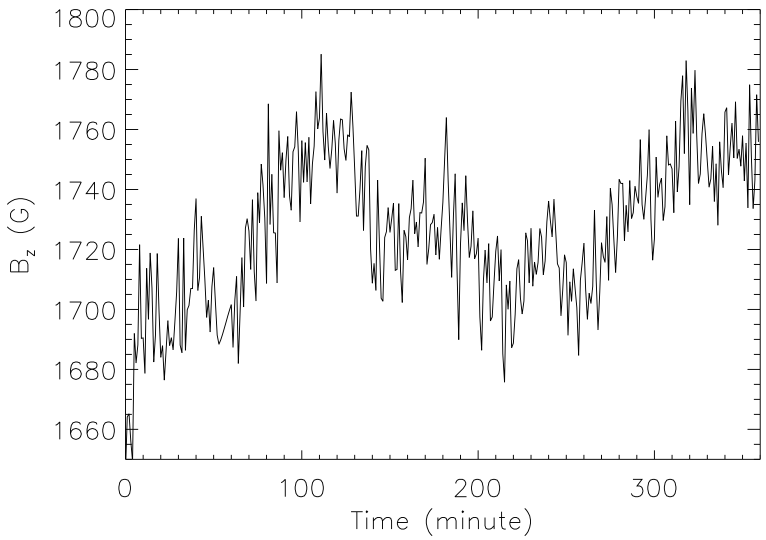

(a)

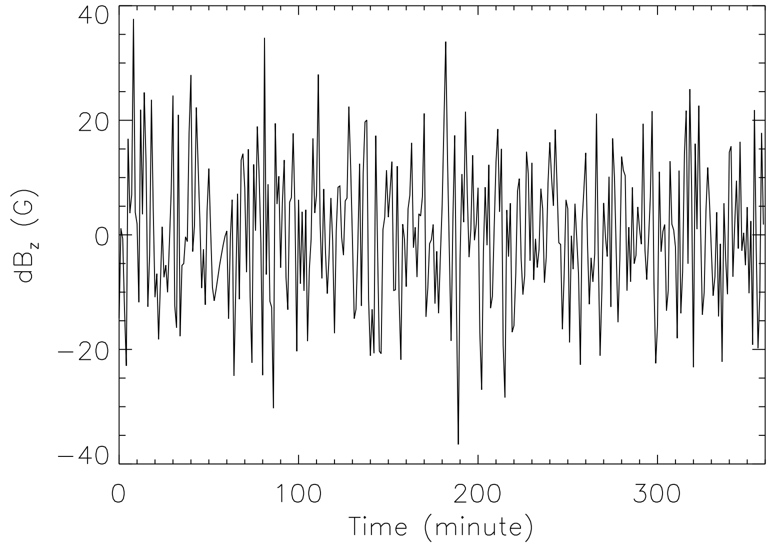

(b)

Figure 4.1: A plot of magnetic field signals versus time are shown here. (a) The magnetic signal obtained from a single pixel with time. (b) Residual magnetic field variations after detrending the signal using a Gaussian filter of 30 minute width. The plot shows that the long term trend has been removed.

4.4.2 Power spectra of the magnetic variations

In all the aforementioned results obtained by various researchers (Section 4.1), the Fast Fourier Transform (FFT) based power spectrum is used as a tool to find the power at particular frequency regimes. The power spectrum tool is used to study periodic and quasi-periodic phenomena. Power spectrum analysis is very useful to distinguish chaotic phenomena from complex dynamics. The power spectrum of a signal from a chaotic system should decay exponentially at high frequencies. On the other hand, the power spectrum should follow the power law for the colored noise system. To see the power, which are concentrated at particular frequency regimes, we used a FFT based power spectrum technique.

In order to see the power at different frequencies and at different locations of the sunspots, we segregated the pixels according to their mean magnetic fields in the classes of 100-300 G, 300-600 G, 600-900 G, 900-1200 G and 1200-1600 G and 1600 G and above. The segregation of the pixels is under the smooth contours of magnetic field strength 100, 300, 600, 900, 1200 and 1600 G regions. Figures 4.2(a) and (b) & 4.3(a) and (b), show the smooth contours of magnetic field (300 G, 900 G and 1200 G) overlaid upon the intensity map of different active regions. The features like moats, moving magnetic features (MMF's) and the penumbra - photospheric boundary comes under 50-300 G regions. The penumbral magnetic field lies in the range of 300-900 G field strength. Umbra and penumbra boundary lies in the field strength range of 900-1200 G. Finally, umbral magnetic field of a sunspot falls in the region above 1200 G.

We first computed the power spectra of individual pixels containing the local structures in time. We then improved the signal-to-noise ratio in the power spectra by averaging the power spectra over the pixels in the segregated field strength regions. The data used for the power spectra were neither smoothed spatially nor detrended temporally. Figure 4.4 shows the power spectra for different absolute mean measured flux which lie in the range 100-300 G, 300-600 G, 600-900 G, 900-1200 G, 1200-1600 G

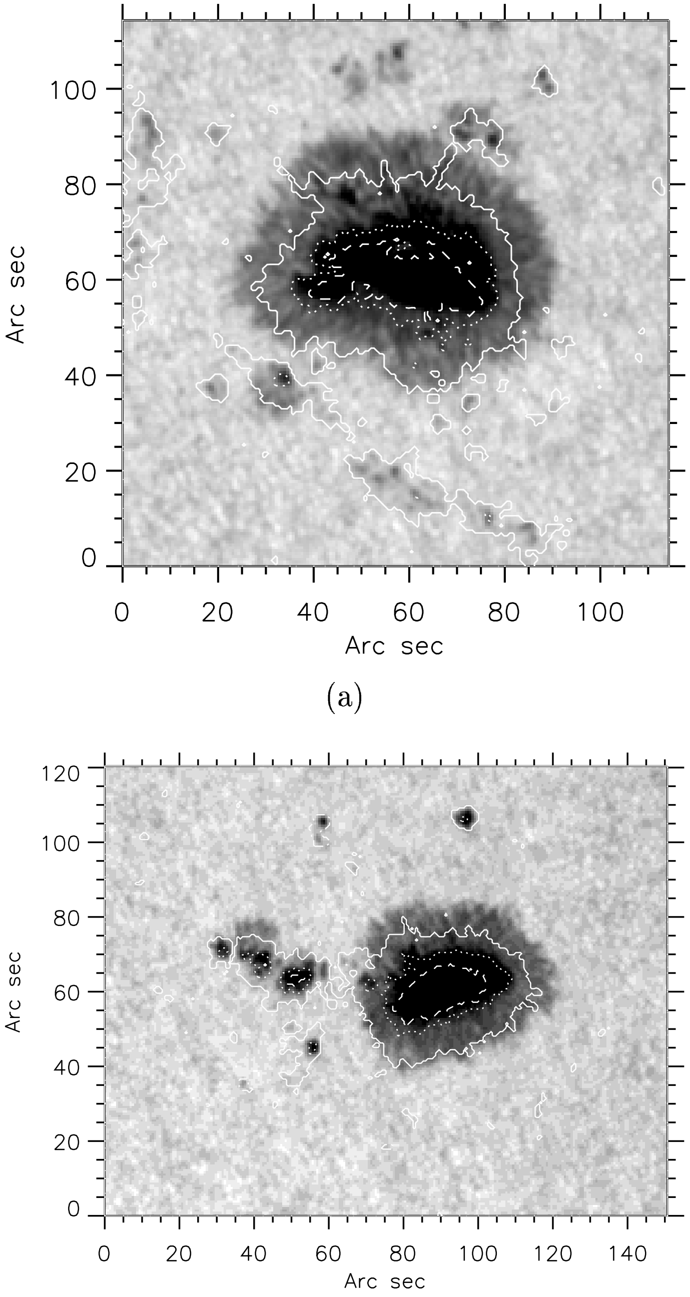

(a)

(b)

Figure 4.2: A contour map of magnetic field overlaid upon the intensity map. The contour levels of 300 G (solid line), 900 G (dotted line) and 1200 G (dashed line) drawn on (a) AR 8113 and (b) AR 8668 image.

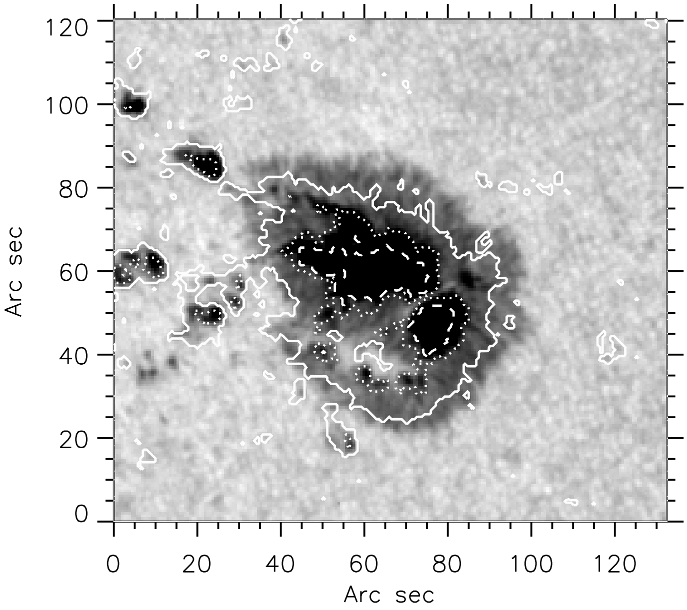

(a)

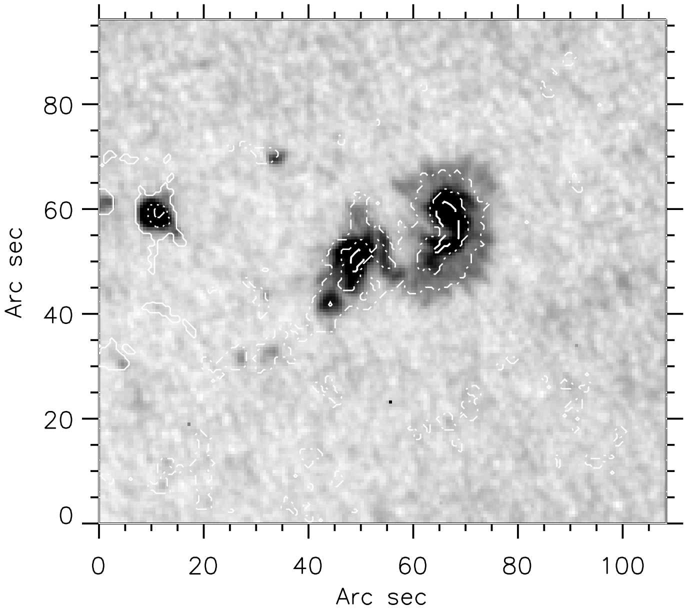

(b)

Figure 4.3: A contour map of magnetic field overlaid upon the intensity map. (a) The contour levels of 300 G (solid line), 900 G (dotted line) and 1200 G (dashed line) drawn on AR 8760 image. (b) The contour levels of -300 G (dash-dot), -900 G (dash-dot-dot) and -1200 G (dashes) drawn on AR 9354 image.

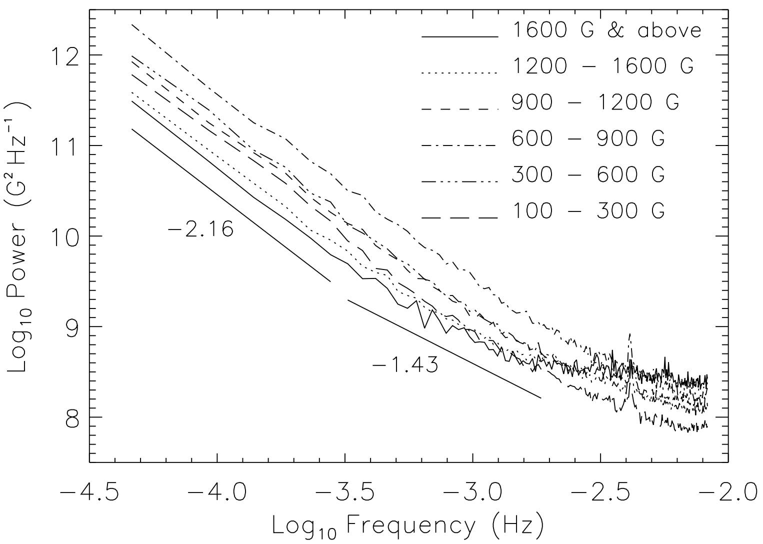

Figure 4.4: Average power spectra of the magnetic signal whose mean absolute field strength in the range 100-300 G, 300-600 G, 600-900 G, 900-1200 G, 1200-1600 G and 1600 G and above are plotted in logarithmic scale. The computed power spectra is for the AR 8760.

and 1600 G and above. The power spectrum shows low as well as high frequency variations. The low frequency variations follow a power law. It is interesting to see that the power in the low frequency regimes (at least up to 1.9 mHz) of the sunspot umbra is lower than the power in other regions of the sunspot. The power in the high frequency regime is flat in the high magnetic field strength regions and it is higher than the other magnetic field regions. Unlike the high field strength regions, the lower field strength power spectrum continues from its low frequency part to high frequency part with little or no turning. The flat power spectrum at higher frequency regimes beyond 7.0 mHz in the higher magnetic field strength regions might be partly due to noise in the measurement. The high frequency power includes the enhancement of power at 3 mHz (-2.5 Hz in logarithmic scale) and at 5.5 mHz (-2.26 Hz in logarithmic scale) frequencies especially in higher magnetic field strength regions. The enhancement of power at 4 - 4.5 mHz (-2.39 to -2.35 Hz in logarithmic scale) is an artifact due to pixel

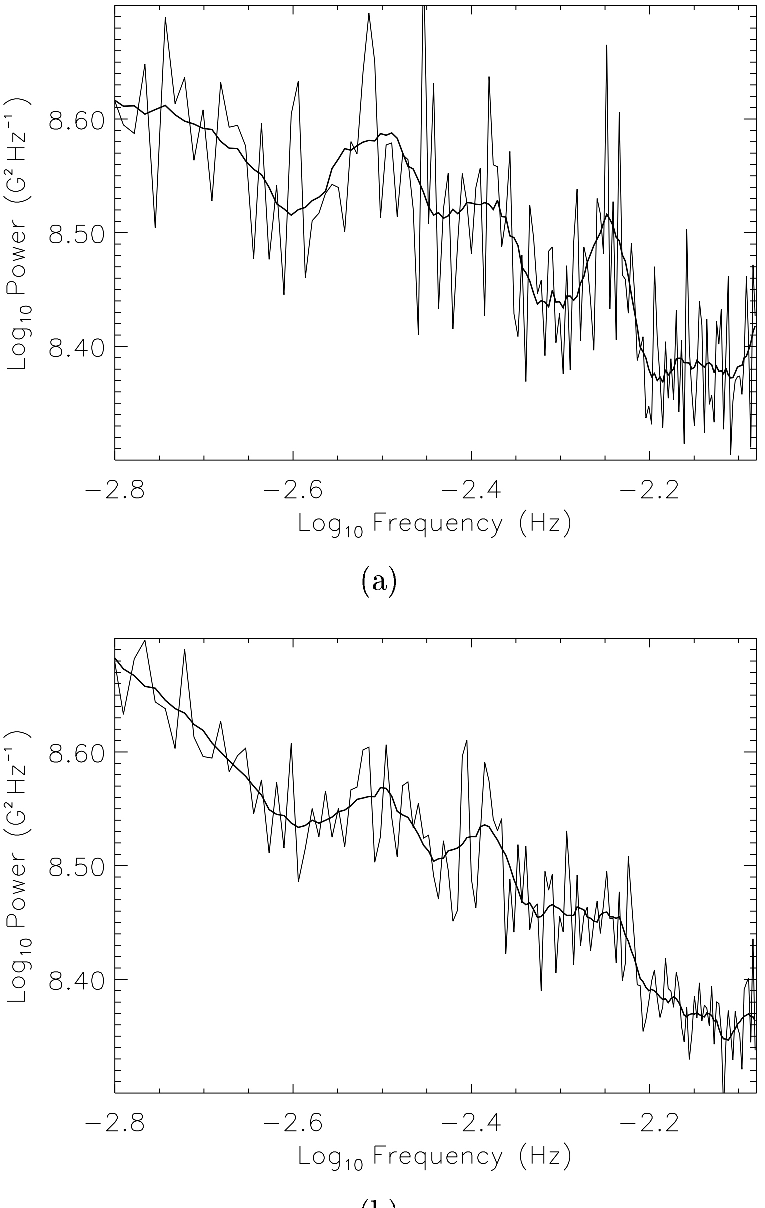

(a)

(b)

Figure 4.5: Average power spectra of the magnetic signal (of AR 8760) with mean absolute magnetic field in the range (a) 1600-2000 G, and (b) 1200-1600 G are plotted with resolved scale.

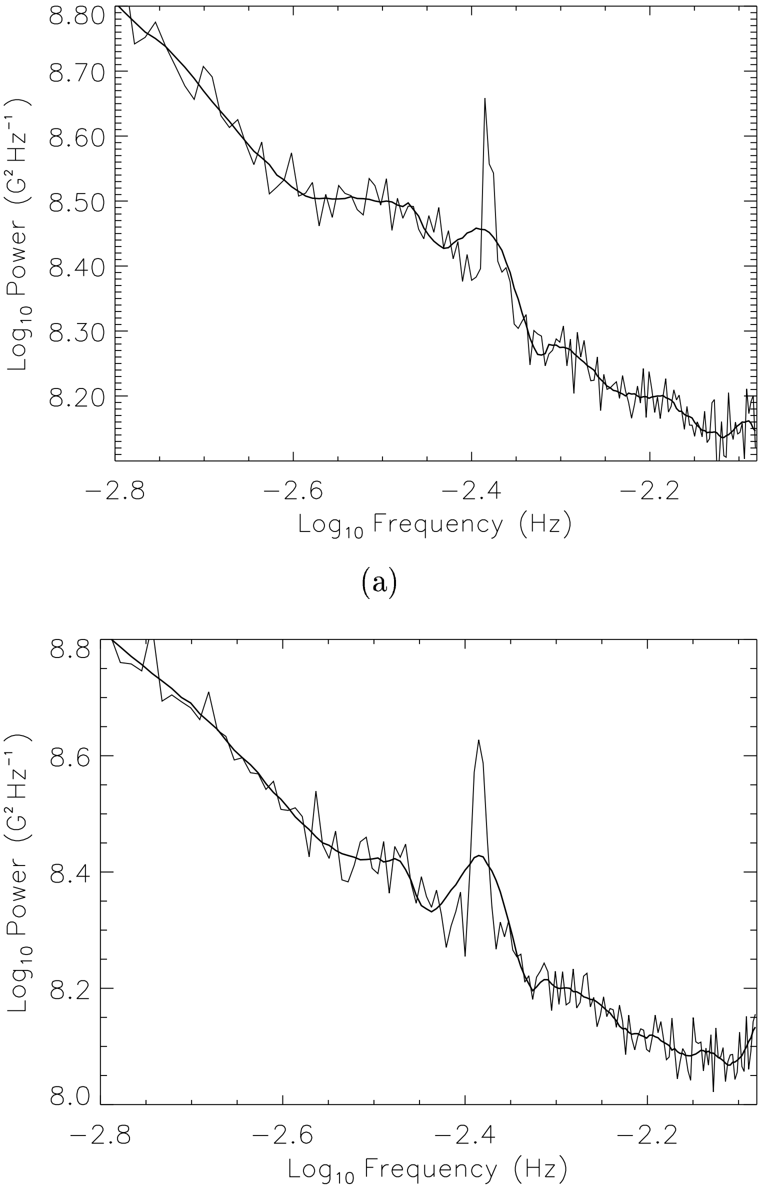

(a)

(b)

Figure 4.6: Average power spectra of the magnetic signal (of AR 8760) with mean absolute magnetic field in the range (a) 900-1200 G and (b) 300-600 G are plotted with resolved scale.

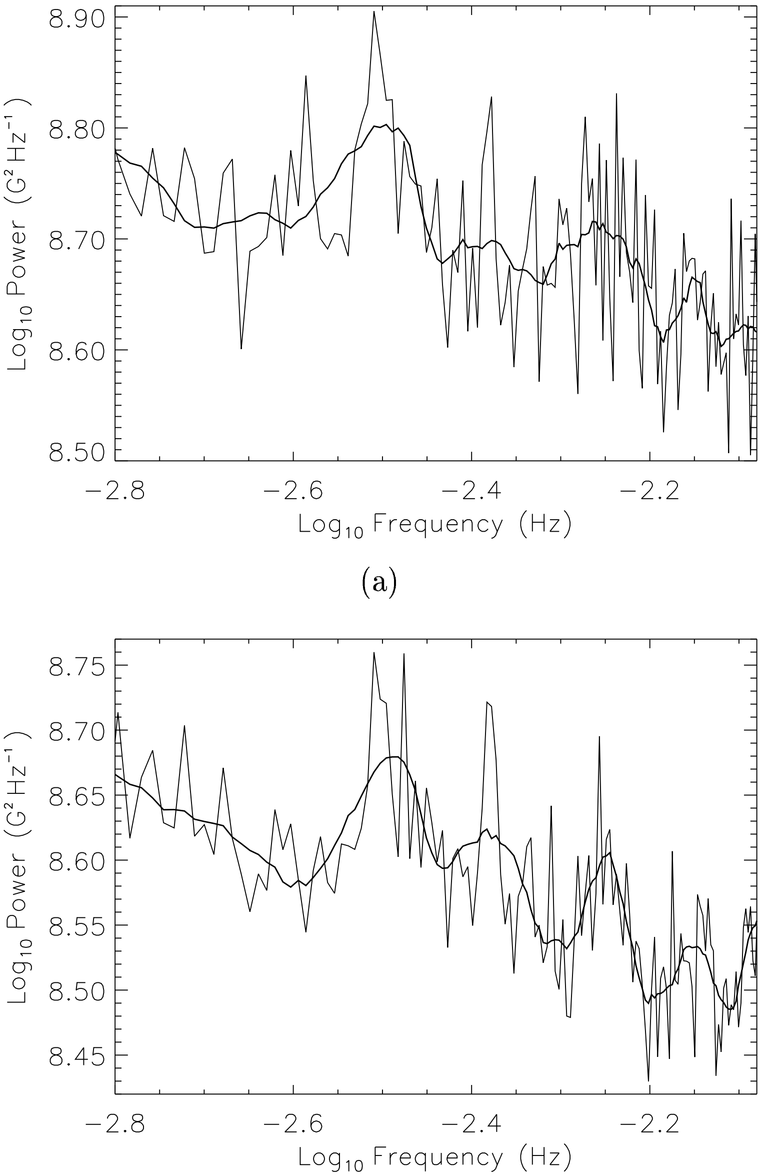

(a)

(b)

Figure 4.7: Average power spectra of the magnetic signal (of AR 8668) with mean absolute magnetic field in the range (a) 1600-1900 G, and (b) 1200-1600 G are plotted.

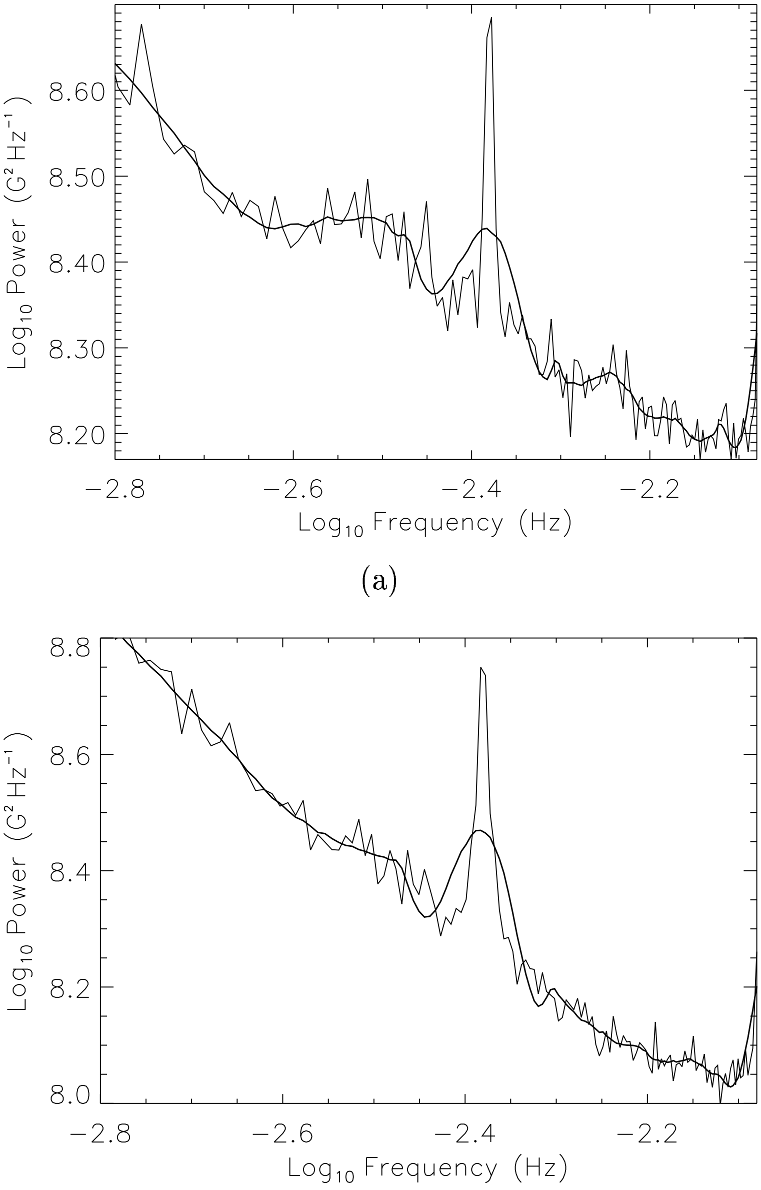

(a)

(b)

Figure 4.8: Average power spectra of the magnetic signal (of AR 8668) with mean absolute magnetic field in the range (a) 900-1200 G and (b) 300-600 G are plotted.

Table 4.2: Power law indices for different classes of structures in AR 8760.

Structures	index (0.32 - 1.8 mHz)	index (46 μHz - 0.27 mHz)
100 to 300 G	-1.84±0.03	-2.06±0.03
300 to 600 G	1.89±0.02	-2.11±0.06
600 to 900 G	-2.0±0.02	-2.1±0.06
900 to 1200 G	-1.88±0.03	-2.1±0.04
1200 to 1600 G	-1.54±0.03	-2.12±0.03
1600 to 2000 G	-1.43±0.05	-2.16±0.02

crossing time of MDI high resolution magnetograms with a plate scale of $0''.6$ pixel^{-1} (Scherrer, private communication).

The enhancement of power at 3 and 5.5 mHz can be seen clearly in Figures 4.5 to 4.8. These figures are same as Figure 4.4 but plotted with resolved scale. The spectrum is smoothed by applying a Savitzky-Golay (S-G) filter (Press *et al.*, 1992). The S-G filter basically smoothes the data by a window function of a predefined number of data points and a polynomial least square fit with proper weighting and then finds the maximum of the smoothed spectrum. After many trials, we chose the best fit with a window of 16 data points and a polynomial of order 4. The thick line in Figures 4.5 to 4.8 represents the best fit using the S-G filter. The plots show that there is an enhancement of power at 3 mHz and 5.5 mHz in the sunspot umbra especially, in 1200-2000 G regions. The increase of high frequency power in strong field region may be either due to the reduced intensity and broad absorption lines or may be due to the increased solar variations: we cannot distinguish between these two. At lower field strength regions, the power at 5.5 mHz reduces.

The power spectrum follows a power law distribution (Figure 4.4) with an index of -1.43 for a highest magnetic field region. These slopes were estimated for the frequency regimes from 0.32 to 1.8 mHz, that is in the low frequency regimes. We also estimated slopes of the power spectrum in the frequency regimes of 46 μHz to 0.27 mHz. These slopes have been estimated by fitting a linear-least-square fit to the mentioned frequency regime data points. In the high frequency regimes the slopes are small and are close to -0.55 in the high magnetic field strength. Table 4.2 shows the power law indices for the magnetized regions with different magnetic field strengths for an active region AR 8760. The other active region shows similar power law index at low frequency regimes.

4.4.3 Power maps

To find the spatial locations of the 3 mHz and 5.5 mHz power in the magnetic images, we have computed the power maps. We first made the 3-dimensional cube of the time series of magnetograms. We then applied FFT on these magnetogram data cube in time. Now the time axis turns out to be frequency axis. By slicing and averaging over 3 to 3.5 mHz and 5.5 to 6.0 mHz in power images, we made the power maps in 5 and 3 minute band. We overlaid contours of the computed power (in 3 and 5 minute) on the intensity map for easy comparison which are shown in Figures 4.9(a) and (b) & 4.10(a) and (b) for two different days of observations. We computed these power maps for the field strength beyond 20 G to reduce the weak field noise. The highest power values at 3 and 5.5 mHz occur in the umbral region. The power map shows that 3 mHz power in almost all parts of the sunspot, especially in higher magnetic field strength with an exception of small portion of the sunspot penumbra. The 5.5 mHz power is enhanced in the sunspot umbra. In Figure 4.9(a) and (b) there are some pores which show the fluctuations at both 3 mHz and 5.5 mHz frequencies.

It is possible that the differential image motion could cause variations in the magnetic field strength. The oscillatory signals caused by such motions would be more in the locations of large magnetic field gradients. The locations of large magnetic field

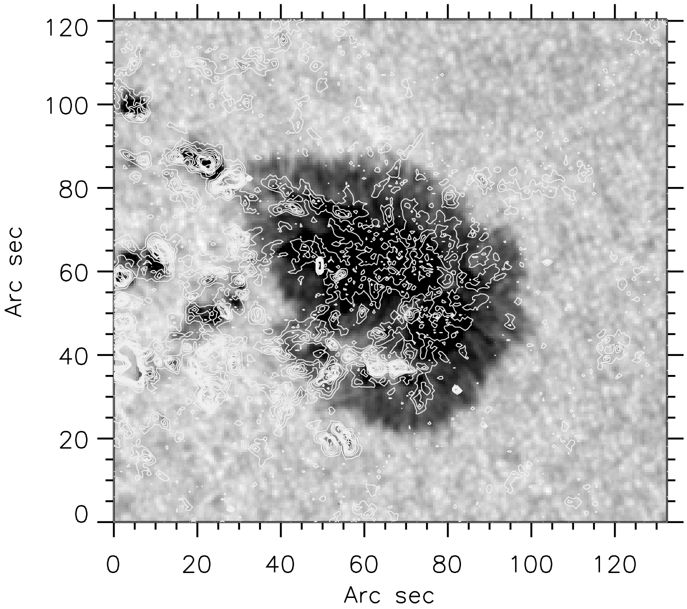

(a)

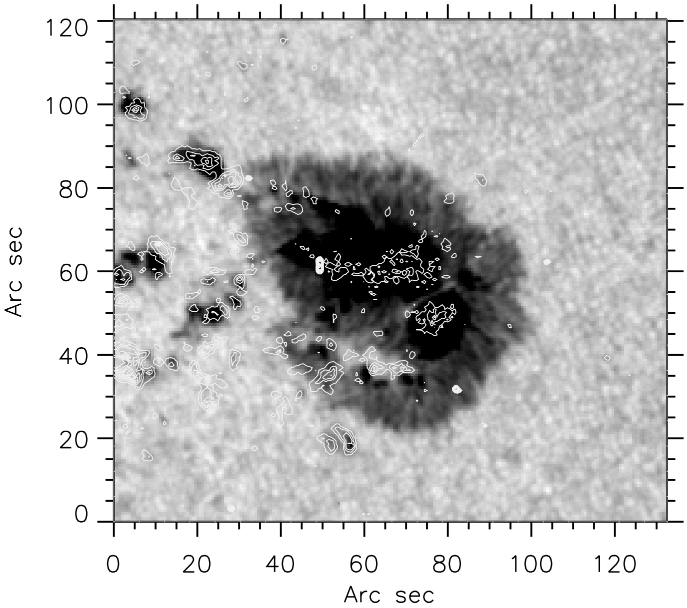

(b)

Figure 4.9: (a) Contour map of power at 5 minute oscillations overlaid upon the intensity map of active region AR 8760. The maximum power in the 5 minute oscillation is 3.8×10^9 G^2 Hz^{-1}. (b) Contour map of power at 3 minute oscillations overlaid upon the intensity map. The maximum power in the 3 minute oscillation is 1.95×10^9 G^2 Hz^{-1}.

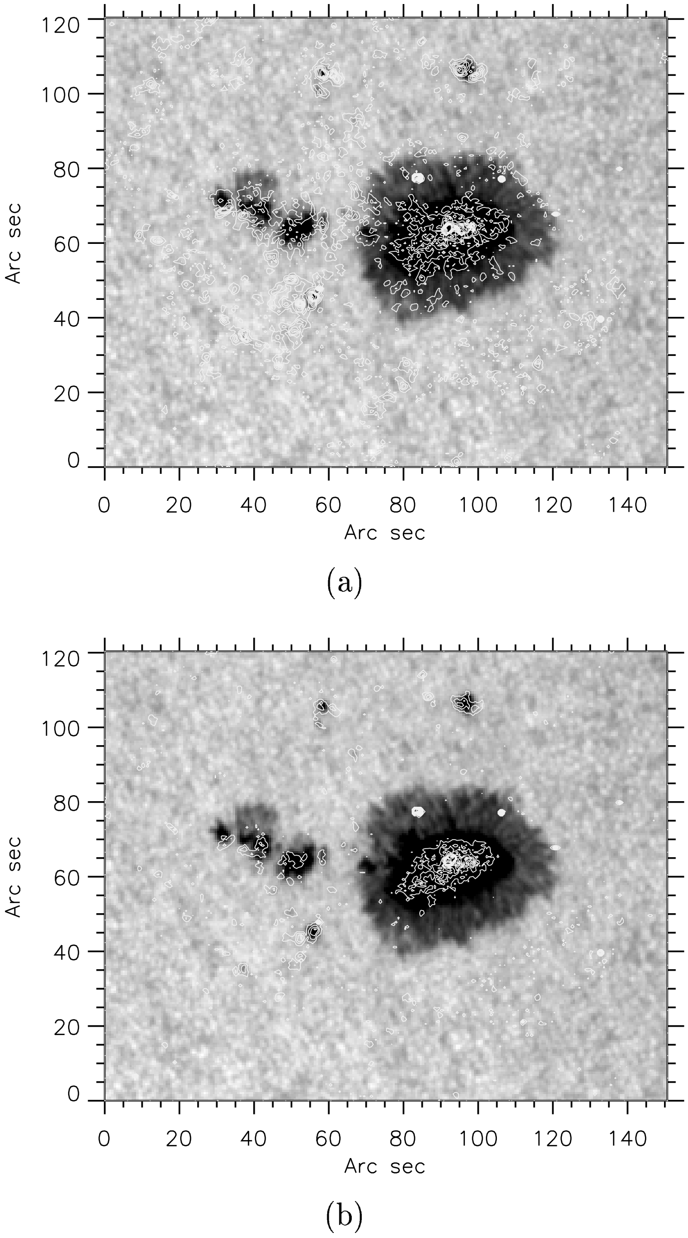

Figure 4.10: (a) Contour map of power at 5 minute oscillations overlaid upon the intensity map of active region AR 8668. The maximum power in the 5 minute oscillation is 2.4×10^{9} G^{2} Hz^{-1}. (b) Contour map of power at 3 minute oscillations overlaid upon the intensity map. The maximum power in the 3 minute oscillation is 1.1×10^{9} G^{2} Hz^{-1}.

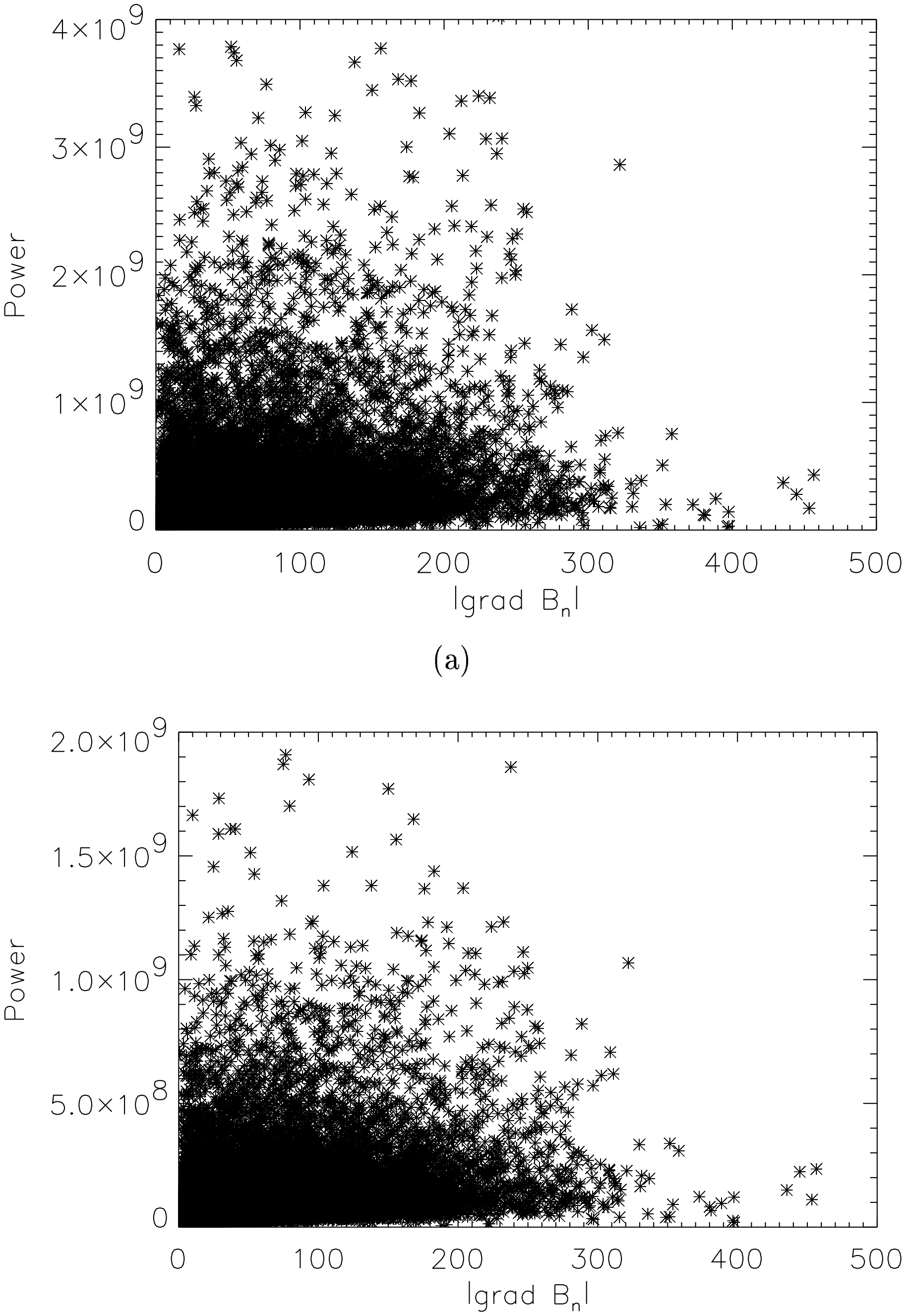

(a)

(b)

Figure 4.11: Scatter plot of power at (a) 5 minute versus gradient of magnetic field (b) 3 minute versus gradient of magnetic field in AR 8760.

gradients are umbra-penumbra and penumbra-photosphere boundary. However, we observe that the oscillatory signals are enhanced in the regions of large magnetic field strength. Figure 4.11(a) and (b) shows a plot of magnetic oscillatory power for the different frequency regimes versus spatial gradients of the magnetic field. The plots show that the power is independent of magnetic field gradient. This clearly suggests that differential image motion is not a likely cause of the magnetic oscillations.

4.4.4 Motions and evolutions in sunspots

Apart from the high frequency magnetic fluctuations, Lites *et al.* (1998) have reported low frequency magnetic field fluctuations throughout sunspots. They found a pattern of inward moving radial features in the inner penumbra and umbra. They also reported that in the sunspot umbra $|\mathrm{B}|$ (strength of the magnetic field) decreased systematically during their observations. In addition to the magnetic oscillations in the 5 minute band, Ulrich (1996) found that there is a broad range of low frequency power in the magnetic oscillations. He also concluded that the field strength variations are probably induced by the supergranular velocities. Our power spectrum also shows that there is a power in the low frequency regimes. In order to study the low frequency fluctuations of the magnetic field, we followed the procedure mentioned in Lites *et al.* (1998) in a slightly different way.

In order to study the low frequency magnetic field fluctuations in sunspots we used the high resolution MDI magnetograms. To separate the small-scale temporal and spatial fluctuations from the large-scale spatial variations and sunspot evolution, we adopted the following method which is similar to the method followed by Solanki and Rüedi (2003). We first smoothed the magnetograms with a mean filter of width $5''.4$ to suppress the fine structures in the sunspots. We then subtracted the smoothed magnetograms from its original magnetogram to remove large-scale features and bring out only the small-scale features. The technique applied to the magnetograms shows

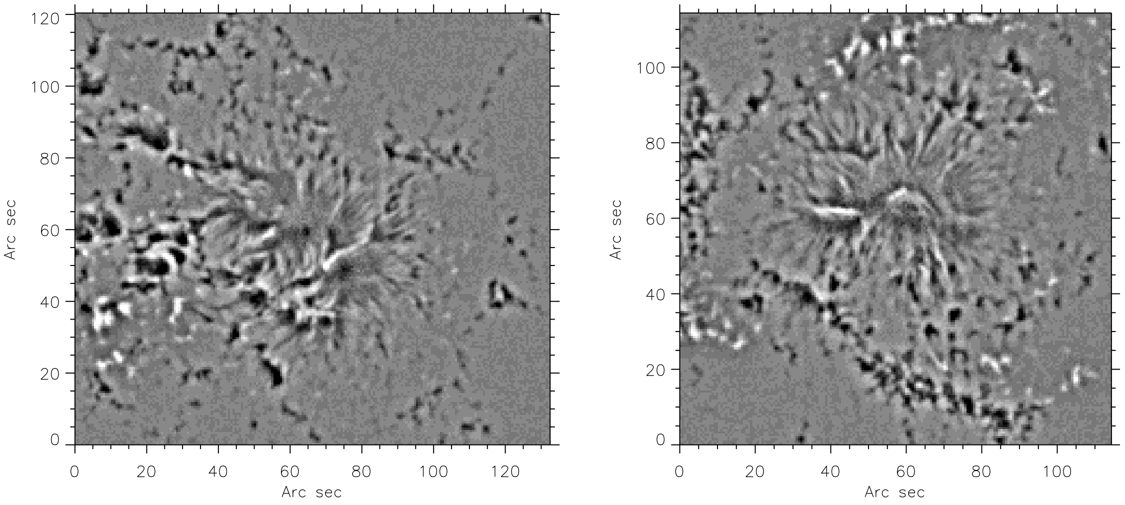

Figure 4.12: Residuals of the magnetograms after subtracting the magnetogram from its spatially smoothed magnetogram. Left side image is the residual of AR 8760 and right side image is the residual of AR 8113.

the fibril structures (Figure 4.12).

In order to study the low frequency behavior of the magnetic field fluctuations, we have made the space-time diagrams. These space-time diagrams are made from the time series of subtracted magnetograms, subtracted from the smoothed magnetograms. By selecting and averaging over the two pixels in the spatial x-direction we have stacked the one-dimensional images next to each other in time. Figures 4.13(a) and 4.14(a) show the slit image of the selected portion on the magnetogram (and hence on the subtracted magnetograms). Figures 4.13(b) and 4.14(b) show the space-time behavior of the magnetic field in the sunspot and its surrounding. In the space-time diagrams one can notice a pattern of features that are migrating radially inward in the umbra and radially outward in the outer penumbra and the surrounding moat.

In order to examine the low frequency behavior of the magnetic field fluctuations we removed the high frequency fluctuations (beyond 2.4 mHz) from the space-time diagram by using a low pass filter of functional form as in Lites *et al.* (1998) and is

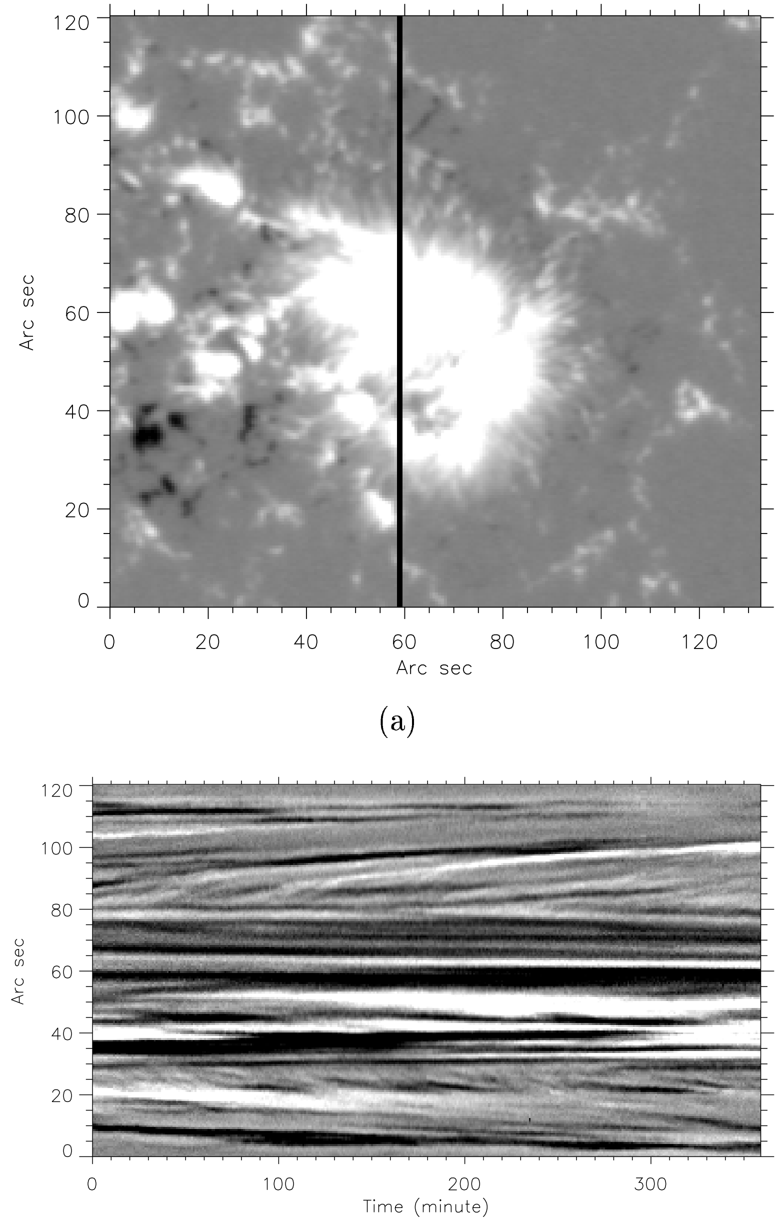

(a)

(b)

Figure 4.13: (a) The black vertical line is the position of the slit, used for making the space-time diagrams. (b) Gray-scale map (of AR 8760) showing the space-time behavior of fluctuations in magnetic field strength. In the map, the bright represents a positive fluctuation and dark, a negative fluctuation.

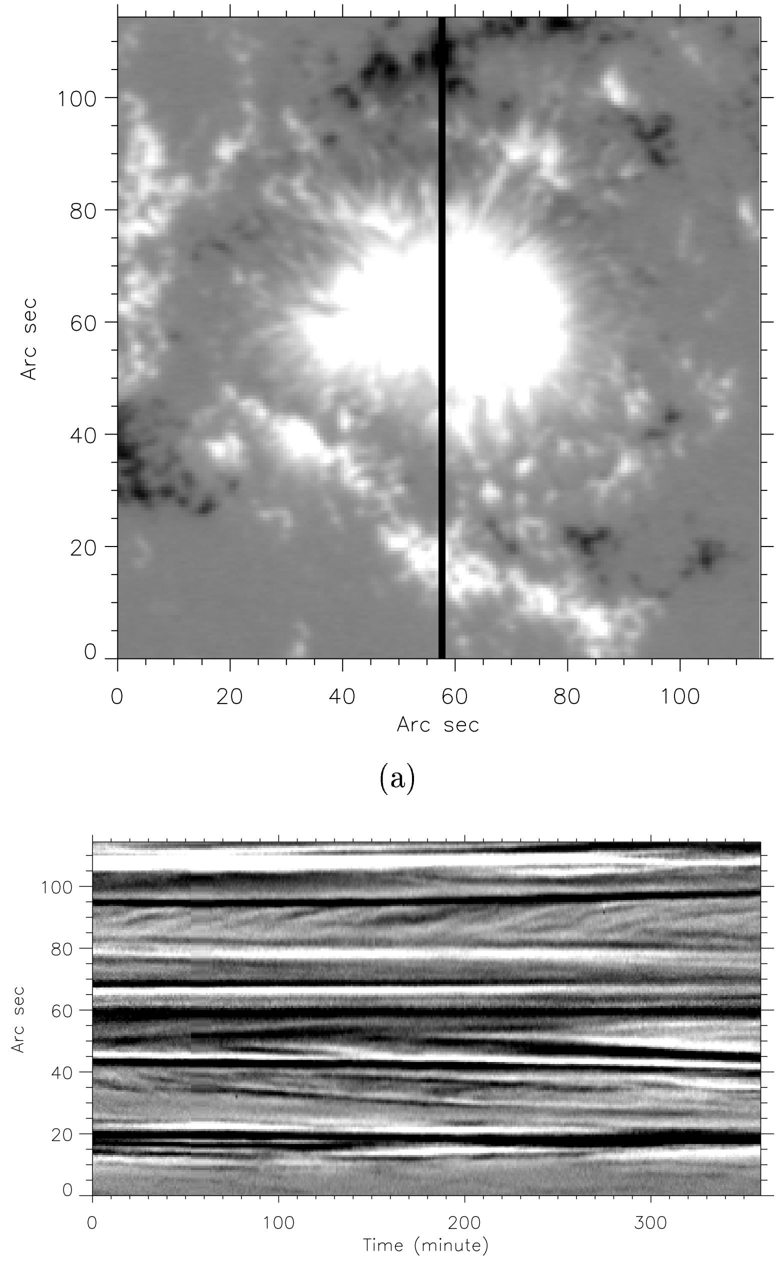

(a)

(b)

Figure 4.14: (a) The black vertical line is the position of the slit, used for making the space-time diagrams. (b) Gray-scale map (of AR 8113) showing the space-time behavior of fluctuations in magnetic field strength. In the map, the bright represents a positive fluctuation and dark, a negative fluctuation.

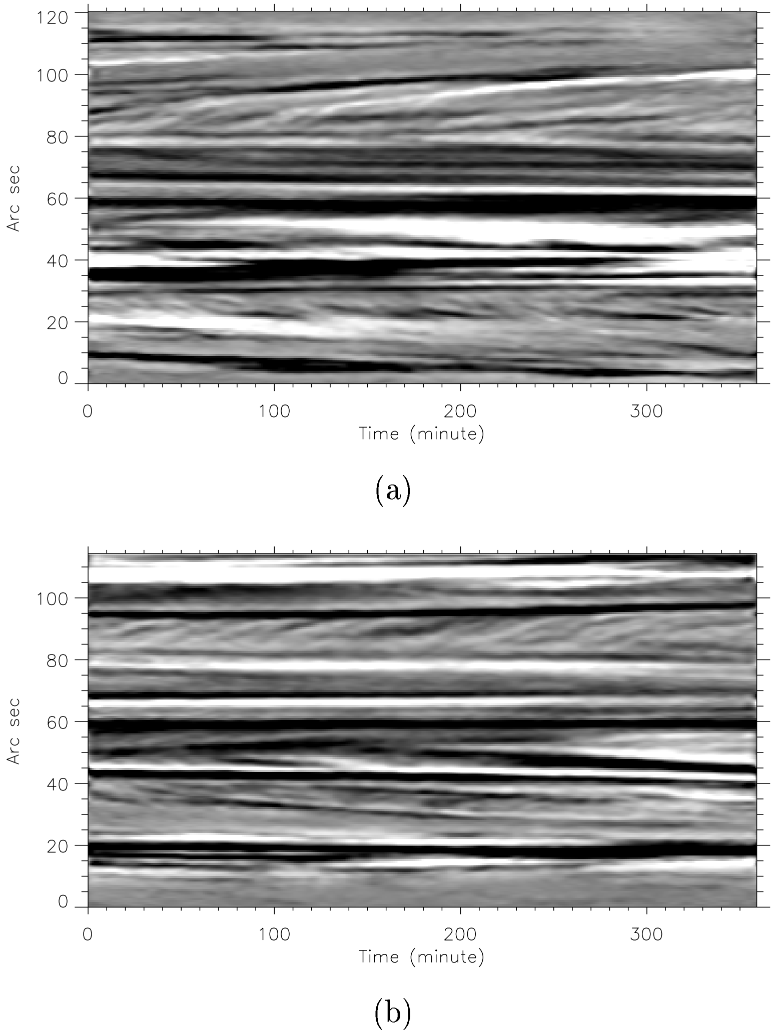

(a)

(b)

Figure 4.15: Gray-scale map (of (a) AR 8760 and (b) AR 8113) similar to those in Figures 4.13(b) and 4.14(b), except that in each case the fluctuations have been passed through low-pass filter that rejects the power at above 2.4 mHz.

given by,

$$f(\nu) = [1 + cos w(\nu - \nu_0)]/2.$$

where, the frequency is in the range of $\nu_0 < \nu < 2\nu_0$. We chose the ν_0=1.195 mHz and $w = \pi/\nu_0$ with cutoff of f=1 ($\nu < \nu_0$) and f=0 ($\nu > 2\nu_0$). This kind of filter rejects the power at frequencies beyond 2.39 mHz. The low pass filtered space-time diagrams are shown in Figures 4.15(a) and (b) for the active region AR 8760 and AR 8113 respectively. Even in the low pass filtered images one can see the inward radial drift from the inner penumbra into the umbra and the outward radial drift in the outer penumbra into the moat. The outward moving features from the outer penumbra could be due to moving magnetic features (Harvey and Harvey, 1973).

In order to identify the spatial locations in which the inward motions occurred, we overlaid the estimated direction of the flow on the intensity map. We computed the flow direction using the local correlation tracking (LCT: November, 1986) technique. The LCT method is commonly used in motion tracking, in solar physics. This method is very effective in tracking the horizontal motions (after correcting for the solar rotation). Previously, the LCT method was applied only on intensity images to track the features. But recently Chae *et al.* (2001) extended it to magnetograms, in order to compute the horizontal motions which are required to compute the change in magnetic helicity. In applying the LCT method to magnetograms, two parameters are critical to the accuracy of LCT, they are (1) the full width at half maximum (FWHM) of the apodizing window function and (2) time interval between a pair of magnetograms. After several trials we arrived at an optimum value of FWHM=$3''.6$ corresponding to a time ΔT of 20 minute.

We have applied the LCT technique on the subtracted images. We computed the flow pattern for the magnetic field strength beyond 50 G. This is to avoid the noise in the magnetograms. Figures 4.16, 4.17, 4.18 and 4.19 show the flow pattern in the sunspots for the active region AR 8760, AR 8113, AR 9354 and AR 8668 respectively. We overlaid the computed average flow direction on the intensity image with magnitude

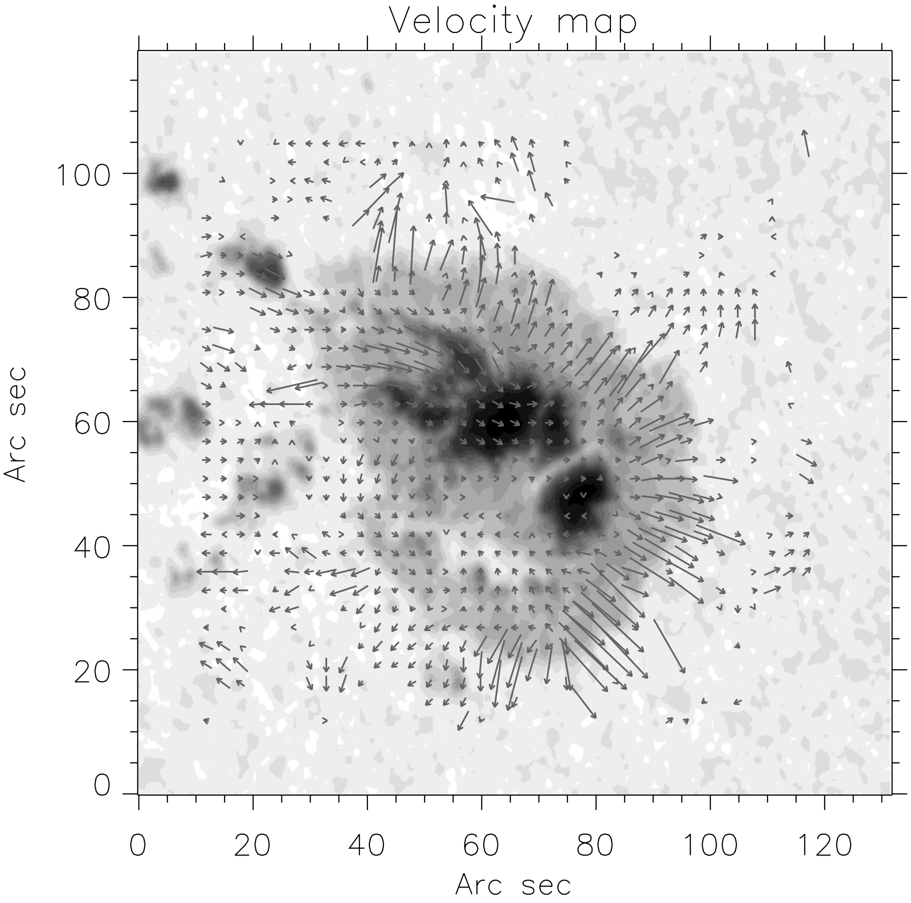

Figure 4.16: Map of horizontal flow patterns in the active region overlaid upon the intensity image of the AR 8760. The maximum length of the arrow corresponds to the velocity magnitude of 0.7 km s^{-1}.

of velocity beyond 30 m s^{-1} which is the maximum error in computing the velocity. The average flow map has been obtained from 50 flow maps computed at a time interval of ΔT=20 minute. The map shows that there is a definite inward motion toward the center of the umbra and there is an outward motion also. We believe that these inward and outward motions are real. In order to rule-out the possibility that these flows may be due to an artifact resulting from the subtraction of the magnetograms from the smoothed magnetograms, we repeated the same for unsubtracted magnetograms and found the same motions were still present. Many researchers (Muller, 1973; Tönjes

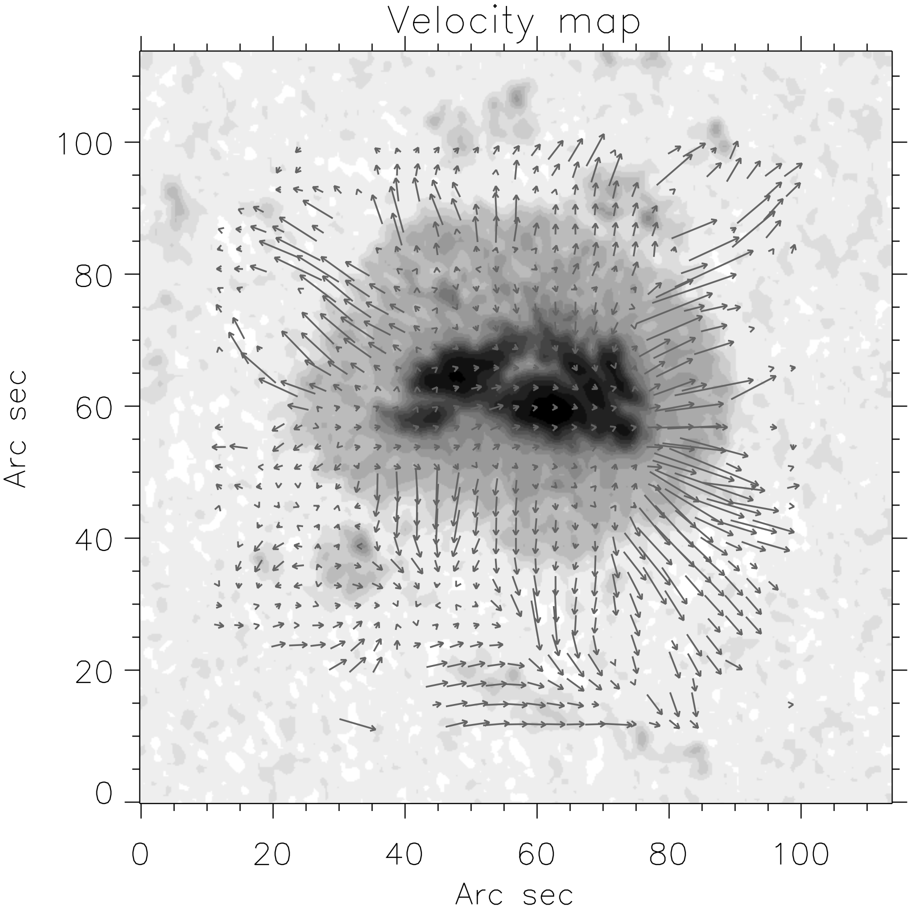

Figure 4.17: Map of horizontal flow patterns in the active region overlaid upon the intensity image of the AR 8113. The maximum length of the arrow corresponds to the velocity magnitude of 0.8 km s^{-1}.

and Wöhl, 1982; Wang and Zirin, 1992; Sobotka and Sutterlin, 2001; and Bovelet and Wiehr, 2003) have found a similar inward-outward motion of intensity features in sunspots. They reported that these inward moving features are the bright penumbral grains moving towards umbra with an average speed of 0.3 - 0.5 km s^{-1} (Muller, 1973; Wang and Zirin, 1992).

The magnitude of velocity in different magnetic field regions is different. We estimated a mean velocity in different magnetic field contours separately by averaging over 50 frames and are as shown in the plot (Figure 4.20). The vertical line indicates

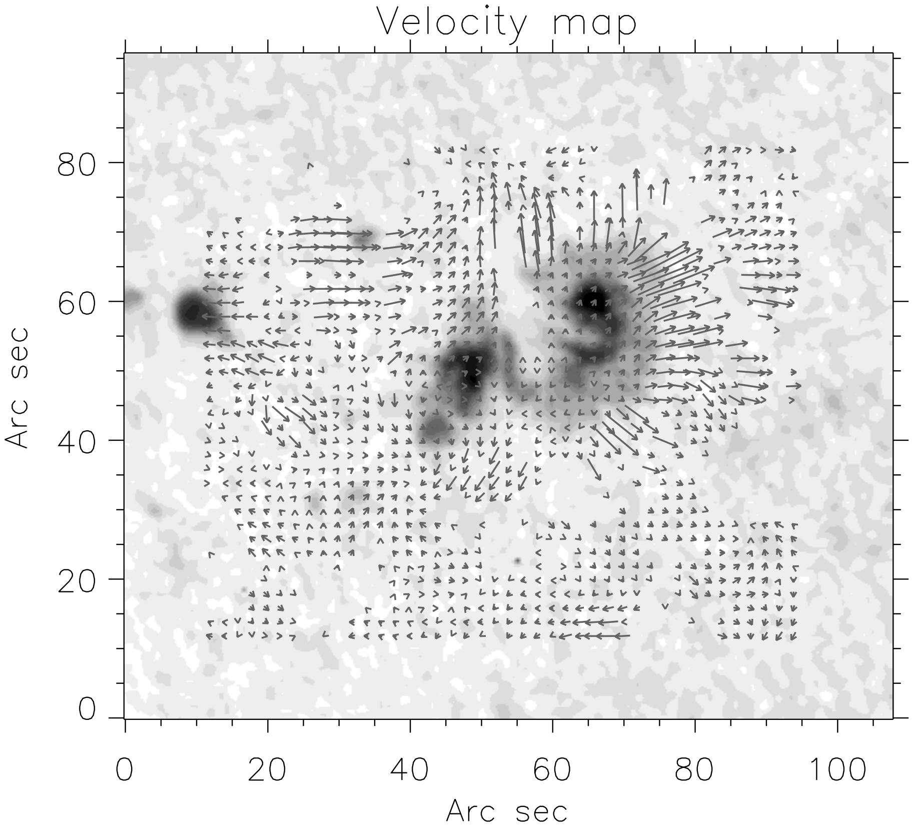

Figure 4.18: Map of horizontal flow patterns in the active region overlaid upon the intensity image of the AR 9354. The maximum length of the arrow corresponds to the velocity magnitude of 0.6 km s^{-1}.

the rms value of the velocity. The plot shows that in the umbra the magnitude of the velocity is small (90 m s^{-1}) and increases as the strength of the magnetic field decreases. The largest velocity is found in the outer penumbral boundary and they are outward moving features. The inward moving features have small velocity. This small velocity may be due to the moderate resolution of the MDI magnetograms, thereby reducing the possibility of detecting the features in the umbra. Apart from these the MDI magnetograms seem to have noise in the large magnetic field strength (Solanki and Rüedi, 2003). Hence, the noise may also reduce the possibility of detecting the features in the MDI magnetograms.

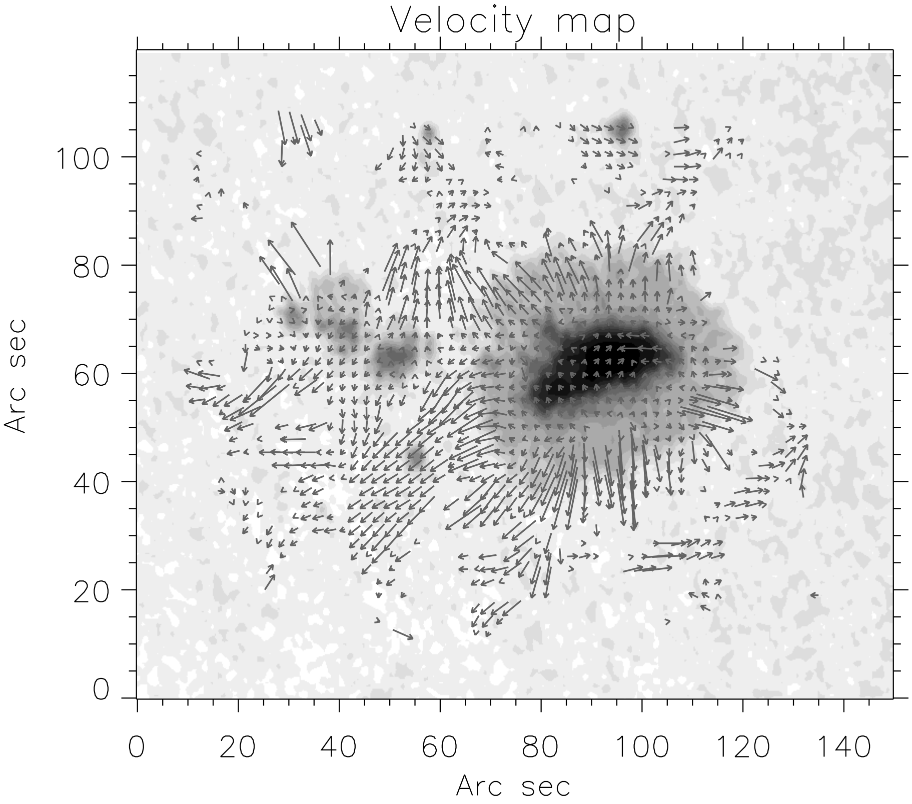

Figure 4.19: Map of horizontal flow patterns in the active region overlaid upon the intensity image of the AR 8668. The maximum length of the arrow corresponds to the velocity magnitude of 0.7 km s^{-1}.

In Figure 4.1(a) we have shown that the strength of the magnetic field changes systematically. This change in strength of the magnetic field has been found in most of the places. The magnitude of the magnetic field change is about 150 G in 1.5 hour interval. In sunspot umbra and near outer penumbra the spatial variation of magnetic field strength is large (Solanki and Rüedi, 2003). If there are secular changes associated with the convective interchange in the sunspots (Solanki and Rüedi, 2003), then these processes governing the slow evolution of the spot, can alter the strength of the magnetic field. In umbra, the feature sizes are $\approx 1''.2$ (Solanki and Rüedi, 2003). If we take half the value as the radius of the features and 90 m s^{-1} (Figure 4.20) as the

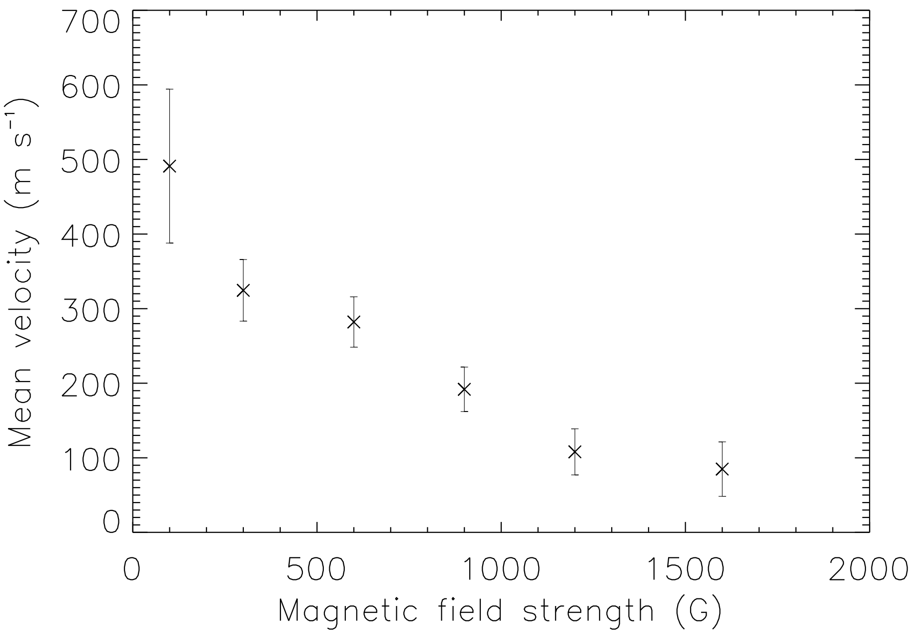

Figure 4.20: A plot of mean velocity as a function of mean magnetic field strength. The vertical lines are the rms value of the mean velocity.

speed at which the features are moving towards the umbra, then the time required to cross a pixel is about 80 minute. This is close to 1.5 hour. In other words, a large part of the slow variation in the magnetic field strength in sunspot is contributed by the motion of patterns in the sunspot.

4.5 Summary and Discussion

The following results were obtained using the MDI high resolution magnetograms.

(1) Power spectrum shows that at higher magnetic field strength, 3 minute as well as 5 minute oscillations are present.

(2) The rms value of the magnetic field fluctuation lies in the range 7-14 G.

(3) Power maps show that 5 minute oscillation is enhanced in most of the places of sunspot and 3 minute oscillation is enhanced in the sunspot umbra.

(4) Power spectrum shows that the magnetized regions follows the power law in the low frequency regimes and it is close to the power index of about -1.5 in the sunspot umbra.
(5) The low frequency fluctuations may be due to the pattern of migration of features towards the sunspot umbra from the inner penumbra and outward motion of features from the outer penumbra.

The first result is in agreement with the results obtained by Norton *et al.* (1999). There are quite a number of questions raised by many researchers as to whether these magnetic oscillations are real or arise due to the cross-talk from the velocity oscillations or the line forming region oscillates due to the temperature and density fluctuations? Rüedi *et al.* (1998) showed that a large part of the measured magnetic field variations is actually due to cross-talk from the density and temperature fluctuations produced by the wave itself. Most of the reports suggest that even if there is a cross-talk from other physical quantities, there is small amount of magnetic fluctuations present. But the magnitude of fluctuations still remain uncertain.

There are various explanations for generating high as well as low frequency magnetic field fluctuations. Recent studies suggest that the magnetic oscillations are due to the flux tube sweeping in and out of the resolution element by horizontal p-mode components (Ulrich, 1996; Norton and Ulrich, 2000; Norton and Ulrich, 2001). A magnetically inhomogeneous media can alter the horizontal p-mode component which propagates perpendicular to the field lines.

Schrijver and Title (2002) provide an interesting insight into the evolution of the topology of the magnetic fields of mixed polarity. A similar phenomena could occur in complex active regions. The stochastic superposition of transient kinks produced in field lines connected to various site (Figure 4.21) could lead to a chaotic field evolution, especially in the regions of highly inhomogeneous media, where the field lines are connected to neighboring sites. This stochastic superposition of magnetic field fluctuations

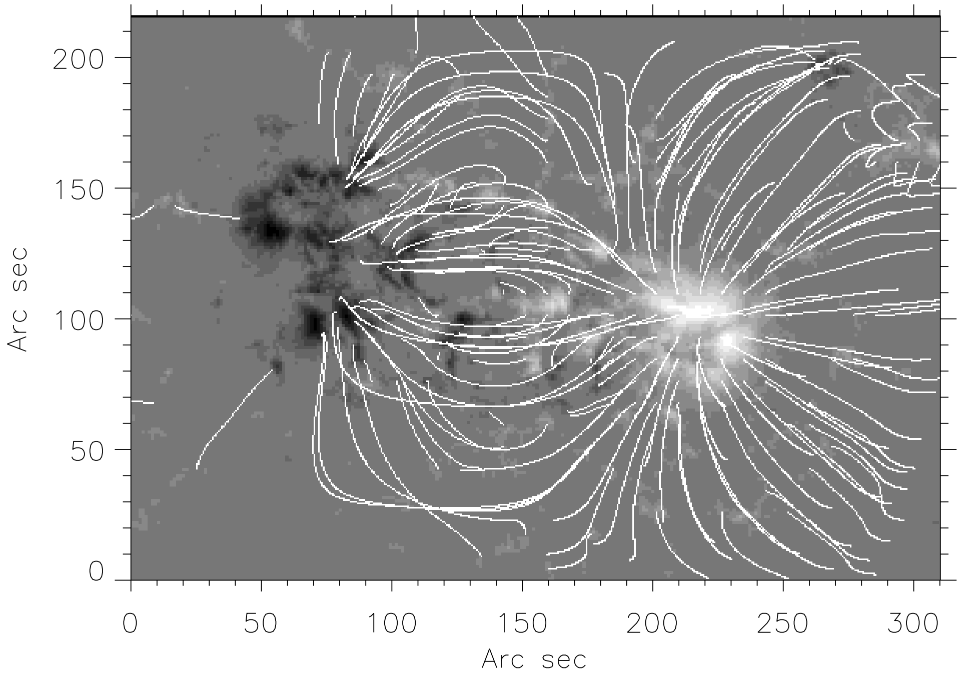

Figure 4.21: A map of potential field lines overlaid upon the magnetogram (AR 8760). Map shows that the field lines connecting the opposite polarity and there are open field lines. These potential field lines have been computed using the Fourier transform method (Sakurai, 1989). These field lines have been computed for the magnetic field strength larger than 100 G.

can produce a broad band fluctuations of magnetic fields at highly connected regions with a power law distribution. Also, these waves could be well guided by the magnetic field lines thereby producing different characteristics in the open and closed magnetic field lines. In open field lines, there may be outgoing waves and in the closed field lines trapped waves may be present. The stochastic superposition of magnetic transients, generated at numerous distributed sites at different epochs seems to be one way of generating waves. This way of generating waves predicts that in complex large active region magnetic field fluctuations could be different than in the isolated active region of one polarity, surrounded by plage. Thus, this prediction can be verified.

It is well known that the five-minute velocity oscillations are suppressed in regions of strong magnetic field like sunspots (Hindman and Brown, 1998; Venkatakrishnan, Kumar, and Tripathy, 2002) compared to its surrounding. The recent results have shown that there are 5 as well as 3 minute magnetic field fluctuations in sunspots. The observed magnetic field fluctuations at 5 and 3 minute may not be excited from the convective motions that are now considered as the driver of the velocity oscillations in quiet Sun. The reduction in the power of velocity fluctuations and increase in power in magnetic field strength fluctuation in AR sunspots may suggest that the energy associated with the velocity oscillations are in equipartition with the magnetic oscillations in sunspots. Further, penumbra and penumbral boundary shows slightly more power than the umbra at low frequency regimes. This higher power may be the manifestation of the migration of features from penumbra. The low pass filtered space-time diagrams show that there is a strong tendency of outer radial drift of features in the outer-penumbra towards moat and inward radial drift in the inner penumbra towards the umbra. The inward radial drift is a pattern of convergence of features towards the umbra. These inward radial drift may be either due to the horizontal propagation of the convective pattern or due to the slow emergence of the active region field bringing deeper magnetic fields into the region of line formation. A horizontal motion should imply vertical flow at the node of convergence. Such flows have not been generally observed. In addition to this, the low frequency magnetic field variations can cause the magnetic field strength variation of about 150 G over a time period of 1.5 hr (Ulrich, 1996; Lites *et al.*, 1998).

The magnetic signal shows two types of variations, slow and fast. If the slow variation is related to the radial drift of the pattern then we speculate that the energy is transported from the longer time scales to the shorter times scales (quite similar to Kolmogorov spectrum seen in fluid turbulence) as indicated by the power law index in the low frequency regimes in the power spectrum. Physically, the non-linearities in the interaction of plasma and magnetic fields is expected to cause this transfer of energy from larger time scale to shorter time scales. The transferring of energy can cause the short period magnetic field variations at least in the low magnetic field strength regions as indicated by the power index.

We now look at the AR corona. As has been mentioned in Section 4.1, coronal images show that active region corona display a pronounced X-ray and EUV emission. Regions associated with sunspots on the surface of the Sun have temperatures of $\approx 10^7$ K. Active region coronal heating is still an unsolved issue. There are many proposed heating mechanisms (Parker, 1988, 1991; Shimizu and Tsuneta, 1997) and most of them share the common ground. According to Alfvén's frozen flux theorem, foot-points of the magnetic field lines are forced to follow the convective motions of the photospheric plasma. By this process, the kinetic energy of the convective motions is converted into magnetic energy, which in turn might be converted into heat higher up in the atmosphere. What is the magnitude of the energy flux one can expect from the magnetic field fluctuations? The observed strength of the magnetic field fluctuations is of the order of 10 G. The energy density associated with the magnetic field variations has two terms. The first term is δB·B/4π, which is linear in δB while the second term is $\delta B^2/8\pi$ and is much smaller than the first term for $\delta B << B$. Then the dynamical pressure is $\frac{B \cdot \delta B}{4\pi} \approx 1200$ dynes cm^{-2}, for $B \approx 1500$ G. The energy density involved in the magnetic variations is ≈ 1200 ergs cm^{-3}. The mechanical energy flux associated with this energy density can be obtained by multiplying it with the Alfvén speed of ≈ 10 km s^{-1} at the solar photosphere. This gives an equivalent mechanical flux of $\approx 10^9$ ergs cm^{-2} s^{-1}. We expect only a fraction of this flux to be actually available for heating the chromosphere and corona. Given that the flux actually required to heat the active region chromosphere and corona are $\approx 10^6$ ergs cm^{-2} s^{-1} and $\approx 10^5$ ergs cm^{-2} s^{-1} respectively (Withbroe and Noyes, 1977), we see that only 0.1% and 0.01% respectively of the estimated flux is needed for this purpose. Thus, these bright active region loops may derive their energy from the magnetic field fluctuations of the sunspot magnetic field.

In this Section, we have shown that there are many possibilities by which magnetic field strength fluctuations can be generated. Even these magnetic field fluctuations may be intrinsic in nature. There are many factors which are affecting the detection of the magnetic field fluctuations in sunspots. Further progress can be made through very high spatial, spectral and temporal resolution observations. By having the high spatial resolution one can avoid the filling factor, which may contribute to the oscillatory part. By having full spectral information in several lines one can estimate the effect of filling factor. Full spectral information provides magnetic as well as velocity fluctuations and the phase angle between these two. Increasing the Zeeman sensitivity and reducing the stray light in observations obtained in infrared lines will give boost to the detection of the magnetic field strength fluctuations. Taking the observation at high cadence is also important because in the case of SOHO/MDI the Nyquist frequency is 8.3 mHz, hence there is a lack of information on the high frequency range of spectrum where the noise is best estimated and where short period oscillations may also be present. Future space-based spectro-polarimeters may give better results in this field of research.

Chapter 5

A study of relationship between the velocity of CME and photospheric magnetic field

5.1 Introduction

Coronal Mass Ejections (CMEs) are the most energetic events in the solar system; the strongest ones release $\sim 10^{32}$ ergs of magnetic energy in $\sim 10^{3}$ sec. CMEs are sudden eruptions of up to 10^{16} gm of coronal material at speeds of typically several hundred to thousand kilometers per second (Hundhausen, 1999; Yashiro *et al.*, 2002b) and their average angular size is about 45°. CMEs are more than just interesting natural phenomena. They are the primary cause of the largest and most damaging space weather disturbances (Gosling, 1993). Effects such as temporary and sometimes permanent failure of satellites, the degradation or disruption of communication, navigation and commercial power systems, and the exposure of astronauts and polar-route airline crews to harmful doses of radiation. Some of these effects are delayed approximately by 3 days, the time it takes for a CME to propagate to the Earth and interact with the magnetosphere. Others begin almost immediately after the CME lifts off from the Sun due to the production of solar energetic particles (SEPs) that travel at relativistic speeds. Clearly, there is a need to understand CMEs and ultimately to predict them before they occur.

CMEs were first observed by space based coronagraph on Orbiting Solar Observatory 7 (OSO-7) (Tousey *et al.*, 1973). Following OSO, they were observed by *Skylab* (MacQueen *et al.*, 1974; Gosling *et al.*, 1974), the Solwind coronagraph on the P78-1 satellite (Michels *et al.*, 1980; Sheeley *et al.*, 1982; Howard *et al.*, 1985), and the Solar Maximum Mission (SMM) satellite (MacQueen *et al.*, 1980). Recently, from 1996 to till now, the Large Angle Spectroscopic Coronagraph (LASCO, Brueckner *et al.*, 1995) on the Solar and Heliospheric Observatory satellite has been observing the Sun continuously and recording several hundreds of CMEs. These coronagraphs can record the CMEs via the Thompson-scattered photospheric light from the free electrons in the corona. In a coronagraph an artificial eclipse is produced by an occulting disk to block the photospheric and chromospheric light, so that the corona and the CME structures are visible in the coronagraph images.

In coronagraph observations, CMEs appear as bright features, generally having spatial scales of the order of a solar radius and expanding outward at speeds of ≈ 2000 km s^{-1}, with the average projected speed of about 400 km s^{-1} (Gosling *et al.*, 1974; Howard *et al.*, 1985; Hundhausen, Burkepile, and St. Cyr, 1994; St. Cyr *et al.*, 1999) which is similar to the speed of solar wind at 1 AU. In interplanetary space, a class of solar wind (SW) structures, referred to as magnetic clouds (MCs), first discovered by Burlaga *et al.* (1981), have been closely associated with CMEs (Wilson and Hildner, 1984; Burlaga *et al.*, 1998; Webb *et al.*, 2000). Although the evolutionary connection between CMEs and MCs has not been directly observed, there is strong observational (Larson *et al.*, 1997) and theoretical (Chen and Garren, 1993) evidence that MCs are flux ropes with their magnetic fields ('legs') connected to the Sun.

For several decades solar physicists believed that geomagnetic storms were caused by flares. It is now known that CMEs are responsible for such large storms (Gosling *et al.*, 1991; Kahler, 1992; Gosling, 1993). The geoeffectiveness of MCs (and therefore CMEs) arises from the fact that they can impose long periods of strong southward interplanetary magnetic field (IMF) on the Earth's magnetosphere (Russel, McPherron, and Burton 1974; Gonzalez and Tsurutani, 1987). "The scientific importance of CMEs also lies in the fact that they may be an archetypal eruptive process; the physics of CMEs may shed new light on other puzzling eruptive phenomenon such as flares" (Chen, 2001).

CMEs are associated with filament eruptions as well as flares in active regions (Munro *et al.*, 1979; Webb and Hundhausen, 1987; St. Cyr and Webb, 1991; Gilbert *et al.*, 2000; Prasad and Dere, 2001). Prediction of CMEs and flares (Ambastha, Hagyard, and West, 1993; Falconer, 2001; Falconer, Moore, and Gary, 2002; Canfield, Hudson, and McKenzie, 1999) are becoming more and more interesting and valuable subject in solar physics and in space science since CME can cause geomagnetic storms.

Active region (AR) associated CMEs are thought to derive their energy from the magnetic field of the AR. CMEs are launched from closed magnetic field regions on the Sun, such as ARs, filament regions or a combination thereof. Understanding the structure, evolution, and stability of these regions is therefore an essential part of CME investigations. Thus, many researchers have started looking for changes in the magnetic field and its parameters. Lara, Gopalswamy, and DeForest (2000) took the first step in searching for changes in the magnetic flux in active regions. During a CME, they detected a change in magnetic flux over a scale, which is smaller than the active regions. During a CME, Kosovichev and Zharkova (1999), detected variations of magnetic field in the form of a rapidly propagating magnetic wave. Moon *et al.* (2002a) and Kusano *et al.* (2002) found a correlation between magnetic helicity injection and Geostationary Operational Environmental Satellites (GOES) X-ray activity. At the same time, Moon *et al.* (2002b) showed a correlation between the GOES X-ray flux integrated over flaring time from the flare on-set to its end with the CME speed. Zhang *et al.* (2001) showed a positive correlation between the flare strength and the maximum velocity of CMEs for four well observed events close to the limb.

One of the major tasks in space weather prediction is the estimation of the severity of geomagnetic storms from the properties of the solar causative agencies of these geomagnetic storms. In a recent paper, Srivastava and Venkatakrishnan (2002) showed that the initial speeds of CMEs could well provide a reliable estimate of the storm severity. The next step is to find out which property of the associated active region determines the initial speed of the CME. In this Chapter, we demonstrate that the CME speeds are related to the magnetic energy of the associated active regions.

A CME produced by an AR near central meridian is directed more or less Earthward and can be seen by a coronagraph as a halo CME (visible around the entire occulting disk) if these ejections are massive enough. The CMEs heading both towards and away from the Earth appear as halos. Improved sensitivity of coronagraphs, larger field of view, and better techniques used in measuring the expansion velocity have improved the prediction of arrival time of CME at the Earth. Availability of continuous line-of-sight magnetogram data from space, free from seeing, night time interruptions and improved sensitivity in measuring the line-of-sight magnetic field (errors are of the order of ±20 G) provide a better opportunity for finding the relationship between the AR magnetic field parameters and velocities of the ejecta. Recently it has become possible to track the CME from its origin using Extreme ultraviolet Imaging Telescope (EIT: Delaboudiniere *et al.*, 1995) out to $30R_\odot$ using Large Angle Spectroscopic Coronagraph. In the present study, we examine the relationship between the projected speed of CMEs and the AR magnetic energy by analyzing 37 halo CME events. Also, we present the relationship between the projected speed of CMEs and the GOES X-ray peak flux.

5.2 Data

To locate the source region of a CME, we used full disk SOHO/EIT λ195 Å images as well as images taken in other wavelengths such as λ171 Å, λ284 Å, and λ304 Å. EIT provides full disk images with a full view of the corona extending up to $1.5R_{\odot}$. During a flare or a CME, EIT obtains images of the Sun at a cadence of 15-20 min. In a few cases of selected CME events the cadence of EIT imaging is $\approx$ 7 hr.

To estimate the total magnetic energy in the CME related AR, we used full disk MDI magnetograms taken at a cadence of 96-minute as well as 1-minute. We could identify the source region of CME in full disk magnetograms with the help of EIT images. In selecting the events we have restricted ourselves to the following conditions: (1) halo CME should have occurred on those days. (2) The active region associated with the CME should be located within 30° from the central meridian. (3) Magnetograms should be available during the events at high cadence or at least at a cadence of 96-minute. (4) The projected speed of the halo CME should be available. White light photospheric images corresponding to each event were obtained from SOHO/MDI to locate and count the saturated pixels in MDI magnetograms (which may be due to the failure in the on board algorithm when the lookup table saturates).

The projected speeds of the halo CMEs used in this study were obtained from the on-line SOHO/LASCO CME catalog in which CME kinematics are estimated and compiled from LASCO C2 and C3 images (http://cdaw.gsfc.nasa.gov/cme-list). The CME speeds were determined (Yashiro *et al.*, 2002a; Gopalswamy, 2003) from linear fits to the height-time plot. The error bars in estimating the speeds are less than 10% (Yashiro *et al.*, 2002a).

Apart from these data sets, we used GOES X-ray flux data recorded in the soft X-rays in the 1-8 Å band and in the 0.5-4 Å band. The GOES data used here (1-8 Å band) were the full disk integrated X-ray flux with a temporal resolution of 1-minute. The magnitude of the GOES X-ray flare is expressed in units of W m^{-2} and classified into classes designated by letters A, B, C, M, and X with corresponding flux starting at 10^{-8}, 10^{-7}, 10^{-6}, 10^{-5} and 10^{-4} W m^{-2} respectively. These X-ray fluxes are good indicators of the magnitude of flares.

5.3 Analysis

In order to determine the magnetic potential energy from the line-of-sight magnetograms, the MDI data must be corrected for the geometrical distortions and instrumental corrections. These include: (1) geometrical foreshortening arising from the spherical geometry of the Sun. By choosing a reference time as the instant at which the active region passed through the central meridian, magnetograms are aligned using differential solar rotation (Howard, Harvey, and Forgach, 1990)

$$\omega = 2.894 - 0.428 sin^2\phi - 0.37 sin^4\phi \ \mu \ rad \ s^{-1}$$

where, 'ϕ' is the latitude. We have employed a sub-pixel interpolation with a pixel size of $1''$ (Chae *et al.*, 2001).

(2) Correction for the angle between the magnetic field direction and the observer's line-of-sight. We corrected for the vertical field strength, by multiplying $1/cos\psi$ to the line-of-sight field strength as in Chae *et al.* (2001), that is,

$$B_l = B_z cos\psi$$

where 'ψ' is the heliocentric angle of the region of interest, B_l is the observed line-of-sight component and B_z is the vertical component of the magnetic field.

(3) Signal-to-noise ratio is increased by averaging 5 successive 1-minute cadence magnetograms, thereby reducing the noise in the magnetograms from ±20 G to ±9 G.

(4) Identifying the corrupted pixels in the magnetograms with the help of white light images. Before doing any analysis, we first located the region of saturated pixels. The scatter plot of intensity versus magnetic field clearly showed the number of saturated

pixels. In our data-set, some active regions had saturated pixels. These saturated pixels introduce an error in potential energy calculation by ≈ 4% (upper limit). The potential magnetic fields were determined from the vertical component of the magnetic fields (B_z) using the Fourier method (Alissandrakis, 1981). Using these computed potential fields, the potential magnetic energy of the active region above $z>0$ was determined by the application of the virial theorem to the photospheric magnetogram, as prescribed by Chandrasekhar (1961), Molodensky (1974) and Low (1985). The potential magnetic energy of the active region is given by the relation,

$$E_p = \frac{1}{4\pi} \int (xB_{px} + yB_{py})B_z dxdy$$

where, E_p is the available potential energy, B_{px} and B_{py} are the potential fields in the x and y-direction. B_z is the vertical magnetic field in the z-direction. The actual available or free magnetic energy can only be determined from vector magnetograms. As we do not have vector magnetograms we make a reasonable assumption that the free energy is closely related to the potential energy.

In order to find the active region magnetic flux, we adopted the following method: A polygonal contour defined by eye is fitted around the AR. The polygonal contour is treated as the boundary between the AR and the surrounding photosphere. The polygonal contour defined by eye introduces some error due to the incorrect border defined by eye. But by doing many trials we could minimize the error. The number of sides to the polygon is determined by the complexity of the AR shape, and is typically around 15. The magnetic flux is summed within the polygonal contour with positive and negative flux separately. The ±9 G noise (after 5 successive magnetogram averages) in MDI magnetograms introduces an error in to the active region flux measurements. For a typical mean field strength of 150 G and for an active region with total flux of the order of 10^{22} Mx, the noise introduces an error of ≈ 6%. We calculated the magnetic flux as $\int B_z \, da$ for positive and negative polarity of an AR separately, where B_z is a vertical magnetic field strength and da is the pixel area.

5.4 Results

The source regions of CMEs are determined from EIT images (Fe XII λ195 Å), using signatures such as coronal dimming (Zarro *et al.*, 1999) and post-flare loops. We made a difference movie of Fe XII λ195 Å images and examined the coronal dimming during CME. Figure 5.1 shows an example of coronal dimming during a CME in a difference image. The arrow in the figure indicates the active region, its surrounding and the coronal dimming. In Figure 5.2, the arrow mark shows the post-flare loops, which has formed after the flare. For some of the events, the time sequence images of EIT were not available; in those cases we used the LASCO CME mail archive to identify the source regions and Solar Geophysical Data reports to locate the flare regions, which may be associated with the CME. In our data-set we have both young as well as decaying ARs. Figures 5.3(a) and (b) show examples of group of sunspots with strong and weak fields respectively.

5.4.1 Velocity of CME and the active region magnetic energy

To study the relationship between the projected speed of CMEs and the total magnetic energy of the AR, we selected 37 AR from 1998 to 2002. In Table 5.1 we list the selected events, date and time of occurrence of each CME as observed by the C2 coronagraph, the active region which may be responsible for the CME, the location and the projected speed of CME corresponding to those dates and times, estimated total magnetic energy and GOES X-ray flare classes respectively. We plot a graph of logarithm of projected speed of the ejecta versus logarithm of magnetic energy (Figure 5.4). The solid line shows that there is a fairly strong relationship between the magnetic energy and projected speed. From the plot we could derive the relation between the estimated energy and speed after fitting a linear least square fit to the scattered points.

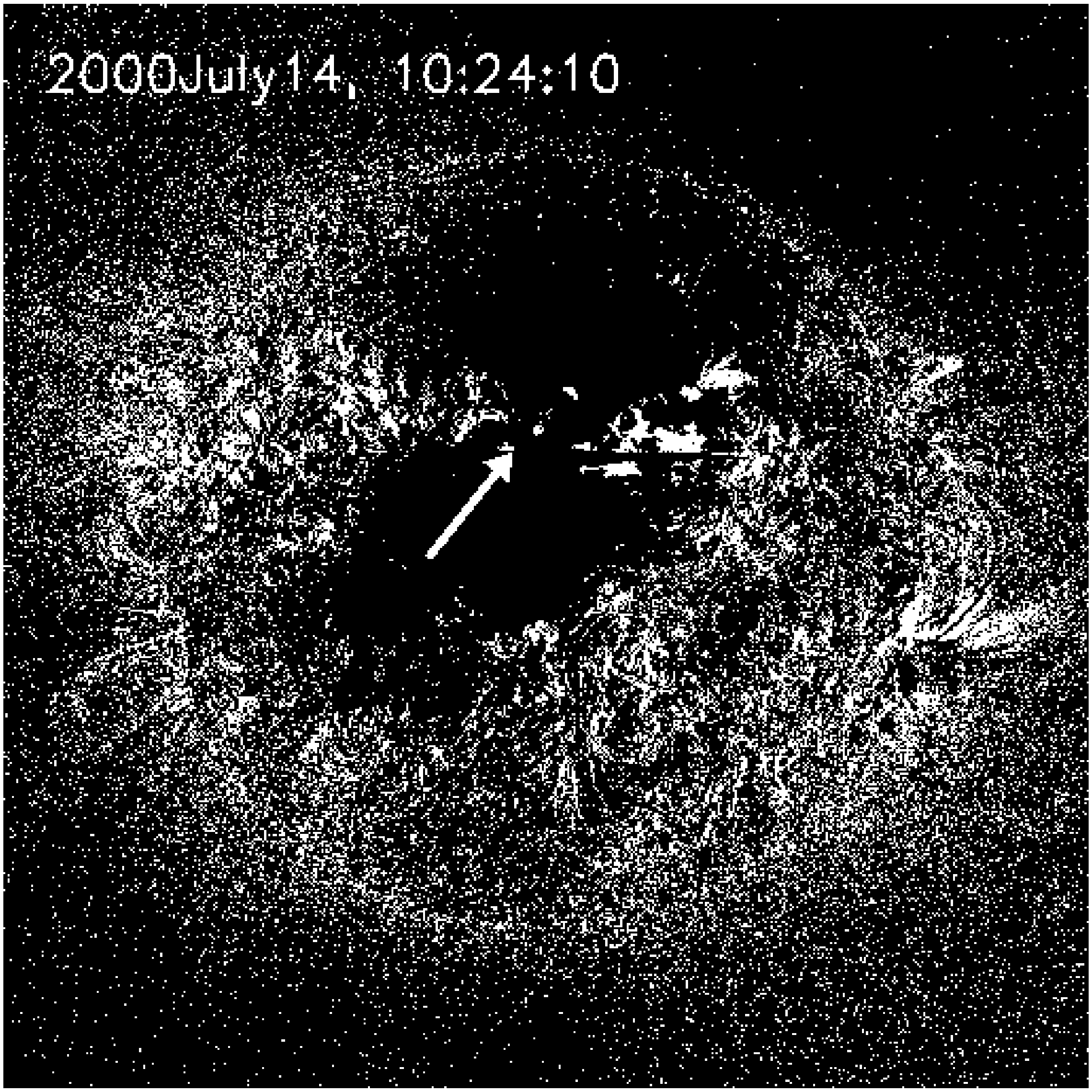

Figure 5.1: An example of coronal dimming during CME. The arrow mark indicates the region of coronal dimming and location of the active region.

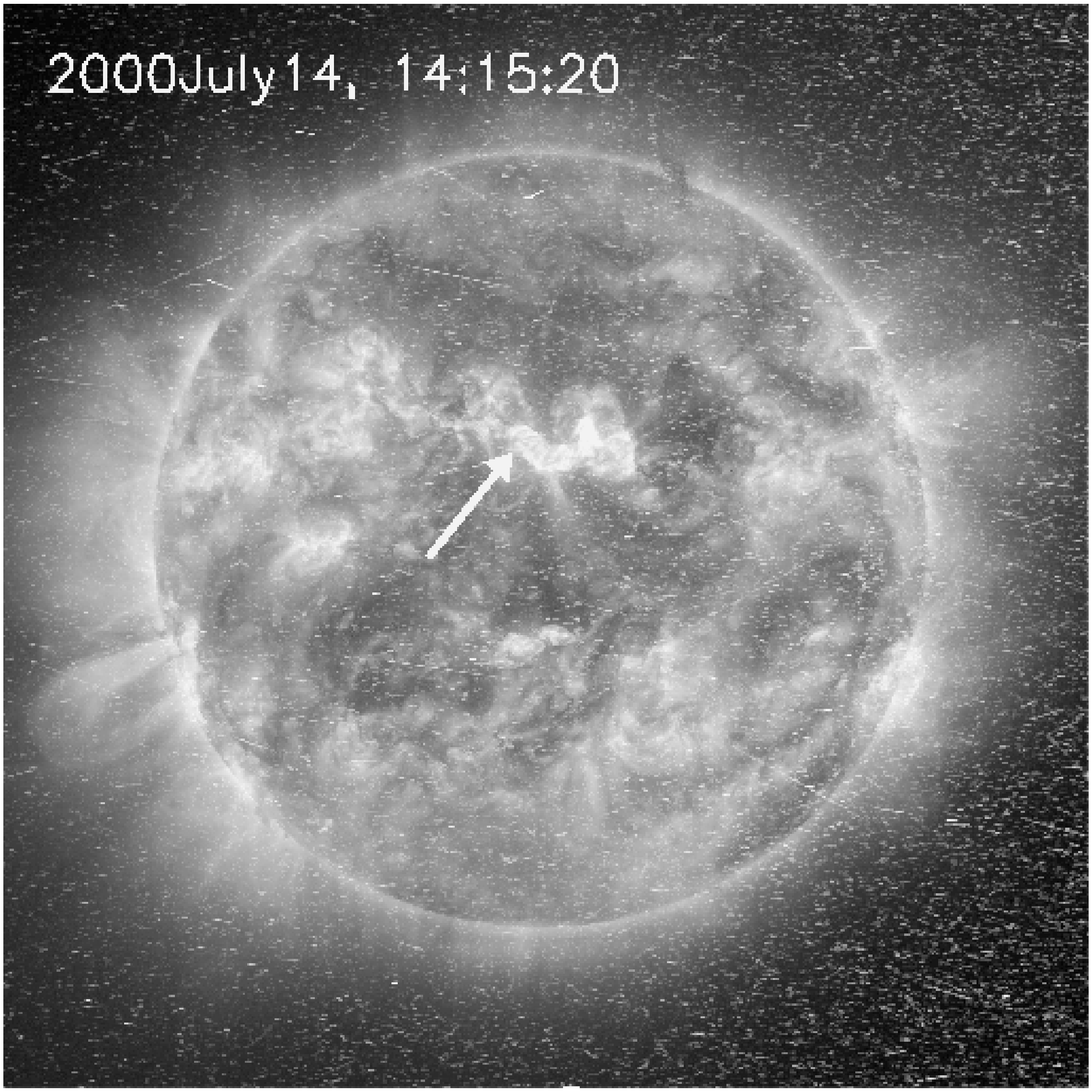

Figure 5.2: An example of post-flare loops formed after the flare as seen in Fe XII λ195 Å image. The arrow mark indicates the location of the post-flare loops.

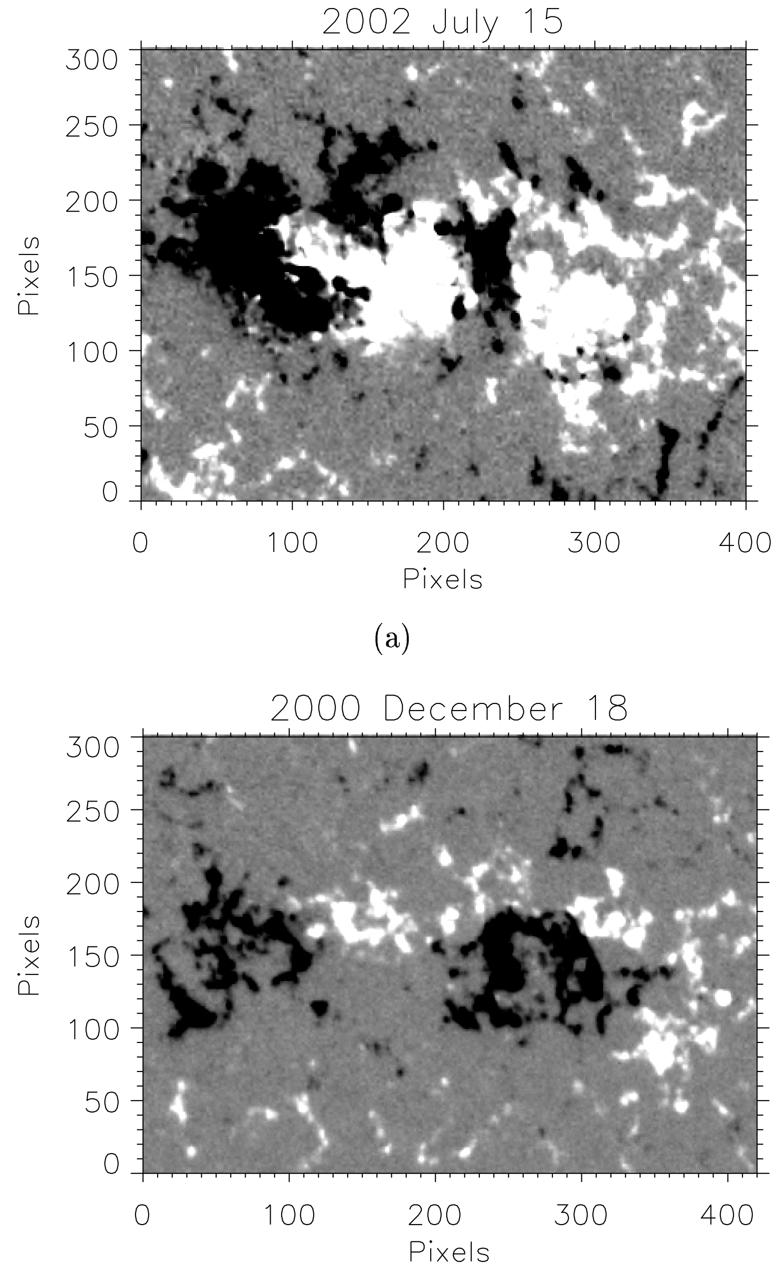

(a)

(b)

Figure 5.3: An example of magnetograms used in our study with different types of activity and field strength. Figure shows an active region magnetogram which is (a) strong in field strength (AR 0030) and (b) weak in field strength (AR 9269). The size of each pixel is 1″.

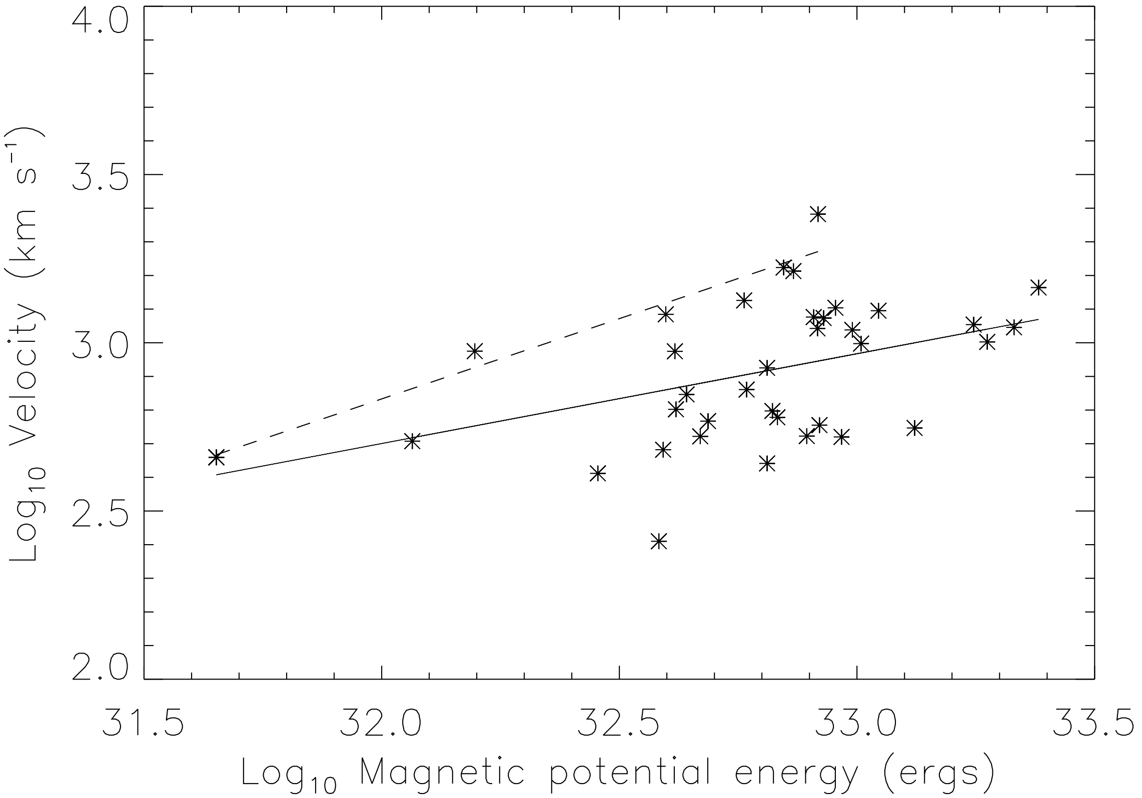

Figure 5.4: A plot of velocity of CME versus magnetic potential energy. The solid line represents the 0.26th slope and the dashed line represents the 0.48th slope.

The plot gives the relationship between the two as,

$$Log_{10}V = -5.84(\pm 2.69) + 0.26(\pm 0.082)Log_{10}E$$

where 'E' is the total magnetic energy and 'V' is the projected speed of CME. The terms in the parentheses show the errors bars.

However, there are several examples in the data where there is a range in the CME speed for a given value of the magnetic energy. This range could well be produced by a range in the fraction of the magnetic energy that actually goes into driving the CME. If this be the case, then one could make an assumption that the uppermost value of the CME speed for a given energy is closer to the maximum possible speed that could

Table 5.1: The date and time of CME occurred, AR which may be responsible for CME, coordinates, projected speed, estimated total magnetic energy (PE) and class of flare respectively are summarized here.

Date	Time (UT)	AR	Location	Speed (km)	Magnetic PE (ergs)	X-ray class
May 01, 1998	23:40	AR8210	S18W05	585	4.86×10^{32}	M1.2
Nov 04, 1998	04:54	AR8375	N17W01	527	4.68×10^{32}	C5.2
Jun 08, 1999	21:50	AR8574	N30E03	726	5.86×10^{32}	C2.6
Jun 26, 1999	07:31	AR8598	N25E00	558	1.32×10^{33}	C7.0
Jun 29, 1999	07:31	AR8602	N18E07	634	4.16×10^{32}	C3.0
Jun 29, 1999	18:54	AR8603	S14E01	438	6.47×10^{32}	C3.0
Jun 30, 1999	11:54	AR8603	S15E00	627	6.64×10^{32}	M1.9
Jul 28, 1999	05:30	AR8649	S15E00	457	4.49×10^{31}	-
Jul 28, 1999	09:06	AR8649	S15E04	456	4.49×10^{31}	-
Feb 10, 2000	02:30	AR8858	N27E01	944	1.57×10^{32}	C7.3
Apr 10, 2000	00:30	AR8948	S14W01	409	2.85×10^{32}	C8.1
Jun 07, 2000	16:30	AR9026	N20E02	842	6.47×10^{32}	X1.2
Jul 14, 2000	10:54	AR9077	N22E07	1674	7.01×10^{32}	X5.7
Jul 25, 2000	03:30	AR9097	N06W08	528	7.84×10^{32}	M8.0
Aug 09, 2000	16:30	AR9114	N11W09	702	4.38×10^{32}	C2.3
Sep 15, 2000	15:26	AR9165	N14E02	481	3.91×10^{32}	M2.0
Sep 15, 2000	21:50	AR9165	N14E01	257	3.83×10^{32}	C7.4
Sep 16, 2000	05:26	AR9165	N14W07	1215	3.96×10^{32}	M5.9
Oct 02, 2000	03:50	AR9176	S08E05	525	9.28×10^{32}	C4.1
Oct 02, 2000	20:26	AR9176	S08E05	569	8.34×10^{32}	C8.4
Nov 24, 2000	05:30	AR9236	N22W02	994	1.02×10^{33}	X2.0
Nov 24, 2000	15:30	AR9236	N22W07	1245	1.11×10^{33}	X2.3
Dec 18, 2000	11:50	AR9269	N14E03	510	1.16×10^{32}	C7.0
Apr 06, 2001	19:30	AR9415	S21E31	1270	9.01×10^{32}	X5.6
Apr 09, 2001	15:54	AR9415	S21W04	1192	8.11×10^{32}	M7.9
Apr 10, 2001	05:30	AR9415	S23W09	2411	8.28×10^{32}	X2.3
Apr 11, 2001	13:31	AR9415	S22W27	1103	8.26×10^{32}	M2.3
Apr 12, 2001	10:31	AR9145	S19W43	1184	8.51×10^{32}	X2.0
Apr 26, 2001	12:30	AR9433	N17W31	1006	1.88×10^{33}	M7.8
Oct 09 2001,	11:54	AR9653	S28E08	943	4.14×10^{32}	M1.4
Oct 22, 2001	15:06	AR9672	S21E18	1336	5.79×10^{32}	M6.7
Oct 25, 2001	15:26	AR9672	S16W21	1092	9.78×10^{32}	X1.3
May 16, 2002	00:50	AR9948	S20E14	600	6.80×10^{32}	C3.5
Jul 15, 2002	20:30	AR0030	N19W01	1132	1.76×10^{33}	X3.0
Jul 18, 2002	08:06	AR0030	N20W30	1111	2.14×10^{33}	X1.8
Aug 16, 2002	12:30	AR0069	S14E20	1459	2.41×10^{33}	M5.2
Nov 09, 2002	13:31	AR0180	S12W29	1633	7.35×10^{32}	M4.6

be produced for that value of energy. We therefore chose these maximum speeds to plot another straight line (dashed line) in Figure 5.4. We omitted the points beyond E $> 10^{32.9}$ ergs, since the speeds were lower than the speed for E $= 10^{32.9}$ ergs, thereby indicating that only a portion of the magnetic energy might have been utilized for such slower CMEs. Clearly, this is only an assumption, but could be easily falsified, had the vector magnetograms been available. This line bears a relation

$$Log_{10}V = -12.4(\pm1.9) + 0.48(\pm0.06)Log_{10}E$$

Thus the maximum speed of a CME for a given energy is seen to be proportional to the square root of the energy.

5.4.2 Active region magnetic flux and total magnetic energy

Because of unavailability of vector magnetograph data (which gives the change in energy before and after the CME), we used time sequence of corrected line-of-sight magnetic field strength (B_z) data to search for the change in magnetic flux before, during and after the CME eruption. We plotted a graph of magnetic flux versus time. Figures 5.5(a) and (b) show the plot of flux versus time for two different active regions AR 8210 and AR 8375 respectively. The dash-dot-dot vertical line indicates that the time at which the AR passes the central meridian and the solid vertical line indicates the CME occurrence time as seen by C2 coronagraph. In Figure 5.5(a) the total magnetic flux is seen to increase with time. Further, there is a clear flux imbalance between the positive and negative polarity fluxes. The flux imbalance is minimum near the central meridian and increases away from the central meridian. On the other hand, in Figure 5.5(b) the total magnetic flux remains constant with time and flux imbalance is less which almost vanishes near the central meridian. In all the 37 cases we could not see any sudden change in the total flux during the eruption of CME when we take an AR as a whole. In most of the cases we could see only continuous increase or no change in

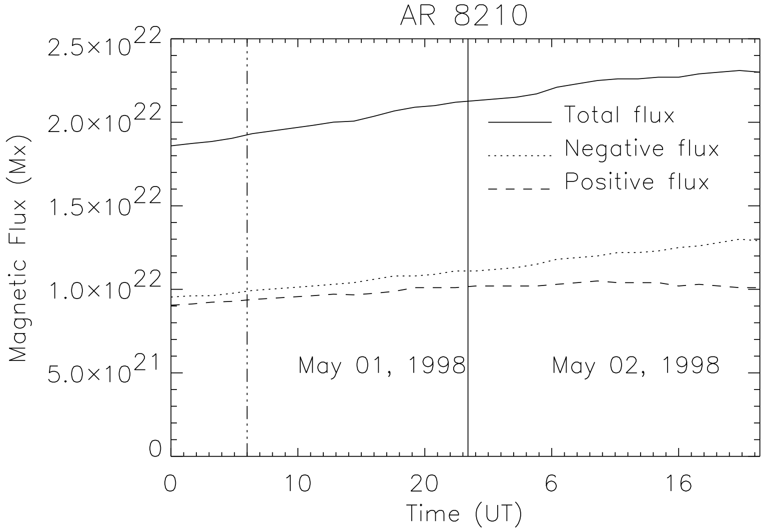

(a)

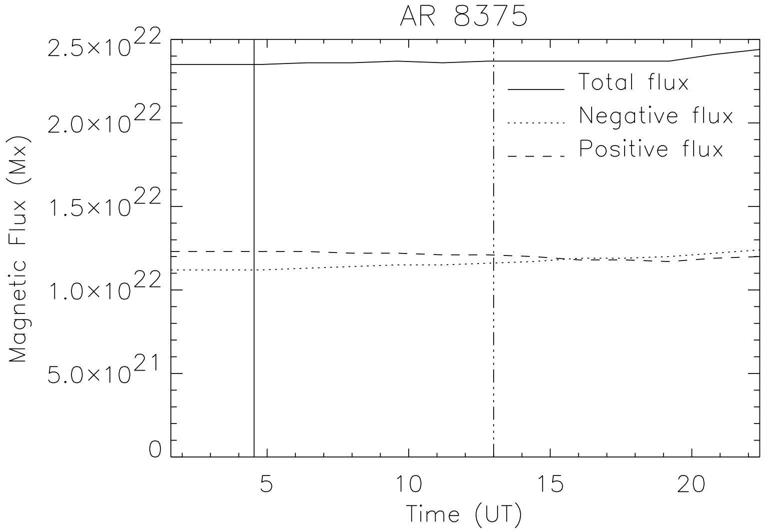

(b)

Figure 5.5: Flux evolution for active regions (a) AR 8210 and (b) AR 8375. The solid vertical line represents the CME occurrence time and dash-dot-dot vertical line represents the time of central meridian passage of an active region. The flux has been corrected for the geometrical effects of area foreshortening and angle between magnetic field direction and the observer.

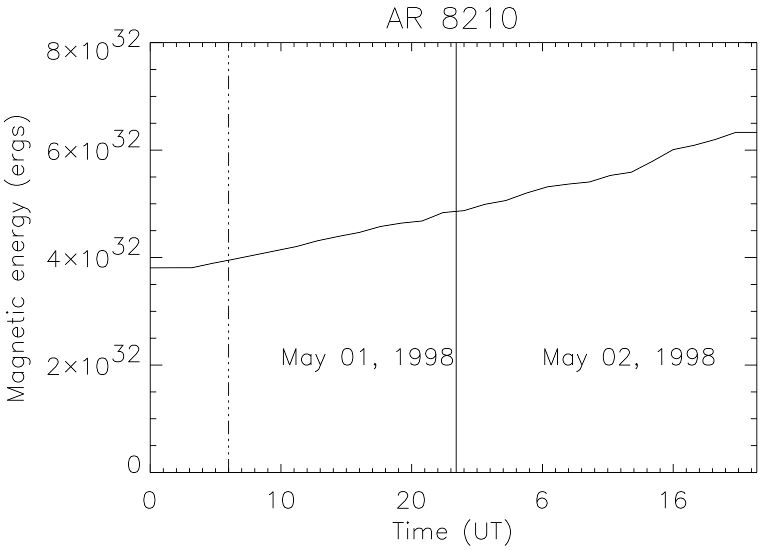

(a)

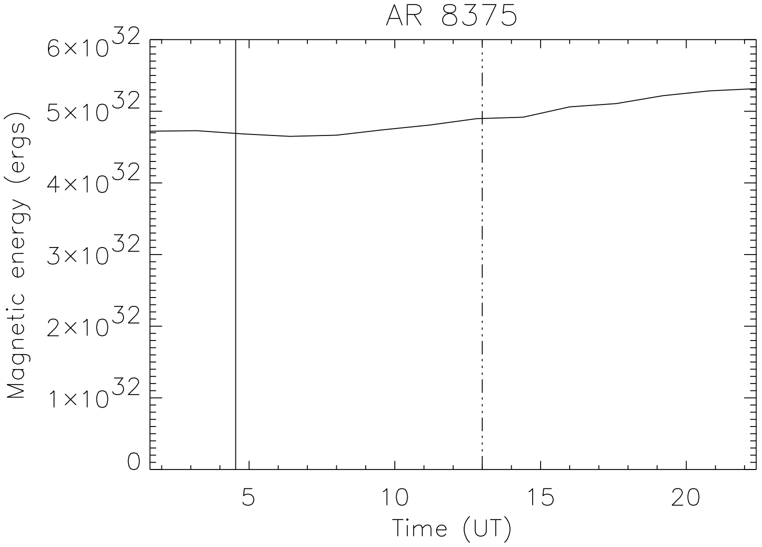

(b)

Figure 5.6: Evolution of total magnetic energy for active regions (a) AR 8210 and (b) AR 8375. The solid vertical line represents the CME occurrence time and dash-dot-dot vertical line represents the active region central meridian passing time.

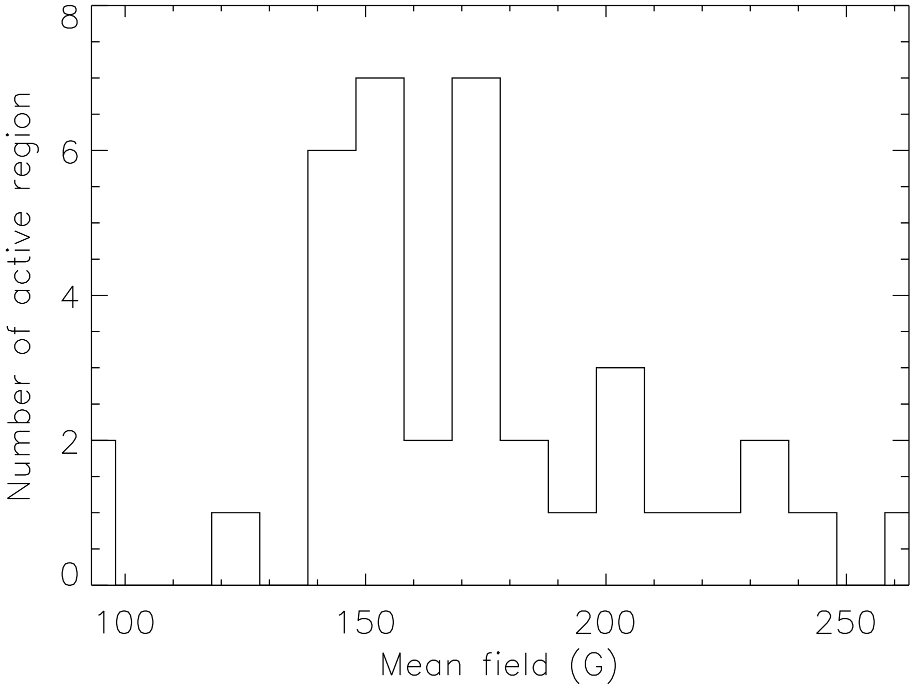

Figure 5.7: A histogram of the mean field of 37 active regions which were associated with halo CMEs.

total flux. The increase in magnetic flux may be due to the continuous emergence of magnetic flux from below.

We also computed the magnetic potential energy for each available magnetogram and then plotted the computed magnetic potential energy versus time (Figure 5.6a and b). The curve looks similar to the total magnetic flux curve in both the cases. We could not see any drastic change in magnetic potential energy during CME. Only the vector magnetic field data can resolve this issue.

If there is no change in the magnetic flux content and magnetic potential energy of an active region during CME, then there should not be any change in the mean field of the active region. We then computed the mean field as the ratio of the total unsigned magnetic flux over the active region to the total area occupied by the active region.

We plotted a histogram of the mean field of the 37 active regions (Figure 5.7). The histogram shows that the mean field peaks at $\approx$ 150 G in AR like sunspot. This is not a surprising result, because one expects the magnetic field in the photosphere to be in equipartition with the plasma pressure.

5.4.3 Non-potentiality of the active region magnetic fields

The active region AR 9415 ejected many CMEs during its passage through the central meridian. Each CME had $\approx$ 1000 km s^{-1} speeds, except the one of 10 April 2001. On that day the active region ejected CME with a speed of 2411 km s^{-1}. Then the question is why did the same AR on 10 April 2001 eject CME at a higher speed? We then started looking for a magnetic field parameter which could be different on that day, viz. the magnetic non-potentiality.

The pattern of fibrils around an active region often resembles that of iron filings aligned around a bar magnet. It suggests magnetic ordering. According to Foukal (1990), comparisons between calculated fields in an active region and the chromospheric H_α fibril patterns observed at about the same time indicate that the main features of the fibril geometry can be reproduced with a potential field ($\nabla\times$ B = 0) calculation. However, better fits can be achieved when substantial currents are assumed to flow along magnetic field lines. Foukal (1971a, 1971b) showed that the H_α fine structures (fibrils) always cross connecting regions of opposite polarity, although not necessarily the nearest opposite polarity. Loughhead (1968) described the characteristics of chromospheric fibrils around isolated sunspots as follows: They are normally directed outwards and are closely packed; the lengths of the individual fibrils are highly variable, and the orientation and general appearance of the fibril pattern is stable over hours or days. He also suggests that in a majority of cases the fibril patterns look like potential fields.

In the absence of vector magnetogram data, we used the BBSO full disk H_α (image scale of $1''.05$ pixel^{-1}) as a proxy for the chromospheric field. We used the H_α images of the active region AR 9415 on 06, 09, 10, 11 and 12th of April 2001. Apart from these data-sets, we also used the H_α images of 14 July 2000 and 16 August 2002. We first co-aligned the full disk H_α images with full disk magnetogram using the limb matching algorithm (as explained in Chapter 2) and then derotated the H_α images to the time of acquisition of the magnetograms. The registration is within an accuracy of a few pixels. We chose the active region and its surrounding area in both the H_α image and in the magnetogram and then overlaid the computed potential field lines (using Fourier transform method (Sakurai, 1989)) on the H_α image.

To examine the non-potentiality or potentiality of the magnetic fields (fibrils are used to follow the local field line in the chromosphere) surrounding the active region, we plotted only low field lines (±30 to ±200 G). Potentiality or non-potentiality of the chromospheric magnetic field depends on the basic assumption that whether the H_α fibrils follow the potential field lines or not. Figures 5.8, 5.9, 5.10, 5.11 and 5.12 show non-potential and potential nature (in these figures, 'P' represents the potential and 'N' represents the non-potential) of the chromospheric magnetic field during and after the time of CME occurrence. On 06, 09 and 10th of April 2001, the active region surrounding shows deviation from potential field direction. However, on 14th July 2000 and 16th August 2002, the active regions magnetic field show potential nature. But the time of observation of H_α image and magnetograms are different (except for the 06th and 09th April 2001) and by that time the fibrils might have changed their direction. In any case on 06, 09 and 10th April of 2001, even though the active region area is small, the non-potentiality of the active region magnetic field might have provided more free energy to the ejecta. To examine in detail all these effects, we need to measure the coronal magnetic field along with the photospheric vector magnetic field. The aforementioned result (non-potentiality nature) provides only a clue that the active region magnetic non-potentiality could have enhanced the speed of the ejecta.

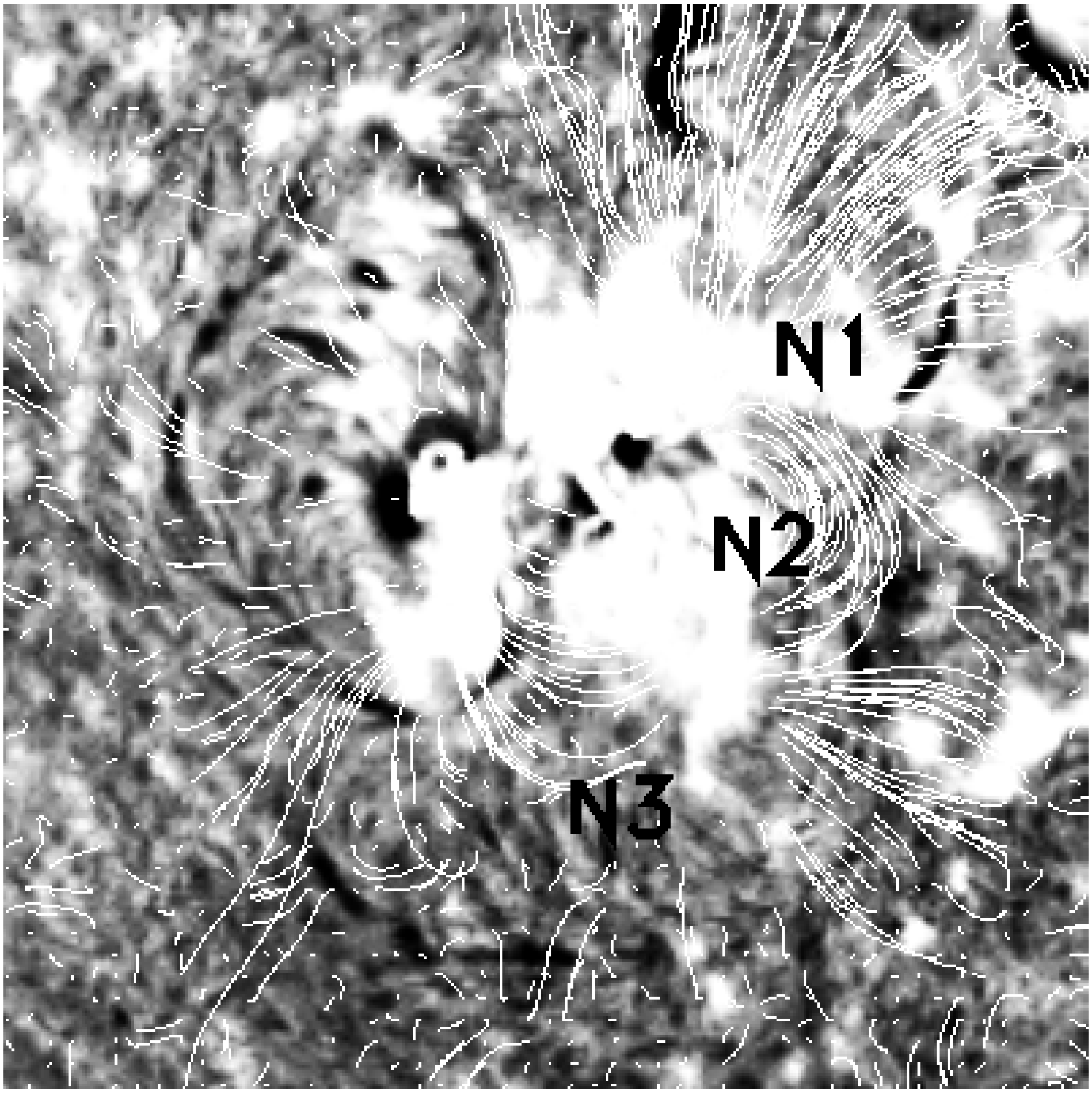

Figure 5.8: Overlay of computed magnetic field lines on the H_α images obtained on 06 April 2001. The H_α image and the magnetogram have been recorded at 18:00:13 UT and 18:00:30 UT respectively. In figure 'N1', 'N2' and 'N3' represent non-potentiality of the magnetic field in AR 9415. The CME occurred at 19:30 UT.

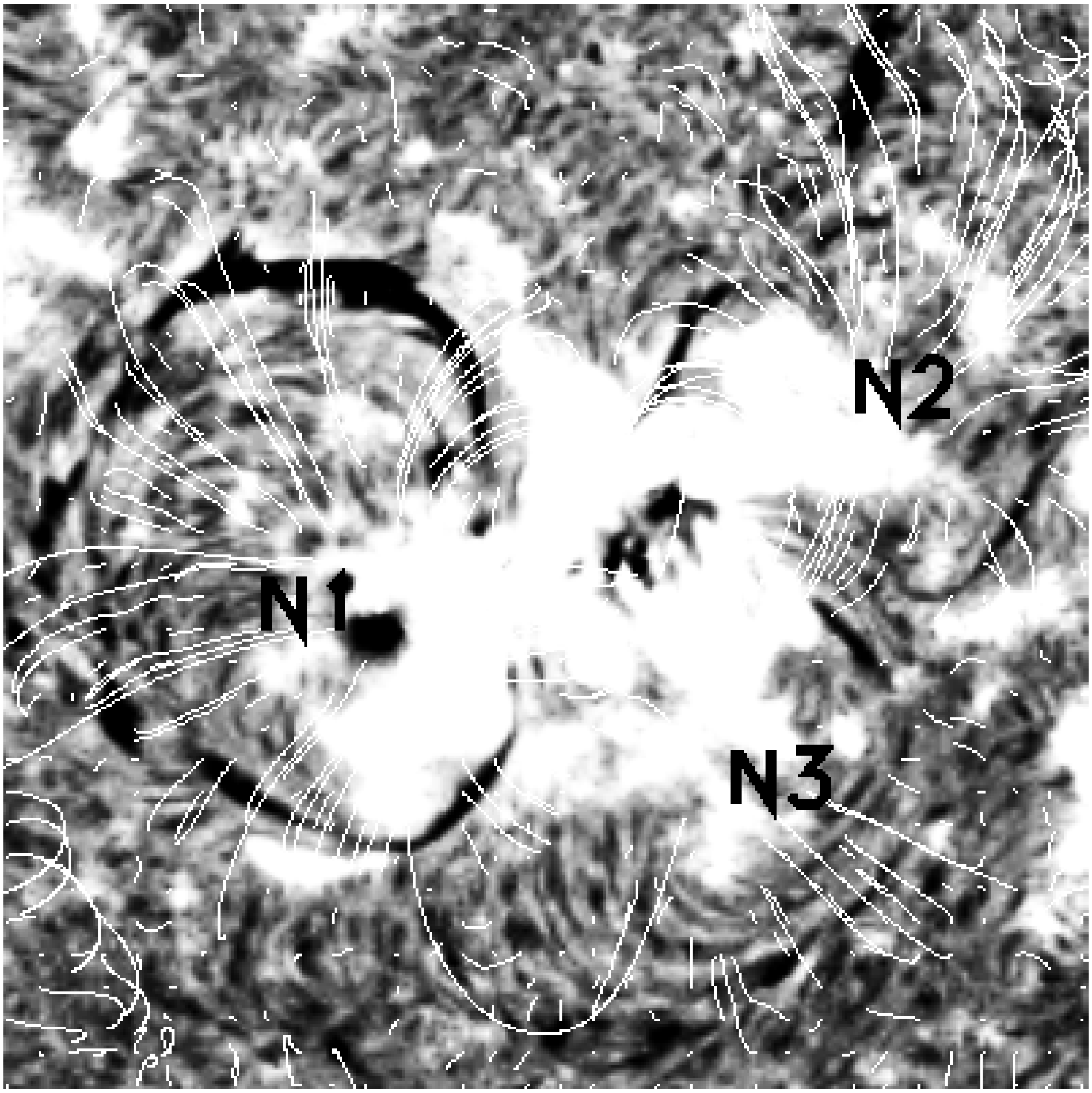

Figure 5.9: Overlay of computed magnetic field lines on the H_α images obtained on 09 April 2001. The H_α image and the magnetogram have been recorded at 17:08:59 UT and 16:59:30 UT respectively. In figure 'N1', 'N2' and 'N3' represent non-potentiality of the magnetic field in AR 9415. The CME occurred at 15:54 UT.

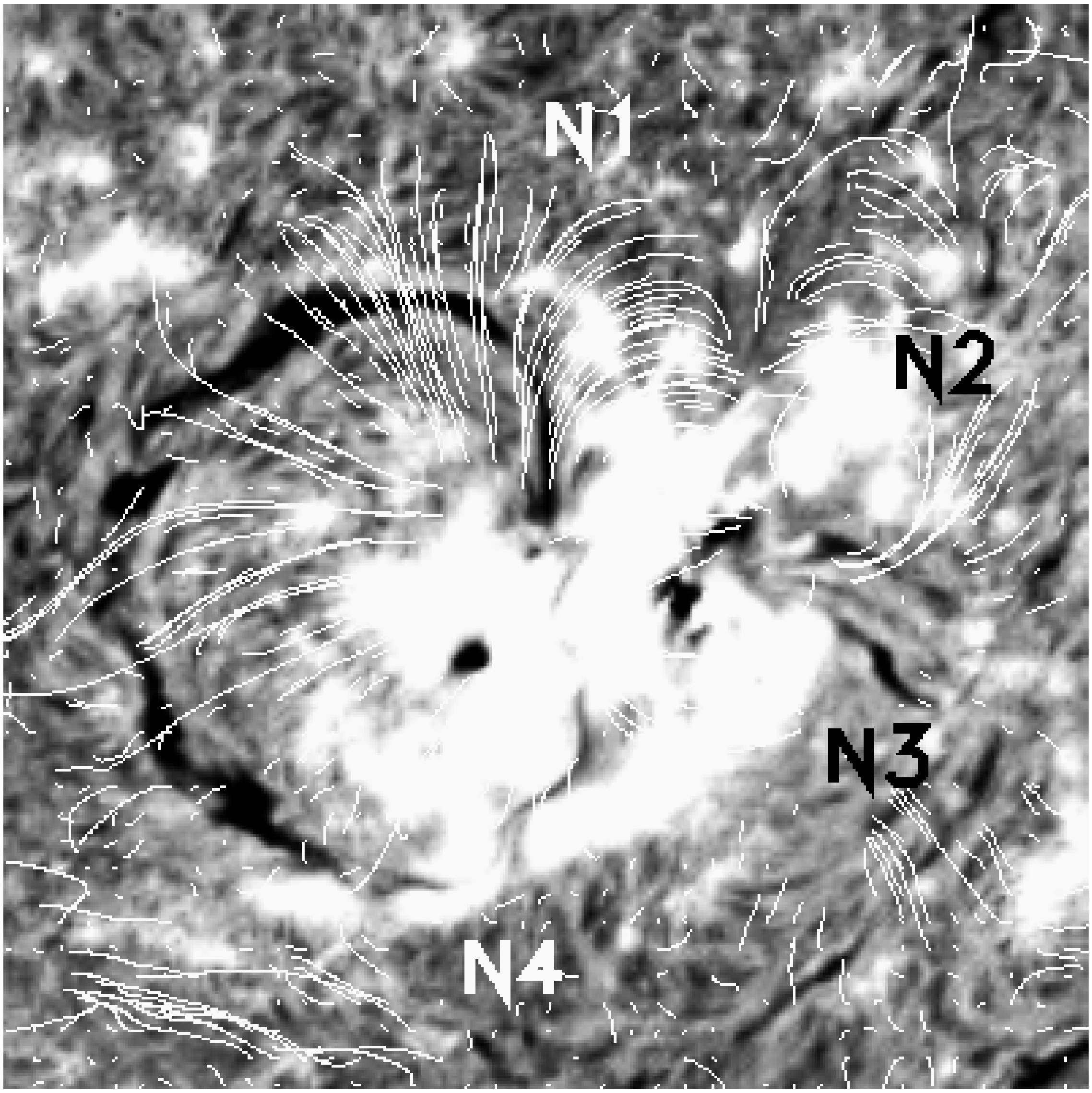

Figure 5.10: Overlay of computed magnetic field lines on the H_α images obtained on 10 April 2001. The H_α image and the magnetogram have been recorded at 20:31:38 UT and 05:30:30 UT respectively. Here, 'N1', 'N2', 'N3' and 'N4' represent the non-potentiality of the active region magnetic field. The CME occurred at 05:30 UT.

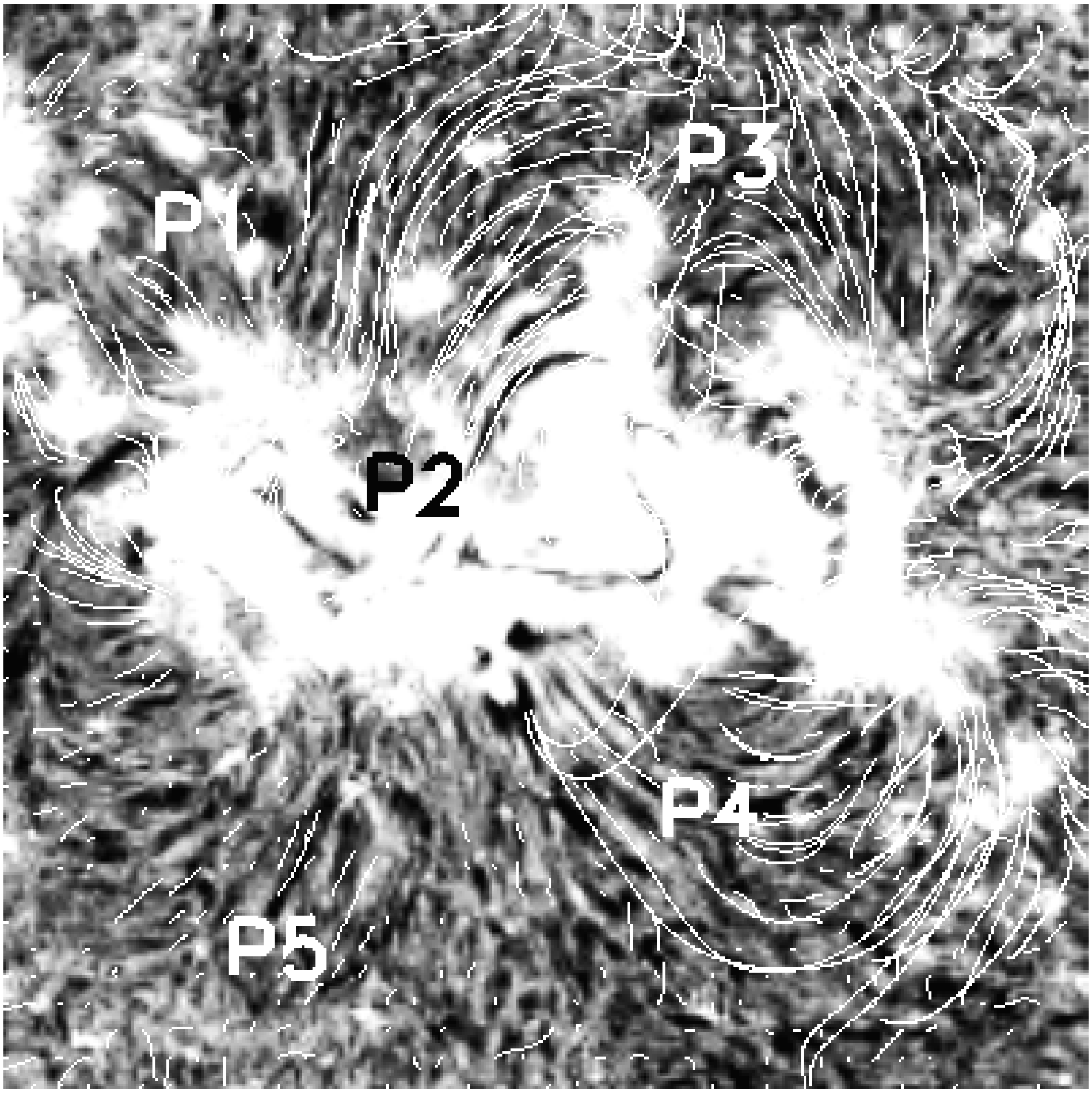

Figure 5.11: Overlay of computed magnetic field lines on the H_α images obtained on 14 July 2000. The H_α image and the magnetogram have been recorded at 15:20:03 UT and 09:36:30 UT respectively. The locations marked with ‘P1’, ‘P2’, ‘P3’, ‘P4’ and ‘P5’ represent the potential nature of the active region magnetic field. The CME occurred at 10:54 UT.

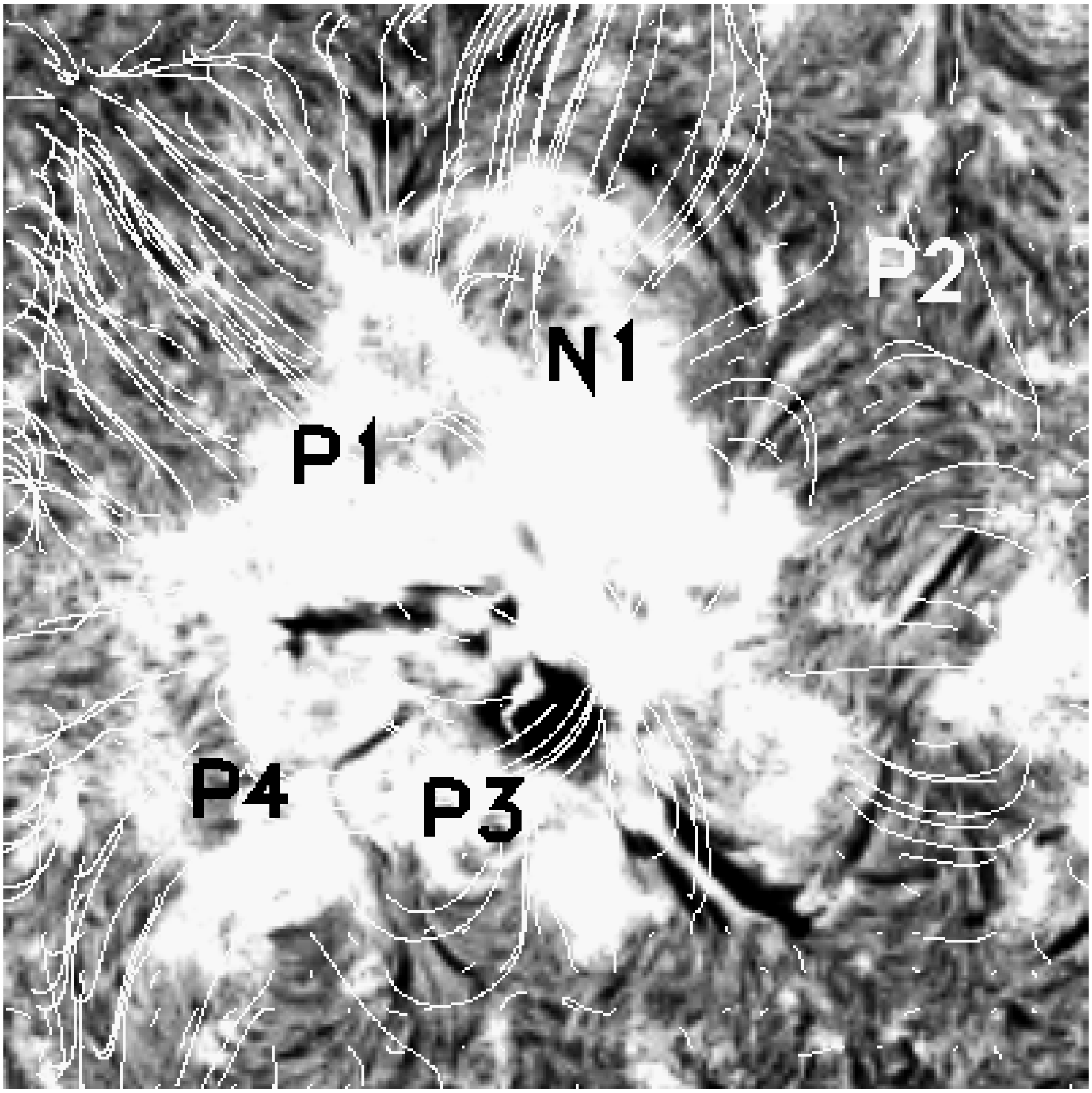

Figure 5.12: Overlay of computed magnetic field lines on the H_α images obtained on 16 August 2002. The H_α image and the magnetogram have been recorded at 16:08:45 UT and 13:30:30 UT respectively. Here the locations marked with ‘P1’, ‘P2’, ‘P3’ and ‘P4’ represent the potentiality and ‘N1’ represents the non-potentiality of the active region magnetic field. The CME occurred at 12:30 UT.

5.4.4 Velocity of CME and GOES X-ray peak intensity

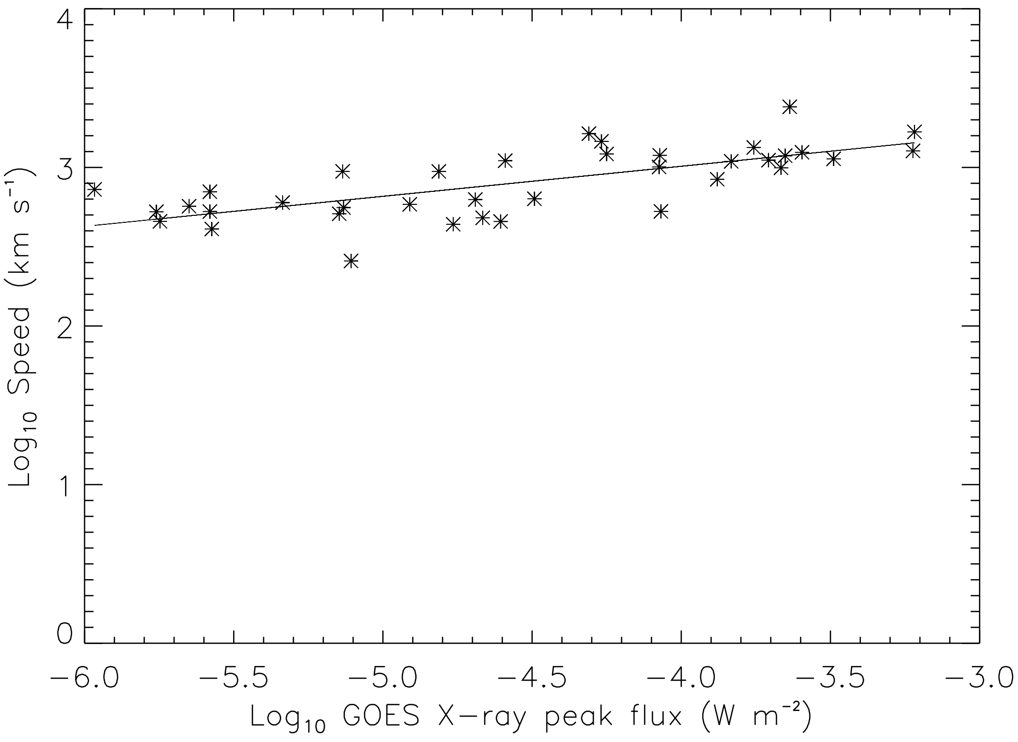

Figure 5.13: A plot of logarithmic speed of CME versus logarithmic X-ray peak flux measured by GOES.

It is well known that the GOES X-ray flux is related to the strength and duration of the flare. However, the exact relation between the GOES peak X-ray flux and speed of CME is not well known. In order to examine their relationship, we plotted a graph of logarithm of soft X-ray peak flux versus the logarithm of projected speed of CME. We selected 37 halo CME events and the corresponding GOES X-ray peak flux. From the 1-minute temporal resolution data of GOES we could obtain the X-ray peak flux intensity (W m^{-2}) associated with the flare. Figure 5.13 shows a plot of GOES X-ray peak flux versus CME speed. The plot shows a clear correlation (correlation coefficient=0.71) between the peak flux and CME speed. From the plot, we derived a relation between the two parameters as

$$Log_{10}V_e = 3.76(\pm 0.15) + 0.19(\pm 0.03)Log_{10}G_f$$

where, V_e is the projected speed (km s^{-1}) of the CME and G_f is the GOES peak X-ray flux (W m^{-2}).

5.5 Discussion and Conclusions

In using the projected speed (V_p) of the halo CMEs we have made the assumption that the actual propagating speed (V) is a function of the projected speed ($V=KV_p$). Figure 6 in Michalek, Gopalswamy, and Yashiro (2003) shows that the difference between the projected speed and the corrected speed is $\approx$ 20%. The results of Berger and Lites (2003) show that MDI systematically measures lower flux densities than Advanced Stokes Polarimeter. MDI underestimates the flux densities in a linear manner for MDI pixel values below $\approx$ 1200 G by a factor of $\approx$ 1.45. For the flux densities higher than 1200 G the under-estimation becomes non-linear. Below 1200 G, our results will be shifted uniformly in the direction of the abscissae (since the energy is proportional to square of the flux density and we use logarithm of energy). Above 1200 G, our results are affected by a very small amount, as the number of pixels contributing to high field values are very small. So, both the projection effect for the expansion velocity and the calibration of MDI magnetograms will not affect our results substantially.

From Figure 5.4 it is clear that there is a fairly strong relationship between the total magnetic energy and the projected speed of halo CME. The following conclusions can be drawn from this study. Although emerging flux in the core of an AR may be responsible for the occurrence of a CME (Nitta and Hudson, 2001), the total kinetic energy released in the CME seems to be well related to the total magnetic energy of the associated active region. This shows that for a large number of cases, it is an individual active region that powers a CME. In fact, the CME speed varies as 0.26th power of the magnetic energy in our study. Now we compare this release of energy to that in a blast wave which evolves in a $self - similar$ fashion, given by Sedov (1959) and Taylor (1950). Suppose an energy E is suddenly released in an explosion producing a spherical blast wave, which progresses in an ambient medium of density ρ, then the velocity of expansion of the spherical blast is given by

$$V_s(t) = \frac{2}{5}\epsilon_0 \left(\frac{E}{\rho t^3} \right)^{\frac{1}{5}}$$

where, ϵ_0 is a dimensionless distance parameter. The expansion velocity in the classical Sedov solution for a blast wave varies as the 1/5th power of the injected energy (Choudhuri, 1999). Thus, the behavior of solid line in Figure 5.4 is very close to the response of an homogeneous plasma to a sudden injection of energy. At the same time, the behavior of the dashed line in Figure 5.4 is closer to the response of a stratified plasma to a sudden injection of energy (Sedov, 1959).

The idea that a CME is generated by a sudden injection of energy into the corona was explored by Dryer (1974). Those calculations were based on the response of the corona to a pressure pulse created by the sudden release of the energy in a flare. We call the injection sudden, whenever the time scale of energy input is shorter than the dynamical time scale of the system. In the case of a CME, the dynamical time scale is the time required for the solar wind to traverse some typical distance, e.g. the pressure scale height. For a typical value of the sound speed in the corona, about 100 km s^{-1}, and the scale height of about 100000 km, we obtain a dynamical time of about 1000 sec. On the other hand, the energy release takes about a few minutes for a flare. Thus, the flare injects energy into the corona at a rate that is faster than the rate at which the coronal plasma can expand to smooth out the pressure enhancement. This was thought to result in a blast wave, as was borne out by the calculations. Later, it was seen that not all the CMEs were related to flares (Munro *et al.*, 1979) and discrepancies in the chronology of flare on-set in relation to CME on-set (Harrison, 1995; Zhang *et al.*, 2001) were also noticed.

However, recent observations have shown considerable dynamics in coronal active regions associated with CMEs (Thompson *et al.*, 1999). Assuming that the coronal loops delineate magnetic field lines, the dynamics of these loops imply that CMEs are associated with re-arrangement of coronal magnetic field lines on the scale of active regions. Theoretically, the on-set of non-equilibrium in a quasi-static evolution of a coronal magnetic structure is known to result in a sudden expansion of a coronal loop to the nearest possible equilibrium state (Low, 1990). This expansion of the magnetic field does imply the launch of a pressure pulse into the corona above the active region. The time scale for the injection of this mechanical energy would be the time required for the rearrangement of the field lines. This time would be the time required for an Alfvén wave to traverse the active region. Assuming a conservative estimate of the magnetic field of 1 G, and a density of 10^8 particles per cm^3, we get an Alfvén speed of 200 km s^{-1}. This Alfvén speed is also consistent with the observed speed of EIT waves. For a typical active region size of 30000 km, this leads to an Alfvén time of 150 sec. Thus, the direct injection of mechanical energy via magnetic field expansion on a time scale which is small compared to the dynamical time scale of the corona probably explains the resemblance of the empirical relationship seen in Figure 5.4 with the Sedov solution. As mentioned earlier, the range in speeds seen for a given value of magnetic energy could well be due to a range in the non-potentiality of the active region magnetic field, a conjecture which can be easily verified with vector magnetic data. It must also be understood that the empirical relationship of projected speed with magnetic energy does not explain what produced the ejecta in the first place, but only provides a possible explanation of the driving mechanism for the ejecta. Classical blast waves do not carry ejecta, while a blast wave accompanied by ejecta has been named as 'quasi-blast' (Dryer, 1974).

The comparison of computed potential field lines with the H_α fibrils and threads show that in compact active regions, the magnetic field is highly non-potential. The highly non-potential nature indicates the availability of free-energy in the system. If the active region magnetic field is highly sheared then the available free-energy is more, since $E_{ff}=\gamma E_p$. where, E_p is the potential energy and γ is a shear dependent constant. As the shear increases, γ increases and hence the free-energy.

Figure 5.13 shows existence of a relationship between the GOES X-ray peak flux and the velocity of the CME. However, many results suggest that there are CMEs without and with flares (e.g., Gosling *et al.*, 1976; MacQueen and Fisher, 1983; Dryer, 1996; Sheeley *et al.*, 1999). At present there is no evidence for the simultaneous occurrence of CME and the flare. This may be because of lack of observational techniques. However, the recent comparisons of GOES-X-ray flux profiles and CME acceleration profiles by Shanmugaraju *et al.* (2003) have shown that the peaks of the acceleration of CME nearly coincide with X-ray flare eruptive phase below $2R_{\odot}$. By using MK3 and SMM coronagraph, it has been demonstrated that CMEs start almost simultaneously with the accompanying flares (Maxwell, Dryer, and McIntosh, 1985; Dryer, 1994). Also, some recent observations showed that flare on-set lags behind the CME on-set by atleast a few minutes (Hundhausen, 1999). Zhang *et al.* (2001) have found that the acceleration phase of CMEs coincide with the rise phase of the X-ray flares. The linear relationship between the GOES peak X-ray flux and CME velocity may indicate that both CMEs and flares are produced by a common process. Flares also provide very useful data for determining the location on the Sun at which a CME originates.

5.6 Summary

We have studied the relation between the velocity of CME and magnetic field parameters. The results are summarized as follows:

(1) The velocity of a CME is well related to the total magnetic energy of the associated active region.

(2) Our results give an upper limit to the initial speed of a CME. The maximum speed of a CME for a given magnetic energy is proportional to the square root of the energy.

(3) The change in photospheric magnetic flux and magnetic potential energy during and after the CME is not detectable when one takes an AR as a whole.

(4) The range in CME speeds for a given value of magnetic energy may be due to the potentiality or non-potentiality nature of the magnetic field of the associated active region.

(5) There is a correlation between the X-ray peak flux measured by GOES and speed of the CME.

In this Chapter, we confined our study to halo CMEs. We have also constrained our study to ARs located near central meridian to avoid severe projection effects in the calculation of the magnetic energy. The empirical relation allows us to make an estimate of the maximum possible speed of any CME that may result from an AR having a given magnetic energy. This capability would be very important for space weather predictions. Other parameters e.g. magnetic complexity, helicity etc. could also be studied. For the present, the magnetic energy seems to be a reasonable indicator for estimating the CME speed. In addition, the resemblance of the speed-energy relationship to the Sedov solution provides an exciting clue for understanding the driving mechanism for a CME. Data from vector magnetic field measurement would give better estimation of the available free energy. Data from space based, 3-dimensional observations of the CME may give a better estimate of the speed (by eliminating the projection effect). With this improvement one can provide a better prediction for the arrival time of CME at the Earth's magnetosphere and the magnitude of the geomagnetic activity.

Chapter 6

Summary, Conclusions and Future Plans

There are two kinds of processes by which the Sun affects the Earth's atmosphere. These are high energy radiation and particle emission. Observational evidences indicate that the magnetic field controls the production of high energy radiation and particle emission, which affect the Earth's climate and space weather. To understand the long term subtle changes in the Earth's climate and to predict the space weather it is very important to study the magnetic field in the solar atmosphere. To start with, one can find empirical relationships between the magnetic field parameters and the intensity of high energy radiation and the kinematics of particle emissions. In this thesis, we have attempted to do the same through the study of EUV radiation and CMEs. In this Chapter, we first summarize Chapter-wise, the results of the thesis and then present the overall conclusions. Further, we briefly describe our future plans.

In the introduction, we briefly described the importance of the study of evolution of magnetic field in the solar atmosphere. We then briefly reviewed the various types of evolution of magnetic fields in the solar atmosphere.

6.1 He II λ304 Å network brightness and the photospheric magnetic field

We chose He II λ304 Å emission for our study because it is a line which is brightest in EUV emission next to H I Lyman α. Because of its short wavelength, it is a dominant source of energy for heating and ionizing the terrestrial upper atmosphere. A good knowledge of He II λ304 Å emission and its variability is essential for the study of photo-chemistry and energy balance of the planetary atmospheres. However, one needs to understand the mechanism which can enhance the brightness of the He II λ304 Å emission in the solar atmosphere. The excitation mechanism of the helium and its ion in the solar atmosphere is still an unsolved problem.

A number of suggestions have been offered by many to explain the enhanced intensity in the resonance line of He II at 304 Å. We made an attempt to relate the observed network intensity with the magnetic field strength. Even though, the coronal EUV radiation beyond λ228 Å is capable of ionizing the helium ion in the solar atmosphere, it would make the features in the transition region more diffused and broader than the coronal features. Since the observed morphologies are different in He II λ304 Å filtergrams and in corona, we concluded that coronal radiation cannot be the source of network brightening observed in He II λ304 Å.

We then showed how the morphology of the photospheric line-of-sight magnetic field (B_z), $|B_z|$ and $|\nabla B_z|$ are matched with the He II λ304 Å network morphology. We found that the network brightness occurs at the foot-points of the magnetic fields by overlaying the contours of the magnetic field upon the He II λ304 Å images. We also found that the brightness of the network features was enhanced near bipoles. Further, we estimated the correlation coefficient between the He II λ304 Å, and B_z, $|B_z|$ and $|\nabla B_z|$ respectively. The obtained cross-correlation coefficient is not very high. The reduction in correlation is because of inclusion of intra-network fields. The temporal correlation between the magnetic field and network elements observed in He II λ304 Å shows that the correlation is maximum when the time difference between the two is minimum and it decreases as the time difference increases. Our study confirms that the magnetic field plays an important role in the temporal evolution of the He II λ304 Å network features. The scatter plots between the He II λ304 Å intensity and absolute value of the magnetic field showed that the network brightness observed in He II λ304 Å has a linear relationship with the strength of the magnetic field. The relationship is almost linear for the stronger magnetic fields, larger than 10 G. It almost disappears below 10 G, where the contribution from the intra-network is more. We could easily segregate the network, intra-network and neutral lines from the 'm' maps. These 'm' maps showed that only monopole regions of the network cells contribute to the linear part of the scatter plot. We estimated the probable height of formation of the network elements observed in He II λ304 Å. We found that at about 3000 km above the photosphere, the size of the extrapolated magnetic network elements matches with the size of the He II λ304 Å network elements. Thus, our study indicates that the role of magnetic field is important in the network brightening observed in He II λ304 Å.

6.2 Structure and evolution of network cells observed in He II λ304 Å

The solar transition region is highly dynamic. Network cells are the dominating features of the transition region. In order to understand the transition region one has to study the characteristics of the network cells (lifetime, size etc.) in relation with the magnetic fields. Even though, some of the characteristics of the transition region network cells are not different from the chromospheric Ca II K network cells, the observed network element sizes are different from that of the photospheric magnetic network elements. From the time of discovery of supergranular network cells (Hart,

1956) to the present epoch, many researchers have estimated the lifetime and size of network cells from the Dopplergrams, magnetograms and Ca II K filtergrams using different techniques. In most of the cases, there was a data-gap due to the diurnal changes on the Earth. In addition, seeing also affects the measurement of size and lifetime. In estimating the lifetime and cell sizes, we used the space-based data observed in He II λ304 Å and the photospheric magnetograms. We also used a new technique namely the "structure function". We compared the results obtained from magnetograms and He II λ304 Å images. We then compared our results with those obtained earlier. While our results were consistent with the earlier results, there was a discrepancy between the results obtained from magnetograms and He II λ304 Å images. However, the results almost tallied when the magnetograms were extrapolated to a height of 3000 km above the photosphere. Similar results were obtained for the network elements. We summarize the results obtained from our study in Table 6.1.

Table 6.1: The lifetime and size of the network cells and elements.

Network Observed in	Life time (hrs)	Size of the network (km)	Size of the element (km)
He II λ304	23-27	25000-30000	12800
Magnetic field (MF)	13-16	12000-15000	5000
Extrapolated MF	>30	$\approx$ 25000	12450

The velocity of the network elements obtained from different techniques is less than 0.1 km s^{-1}, which is in agreement with the results obtained by various researchers using different methods. The probable height of the loop in intra-network field is $\approx$ 3000 km (above the photosphere).

6.3 Magnetic field fluctuations in sunspots

Coronal images exhibit pronounced EUV and X-ray emission in the regions that are spatially related to sunspots (active region). These regions have temperatures of 8-20 MK, equivalent to an energy budget of 10^7 erg cm^{-2} s^{-1}. Motivated by the earlier results (Ulrich, 1996) that this pronounced EUV and X-ray emission is related to the magnetic field fluctuations in sunspots, we examined the magnetic field fluctuations and their magnitudes in sunspots.

We found, using four sets of high resolution ($1''.2$) time sequence of magnetograms of active regions, that there is a 3 mHz oscillation in most of the locations in sunspots. In addition to 3 mHz, there is a 5.5 mHz oscillation in the sunspot umbra. The magnitude of magnetic field fluctuations in the sunspot umbra is 7-14 G. In the absence of saturated pixels in the sunspot umbra of the selected active regions, the non-linearities of the MDI magnetograms for magnetic field strengths above 1200 G (Berger and Lites, 2003) may affect our results. But the sunspots which are weak in field strength (AR 9354) also showed field strength fluctuations. Hence, we could rule-out, up to some extent, the possibility of non-linearity of the MDI magnetograms introducing the magnetic field fluctuations in the sunspot umbra. Apart from the high frequency fluctuations, we found low frequency magnetic field fluctuations in sunspots. The power spectrum shows that a broad range of low frequency power is present in the magnetic field fluctuations. These low frequency fluctuations may be due to the inward and outward drift of features in sunspots. The inward and outward motion of features can be seen in the space-time map and is confirmed by applying LCT technique on magnetograms. We found that the velocity of the inward moving features is small ($\approx$ 0.1 km s^{-1}) and the velocity of the outward moving features lies in the range of 0.4-0.7 km s^{-1}. Further, the estimated mechanical energy flux ($\approx 10^9$ erg cm^{-2} s^{-1}) from the magnetic field fluctuations ($\approx$ 10 G) is sufficient to heat the AR corona.

6.4 CME velocity and active region magnetic energy

The fastest coronal mass ejections blast out through the corona at a speed greater than 1000 km s^{-1}, driving a bow shock that accelerates protons and other ions to cosmic ray energies of 100 MeV or more. Most of these CMEs originate from the strong magnetic fields in ARs like sunspots. The explosions produce a flare in tandem with the CME. Motivated by the earlier results on the prediction of arrival time of CMEs at the Earth and that the intensity of the geomagnetic severity is well related to the initial velocity of the CME, we proceeded to identify the property of the associated AR that determines the initial velocity of a CME.

To start with, we used 37 halo CME events with their source regions located within 30° from the disk center. We used the differential rotation technique to compensate for the geometrical foreshortening and we multiplied the line-of-sight field strength by $\cos^{-1}\phi$ to remove the projection effects. We improved the signal to noise ratio by adding five succesive magnetograms, thereby reducing the noise in the magnetograms from ±20 G to ±9 G. We used a virial relationship to estimate the volume magnetic energy using the three components of the potential magnetic field of the associated AR. Using all these inputs, for all the selected events we found that the initial speed of the halo is related to the magnetic energy of the associated AR. Interestingly enough, the expansion velocity of the CME varies as 0.26th power of the magnetic energy. This power is in close resemblance with the Sedov solution for the spherical blast wave expansion, where the expansion velocity of the spherical blast wave varies as the 0.2th power of the injected energy. This resemblance suggests that the magnetic energy of the individual AR is the engine for the CME. Our result allows us to make an estimate of the maximum possible speed of any CME that may result from an AR having a given magnetic energy. The maximum speed of a CME is seen to be proportional to the square root of the AR magnetic energy. If the individual AR magnetic energy is responsible for the CME velocity, then there should be a change in magnetic flux of the active region magnetic field during the CME. But our study shows that there is no change in magnetic flux during the CME when we take the entire AR into account. Apart from the magnetic flux, we also searched for the change in the total magnetic energy during the CME. But the answer was negative, that is the total magnetic energy remained unchanged. The estimated mean field for most of the regions was ≈ 150 G. We computed the magnetic field lines (using potential field approximation) for individual ARs at the photosphere, and then compared them with the observed chromospheric magnetic field using H_α fibril structure as a proxy for the transverse field lines. The result showed that the magnetic fields in δ-type compact sunspots are mostly non-potential and in bigger sunspots they are potential in nature. We also found that there exists a relationship between the X-ray peak flux measured by GOES and the velocity of the CME. The obtained relationship between the two does not indicate the cause and effect relationship; it simply suggests that both the processes are two different manifestations of the common processes that occur in the solar corona.

6.5 Synthesis

The network brightness observed in He II $\lambda 304$ Å is well related to the strength of the magnetic field. This is also true for the network brightness observed in Ca II K (Nindos and Zirin, 1998). Perhaps the observed relation between network brightness and the strength of the magnetic field is valid for most of the transition region network cells observed in different EUV radiation emitted by different ions. The linear relationship between network brightness and the strength of the magnetic field might simply suggest that the network heating depends on the number of flux tubes within the resolution element. Just from the linear relationship, one cannot arrive at the mechanism that causes the brightness of the network cells. Even though, the static magnetic field strength is related to the network brightness, dynamic process like velocity redistribution (micro-turbulence), which could result from a magnetohydrodynamic instability can enhance the brightness of the network elements, particularly in He II λ304 Å. The potential extrapolation of the photospheric magnetic field shows that the size of the magnetic network element matches well with the size of the He II 304 Å network element at 3000 km above the photosphere. As the height above the photosphere increases, only large size structures survive. The evolution of magnetic fields in large size structures controls the plasma in the upper atmosphere and hence the brightness of the network elements observed in EUV.

The characteristics of the network cells such as lifetime and size, observed in He II 304 Å filtergrams and the photospheric magnetograms are different. Although the extrapolated magnetic network cells showed similar sizes, the estimated lifetime was longer than that of the transition region network cells. At higher heights only large-size magnetic elements remain and the lifetime of these large-size network features are longer. This means that most of the observed He II 304 Å network elements are associated with the large-size magnetic elements. In other words, the large-size network magnetic fields decide the characteristics of the network cells observed in He II 304 Å, which in turn are guided by the underlying magnetic field. As the underlying magnetic field varies, the upper atmospheric magnetic field evolves in a different way. The computed potential extrapolated magnetic field can be used as proxy for the in-situ network magnetic field. The potential extrapolation is a model of flux tube in vacuum. It does not account for the plasma pressure. The field in a flux tube can be potential if it is axially symmetric and untwisted. As the plasma β is small in the transition region, one can treat the transition region as a vacuum. This suggests that the evolution of magnetic fields in large size network structures controls the physical characteristics of the network cells which are topologically connected to the underlying magnetic field.

The solar corona is magnetically structured. Magnetic heating of the solar corona can occur in a variety of ways, such as heating by slow and fast MHD waves, Alfvén waves, magnetic field dissipation and micro-flares. The pronounced EUV and X-ray emission from the active region corona may be related to the wave heating mechanism. Magnetic field inside umbra exhibits three and five minutes oscillations. The mechanical energy flux associated with these high frequency fluctuations is sufficient enough to heat the active region corona. This implies that the small-scale evolution of the magnetic field in large-size structures can feed the energy to heat the active region corona.

The relationship between the total magnetic energy and velocity of the CME and its close resemblance with the Sedov solution for speed and energy of a blast wave suggests that the source active region is the engine for the CME. Lack of any change in active region magnetic flux and magnetic energy in the photospheric level during CME suggests that the photospheric magnetic field is not affected by the upper atmospheric eruptive phenomena. Mass motions associated with the CMEs have a speed of 1000 km s^{-1} and photospheric speeds are of the order of 1 km s^{-1}. There are two time scales, 'slow' in the photosphere and 'fast' in the corona which represent two different types of physical processes, namely the quasi-static processes and the dynamic processes. The coronal field evolves with the quasi-static motions of the photospheric foot-points (Gold and Hoyle, 1960; Antiochos, Devore, and Klimchuk, 1999). Hence, the coronal structures are in the state of stress and when a critical point is reached beyond which there is no equilibrium, the restructuring of the magnetic field lines over an active region scale releases the energy that can push the material to the distant interplanetary medium. This means that the large-scale evolution of the magnetic fields can provide the energy for the large-scale mass ejection.

Thus, the evolution of magnetic fields in the solar atmosphere shows different phases on different spatial and temporal scales. More clearly, the brightness of the quiet Sun network and brightness of the active region chromosphere and corona as well as the kinetic energy carried by the CMEs are different manifestations of the magnetic field dynamics in the solar atmosphere. The small-scale dynamics of the magnetic field seems to power the sources of high energy radiation and the large-scale dynamics seems to power the sources of particle emission. In summary, the evolution of the solar magnetic field on different spatial and temporal scales provides the energy for both high energy radiation and particle emission from the Sun.

6.6 Outlook

The Sun is a virtual laboratory for plasma and nuclear physicists, because experiments involving large-scale magnetic fields and high temperatures that are available on the Sun cannot be carried out in the terrestrial laboratory. Helium was first detected in the solar atmosphere. Evidence for thermo-nuclear reactions, convective zone, oscillations, magnetic field, and energetic eruption, give rich information about the Sun and these results can be extended to any other star of similar type, where the features are unresolvable. There are many interesting phenomena occuring on the Sun at large and small-scales. Each of these phenomena needs observation with high spatial, temporal and spectral resolution. Some of the problems which are the extensions of the current work and which can be solved in the near future are described below:

(1) *Excitation of Helium ion in coronal holes and active regions*

Like in quiet part of the Sun, one can find network cells in coronal holes too. The coronal hole network brightness observed in He II 304 Å is three times lower than the quiet Sun network brightness (Feldman, Dammasch, and Wilhelm, 2000; Venkatakrishnan, 1999). According to Brueckner (1973), the network contrast in coronal hole, observed in He II 304 Å is lower than the normal transition region network cells. Munro and Withbroe (1972) have shown that the temperature of the corona in coronal holes is reduced, where the number density of electrons is lower. In coronal holes the temperature gradient is reduced by an order of magnitude. A decrease in temperature gradient would make the mixing of the 'hotter' electrons with the 'cooler' atoms and ions more difficult. That is, the diffusion would be reduced in coronal holes. Over coronal hole areas, the structures are larger with heights of $12''$ (8600 km) (Feldman, Winding, and Warren, 1999; Feldman, Dammasch, and Wilhelm, 2000). Observations show that the coronal hole boundary is sharp, suggesting that the excitation cannot be due to the coronal radiation. This problem can be further examined by comparing near simultaneous intensity images of He II $\lambda 304$ Å with the images acquired in coronal and chromospheric spectral lines and with the corresponding magnetograms. Apart from this, spectroscopic measurements are very important in this field of research. The analysis of line widths, shifts and time variations (e.g., Judge, Carlsson, and Wilhelm, 1997) is more reliable than just intensity correlation of the transition region images with the coronal and chromospheric images. Combination of intensity image correlation and results obtained from the radiative transfer calculations may further improve our knowledge. Recent observations show that the resonance lines are collisionally dominated, at least in the quiet Sun and in coronal holes (Jordan *et al.*, 1997). This domination in intensity is at the network boundaries where the magnetic pressure dominates over the gas pressure. Unlike in the quiet Sun network, the coronal hole magnetic field is open at the network boundaries. This means that the coronal hole magnetic field topology is different from the quiet Sun network magnetic field. The near simultaneous coronal, transition region and chromospheric intensity images taken in coronal hole and their line intensities and widths along with the magnetogram data would help in understanding the excitation of helium and its ions in coronal holes.

Most of the recent results support the formation of the He II $\lambda 304$ Å resonance line by collisional excitation in the quiet Sun. However, the formation mechanism is less clear in active regions and flares. Jordan, *et al.* (1993) conclude that the photo-ionization recombination mechanism plays a significant role in the coronal active regions, and is even predominant in many flares. In order to find the excitation mechanism of helium ions in the active regions we need to have reliable data. The existing EIT data is not suitable for such kind of analysis, since the active region photons are contaminated by the Si XI 303.3 Å spectral line (coronal line) (Delaboudiniere, 1995). Data taken from Coronal Diagnostic Spectrometer (CDS, Harrison *et al.*, 1995) would be more reliable for understanding the active region helium excitation. Continuous high resolution observation of active region in He II λ304 Å along with the magnetograms taken at a high cadence would be useful for studying this problem.

(2) *Flows and motions in and around sunspots*

Sunspots are magnetically structured clumpy plasma. The dynamics and evolution of a sunspot are influenced by plasma flows within and below photosphere in its vicinity. A variety of plasma flows have been observed in and around sunspots. They are: Evershed flow (Evershed, 1909), moat flows, radial flows around decaying spots (Sheeley and Bhatnagar, 1971; Sheeley, 1972), upflow and downflow in the umbra (Sigwarth, Schmidt, and Schuessler, 1998). High resolution observations have shown that there are other types of flows in sunspots. Muller (1973), Wang and Zirin (1992), Tönjes and Wöhl (1982) and Sobotka and Sutterlin (2001) have reported that the penumbral bright grains move horizontally towards the umbra of the sunspot. All these observations are based on the intensity images of a sunspot. Our own study (using magnetograms) suggests that there are persistent motions of features inside a sunspot. The magnitude of velocity is small in the umbra and it increases as the magnetic field strength decreases. These observations lead to a number of questions, viz. What determines the flow and its direction in sunspots? Are there flows in all the sunspots? What is the direction of flow, when the sunspot is at its different activity and evolutionary stages? Whether these flow patterns are same or opposite in the preceding and the following spot? Whether these steady flow direction and magnitude changes during a flare or CME? What are the lifetime and size of the features which are involved in the flows? In order to answer these questions one needs to study the flow patterns using high resolution intensity and magnetic images of sunspots. The study of the characteristics of the flow pattern in sunspots is essential since it may throw some light on the underlying process beneath the sunspots (Hurlburt and Rucklidge, 2000).

(3) *Origin of the speed of CME*

We have shown that the initial speed of a CME is related to the AR magnetic energy. As we did not have the vector magnetic field data, we could not find the available energy for the CME and the energy carried away by the CME. In future, we plan to measure the available energy using vector magnetic field data by computing the difference in energy estimated from the potential and actual vector field parameters. With the method of transformation from image co-ordinate to the heliographic co-ordinate systems (Venkatakrishnan and Gary, 1989) we can extend our work to all active regions which have produced CMEs and are located at different longitudes and latitudes. That is, one can extend the study to the active regions, which are close to the limb. Thus, our statistics would improve and we can confirm our results (Venkatakrishnan and Ravindra, 2003). Also, we would like see how the magnetic shear (Ambastha, Hagyard, and West, 1993) and magnetic helicity (Moon *et al.*, 2002a) change during the CME and compare these changes with the changes occurring in the same active regions in the absence of CMEs.

Bibliography

[1] Alissandrakis, C. E.:1981, "On the computation of constant α force-free magnetic field", *Astron. Astrophys.* **100**, 197.

[2] Ambastha, A., Hagyard, M. J., and West, E. A.:1993, "Evolutionary and flare-associated magnetic shear variations observed in a complex flare-productive active region", *Solar Phys.* **148**, 277.

[3] Andretta, V. and Jones, H. P.:1997, "On the role of the solar corona and transition region in the excitation of the spectrum of neutral helium", *Astrophys. J.* **489**, 375.

[4] Andretta, V., Jordan, S. D., Brosius, J. W., Davila, J. M., Thomas, R. J., Behring, W. E., Thompson, W. T., and Garcia, A.:2000, "The role of velocity redistribution in enhancing the intensity of the He II 304 Å line in the quiet-sun spectrum", *Astrophys. J.* **535**, 438.

[5] Antia, H. M. and Chitre, S. M.:1979, "Waves in the sunspot umbra", *Solar Phys.* **63**, 67.

[6] Antiochos, S. K., DeVore, C. R., and Klimchuk, J. A.:1999, "A model for solar coronal mass ejections", *Astrophys. J.* **510**, 485.

[7] Arfken, G. B. and Weber, H. J.:1995, *Mathematical methods for physicists*, Academic Press, Inc., San Diego, USA.

[8] Aschwanden, M. J., Poland, A. I., and Rabin, D. M.:2001, "The new solar corona", *Ann. Rev. Astron. Astrophys.* **39**, 175.

[9] Athay, R. G.:1988, "The origin of solar He II radiation", *Astrophys. J.* **329**, 482.

[10] Avrett, H. E., Vernazza, J. E., and Linsky, J. L.:1976, "Excitation and ionization of Helium in the solar atmosphere", *Astrophys. J.* **207**, L199.

[11] Balthasar, H. and Schmidt, W.:1993, "Polarimetry and spectroscopy of a simple sunspot. 2: On the height and temperature dependence of the magnetic field", *Astron. Astrophys.* **279**, 243.

[12] Balthasar, H.:1999, "Temporal fluctuations of the magnetic field in sunspots", *Solar Phys.* **187**, 389.

[13] Beckers, J. M. and Schultz, R. B.:1972, "Oscillatory motions in sunspots", *Solar Phys.* **27**, 61.

[14] Beckers, J. M. and Tallant, P. E.:1969, "Chromospheric inhomogeneities in sunspot umbrae", *Solar Phys.* **7**, 351.

[15] Bellot Rubio, L. R., Collados, M., Ruiz Cobo, B., and Hidalgo, R. I.:2000, "Oscillations in the photospheric of a sunspot umbra from the inversion of infrared stokes profiles", *Astrophys. J.* **534**, 989.

[16] Berger, T. E. and Lites, B. W.:2003, "Weak-field magnetogram calibration using stokes polarimeter flux density maps-II. SOHO/MDI full-disk mode calibration", *Solar Phys.* **213**, 213.

[17] Berrilli, F., Florio, A., and Ermolli, I.:1998, "On the geometrical properties of the chromospheric network", *Solar Phys.* **180**, 29.

[18] Bhatnagar, A., Livingston, W. C., and Harvey, J. W.:1972, "Observations of sunspot umbral velocity oscillations", *Solar Phys.* **27**, 80.

[19] Bhatnagar, A. and Tanaka, K.:1972, "Intensity oscillation in H_α: fine structure", *Solar Phys.* **24**, 87.

[20] Boberg, F. and Lindstedt, H.:2000, "Coronal mass ejections detected in solar mean magnetic field", *Geophys. Res. Lett.* **27**, 3141.

[21] Bogdan, T. J., Brown, T. M., Lites, B. W., and Thomas, J. H.:1993, "The absorption of p-modes by sunspots - Variations with degree and order", *Astrophys. J.* **406**, 723.

[22] Bogdan, T. J., Braun, D. C., Lites, B. W., and Thomas, J. H.:1998, "The seismology of sunspots: A comparison of time-distance and frequency-wavenumber methods", *Astrophys. J.* **492**, 379.

[23] Bogdan, T. J.:2000, "Sunspot oscillations: A review", *Solar Phys.* **192**, 373.

[24] Bovelet, B. and Wiehr, E.:2003, "Dynamics of the solar active region fine structure", *Astron. Astrophys.* **412**, 249.

[25] Boynton, G. C. and Torkelsson, U.:1996, "Dissipation of non-linear Alfven waves", *Astron. Astrophys.* **308**, 299.

[26] Braun, D. C., Duvall, T. L., Jr., and LaBonte, B. J.:1987, "Acoustic absorption by sunspots", *Astrophys. J.* **319**, 27.

[27] Braun, D. C., Duvall, T. L., Jr., and LaBonte, B. J.:1988, "The absorption of high-degree p-mode oscillations in and around sunspots", *Astrophys. J.* **335**, 1015.

[28] Braun, D. C., LaBonte, B. J., and Duvall, T. L., Jr.:1990, "The spatial distribution of p-mode absorption in active regions", *Astrophys. J.* **354**, 372.

[29] Braun, D. C.:1995, "Scattering of p-modes by sunspots. I. observations", *Astrophys. J.* **451**, 859.

[30] Brueckner, G. C.:1973, *Paper presented at IAU symposium 56, Surfers Paradise.*

[31] Brueckner, G. E., *et al.*:1995, "The Large Angle Spectroscopic Coronagraph (LASCO)", *Solar Phys.* **162**, 357.

[32] Bruls, J. H. M. J., Solanki, S. K., Rutten, R. J., and Carlsson, M.:1995, "Infrared lines as probes of solar magnetic features. VIII. MgI 12 μm diagnostics of sunspots", *Astron. Astrophys.* **293**, 225.

[33] Burlaga, L., Sittler, E., Mariani, F., and Schwenn, R.:1981, "Magnetic loop behind an interplanetary shock - Voyager, Helios, and IMP 8 observations", *J. Geophys. Res.* **86**, 6673.

[34] Burlaga, L., *et al.*:1998, "A magnetic cloud containing prominence material - January 1997", *J. Geophys. Res.* **103**, 277.

[35] Canfield, R. C., Hudson, H. S., and McKenzie, D. E.:1999, "Sigmoidal morphology and eruptive solar activity", *Geophys. Res. Lett.* **26**, 627.

[36] Chae, J., Wang, H., Qiu, J., Goode, P. R., Strous, L., and Yun, H. S.:2001, "The formation of a prominence in active region NOAA 8688. I. SOHO/MDI observations of magnetic field evolution", *Astrophys. J.* **560**, 476.

[37] Chandrasekhar, S.:1961, *Hydrodynamic and Hydromagnetic Stability*, Oxford Univ. Press, U.K.

[38] Chen, J. and Garren, D.:1993, "Interplanetary magnetic clouds: Topology and driving mechanism", *Geophys. Res. Lett.* **20**, 2319.

[39] Chen, J., Wang, H., Zirin, H., and Ai, G.:1994, "Observations of vector magnetic fields in flaring active regions", *Solar Phys.* **154**, 261.

[40] Chen, J.:2001, "Physics of coronal mass ejections: A new paradigm of solar eruptions", *Space Sci. Rev.* **95**, 165.

[41] Chitre, S. M.:1992, "Theory of umbral oscillations and penumbral waves", *in Sunspots: Theory and observations; proceedings of the NATO advanced research workshop on the theory of sunspots*, Cambridge, United Kingdom **A93**, 333.

[42] Choudhuri, A. R.:1999, *The physics of fluids and plasmas, An introduction to Astrophysics*, Cambridge University Press, UK.

[43] Christopoulou, E. B., Georgakilas, A. A., and Koutchmy, S.:2000, "Oscillations and running waves observed in sunspots", *Astron. Astrophys.* **354**, 305.

[44] Cranmer, S. R.:2000, "Ion cyclotron wave dissipation in the solar corona: The summed effect of more than 2000 ion species", *Astrophys. J.* **532**, 1197.

[45] Delaboudiniere, J. -P., *et al.*:1995, "EIT: Extreme-Ultraviolet Imaging Telescope for the SOHO mission", *Solar Phys.* **162**, 291.

[46] Domingo, V., Fleck, B., and Poland, A. I.:1995, "The SOHO mission: An overview", *Solar Phys.* **162**, 1.

[47] Dowdy, J. F., Jr.:1993, "Observational evidence for hotter transition region loops within the supergranular network", *Astrophys. J.* **411**, 406.

[48] Dryer, M.:1974, "Interplanetary shock waves generated by solar flares", *Space Sci. Rev.* **15**, 403.

[49] Dryer, M.:1994, "Interplanetary studies: propagation of disturbances between the sun and the magnetosphere", *Space Sci. Rev.* **67**, 363.

[50] Dryer, M.:1996, "Comments on the origins of coronal mass ejections", *Solar Phys.* **169**, 421.

[51] Eddy, J. A.:1983, "The maunder minimum: A reappraisal", *Solar Phys.* **89**, 195.

[52] Edwin, P. M. and Roberts, B.:1983, "Wave propagation in a magnetic cylinder", *Solar Phys.* **88**, 179.

[53] Evershed, J.:1909, "Radial movement in sun-spots", *Monthly Notices Royal Astron. Soc.* **69**, 454.

[54] Falconer, D. A.:2001, "A prospective method for predicting coronal mass ejections from vector magnetograms", *J. Geophys. Res.* **106**, 25185.

[55] Falconer, D. A., Moore, R. L., and Gary, G. A.:2002, "Correlation of the coronal mass ejection productivity of solar active regions with measures of their global non-potentiality from vector magnetograms: Baseline results", *Astrophys. J.* **569**, 1016.

[56] Falconer, D. A., Moore, R. L., and Gary, G. A.:2003, "CME prediction from line-of-sight magnetograms", *American Astronomical Society* **34**, 05.03.

[57] Feldman, U., Winding, K. G., and Warren, H. P.:1999, "Morphology of the quiet solar atmosphere in the 4×10^4 K$<$T$_e<1.4\times10^6$ K temperature regime", *Astrophys. J.* **522**, 1133.

[58] Feldman, U., Dammasch, I. E., and Wilhelm, K.:2000, "The morphology of the solar upper atmosphere during the sunspot minimum", *Space Sci. Rev.* **93**, 411.

[59] Foukal, P.:1990, *Solar Astrophysics*, John Wiley and Sons, Inc., New York.

[60] Foukal, P.:1971a, "Morphological relationships in the chromospheric H_α fine structure", *Solar Phys.* **19**, 59.

[61] Foukal, P.:1971b, "H_α fine structure and the chromospheric field", *Solar Phys.* **20**, 298.

[62] Freeland, S. L. and Handy, B. N.:1998, "Data analysis with the SolarSoft system", *Solar Phys.* **182**, 497.

[63] Gabriel, A. H.:1976, "A magnetic model of the solar transition region", *Philos. Trans. Roy. Soc. London* **281**, 339.

[64] Gaizauskas, V., Mandrini, C. H., Demoulin, P., Luoni, M. L., and Ovira, M. G.: 1998, "Interactions between nested sunspots. II. A confined X1 flare in a delta-type sunspot", *Astron. Astrophys.* **332**, 353.

[65] Gary, A.:1989, "Linear force-free magnetic fields for solar extrapolation and interpretation", *Astrophys. Suppl. Ser.* **69**, 323.

[66] Gilbert, H. R., Holzer, T. E., Burkepile, J. T., and Hundhausen, A. J.:2000, "Active and eruptive prominences and their relationship to coronal mass ejections", *Astrophys. J.* **537**, 503.

[67] Giovanelli, R. G.:1972, "Oscillations and waves in a sunspot", *Solar Phys.* **27**, 71.

[68] Gold, T. and Hoyle, F.:1960, "On the origin of solar flares", *Monthly Notices Royal Astron. Soc.* **120**, 89.

[69] Goldberg, L.:1939, "The temperature of the solar chromosphere", *Astrophys. J.* **89**, 673.

[70] Gonzalez, W. D. and Tsurutani, B. T.:1987, "Criteria of interplanetary parameters causing intense magnetic storms (Dst<-100 nT)", *Planet. Space Sci.* **35**, 1101.

[71] Goodman, J. W.:1985, *Statistical Optics*, John Wiley and Sons, New York.

[72] Gopalswamy, N.:2003, "Solar and geospace connections of energetic particle events", *Geophys. Res. Lett.* **30**, 8013.

[73] Gosling, J. T., Hildner, E., MacQueen, R. M., Munro, R. H., Poland, A. I., and Ross, C. L.:1974, "The outer solar corona as observed from Skylab: Preliminary results", *J. Geophys. Res.* **79**, 4581.

[74] Gosling, J. T., Hilder, E., MacQueen, R. M., Munro, R. H., Poland, A. I., and Ross, C. L.:1976, "The speeds of coronal mass ejection events", *Solar phys.* **48**, 389.

[75] Gosling, J. T., McComas, D. J., Phillips, J. L., and Bame, S. J.:1991, "Geomagnetic activity associated with earth passage of interplanetary shock disturbances and coronal mass ejections", *J. Geophys. Res.* **96**, 7831.

[76] Gosling, J. T.:1993, "The solar flare myth", *J. Geophys. Res.* **98**, 18937.

[77] Gurman, J. B. and House, L. L.:1981, "Vector magnetic fields in sunspots. I - Weak-line observations", *Solar Phys.* **71**, 5.

[78] Hagenaar, H. J., Schrijver, C. J., and Title, A. M.:1997, "The distribution of cell sizes of the solar chromospheric network", *Astrophys. J.* **481**, 988.

[79] Hagyard, M. J., Stark, B. A., and Venkatakrishnan, P.:1999, "A search for vector magnetic field variations associated with the M-class flares of 10 June 1991 in AR 6659", *Solar Phys.* **184**, 133.

[80] Harrison, R. A.:1995, "The nature of solar flares associated with coronal mass ejections", *Astron. Astrophys.* **304**, 585.

[81] Harrison, R. A., *et al.*:1995, "The Coronal Diagnostic Spectrometer for the Solar and Heliospheric Observatory", *Solar Phys.* **162**, 233.

[82] Hart, A. B.:1954, "Motions in the sun at the photospheric level, IV. The equatorial rotation and possible velocity fields in the photosphere", *Monthly Notices Royal Astron. Soc.* **114**, 17.

[83] Hart, A. B.:1956, "Motions in the sun at the photospheric level, VI. Large scale motions in the equatorial region", *Monthly Notices Royal Astron. Soc.* **116**, 38.

[84] Harvey, K. and Harvey, J.:1973, “Observations of moving magnetic features near sunspots”, *Solar Phys.* **28**, 61.

[85] Harvey, J. W. and Sheeley, N. R.:1977, “A comparison of He II 304 Å and He I 10830 Å spectroheliograms”, *Solar Phys.* **54**, 343.

[86] Hearn, A. G.:1969a, “A suggestion for the measurement of He II line intensities emitted by the Sun”, *Monthly Notices Royal Astron. Soc.* **142**, 259.

[87] Hearn, A. G.:1969b, “The differences between quiet and active regions measured by spectroheliograms in the neutral Helium resonance lines”, *Monthly Notices Royal Astron. Soc.* **144**, 351.

[88] Herbold, G., Ulmschneider, P., Spruit, H. C., and Rosner, R.:1985, “Propagation of nonlinear, radiatively damped longitudinal waves along magnetic flux tubes in the solar atmosphere”, *Astron. Astrophys.* **145**, 157.

[89] Hindman, B. W. and Brown, T. M.:1998, “Acoustic power maps of solar active region”, *Astrophys. J.* **504**, 1029.

[90] Hirayama, T.:1971, “Spectral analysis of four quiescent prominences observed at the peruvan eclipse”, *Solar Phys.* **17**, 50.

[91] Horn, T., Staude, J., and Landgraf, V.:1997, “Observations of sunspots umbral oscillations”, *Solar Phys.* **172**, 69.

[92] Howard, R. A., Sheeley, N. R., Jr., Michels, D. J., and Koomen, M. J.:1985, “Coronal mass ejections - 1979-1981”, *J. Geophys. Res.* **90**, 8173.

[93] Howard, R. F., Harvey, J. W., and Forgach, S.:1990, “Solar surface velocity fields determines from small magnetic features”, *Solar Phys.* **130**, 295.

[94] Hundhausen, A. J., Burkepile, J. T., and St. Cyr, O. C.:1994, "Speeds of coronal mass ejections: SMM observations from 1980 and 1984-1989", *J. Geophys. Res.* **99**, 6543.

[95] Hundhausen, A.:1999, "Coronal Mass Ejections" in K. T. Strong, J. L. R. Saba, B. M. Haisch, and J. T. Schmelz (eds.), *The many faces of the sun : a summary of the results from NASA's Solar Maximum Mission*, Springer-Verlag, Newyork, 143.

[96] Hurlburt, N. E. and Rucklidge, A. M.:2000, "Development of structure in pores and sunspots: flows around axisymmetric magnetic flux tubes", *Monthly Notices Royal Astron. Soc.* **314**, 793.

[97] Jones, H. P., Duvall, T. L. Jr., Harvey, J. W., Mahaffey, C. T., Schwitters, J. D., and Simmons, J. E.:1992, "The NASA/NSO spectromagnetograph", *Solar Phys.* **139**, 211.

[98] Jordan, C.:1975, "The intensities of Helium lines in the solar EUV spectrum", *Monthly Notices Royal Astron. Soc.* **170**, 429.

[99] Jordan, S. D., Thompson, W. T., Thomas, R. J., and Neupert, W. M.:1993, "Solar coronal observation and formation of the He II 304 Å line", *Astrophys. J.* **406**, 346.

[100] Jordan, S., Andretta, V., Garcia A., and Falconer, D.:1997, "Understanding the He II 304 Å resonance line in the Sun", *Proceedings of fifth SOHO workshop*, 17.

[101] Judge, P., Carlsson, M., and Wilhelm, K.:1997, "SUMER observations of the quiet solar atmosphere: The network chromosphere and lower transition region", *Astrophys. J.* **490**, L195.

[102] Kahler, S. W.:1992, "Solar flares and coronal mass ejections", *Ann. Rev. Astron. Astrophys.* **30**, 113.

[103] Kohl, J. L.:1977, "The components of the Balmer-alpha line of He II in the sun", *Astrophys. J.* **211**, 958.

[104] Komle, N.:1979, "Structure and evolution of magnetic network features", *Solar Phys.* **64**, 213.

[105] Kosovichev, A. G. and Zharkova, V. V.:1999, "Variations of photospheric magnetic field associated with flares and CMEs", *Solar Phys.* **190**, 459.

[106] Kosovichev, A. G. and Zharkova, V. V.:2001, "Magnetic energy release and transients in the solar flare of 2000 July 14", *Astrophys. J.* **550**, L105.

[107] Kupke, R., LaBonte, B. J., and Mickey, D. L.:2000, "Observational study of sunspot oscillations in stokes I, Q, U, V", *Solar Phys.* **191**, 97.

[108] Kusano, K., Maeshiro, T., Yokoyama, T., and Sakurai, T.:2002, "Measurement of helicity injection and free energy loading into the solar corona", *Astrophys. J.* **577**, 2002.

[109] Landgraf, V.:1997, "Search for magnetic field oscillations in a sunspot umbra", *Astron. Nachr.* **318**, 129.

[110] Lara, A., Gopalswamy, N., and DeForest, C.:2000, "Change in photospheric magnetic flux during mass ejections", *Geophys. Res. Lett.* **27**, 1435.

[111] Larson, D. E., *et al.*:1997, "Tracing the topology of the October 18-20, 1995, magnetic cloud with 0.1 - 10^2 keV electrons", *Geophys. Res. Lett.* **24**, 1991.

[112] Leighton, R. B., Noyes, R. W., and Simon, G. W.:1962, "Velocity fields in the solar atmosphere I. preliminary report", *Astrophys. J.* **135**, 474.

[113] Li, H., Sakurai, T., Ichimoto, K., and Ueno, S.:2000, "Magnetic field evolution leading to solar flares II. cases with high magnetic shear and flare-related shear change", *Publ. Astron. Soc. Japan* **52**, 483.

[114] Li, X.:2002, "Heating in coronal funnels by ion cyclotron waves", *Astrophys. J.* **571**, L67.

[115] Lites, B. W., Thomas, J. H., Bogdan, T. J., and Cally, P. S.:1998, "Velocity and magnetic field fluctuations in the photosphere of a sunspot", *Astrophys. J.* **497**, 464.

[116] Liu, Y. and Norton, A. A.:2001, "MDI measurement errors: The magnetic perspective", *SOI-Technical Note*, **TN-01-144**.

[117] Loughhead, R. E.:1968, "High resolution photography of the solar chromosphere", *Solar Phys.* **5**, 489.

[118] Low, B. C.:1985, "Modeling solar magnetic structures, measurement of solar vector magnetic fields", in M. J. Hagyard (ed.), *NASA conference publication* **2374**, 49.

[119] Low, B. C.:1990, "Equilibrium and dynamics of coronal magnetic fields", *Ann. Rev. Astron. Astrophys.* **28**, 491.

[120] Macpherson, K. P. and Jordon, C.:1999, "The anomalous intensities of helium lines in the quiet solar transition region", *Monthly Notices Royal Astron. Soc.* **308**, 510.

[121] MacQueen, R. M., Eddy, J. A., Gosling, J. T., Hildner, E., Munro, R. H., Newkirk, G. A., Jr., Poland, A. I., and Ross, C. L.:1974, "The outer solar corona as observed from Skylab: Preliminary results", *Astrophys. J.* **187**, L85.

[122] MacQueen, R. M., Csoeke-Poeckh, A., Hildner, E., House, L., Reynolds, R., Stanger, A., Tepoel, H., and Wagner, W.:1980, "The High Altitude Observatory coronagraph/polarimeter on the Solar Maximum Mission", *Solar Phys.* **65**, 91.

[123] MacQueen, R. M. and Fisher, R. R.:1983, "The kinematics of solar inner coronal transients", *Solar Phys.* **89**, 89.

[124] Martres, M. J., Michard, R., Soru-Iscovici, I., and Tsap, T. T.:1968, "Etude De la localisation des eruptions dans la structure magnetique evolutive des regions active solaries", *Solar Phys.* **5**, 187.

[125] Maxwell, A., Dryer, M., and McIntosh, P.:1985, "A piston-driven shock in the solar corona", *Solar Phys.* **97**, 401.

[126] Michalek, G., Gopalswamy, N., and Yashiro, S.:2003, "A New method for estimating widths, velocities and source locations of halo coronal mass ejections", *Astrophys. J.* **584**, 472.

[127] Michels, D. J., Howard, R. A., Koomen, M. J., Sheeley, N. R., Jr., and Rompolt, B.:1980, "The solar mass ejection of 8 May 1979", in M. Dryer and Tandberg-Hanssen (eds.), *Solar and interplanetary dynamics* **91**, 387.

[128] Milovanov, V. N.:1980, "Magnetographic studies of oscillations in the solar atmosphere", *Physica Solariterrestris* **13**, 109.

[129] Molodensky, M. M.:1974, "Equilibrium and stability of force-free magnetic field", *Solar Phys.* **39**, 393.

[130] Moon, Y. J., Chae, J., Choe, G. S., Wang, H., Park, Y. D., and Yun, H. S.: 2002a, "Flare activity and magnetic helicity injection by photospheric horizontal motions", *Astrophys. J.* **574**, 1066.

[131] Moon, Y. J., Choe, G. S., Wang, H., Park., Y. D., Gopalswamy, N., Yang, G., and Yashiro, S.:2002b, "A statistical study of two classes of coronal mass ejections", *Astrophys. J.* **581**, 694.

[132] Moore, R. L. and Tang, F.:1975, "Umbral oscillations and penumbral waves in H alpha", *Solar Phys.* **41**, 81.

[133] Moore, R., McKenzie, D. L., Svestka, Z., Widing, K. G., Dere, K. P., Antiochos, S. K., Dodson-Prince, H. W., Hiei, E., Krall, K. R., and Krieger, A. S.:1980, "The thermal X-ray flare plasma", in P. A. Sturrock (ed.), *Solar flares: A monograph from Skylab Solar Workshop II., Boulder, Colo.*, Colorado Associated University Press, Chapter 8, 341.

[134] Muller, R.:1973, "Etude morphologique et cinemtique des structures fines d'une tache solaire", *Solar Phys.* **29**, 55.

[135] Munro, R. H. and Withbroe, G. L.:1972, "Properties of a coronal "hole" derived from extreme-ultraviolet observations", *Astrophys. J.* **176**, 511.

[136] Munro, R. H., Gosling, J. T., Hildner, E., MacQueen, R. M., Poland, A. I. and Ross, C. L.:1979, "The association of coronal mass ejections with other forms of solar activity", *Solar Phys.* **61**, 201.

[137] Musielak, Z. E., Rosner, R., and Ulmschneider, P.:1990, "Generation of transverse magnetic tube waves and X-ray emissions from late-type dwarfs", in G. Wallerstein (ed.), *Astron. Soc. Pacific Conference Series,* Vol. 6, ASP, San Francisco, 79.

[138] Nakagawa, Y. and Raadu, M. A.:1972, "On practical representation of magnetic field", *Solar Phys.* **25**, 127.

[139] Nakariakov, V. M., Zhugzhda, Y. D., and Ulmschneider, P.:1996, "On the interaction of longitudinal and transversal waves in thin magnetic flux tubes", *Astron. Astrophys.* **312**, 691.

[140] Narain, U. and Ulmschneider, P.:1990, "Chromospheric and coronal heating mechanisms", *Space Sci. Rev.* **54**, 377.

[141] Nindos, A. and Zirin, H.:1998, "The relation of Ca II K features to magnetic field", *Solar Phys.* **179**, 253.

[142] Nitta, N. V. and Hudson, H. S.:2001, "Recurrent flare/CME events from an emerging flux region", *Geophys. Res. Lett.* **28**, 19.

[143] Norton, A. A., Ulrich, R. K., Bush, R. I., and Tarbell, T. D.:1999, "Characteristics of magnetohydrodynamic oscillations observed with the Michelson Doppler Imager", *Astrophys. J.* **518**, L123.

[144] Norton, A. A.:2000, " Study of solar photospheric MHD oscillation", *Ph.D. Thesis*, University of California, Los Angeles.

[145] Norton, A. A. and Ulrich, R. K.:2000, "Measuring magnetic oscillations in the solar photosphere: coordinated observations with MDI, ASP and MWO", *Solar Phys.* **192**, 403.

[146] Norton, A. A. and Ulrich, R. K.:2001, "Center-to-limb angle dependence of phases (v, $\delta|\mathrm{B}|$) observed with the Michelson Doppler Imager", *Astrophys. J.* **561**, 435.

[147] November, L. J.:1986, "Measurement of geometric distorion in a turbulent atmosphere", *Appl. Optics* **25**, 392.

[148] Parker, E. N.:1988, "Nanoflares and the solar X-ray corona", *Astrophys. J.* **330**, 474.

[149] Parker, E. N.:1991, "The phase mixing of Alfven waves, coordinated modes, and coronal heating", *Astrophys. J.* **376**, 355.

[150] Parker, E. N.:1994, *Spontaneous current sheets in magnetic fields: With applications to stellar X-rays*, Oxford University Press, New York.

[151] Parker, E. N.:1999, "Solar Physics: Sunny side of global warming", *Nature* **399**, 416.

[152] Patsourakos, S., Vial, J. -C., Gabriel, A. H., and Bellamine, N.:1999, "Transition-region network boundaries in the quiet Sun: Width variation with temperature as observed with CDS on SOHO", *Astrophys. J.* **522**, 540.

[153] Poedts, S. and Boynton, G. C.:1996, "Nonlinear magnetohydrodynamics of footpoint-driven coronal loops", *Astron. Astrophys.* **306**, 610.

[154] Prasad, S. and Dere, K. P.:2001, "Source regions of coronal mass ejections", *Astrophys. J.* **561**, 372.

[155] Press, W. H., Teukolsky, S. A., Vellerling, W. T., and Flannery, B. P.:1992, *Numerical recipes in C; The art of scientific computing*, Cambridge University Press, New Delhi.

[156] Raghavan, N.:1983, "A quantitative study of Ca II network geometry", *Solar Phys.* **89**, 35.

[157] Raju, K. P., Srikanth, R., and Singh, J.:1998, "The correlation lifetime of chromospheric Ca II K network cells", *Solar Phys.* **178**, 251.

[158] Ravindra, B. and Venkatakrishnan, P.:2003a, "On the correlation between the He II λ304 network brightening and the photospheric magnetic field", *Solar Phys.* **214**, 267.

[159] Ravindra, B. and Venkatakrishnan, P.:2003b, "Structure and evolution of the transition region network observed in He II λ304", *Solar Phys.* **215**, 239.

[160] Roberts, B.:1992, "Magnetohydrodynamic waves in structured magnetic fields", in *Sunspots: Theory and observations; proceedings of the NATO advanced research workshop on the theory of sunspots, Cambridge UK* **A93**, 303.

[161] Rogers, E. H.:1970, "Lifetime of the H_α chromospheric network", *Solar Phys.* **13**, 57.

[162] Rüedi, I., Solanki, S. K., Stenflo, J. O., Tarbell, T., and Scherrer, P. H.:1998, "Oscillations of sunspot magnetic fields", *Astron. Astrophys.* **335**, L97.

[163] Rüedi, I., Solanki, S. K., Bogdan, T., and Cally, P.:1999, "Sunspot magnetic oscillations: Comparison between observations and models", in K. N. Nagendra and J. O. Stenflo (eds.), *Solar Polarization*, Kluwer Academic Publishers, 337.

[164] Russell, C. T., McPherron, R. L., and Burton, R. K.:1974, "On the cause of geomagnetic storms", *J. Geophys. Res.* **79**, 1105.

[165] Sakurai, T.:1989, "Computational modeling of magnetic fields in solar active regions", *Space Sci. Rev.* **51**, 11.

[166] Sakurai, T., Shibata, K., Ichimoto, K., Tsuneta, S., and Acton, L. W.:1992, "Flare-related relaxation of magnetic shear as observed with the Soft X-ray Telescope of YOHKOH and with vector magnetographs", *Publ. Astron. Soc. Japan.* **44**, L123.

[167] Scherrer, P. H., *et al.*:1995, "The solar oscillations investigation - Michelson Doppler Imager", *Solar Phys.* **162**, 129.

[168] Scherrer, P. H.:2003, "Rapid variations of solar magnetic fields as seen in SOHO/MDI magnetograms", private communication.

[169] Schrijver, C. J. and Title, A. M.:2002, "The topology of a mixed-polarity potential field, and inferences for the heating of the quiet solar corona", *Solar Phys.* **207**, 223.

[170] Settele, A., Sigwarth, M., and Muglach, K.:2002, "Temporal and spatial variations of the magnetic field vector in sunspots", *Astron. Astrophys.* **392**, 1095.

[171] Sedov, L.:1959, *Similarity and dimensional methods in mechanics*, Academic Press, London/NY, 260.

[172] Shanmugaraju, A., Moon, Y. -J., Dryer, M., and Umapathy, S.:2003, "On the kinematic evolution of flare-associated CMEs", *Solar Phys.* **215**, 185.

[173] Sheeley, N. R., Jr. and Bhatnagar, A.:1971, "Two-dimensional observations of the velocity fields in and around sunspots", *Solar Phys.* **19**, 338.

[174] Sheeley, N. R., Jr.:1972, "Observations of the horizontal velocity field surrounding sunspots", *Solar Phys.* **25**, 98.

[175] Sheeley, N. R., Jr., Howard, R. A., Koomen, M. J., Michels, D. J., Harvey, J. W., and Harvey, K. L.:1982, "Observations of coronal structure during sunspot maximum", *Space Sci. Rev.* **33**, 219.

[176] Sheeley, N. R., Jr., Watter, J. H., Wang, Y. -M., and Howard, R. A.:1999, "Continuous tracking of coronal outflows: two kinds of coronal mass ejections", *J. Geophys. Res.* **104**, 24739.

[177] Shimizu, T. and Tsuneta, S.:1997, "Deep survey of solar nanoflares with YOHKOH", *Astrophys. J.* **486**, 1045.

[178] Shine, R., Gerola, H., and Linsky, J. L.:1975, "Diffusion effects on the line intensities of He I and He II in the solar transition region", *Astrophys. J.* **202**, L101.

[179] Sigwarth, M., Schmidt, W., and Schüssler, M.:1998, "Upwelling in a young sunspot", *Astron. Astrophys.* **339**, L53.

[180] Simon, G. W. and Leighton, R. B.:1964, "Velocity fields in the solar atmosphere. III. large-scale motion, the chromospheric network, and magnetic fields", *Astrophys. J.* **140**, 1120.

[181] Singh, J. and Bappu, K. P.:1981, "A dependence on solar cycle of the size of the Ca^+ network", *Solar Phys.* **71**, 161.

[182] Sobotka, M. and Sutterlin, P.:2001, "Fine structure in sunspots. IV. penumbral grains in speckle reconstructed images", *Astron. Astrophys.* **380**, 714.

[183] Solanki, S. K. and Hammer, R.:2001, "The solar atmosphere", *Kluwer Academic Publisheres*, Netherlands, 1065.

[184] Solanki, S. K.:2003, "Sunspots: An overview", *Astron. Astrphys. Rev.* **11**, 153.

[185] Solanki, S. K. and Rüedi. I.:2003, "Spatial and temporal fluctuations in sunspots derived from MDI data", *Astron. Astrophys.* **411**, 249.

[186] Spirock, J., Yurchyshyn, V. B., and Wang, H.:2002, "Rapid changes in the longitudinal magnetic field related to the 2001 April 2 X20 flare", *Astrophys. J.* **572**, 1072.

[187] Spruit, H. C.:1982, "Propagation speeds and acoustic damping of waves in magnetic flux tubes", *Solar Phys.* **75**, 3.

[188] Sridharan, R.:2003, "Techniques for achieving higher spatial resolution", *Ph. D. Thesis*, Indian Institute of Astrophysics, Bangalore University, Bangalore, India.

[189] Srikanth, R., Raju, K. P., and Singh, J.:1999, "The chromospheric network: dependence of cell lifetime on length-scale", *Solar Phys.* **184**, 267.

[190] Srikanth, R., Singh, J., and Raju, K. P.:2000, "Distribution of supergranular sizes", *Astrophys. J.* **534**, 1008.

[191] Srivastava, N. and Venkatakrishnan, P.:2002, "Relationship between CME speed and geomagnetic storm intensity", *Geophys. Res. Lett.* **29**, 9.

[192] Staude, J.:1999, "Sunspot Oscillations", in B. Schmieder, A. Hofmann, and J. Staude (eds.), *ASP Conf.ser.* **184**, 113.

[193] St. Cyr, O. C. and Webb, D. F.:1991, "Activity associated with coronal mass ejections at solar minimum-SMM observations from 1984-1986", *Solar Phys.* **136**, 379.

[194] St. Cyr, O. C., Burkepile, J. T., Hundhausen, A. J., and Lecinski, A. R.:1999, "A comparison of ground-based and spacecraft observations of coronal mass ejections from 1980-1989", *J. Geophys. Res.* **104**, 12493.

[195] Sturrock, P. A.:1980, "Solar flares", in P. Sturrock (ed.), *A monograph from SKYLAB solar workshop II*, Colorado associated university press, Boulder, A., Chapter 9, 411.

[196] Taylor, G. I.:1950, *Proc. Roy. Soc. America* **201**, 159.

[197] Thomas, J. H., Cram, L. E., and Nye, A. H.:1981, "Five-minute oscillations in sunspots", *BAAS* **13**, 858.

[198] Thompson, W. T., Neupert, W. M., Jordan, S. D., Jones, H. P., Thomas, R. J., and Schmieder, B.:1993, "Correlation of He II Lyman alpha with He I 10830 Å, and with chromospheric and EUV coronal emission", *Solar Phys.* **147**, 29.

[199] Thompson, B. J., Gurman, J. B., Neupert, W. M., Newmark, J. S., Delaboudiniere, J. -P., Cyr, O. C., and Stezelberger, S.:1999, "SOHO/EIT observations of the 1997 April 7 coronal transient: possible evidence of coronal moreton waves", *Astrophys. J.* **517**, L151.

[200] Tönjes, K. and Wöhl, H.:1982, "Motions and lifetimes of the penumbral bright grains in sunspots", *Solar Phys.* **75**, 63.

[201] Tousey, R. J. -D., Bartoe, J. -D., Bohlin, J. D., Brueckner, G. E., Purcell, J. D., Scherrer, V. E., Sheeley, N. R., Jr., Schumucher, R. J., and Vanhooser, M. E.:1973, "A preliminary study of the extreme ultraviolet spectroheliograms from Skylab", *Solar Phys.* **33**, 265.

[202] Ulmschneider, P., Priest, E. R., and Rosner, R.:1991, "Mechanisms of chromospheric and coronal heating", *Springer-Verlag New York*, **XV**, 649.

[203] Ulrich, R. K.:1996, "Observations of magnetohydrodynamic oscillations in the solar atmosphere with properties of Alfvén waves", *Astrophys. J.* **465**, 436.

[204] Venkatakrishnan, P. and Gary, G. A.:1989, "Off disk-center potential field calculations using vector magnetograms", *Solar Phys.* **120**, 235.

[205] Venkatakrishnan, P.:1999, "Comparative morphology of EIT/SOHO images and He II excitation", *Solar Phys.* **187**, 23.

[206] Venkatakrishnan, P., Kumar, B., and Tripathy, S. C.:2002, "Variation of acoustic power with magnetic field as seen in GONG+ data", *Solar Phys.* **211**, 77.

[207] Venkatakrishnan, P. and Ravindra, B.:2003, "Relationship between CME velocity and active region magnetic energy", *Geophys. Res. Lett.* **30**, 2181.

[208] Wang, H.:1988, "Structure of magnetic fields on the quiet sun", *Solar Phys.* **116**, 1.

[209] Wang, H., Zirin, H., Patterson, A., Ai, G., and Zhang, H.:1989, "Seventy-five hours of coordinated videomagnetograph observations", *Astrophys. J.* **343**, 489.

[210] Wang, H., Zirin, H., and Ai, G.:1991, "Magnetic flux transport of decaying active regions and enhanced magnetic network", *Solar Phys.* **131**, 53.

[211] Wang, H. and Zirin, H.:1992, "Flows around sunspots and pores", *Solar Phys.* **140**, 41.

[212] Wang, H., Ewell, M. W., Zirin, H., and Ai, G.:1994, "Vector magnetic field changes associated with X-class flares", *Astrophys. J.* **424**, 436.

[213] Wang, H., Spirock, T. J., Qiu, J., Ji, H., Yurchyshyn, V., Moon, Y. -J., Denker, C., and Goode, P. R.:2002a, "Rapid changes of magnetic fields associated with six X-class flares", *Astrophys. J.* **576**, 497.

[214] Wang, H., Ji, H., Schmahl, E. J., Qiu, J., Liu, C., and Deng, N.:2002b, "Sudden disappearance of a small sunspot associated with the 2002 February 20 M2.4 flare", *Astrophys. J.* **580**, L177.

[215] Wang, Y. -M., *et al.*:1997, "Association of Extreme-Ultarviolet Imaging Telescope (EIT) polar plumes with mixed-polarity magnetic network", *Astrophys. J.* **484**, L75.

[216] Webb, D. F. and Hundhausen, A. J.:1987, "Activity associated with the solar origin of coronal mass ejections", *Solar Phys.* **108**, 383.

[217] Webb, D. F., Cliver, E. W., Crooker, N. U., St. Cry, O. C. and Thompson, B. J.:2000, "Relationship of halo coronal mass ejections, magnetic clouds, and magnetic storms", *J. Geophys. Res.* **105**, 7491.

[218] Wilson, R. M. and Hildner, E.:1984, "Are interplanetary magnetic clouds manifestations of coronal transients at 1 AU?", *Solar Phys.* **91**, 169.

[219] Withbroe, G. L. and Noyes, R. W.:1977, "Mass and energy flow in the solar chromosphere and corona", *Ann. Rev. Astron. Astrophys.* **15**, 363.

[220] Wittmann, A.:1974, "Computation and observation of Zeeman multiplet polarization in fraunhofer Lines. III: Magnetic field structure of spot Mt. Wilson 18488", *Solar Phys.* **36**, 29.

[221] Wright, A. N. and Rickard, G. J.:1995, "A numerical study of resonant absorption in a magnetohydrodynamic cavity driven by a brodband spectrum", *Astrophys. J.* **444**, 458.

[222] Yashiro, S., Gopalswamy, N., Michalek, G., Rich, N., St Cyr, C. O., Plunckett, S. P., and Howard, R. A.:2002a, *J. Grophys. Res., Submitted.*

[223] Yashiro, S., Gopalswamy, N., Michalek, G., St. Cyr, O. C., Plunkett, S. P., and Howard, R. A,:2002b, "Properties of coronal mass ejections observed by SOHO", *American Geophysical Union, Spring Meeting.*

[224] Zarrow, D. M., Sterling, A. C., Thompson, B. T., Hudson, H. S., and Nitta, N.: 1999, "SOHO EIT observations of Extreme-Ultaviolet "Dimming", associated with a halo coronal mass ejections", *Astrophys. J.* **142**, L520.

[225] Zhang, J., Dere, K. P., Howard, R. A., Kundu, M. R., and White, S. M.:2001, "On the temporal relationship between coronal mass ejections and flares", *Astrophys. J.* **559**, 452.

[226] Zhang, J. and Wang, J.:2002, "Are homologous flare-coronal mass ejection events triggred by moving magnetic features?", *Astrophys. J.* **566**, L117.

[227] Zhugzhda, Y. D., Balthasar, H., and Staude, J.:2000, "Multi-mode oscillations of sunspots", *Astron. Astrophys.* **355**, 347.

[228] Zirin, H. and Stein, A.:1972, "Observations of running penumbral waves", *Astrophys. J.* **178**, 85.

[229] Zirin, H.:1975, "The helium chromosphere, coronal holes, and stellar X-rays", *Astrophys. J.* **199**, L23.

[230] Zirker, J. B.:1993, "Coronal heating", *Solar Phys.* **148**, 43.

List of Publications

I. Papers in Journals:

1. *On the correlation between the He II $\lambda 304$ network brightening and the photospheric magnetic field*, B. Ravindra and P. Venkatakrishnan, *Solar Phys.* **214**, 267 (2003).

2. *Structure and evolution of the transition region network observed in He II $\lambda 304$*, B. Ravindra and P. Venkatakrishnan, *Solar Phys.* **215**, 239 (2003).

3. *Relationship between CME velocity and active region magnetic energy*, P. Venkatakrishnan and B. Ravindra, *Geophy. Res. Lett.* **30**, 2181 (2003).

II. In Proceedings:

1. *Quiet Sun chromospheric network magnetic field*, B. Ravindra, *BASI* **31**, 297 (2003).

2. *On the rapid variations of solar magnetic fields*, P. Venkatakrishnan, Brajesh Kumar and B. Ravindra, *BASI* **31**, 299 (2003).

3. *The excitation of He ion in the solar atmosphere*, B. Ravindra and P. Venkatakrishnan, "Probing the Sun with high resolution", eds: S. C. Tripathy and P. Venkatakrishnan, Narosa Publishing House, New Delhi, 217 (2003).